Mechanical Engineering Series

Weinong Chen
Bo Song

Split Hopkinson (Kolsky) Bar

Design, Testing and Applications

Springer

Mechanical Engineering Series

For other titles published in this series,
www.springer.com/series/1161

Weinong W. Chen • Bo Song

Split Hopkinson (Kolsky) Bar

Design, Testing and Applications

Springer

Weinong W. Chen
School of Aeronautics and Astronautics
School of Materials Engineering
Purdue University
701 W. Stadium Avenue
West Lafayette, Indiana 47907-2045
USA
wchen@purdue.edu

Bo Song
Department of Mechanics of Materials
Sandia National Laboratories
7011 East Avenue
Livermore, California 94551-0969
USA
bsong@sandia.gov

ISSN 0941-5122
ISBN 978-1-4419-7981-0 e-ISBN 978-1-4419-7982-7
DOI 10.1007/978-1-4419-7982-7
Springer New York Dordrecht Heidelberg London

Preface

The objective of this book is to provide the readers with a working knowledge of dynamic experiments with a Kolsky bar, also widely known as a split Hopkinson pressure bar (SHPB). Kolsky bar has been extensively used for the characterization of material properties at high rates, where the results are a family of stress-strain curves with the strain rate as a parameter. Unlike quasi-static experiments for constitutive responses of materials, there is no standard approach currently available to measure the responses at high rates of deformation. Consequently, inconsistencies may exist in the results generated from different laboratories, with different bars, and by different operators. This book provides practical guidelines to design and perform Kolsky-bar experiments. The focus is on the improvement of experimental consistency using methods that facilitate the specimen to deform under desirable valid testing conditions. This book is not an extensive review of the Kolsky-bar technique. A number of review articles are available in literature. Rather, this book illustrates the design, execution, evaluation and application of Kolsky-bar experiments in details.

The presented topics start with the general concepts and fundamental principles of the Kolsky bars; followed by the design guidelines for various types of Kolsky-bar experiments; ranging from compression experiments on brittle, soft, and ductile materials; to experiments under multiaxial compression and at high/low temperatures; to tension/torsion experiments; as well as to intermediate strain rate experiments. Finally, the use of Kolsky bars for structural experiments are outlined. For each type of experiments, the design principles are introduced, critical issues are outlined, detailed examples are illustrated, and selected experimental results are summarized.

This book is the outgrowth of class notes developed for senior/graduate level classes on Dynamic Behavior of Materials at The University of Arizona, Purdue University, and a short course, Kolsky Bar, taught for the Society for Experimental Mechanics (SEM) at 2009 SEM Anneal Conference and Exposition on Experimental and Applied Mechanics. Due to the detailed levels of the materials presented in this book, the selection of the examples is mostly from the authors' own research experiences. However, we present the design guidelines and experimental setup for each class of Kolsky-bar experiments with a general sense such that the readers can utilize this book to design his/her own experiments per their specific requirements.

The authors are very fortunate to have the opportunities to focus their research on this specific area for an extended period of time. This is not possible without the guidance from our mentors, the long-term support by funding agencies and the collaboration/assistance by colleagues

and students. We are truly thankful to many people we have worked with over the past two decades.

Weinong Chen would like to express special acknowledgement to two people who brought him into the subject of the book and provide continuous support and interactions: Professor G. Ravichandran who is currently Director of Graduate Aerospace Laboratories at California Institute of Technology, and Dr. Michael J. Forrestal who retired as a Distinguished Member of Technical Staff from Sandia National Laboratories. The assistance of three bright Purdue graduate students, Hwun Park, Oscar Guzman, and Xu Nie, in making the figures consistent in this book is highly appreciated. The proofreading of portions of the manuscript by Drs. Danny Frew and John Foster is also appreciated.

Table of Contents

Chapter 1. Conventional Kolsky bars

A Kolsky bar, also widely known as a split Hopkinson pressure bar (SHPB), is a characterization tool for the mechanical response of materials deforming at high strain rates ($10^2 – 10^4$ s^{-1}). This chapter presents the brief history, general working principles, considerations in design, and data reduction process of a Kolsky bar, illustrated by its compression version.

1.1 Background

Generally, material properties such as yield stress and ultimate strength, listed in handbooks and design manuals, are obtained under quasi-static loading conditions using common testing load frames with the guidance of standardized testing procedures. To ensure product quality and reliability under impact conditions such as those encountered in the drop of personal electronic devices, vehicle collision, and sports impact, the mechanical responses of materials under such loading conditions must be characterized accurately. However, high-rate loading conditions are beyond the scope of conventional material testing machines.

For example, if one end of a 10-mm long specimen is deforming at speeds of 1 – 100 m/s, the strain rate in the specimen is $10^2 – 10^4$ s^{-1}. This strain-rate range is commonly faced in collision-related loading situations. However, this range is difficult for most testing machines to reach in a well-controlled manner. On the other hand, the strain-rate range produced by hammer impact corresponds to dynamic events commonly encountered in engineering applications, such as club impact on golf balls, helmet impact on hard surfaces, and bird impact on aircraft engine components. Therefore, it is desired to determine the material properties under hammer-blowing conditions.

A hammer can deform a specimen to failure; however, there are two major issues if the purpose of such a hammer impact is to characterize material properties. The first issue is that there is little detailed information that can be recorded. The second issue is that the conditions on the specimen are not well controlled. To obtain dynamic response of materials under laboratory controlled conditions, Kolsky (1949) solved these problems with a very cleaver solution. Instead of direct impact on the specimen, he placed two elastic rods on both sides of the specimen and then struck one of the rods with an explosive blast. This concept is schematically shown in Fig. 1.1, where the elastic rod between the external impact and the specimen is called the incident bar and the rod on the

W.W. Chen and B. Song, *Split Hopkinson (Kolsky) Bar: Design, Testing and Applications*, Mechanical Engineering Series, DOI 10.1007/978-1-4419-7982-7_1,

other side the transmission bar. The elastic rods are also called “input bar” and “output bar”, respectively, by many researchers. With this arrangement, when the incident bar is loaded by external impact such as a hammer strike, a compressive stress wave is generated and then propagates towards the specimen, moving the bar material towards the specimen as it sweeps by. When the wave arrives at the interface between the incident bar and the specimen, part of the wave is reflected back into the incident bar towards the impact end and the rest transmits through the specimen into the transmission bar. Laboratory instrumentation can record the stress waves in the incident bar propagating towards the specimen and being reflected back from the specimen and the wave in the transmission bar. Under this arrangement the impact event is controllable and quantitative. The impact velocity and specimen size may be varied to achieve different strain rates. Further analysis on the waves recorded in the impact event results in information regarding the loading conditions and deformation states in the specimen. Since it was first introduced by Kolsky in 1949, this system has been called the Kolsky bar or, as explained later, a split-Hopkinson pressure bar (SHPB).

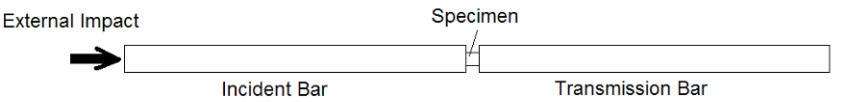

Figure 1.1 Illustration of Kolsky bar design

The Kolsky bar has two distinct features that are different from a conventional material testing machine. One difference is that the relatively small-diameter Kolsky bar is not drastically stiffer than the specimen, in contrast to the typical massive loading axis stiffness in hydraulic or screw-driven testing machines. The other difference is that the Kolsky bar does not have a closed-loop feed-back control system for real-time monitoring and adjustment of the loading conditions being applied to the specimen. The low stiffness ratio between the Kolsky bar and the specimen indicates that the specimen response cannot be ignored in experiment design. For example, loaded by identical loading pulses, the deformation of a rubber specimen is drastically different from that of a rock

specimen. Without a feed-back control system, the Kolsky-bar experiments can only be conducted, at most, in an open-loop manner that is iterated to approach desired testing conditions. These features lead to a complexity in the design of Kolsky-bar experiments. In order to achieve a desirable set of testing conditions on the specimen, the loading conditions in Kolsky-bar experiments must be determined according to the specimen's response that is initially unknown. Proper design of a Kolsky-bar experiment plays a critical role in obtaining valid results.

The original version of the Kolsky bar is for dynamic compression experiments. The Kolsky compression bar technique has been extensively developed in the past decades. Versions for other stress states, such as tension, torsion, triaxial, and axial/shear combination, have been developed based on the same principles and similar mechanisms. The differences among these methods are only in loading and specimen gripping methods. In the following section of this chapter, the compression version of the Kolsky bar is presented in more details such that the main features of the experimental method can be illustrated.

1.2 A Brief History of the Kolsky Bar

The compression version of the Kolsky bar is the original setup constructed by Herbert (Harry) Kolsky (1917-1992) in 1949. The Kolsky bar in compression is also widely called a split-Hopkinson pressure bar (SHPB) in memory of John Hopkinson (1849-1898) and his son, Bertram Hopkinson (1874-1918). In 1872, John Hopkinson conducted rupture tests of an iron wire by the impact of a drop weight. The schematic of this experiment is shown in Fig. 1.2. The rupture of the iron wire was found to locate at either the impact end or the fixed end depending on the speed of the impact, but regardless of the mass of the weight. This experiment originally reveals the propagation of stress waves in the wire; however, it was very challenging to measure stress wave propagation in the 19th century. His son, Bertram Hopkinson, in 1914, invented a pressure bar to measure the pressure produced by high explosives or high-speed impact of bullets (Fig. 1.3). As shown in Fig. 1.3, Bertram Hopkinson (1914) used pendulums with a pencil and paper to record the movements of the cylinders. The momentum of a cylinder (B) impacted by the detonation of the gun cotton (A) and a small rod (C) attached to the other end of B by magnetic attraction was calculated, which was a measure of the pressure generated by the detonation. When the length of C is shorter than half of the travel distance of stress wave over the load-

ing duration, both C and B would fly away. The length of C was then increased until B was at rest after loading. Only C flew away. The loading pulse duration was the round-trip time for the stress wave traveling in C. Therefore, a pressure-time curve produced by the detonation of the gun cotton was obtained. However, the measurements were approximate in nature due to the very limited measurement techniques at that time. This technique was further discussed by Landon and Quinney (1923). In 1948, Davis conducted a critical study of this technique. He used parallel plate and cylindrical condenser microphones to electrically measure the axial and radial movements of the bar loaded by detonation, as shown in Fig. 1.4. These electrical measurements are more accurate than Hopkinson's method. Davis (1948) also discussed the dispersion of stress waves when propagating in a long rod. The motivation of the works from Hopkinson to Davis was to measure the pressure-time curves produced by a detonation or a bullet impact.

Kolsky is the first person to extend the Hopkinson bar technique to measure stress-strain response of materials under impact loading conditions. The pressure bar technique developed by Kolsky (1949) was similar to that described by Davis (1948) except that Kolsky used two bars where a specimen was sandwiched in between, as shown in Fig. 1.5. With this unique technique, Kolsky (1949) obtained the dynamic stress-strain responses of several materials including polythene, natural and synthetic rubbers, polymethylmethacrylate (PMMA), copper, and lead.

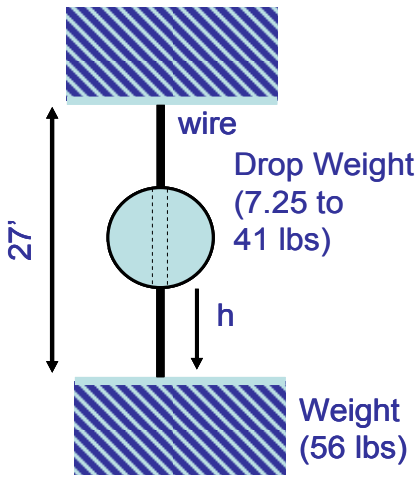

Figure 1.2 John Hopkinson experiment

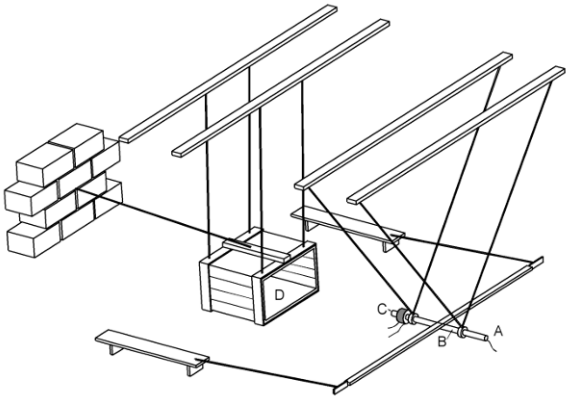

Figure 1.3 Bertram Hopkinson experiment
(*Reproduced from Hopkinson (1914)*)

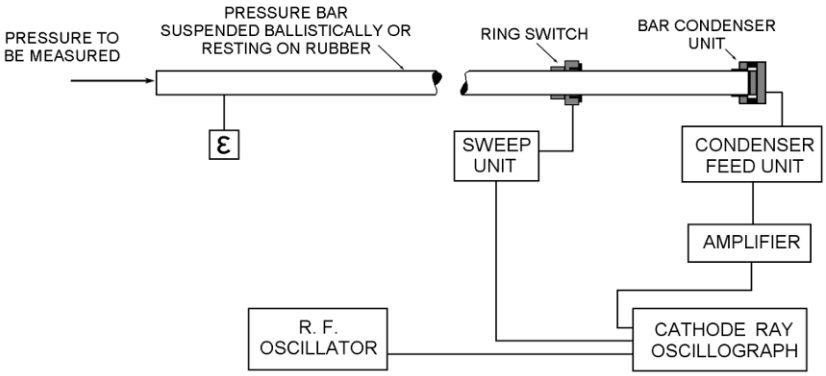

Figure 1.4 Davis bar
(Reproduced from Davis (1948) with permission)

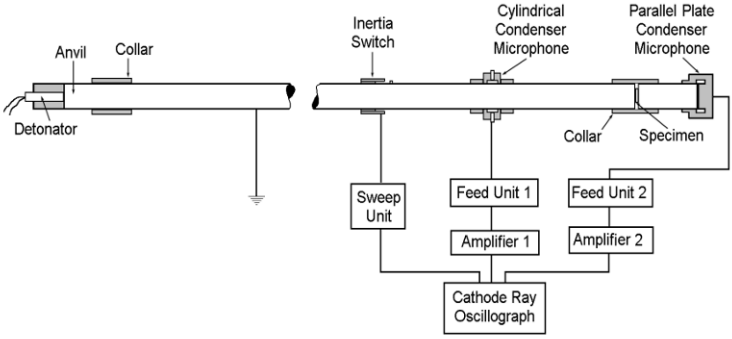

Figure 1.5 The original Kolsky bar
(Reproduced from Kolsky (1949) with permission)

In his paper, Kolsky (1949) presented a detailed procedure to calculate the stress-strain curves using the signals measured by the condenser microphones (Fig. 1.5). He pointed out that the specimen for a Kolsky-bar experiment must be sufficiently thin to neglect the axial inertia in the specimen. In addition, the interfacial frictions between the specimen and bar ends and the radial inertia in the specimen may bring uncertainties to the measured stress-strain response of the material being tested. It was found that larger-than-expected loading stresses were required to achieve a certain strain due to the friction between the specimen and the bars. Lubricants were therefore recommended by Kolsky (1949) to minimize the interfacial frictions. From an energy point of view, Kolsky (1949) also quantitatively analyzed the radial inertia in the specimen during high-rate deformation. The radial inertia was found to be only important when the strain rate is changing rapidly. Moreover, the radial inertia is proportional to the square of the radius of the specimen, indicating that smaller specimens should be used to minimize the radial inertia. Techniques for eliminating the inertia effects were later proposed through the design of length-to-diameter ratio of the specimen.

During the first several years after the Kolsky bar was developed, the stress waves in the bars were measured with condenser microphones. In 1954, Krafft et al. (1954) applied strain gage technique to the Kolsky bar to measure the stress waves, which has become a standard measurement technique for Kolsky-bar experiments. With regard to generating an impact stress pulse, Kolsky originally used an explosive detonator; however, generating repeatable results wth this method was difficult. A gun

was used by Krafft et al. (1954) to launch a projectile, typically called a striker bar, to impact on the incident bar. The impact of a striker bar generates a trapezoidal shaped pulse. Hauser et al. (1961) used a Hyge velocity generator to successfully produce a stress wave with constant amplitude. Trapezoidal incident pulses have been traditionally recognized as ideal for Kolsky-bar experiments. In 1964, Lindholm incorporated most of the previous improvements and presented an updated version of the Kolsky bar for valid dynamic characterization. Lindhom's design became a popular template of Kolsky bars in laboratories around the world thereafter, even though it is still being modified to obtain more accurate high-rate data for different materials. Recent reviews regarding the Kolsky-bar techniques have been conducted by Follansbee (1995), Gray (2000), Nemat-Nasser (2000), Subhash and Ravichandran (2000), Field et al. (2004), and Gama et al. (2004). The Kolsky-bar techniques have also been extended for tension and torsion tests based on very similar mechanisms but different loading and specimen gripping methods.

1.3 General Description of Kolsky Compression Bar

A general Kolsky compression bar apparatus consists of three major components: a loading device, bar components, and a data acquisition and recording system, as schematically shown in Fig. 1.6 (Song et al. 2009b).

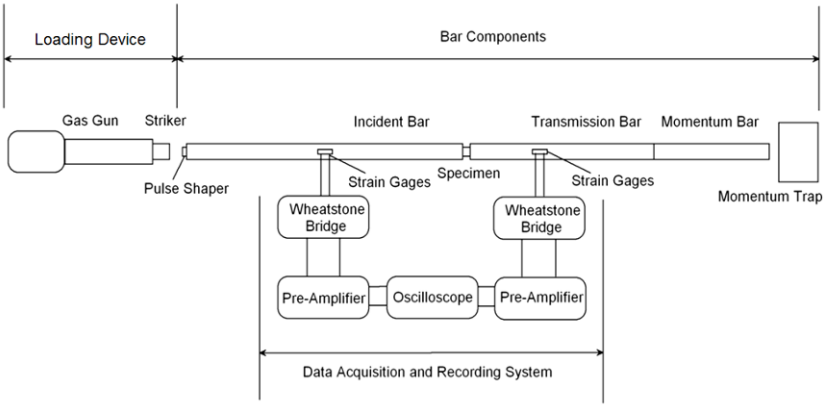

Figure 1.6 A general Kolsky compression bar apparatus
(Reproduced from Song et al. (2009b) with permission)

1. Loading device: In Kolsky-bar experiments, the loading should be controllable, stable and repeatable. Generally, the loading method can be static or dynamic type. The static type loading for Kolsky compression bar is schematically shown in Fig. 1.7. The section of the incident bar between the far end from the specimen and a clamp (Fig. 1.7) is statically loaded in compression. The stored energy due to such pre-compression is released into the initially unstressed section of the incident bar when the clamp is suddenly released. This produces a compression wave propagating in the incident bar towards the specimen. Now such a static type of loading has been seldom used for Kolsky compression bars. Instead, dynamic type of loading has been commonly used.

The detonation method used by Kolsky (1949) is a type of dynamic loading. However, the most common method for dynamic loading is to launch a striker impacting on the incident bar. Gas guns have been found to be efficient, controllable, and safe for Kolsky compression bars. The striker is launched by a sudden release of the compressed air or a light gas in a pressure storage vessel and accelerates in a long gun barrel until it impacts on the end of the incident bar. Gas venting holes are drilled on the side of the gun barrel near the exit such that the striker impacts the incident bar at constant speeds. The striking velocities are measured optically or magnetically just before the impact. This kind of striker launching mechanism produces a controllable and repeatable impact on the incident bar. The striking speed can be simply controlled by changing the pressure of the compressed gas in the tank and/or the depth of the striker inside the gun barrel. The loading duration is proportional to the length of the striker.

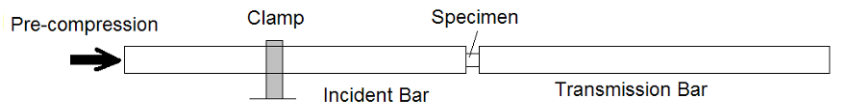

Figure 1.7. Static load type of Kolsky compression bar

2. Bar components: A typical Kolsky compression bar consists of an incident bar, a transmission bar, an optional extension bar, and a momentum trap device at the end. Typically, all bars are fabricated from the same material and of the same diameter. Since the stress waves inside the bars are measured by surface strains, the bar material is desired to be linearly elastic with a high yield strength. To ensure one-dimensional wave propagation in the bars, the bars must be physically straight, free to move on their supports with minimized friction. The whole bar system must be perfectly aligned along a common straight axis, which is the loading axis of the system. The incident bar should be at least twice as long as the striker to avoid overlapping between the incident and reflected pulses. The specimen is sandwiched between the incident and transmission bars (Fig. 1.6). The specimen axis is aligned with the common axis of the bar system.

3. Data acquisition and recording system: Strain gages have become a standard technique to measure bar strains in Kolsky-bar experiments. Two strain gages are usually attached symmetrically on the bar surface across a bar diameter. The signals from the strain gages are conditioned with a Wheatstone bridge. In a typical Kolsky-bar experiment, the voltage output from the Wheatstone bridge is of small amplitude, generally on the order of milli-volts. Therefore, a signal amplifier may be necessary to accurately record the low-amplitude voltage with an oscilloscope or a high-speed A/D computer board. Both the amplifier and the oscilloscope should have a sufficiently high frequency response to record the signal, the duration of which is usually shorter than one millisecond in a typical Kolsky-bar experiment. Generally speaking, the minimum frequency response of all the components in the data-acquisition system should be 100 KHz. Figure 1.8 shows a comparison of oscilloscope records of the same signal produced in a Kolsky-bar experiment where different low-pass filters (no filter or full, 100 kHz, 3 kHz, and 100 Hz) were applied to the pre-amplifier. It is clearly shown that, when the filters with 3 kHz and 100 Hz are applied, the recorded signals are significantly distorted even though the oscilloscope has an adequate frequency response.

In a typical Kolsky compression bar experiment, the stress wave is generated by impact of the striker on the incident bar. Figure 1.9 shows a position-time (X-t) diagram of the stress wave propagation in the bars. When the compression wave in the incident bar propagates to the interface between the incident bar and the specimen, part of it is reflected back into the incident bar while the rest transmits into the specimen and gets reflected back and forth inside the specimen due to wave impedance mismatch between the specimen and bars. These reflections build up the stress level in the specimen gradually and compress the specimen. The

interaction of the stress waves in the specimen with the specimen/transmission bar interface builds the profile of the transmitted signal. Due to the thin specimen used in Kolsky-bar experiment, the stress wave propagation in the specimen is usually ignored by assuming equilibrated stress in the specimen. This assumption and validation of stress equilibration in the specimen will be discussed in detail in Chapter 2.

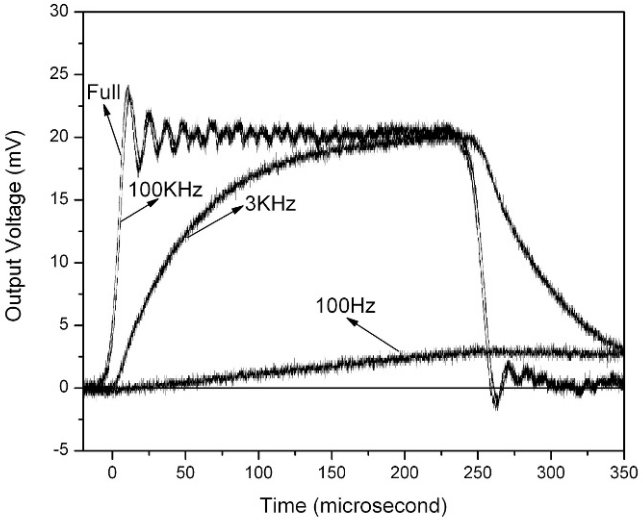

Figure 1.8. A comparison of oscilloscope records with different filters.

The impact of the striker also generates a compression wave in the striker, which is reflected back at the free end as a tension wave (Fig. 1.9). This tension wave transmits in the incident bar as an unloading wave. Similar to the compression wave, part of this unloading wave is reflected back and the rest transmits into the transmission bar at the bar/specimen interface, while the specimen is unloaded (Fig. 1.9). Hence, the loading duration, T, produced in a Kolsky-bar experiment is determined by the striker length, L,

$$T = \frac{2L}{C_{st}} \tag{1.1}$$

where C_{st} is the elastic wave speed of the striker material. Commonly, the striker has the same material and cross section as the incident and transmission bars. The length of generated stress wave is double of the striker length.

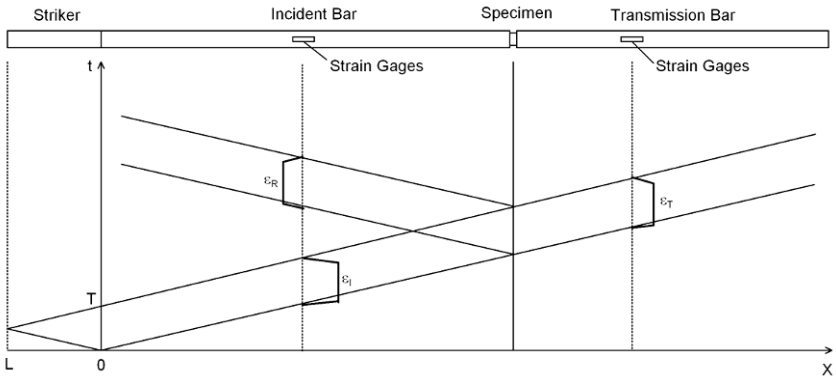

Figure 1.9. X-t diameter of stress wave propagation in a Kolsky bar system
(Reproduced from Song et al. (2009b) with permission)

In the case where the striker has the same material and diameter as the incident bar, the stress (or strain) amplitude of the incident pulse, σ_I (or ε_I), produced by the striker impact depends on the striking velocity, v_{st},

$$\sigma_I = \frac{1}{2}\rho_B C_B v_{st} \tag{1.2}$$

or

$$\varepsilon_I = \frac{1}{2} \cdot \frac{v_{st}}{C_B} \tag{1.3}$$

where ρ_B and C_B are the density and elastic bar wave speed of the bar material, respectively. The incident and reflected pulses are measured by the strain gages on the incident bar; whereas, the transmitted pulse is measured by the strain gages on the transmission bar (Fig. 1.9). The relation expressed by (1.3) is often used as a calibration for the Kolsky-bar system before mechanical experiment.

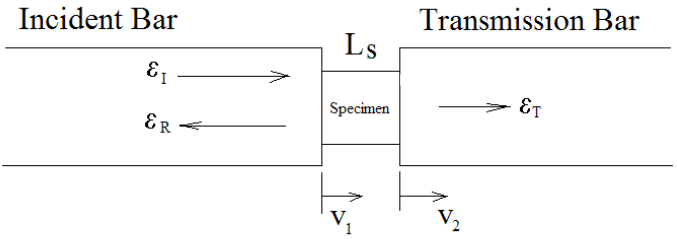

Figure 1.10 Testing section of Kolsky bar

Assuming that the stress waves propagate in both the incident and transmission bars without dispersion, i.e., the pulses recorded at the strain gage locations represent those at the bar ends in contact with the specimen, one dimensional stress wave theory relates the particle velocities at both ends of the specimen to the three measured strain pulses (Fig. 1.10),

$$v_1 = C_B(\varepsilon_I - \varepsilon_R) \tag{1.4}$$

$$v_2 = C_B\varepsilon_T \tag{1.5}$$

where the subscripts, I, R, and T, represent the incident, reflected, and transmitted pulses, respectively. The average engineering strain rate and strain in the specimen are

$$\varepsilon = \frac{v_1 - v_2}{L_s} = \frac{C_B}{L_s}\left(\varepsilon_I - \varepsilon_R - \varepsilon_T\right) \tag{1.6}$$

$$\varepsilon = \int_0^t \varepsilon dt = \frac{C_B}{L_s} \int_0^t \left(\varepsilon_I - \varepsilon_R - \varepsilon_T\right) dt \tag{1.7}$$

where L_s is the initial length of the specimen. The stresses at both ends of the specimen are calculated with the following elastic relations,

$$\sigma_1 = \frac{A_B}{A_s} \cdot E_B \left(\varepsilon_I + \varepsilon_R\right) \tag{1.8}$$

$$\sigma_2 = \frac{A_B}{A_s} \cdot E_B \cdot \varepsilon_T \tag{1.9}$$

where A_B and A_s are the cross-sectional areas of the bars and the specimen, respectively; and E_B is Young's modulus of the bar material.

As mentioned earlier, the specimen is assumed to be stress equilibrated in a Kolsky-bar experiment. This assumption must be satisfied in dynamic characterization of material properties. Consequently, the specimen deforms nearly uniformly such that the specimen response averaged over its volume is a good representative of the point-wise valid material behavior. The stress equilibration is expressed as,

$$\sigma_1 = \sigma_2 \tag{1.10}$$

or from (1.8) and (1.9)

$$\varepsilon_I + \varepsilon_R = \varepsilon_T \tag{1.11}$$

Equations (1.6), (1.7), and (1.9) can thus be simplified as the follows

$$\varepsilon = -2 \frac{C_B}{L_s} \varepsilon_R \tag{1.12}$$

$$\varepsilon = -2 \frac{C_B}{L_s} \int_0^t \varepsilon_R dt \tag{1.13}$$

$$\sigma = \frac{A_B}{A_s} E_B \varepsilon_T \tag{1.14}$$

The above equations are in engineering measurements and the symbol is taken positive in compression. When the specimen stress is not in perfect equilibrium, the stress in the specimen may be calculated by taking the mean value of the stresses at both specimen ends,

$$\sigma = \frac{1}{2}(\sigma_1 + \sigma_2) = \frac{1}{2} \cdot \frac{A_B}{A_s} \cdot E_B(\varepsilon_I + \varepsilon_R + \varepsilon_T) \tag{1.15}$$

This procedure produces an averaged specimen stress. When the stress or strain in the specimen is in a drastic non-uniformity, Equation (1.15) is not a valid stress measurement. After the specimen stress and strain histories are obtained, the stress-strain relation is found by eliminating the time variable.

All above equations were derived from the conservations of mass and momentum with the assumption of one-dimensional wave propagation. Now we analyze the energy distribution in a Kolsky compression bar experiment on a perfectly plastic specimen through conservation of energy (Song and Chen 2006).

When stress wave propagates in a long rod, the mechanical energy of the stress wave takes the form of the strain energy through bar deformation and the kinetic energy through bar motion. When the stress wave propagates in the incident bar, the elastic strain energy (E_I) carried by the incident wave can be calculated, on an average sense, through the incident strain, ε_I

$$\mathrm{E}_I = V_1 \int_0^{\varepsilon_I} \sigma d\varepsilon \tag{1.16}$$

where V_1 is the deformed volume in the incident bar. It is noted that, during stress wave propagation, only a portion of the incident bar, at any moment, is involved in the elastic deformation by the incident pulse. The deformed volume (V_1) in an incident bar depends on loading duration and bar cross-sectional area, which can be expressed as

$$V_1 = A_0 C_0 T \tag{1.17}$$

where T is the loading duration (1.1). For a linearly elastic bar,

$$\sigma = E_B \varepsilon \tag{1.18}$$

Equation (1.16) can be rewritten as

$$\mathrm{E}_I = \frac{1}{2} A_B C_B E_B T \varepsilon_I^{\,2} \tag{1.19}$$

The elastic strain energies, E_R and E_T, associated with the reflected and transmitted waves, respectively, can be calculated by similar derivations

$$\mathrm{E}_R = \frac{1}{2} A_B C_B E_B T \varepsilon_R^{\,2} \tag{1.20}$$

$$\mathrm{E}_T = \frac{1}{2} A_B C_B E_B T \varepsilon_T^{\,2} \tag{1.21}$$

The contribution of elastic strain energy in the bars to the specimen deformation can be calculated as

$$\delta_{\mathrm{E}} = \mathrm{E}_I - \mathrm{E}_R - \mathrm{E}_T = \frac{1}{2} A_B C_B E_B T \left(\varepsilon_I^{\,2} - \varepsilon_R^{\,2} - \varepsilon_T^{\,2} \right) \tag{1.22}$$

or

$$\delta_{\mathrm{E}} = -A_B C_B E_B T \varepsilon_R \varepsilon_T \tag{1.23}$$

when the specimen is under dynamic stress equilibrium. It is understood that the energy difference (δ_{E}) in (1.23) is positive since the reflected strain, ε_R, takes the opposite sign of the incident and transmitted strains.

Now we consider the kinetic energy contribution. The kinetic energy (K_I) of the incident bar after the incident wave passes can be expressed as

$$\mathrm{K}_I = \frac{1}{2} m v_I^{\,2} \tag{1.24}$$

where m and v_I are mass and particle velocity of the deformed portion in the incident bar, respectively,

$$m = \rho_B A_B C_B T \tag{1.25}$$

$$v_I = C_B \varepsilon_I \tag{1.26}$$

Equation (1.24) is thus rewritten as

$$\mathrm{K}_I = \frac{1}{2} \rho_B A_B C_B{}^3 T \varepsilon_I{}^2 \tag{1.27}$$

The kinetic energies associated with the reflected and transmitted pulses are

$$\mathrm{K}_R = \frac{1}{2} \rho_B A_B C_B{}^3 T \varepsilon_R{}^2 \tag{1.28}$$

$$\mathrm{K}_T = \frac{1}{2} \rho_B A_B C_B{}^3 T \varepsilon_T{}^2 \tag{1.29}$$

The contribution of kinetic energy to the specimen deformation is

$$\delta_{\mathrm{K}} = \mathrm{K}_I - \mathrm{K}_R - \mathrm{K}_T = \frac{1}{2} \rho_B A_B C_B{}^3 T \left(\varepsilon_I{}^2 - \varepsilon_R{}^2 - \varepsilon_T{}^2 \right) \tag{1.30}$$

or

$$\delta_{\mathrm{K}} = -\rho_B A_B C_B{}^3 T \varepsilon_R \varepsilon_T \tag{1.31}$$

when the specimen is in stress equilibrium. For linear elastic bars, it yields

$$E_B = \rho_B C_B{}^2 \tag{1.32}$$

Equation (1.31) now becomes

$$\delta_{\mathrm{K}} = -A_B E_B C_B T \varepsilon_R \varepsilon_T \tag{1.33}$$

It is observed that (1.33) has the same form as (1.23).

If we assume the specimen possesses a perfectly plastic response, the specimen deformation energy is simplified as

$$\mathrm{E}_s = A_s L_s \sigma_y \varepsilon_p \tag{1.34}$$

where A_s and L_s are initial cross-sectional area and length of the specimen, respectively; σ_y and ε_p are yield strength and plastic strain of the specimen,

$$\sigma_y = \frac{A_B}{A_s} E_B \varepsilon_T \tag{1.35}$$

$$\varepsilon_p = \varepsilon \cdot T = -2\frac{C_B}{L_s}\varepsilon_R T \tag{1.36}$$

Equation (1.36) is based on constant strain rate deformation in the specimen. Therefore, (1.34) is expressed as

$$\mathrm{E}_s = -A_B E_B C_B T \varepsilon_R \varepsilon_T = 2\delta_{\mathrm{E}} = 2\delta_{\mathrm{K}} \tag{1.37}$$

Equation (1.37) indicates that the energy coming from the elastic strain energy in the bars provides half of the energy necessary for the specimen plastic deformation while the incident kinetic energy contributes the other half of the energy. This analysis does not include the kinetic energy in the specimen.

1.4 Design of Kolsky Compression Bar

The design of a Kolsky compression bar aims at a robust dynamic experimental facility that has:

- Controllable and consistent impact by the striker
- Straight and long bars for one-dimensional stress wave propagation
- Minimized friction between the bars and their supports
- Highly precise alignment of the bar system
- High resolution data acquisition

As in any engineering development, there are many possible valid designs of the Kolsky-bar setup. We give one design example of the Kolsky compression bar here. The perspective view and actual photograph of the Kolsky compression bar at Sandia National Laboratories, California are shown in Figs. 1.11 and 1.12, respectively (Song et al. 2009b).

To facilitate precision alignment, the Kolsky-bar system is built on the base of a long optical table. The striker is launched by a gas gun. A thin layer of Teflon® is coated on the surface of the striker in order to minimize the friction between the striker and the gun barrel. A series of pillow blocks with built-in Frelon®-coated linear bearings are mounted on aluminum stands on the optical table and support the bars. The coefficient of friction between the self-lubricated Frelon® and a standard Rockwell C60 steel shaft is 0.125 which is lower than most metal-to-metal contacts. Using additional lubricant, such as lightweight petroleum-based grease, the friction is further reduced. The pillow blocks are made of 6061-T6 aluminum with clear anodized finish. The centerline dimensions of the pillow blocks have a tolerance within ±0.015 mm.

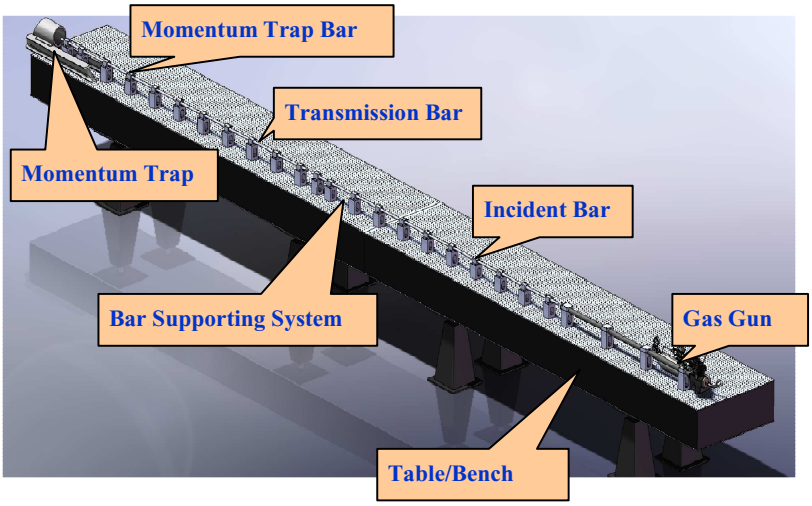

Figure 1.11 A perspective view of the Kolsky compression bar
(Reproduced from Song et al. (2009b) with permission)

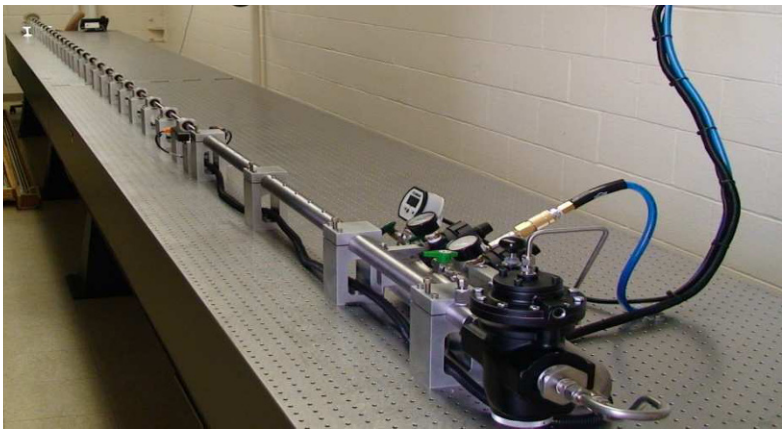

Figure 1.12 Photograph of the Kolsky compression bar
(Reproduced from Song et al. (2009b) with permission)

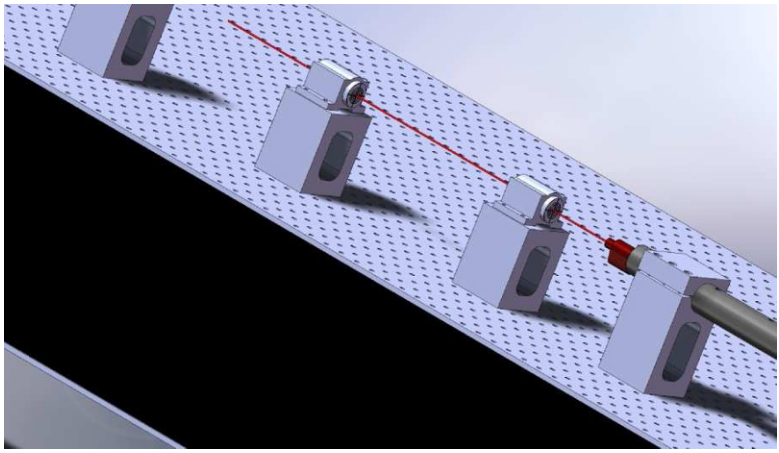

Figure 1.13 Laser alignment system
(Reproduced from Song et al. (2009b) with permission)

A laser alignment system is used for the fine adjustments of the bar system alignment. As shown in Fig. 1.13, this laser alignment system consists of a laser bore scope, a precisely machined sleeve as the laser scope holder, and targets with a 0.254-mm diameter pinhole on the center. The machined sleeve is placed inside the gun barrel. The centerline of the sleeve and the laser is aligned with the axis of the Kolsky bar system. The targets with the same diameter as the bars are fit snugly into the linear bearings in the pillow blocks. The pillow blocks are carefully adjusted until the laser beam passes through all the pinholes on the targets.

Metallic high strength bars are most commonly used as the choice for bar material. When characterizing soft materials, bars with lower stiffness such as aluminum bars and/or smaller cross-sectional areas are needed to amplify the transmitted stress. Usually the bars are heat-treated, straightened, and centerless ground to the desired diameters.

The momentum trapper absorbs the axial impact energy in an experiment. Ideally, it should be on a support system separate from the bar supports to minimize the effects of impact loading on the bar alignment, in particular, when the impact energy is high to deform a strong specimen or to deform a specimen to large strains.

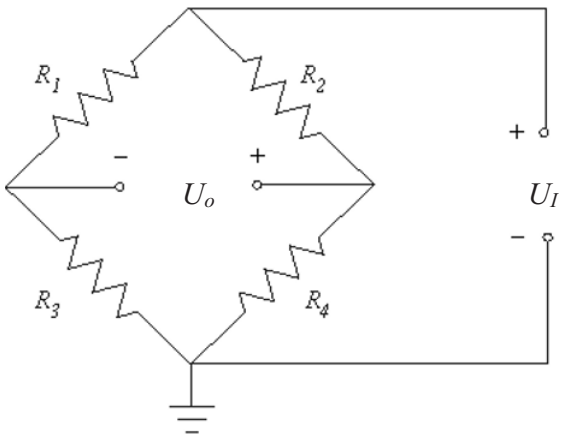

Figure 1.14 The Wheatstone bridge.

To measure the striker velocity just before impact, a laser-beam measurement system is used. A transmitter in the laser system generates a parallel light curtain. When the striker moves in, the light curtain is blocked progressively. The receiver detects the light intensity change and outputs an analog signal in voltage, which is recorded as a function of time with a digital oscilloscope.

The strains associated with the stress waves in the bars are recorded with strain gages on the bar surfaces through Wheatstone bridges, a diagram of which is shown in Fig. 1.14. There are two options for connecting the strain gages to the Wheatstone bridge.

Option 1: the strain gages are connected to the opposite legs of the bridge, e.g., $R_1 = R_4 = R_{sg}$, in the Wheatstone bridge, which is a typical half bridge configuration. The resistance of the strain gages should match with the dummy resistors on the other legs of the bridge. Axial deformation of the bar, in either compression or tension, results in the change of resistance (ΔR) of the strain gages on its surface,

$$R_1 = R_4 = R_{sg} = R + \Delta R \tag{1.38}$$

where $R = R_2 = R_3$. The voltage output, U_O, from the Wheatstone bridge under a certain excitation voltage (U_I) is

$$U_O = \left(\frac{R_4}{R_2 + R_4} - \frac{R_3}{R_1 + R_3} \right) \cdot U_I \tag{1.39}$$

Then we have

$$U_0 = \frac{\Delta R/R}{2 + \Delta R/R} U_I \approx \frac{1}{2} \frac{\Delta R}{R} U_I \tag{1.40}$$

The gage factor of the strain gage is defined as

$$G_F = \frac{\Delta R}{R} \frac{1}{\varepsilon} \tag{1.41}$$

Then we have the following relationship between U_O and ε,

$$\varepsilon = \frac{2 \cdot U_O}{G_F \cdot U_I} \tag{1.42}$$

Therefore, the bar strain can be calculated from the voltage output of the Wheatstone bridge with (1.42). The equation (1.42) also indicates that, for a fixed amount of strain, a higher gage factor and/or a higher input voltage generates a higher output voltage. This can provide a guideline in selections of strain gages and excitation voltage of the Wheatstone bridge, especially when the strain is small.

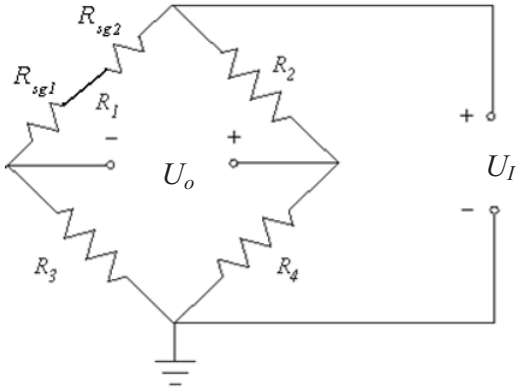

Figure 1.15 Wheatstone bridge (option 2)

Option 2. Both strain gages across the bar diameter at a bar location are connected in serial to the same leg ($R_{sg1} = R_{sg2} = R_{sg}$) in the Wheatstone bridge, as shown in Fig. 1.15. Such an assembly is called a quarter bridge,

$$R_1 = 2R_{sg} \tag{1.43}$$

$$R_2 = R_3 = R_4 = R \tag{1.44}$$

Note that, in this case, the resistance of the resistors on the other legs of the bridge should be twice as much as each strain gage, or the sum of both strain gages to balance the Wheatstone bridge,

$$R = 2R_{sg} \tag{1.45}$$

When the bar is subject to deformation, the total resistance change on the strain gage leg is ΔR, where each strain gage contributes half ,

$$R_1 = R + \Delta R \tag{1.46}$$

The voltage output of the Wheatstone bridge is calculated with (1.39) as

$$U_o = \left(\frac{1}{2} - \frac{1}{2 + \Delta R/R} \right) \cdot U_I \tag{1.47}$$

Applying (1.41) to (1.47) yields the bar strain

$$\varepsilon = \frac{4 \cdot U_O}{G_F \cdot U_I} \tag{1.48}$$

In Kolsky-bar experiments, minor misalignment along the bar system can result in bending wave, which can also be sensed by the strain gages on the bar surface. The signals associated with the bending waves can cause confusion and distortion in the strain gage measurements. When a bar is loaded in bending, one surface, e.g., the top surface, is subjected to tension; whereas, the opposite surface, i.e., the bottom surface, is in compression. Accordingly, in addition to the resistance change due to axial compression or tension, there is an additional resistance change due to the bending for each strain gage. The additional resistance change ($\Delta R'$) is the same in amplitude but with opposite signs in the pair of strain gages,

$$R_{sg1} = R' + \Delta R' \tag{1.49}$$

$$R_{sg2} = R' - \Delta R' \tag{1.50}$$

Here, R' has accounted for the resistance change due to axial compression or tension. Whether the strain gages are connected on the opposite legs (option 1) or on the same leg (option 2) in the bridge, the bending

effect ($\Delta R'$) is eliminated automatically. Only axial deformation is measured. It has to be emphasized, however, that proper connection of the strain gages just removes the bending from the strain gage measurements. The bending wave should be physically eliminated with a carefully aligned bar system.

Again, the data acquisition and recording system should have at least 100 kHz frequency response to record sufficient details from Kolsky-bar experiments.

1.5 Kolsky Bars of Large and Small Diameters

The diameter of most Kolsky compression bar systems is between 10-25 mm. Some special material characterization may require a larger-diameter Kolsky bar. However, the strain rate is limited for large-diameter Kolsky-bar experiment due to relatively large specimen size. By contrary, miniature Kolsky compression bars as small as 1.6-mm in diameter have also been developed for higher strain rate testing because the specimen size is drastically reduced.

When characterizing the dynamic mechanical response of some materials at high rate, the materials may require a certain size of specimens to produce meaningful representative volume. Such materials include concrete and composites. In Kolsky-bar experiments with these materials in gage section, the diameter of the bars may have to be sufficiently large to accommodate the large-size specimens. Figure 1.16 shows a 75-mm diameter Kolsky compression bar with a uniform diameter for both incident and transmission bars. A larger 100-mm-diameter Kolsky compression bar has recently been built in China for characterizing large concrete specimens (Chen et al. 2005, Wu 2006). Figure 1.17 shows the photograph of this 100-mm-diameter Kolsky bar (Wu 2006). The large diameter Kolsky bar challenges the striking system because of the heavy striker. A high capacity gas gun is required. Another method that uses a small diameter striker to impact on a tapered incident bar has been developed. Figure 1.18 shows an illustration of the tapered Kolsky bar system (Liu and Hu 2000). The incident bar has a 37 mm diameter at the impact end, which is the same as the striker diameter, and then enlarges to a 74 mm in diameter. The large diameter Kolsky bar also requires special design for the bar supports, using either linear ball bearings or air bearings, to minimize the friction between the heavy bars and their supports.

Figure 1.16 A 75-mm diameter Kolsky compression bar.

Figure 1.17 100-mm-diameter Kolsky bar
(Reproduced from Wu (2006) with permission)

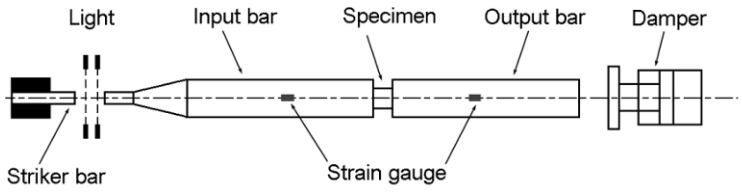

Figure 1.18 Kolsky bar with a tapered incident bar
(Reproduced from Liu and Hu (2000) with permission)

The large diameter Kolsky bar also makes stress wave dispersion more severe. The wave dispersion due to radial inertia will be presented in Chapter 2. Furthermore, even though the diameter of the specimen may be enlarged, the specimen still needs to be subjected to dynamic equilibrium requirements. Since the strain rate in the specimen is inversely proportional to the specimen thickness, the thicker specimens will limit the achievable strain rates. These issues should be accounted for in experiment design for large-size specimen characterization. The achievable ultimate strain rates on large brittle specimen are likely lower than 100 s^{-1}. Another issue associated with large specimens is inertia in the specimen which will be discussed in Chapter 2, the radial inertia induced stress is proportional to the square of the specimen diameter. If the specimen material is weak, the inertia effects on the large-diameter specimens can bring serious errors to the force history in the specimen.

On the other extreme of the bar size, miniature bars have been used to extend the strain rate range to 10^5 s^{-1} (Follansbee et al. 1984, Jia and Ramesh 2004, Nemat-Nasser et al. 2005, Casem 2009, Casem et al. 2010). Figure 1.19 shows a picture of miniaturized Kolsky tension bar for characterizing single high-performance fibers (Cheng et al. 2005, Lim et al. 2010). When the length of the specimen becomes small, the eventual strain rate achieved in the specimen will increase. Due to the nature of specimen acceleration from rest to the high rate, strain can be

accumulated to a significant amount during this acceleration process. Therefore, the resultant stress-strain curves may not be valid until this initial strain accumulation is completed. For example, if the target strain rate is 2×10^5 s^{-1} and the acceleration time is 5 μs (only realistic in miniaturized bars). The strain accumulated in the specimen is 50% when the strain rate reaches the target value (2×10^5 s^{-1}). Therefore, the high strain rate can be only achieved in ductile materials deforming to large strains. More details will be presented in Chapter 2.

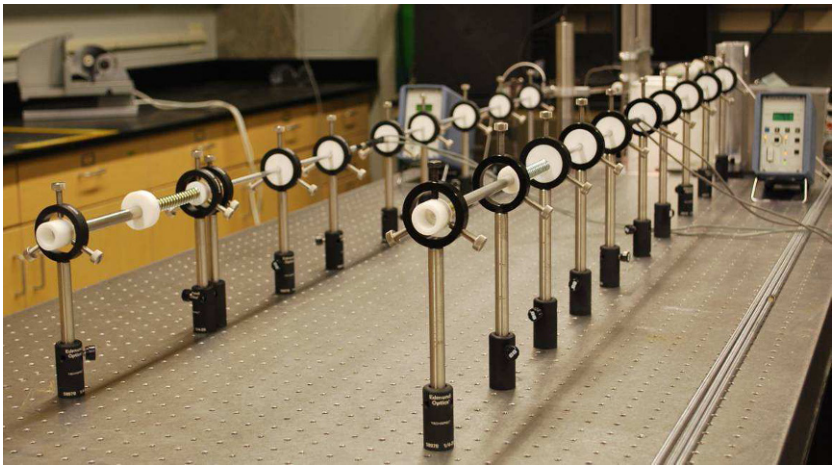

Figure 1.19 Miniaturized tension bars for fiber characterization.

1.6 Calibration and Data Reduction of Kolsky Compression Bar Experiments

After a Kolsky compression bar is designed and constructed, it needs to be calibrated. As a measurement instrument subjected to dynamic loading, calibration should be performed regularly, especially before a new set of Kolsky-bar experiments.

A simple approach to check the alignment condition of the bar system is to launch the striker directly on the incident bar which is in contact with the transmission bar without any specimen in between. A good alignment between the striker and the incident bar produces an analytically predictable trapezoidal profile of the incident pulse with a clean baseline. An example of such a set of signals is shown in Fig. 1.20(a). However, if the incident bar is not in good alignment with the striker, the incident pulse is distorted while the baseline is fluctuating, an example of which is shown in Fig. 1.20(b). Since the transmission bar is directly in contact with the incident bar, the complete incident pulse in the incident bar should be transmitted into the transmission bar without any reflection (Fig. 1.20(a)). However, if there is a misalignment between the incident and transmission bars, a reflected pulse is generated and the transmitted pulse profile deviates from that of the incident pulse, as shown in Fig. 1.20(b). When signals such as those shown in Fig. 1.20(b) are recorded from the calibration experiment, the Kolsky-bar system should not be used for material characterization until an expected pulse shown in Fig. 1.20(a) is produced in the incident bar and transmits into the transmission bar with little or no reflection.

When the bar system is aligned, more quantitative calibrations can be performed. The bar stress and strain can be predicted from the striking velocity with (1.2) and (1.3), respectively. Hence, the measurement system can be calibrated through checking if the relationship between the striker speed and the bar stress in (1.2), or the bar strain in (1.3) is satisfied. In (1.2) and (1.3), the elastic bar stress wave speed, C_B, is needed. This can be determined by experiments using the incident bar alone,

$$C_B = \frac{2l}{\Delta t} \tag{1.51}$$

where l is the distance from the strain gage location to the specimen end of the incident bar; and Δt is the time interval between the incident and reflected pulses when subjected to the impact by the striker. Figure 1.21 shows the actually measured strain in the incident bar and the predicted amplitude with (1.3) upon the striking velocity of 8.7 m/s (Song et al. 2009b). In addition to the analytically predicted pulse being measured, the consistency of the amplitude of the incident pulse measured from the experiment and predicted with (1.3) indicates good working condition of the Kolsky-bar measurement system.

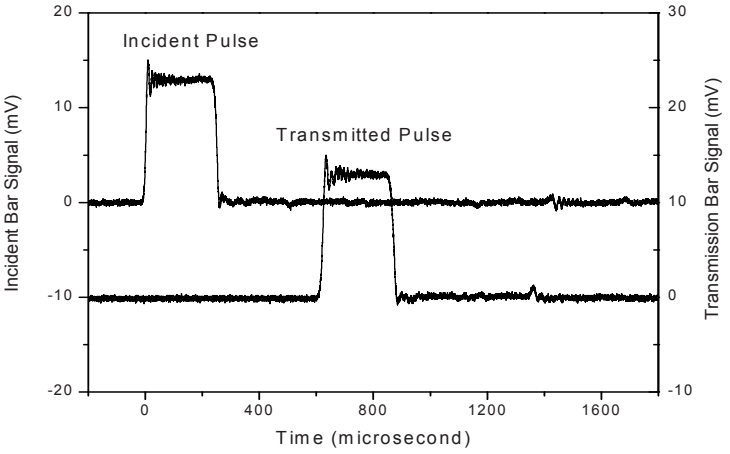

(a)

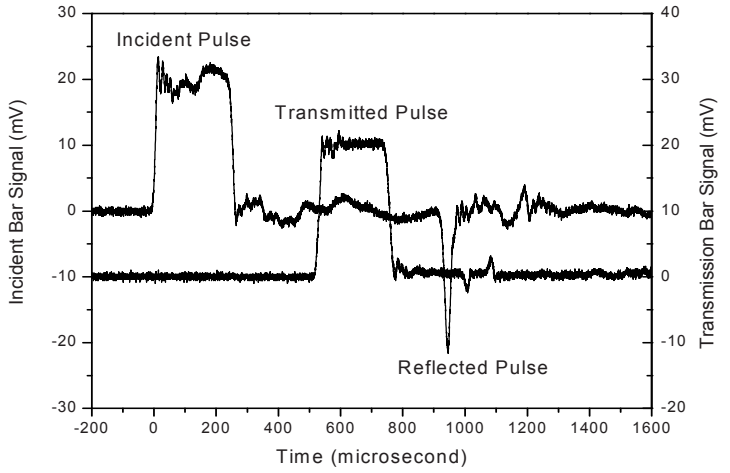

(b)

Figure 1.20 Stress waves in the bars
(a) in good alignment and (b) misaligned
(Reproduced from Song et al. (2009b) with permission)

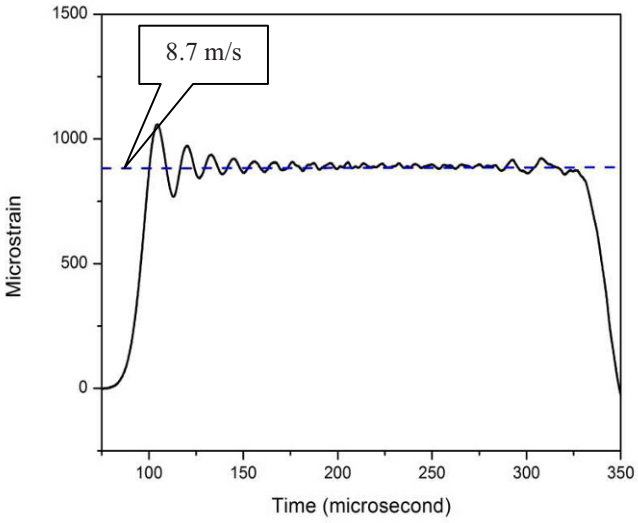

Figure 1.21 Calibration of incident pulse amplitude
(Reproduced from Song et al. (2009b) with permission)

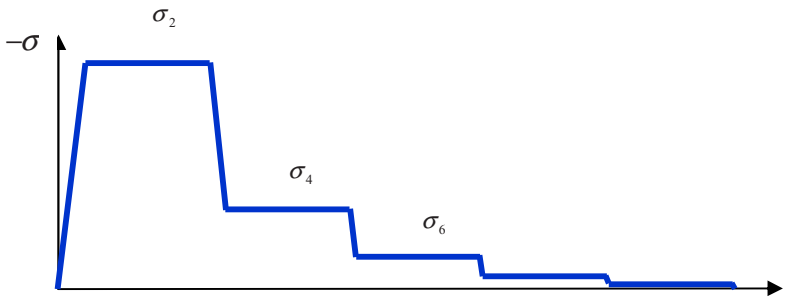

Figure 1.22 The incident pulse due to wave impedance mismatch between the striker and the incident bar
(Reproduced from Song et al. (2009b) with permission)

Equation (1.2) or (1.3) is satisfied only when the striker has the same wave impedance, which combines elastic wave speed, density, and cross-sectional area, as the incident bar. Mismatched wave impedance between the striker and the incident bar results in changes in not only the amplitude of the incident pulse but also its profile. If the impedance of the striker is higher, the incident pulse will exhibit a long unloading portion with progressively decreasing amplitudes, as schematically illustrated in Fig. 1.22. This is because the momentum of the striker cannot be transferred completely to the incident bar during the first wave reflection cycle in the striker. Each reflection cycle generates a step in the incident pulse with a lower amplitude. The amplitude of each step illustrated in Fig. 1.22 can be calculated as

$$\sigma_{2n} = \frac{\rho_{st}C_{st} \cdot \rho_B C_B}{\rho_{st}C_{st} + \rho_B C_B} \cdot \left(\frac{\rho_{st}C_{st} - \rho_B C_B}{\rho_{st}C_{st} + \rho_B C_B} \right)^{n-1} V_{st} \quad (n = 1,2,\ldots) \tag{1.52}$$

Again, the stress is considered negative in compression here.

The bar consistency can be checked by an experiment on a "standard" specimen, such as a 1100-O aluminum specimen. The experimental record of the incident, reflected and transmitted waves from this experiment is compared to the record from previous experiments on the same material under identical conditions to check consistency. After the bar system is calibrated and consistency checked, the bar is ready for dynamic characterization of materials.

The strain and stress histories of the material under investigation are calculated with (1.13) and (1.14). However, the reflected and transmitted signals are measured at different locations on the bars and thus at different times. But (1.13) and (1.14) are based on the pulses at the specimen/bar interfaces. The measured pulses thus must be synchronized, which turns out to be critical in data reduction.

In principle, the measured pulses at the strain gage locations should be shifted to the specimen/bar interfaces before the equations are applied. There are two issues in practical experiments associated with the shift. One is the wave dispersion associated with the inertia effects of waves propagating along an actual 3-D rod; and another is the determination of starting point of each of the pulses for proper synchronization. Wave dispersions should be either experimentally eliminated or numerically corrected, which will be discussed in Chapter 2.

Determination of starting points can significantly affect the resultant stress-strain curve. When synchronizing all three signals, the starting

point in the incident pulse (T_I) is estimated. Based on the estimated starting point of the incident pulse, the corresponding starting points in the reflected (T_R) and transmitted pulses (T_T) are determined by

$$T_R = T_I + \frac{2L_0}{C_B} \tag{1.53}$$

$$T_T = T_I + \frac{L_0 + L_1}{C_B} + \frac{L_s}{C_s} \tag{1.54}$$

where L_0 and L_1 are the distances from the strain gage locations on the incident and the transmission bars to the bar/specimen interfaces, respectively (Fig. 1.23); C_s is the stress wave speed in the specimen material, which often needs to be estimated. Figure 1.24 shows the correct and incorrect starting-point determinations of the reflected pulse for a certain incident pulse. The correct determination of the starting point corresponds to the stress equilibrium across the specimen length if the experiment is properly designed (more discussions on this later). These incorrect starting points of the reflected pulse resulted in erroneous calculation of the force at the front end of the specimen which provides a wrong assessment of dynamic stress equilibrium, as shown in Fig. 1.25. The incorrect starting-point determination eventually leads to erroneous resulting stress-strain curves, an example of which is shown in Fig. 1.26.

When stress equilibrium in the specimen is achieved, the stress history measurement by the transmitted signal is straight forward and accurate. The measurement of the specimen strain from the reflected wave is less accurate, especially at small strains. Generally, it is more challenging to measure the deformation than stress on the specimen in Kolsky-bar experiments. Techniques of direct measurement of specimen deformation have been developed that are complementary to conventional Kolsky-bar experiments.

Similar to the striker speed measurement, the laser system has been used to measure the distance change between the incident and transmission bar ends (or the front and back ends of the specimen) (Cheng et al. 2009) or the deformation of a tensile specimen (Li and Ramesh 2007). This technique measures the deformation averaged over the entire specimen along axial direction.

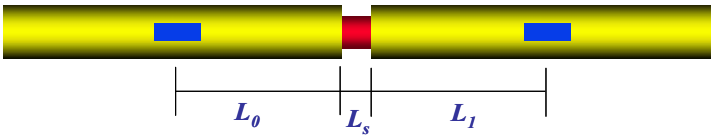

Figure 1.23 Determination of starting points

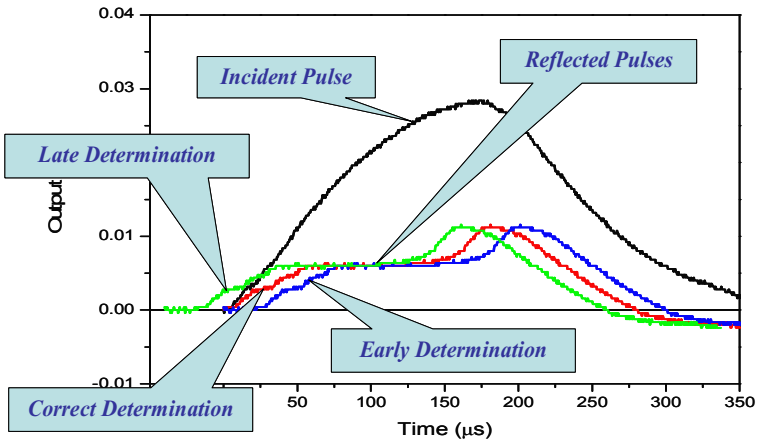

Figure 1.24 Correct and incorrect determination of reflected pulse

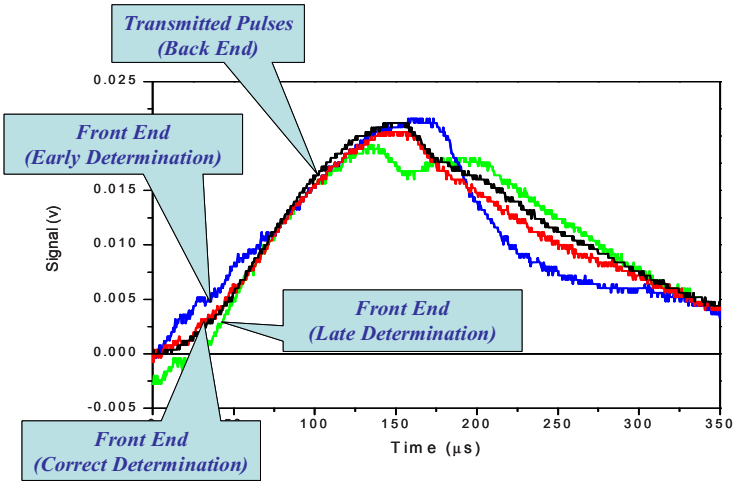

Figure 1.25 Correct and incorrect determination of stress equilibrium

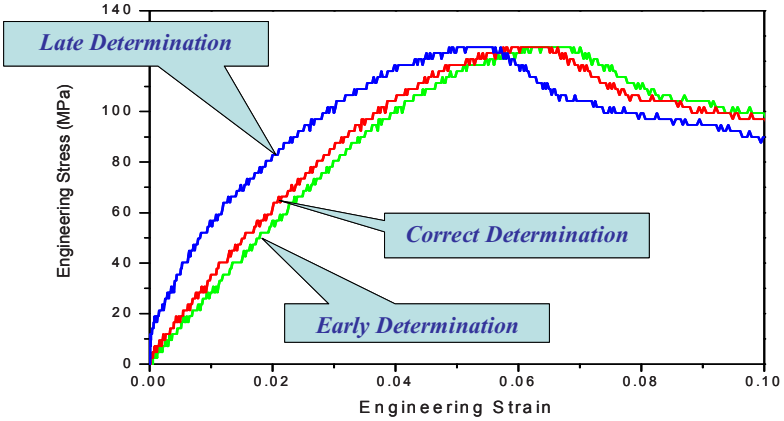

Figure 1.26 Correct and incorrect determination of stress-strain curves

Digital image correlation (DIC) has been applied to dynamic experiments including Kolsky-bar experiments. The DIC technique provides a full field measurement of deformation in the specimen. More comprehensive information of the distribution of strain over the entire specimen is obtained. DIC is a non-contact measurement technique. In this technique a random or regular pattern with high contrast is applied to the specimen surface. High speed digital camera is used to image the consecutive changes of the pattern when the specimen is subject to high-speed deformation. The patterns are correlated to yield a full field deformation in the specimen. Figure 1.27 shows an example of deformation distribution in an RTV630 rubber specimen in Kolsky compression bar experiment (Chen and Song 2005). The DIC method can also be used for 3-D full-field measurements when two high speed cameras are synchronized, or two images from different angles are projected to the aperture of one camera, to photograph the specimen deformation.

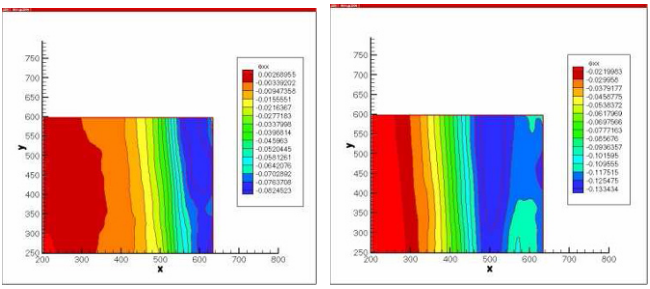

(a) t=35.7 μs (b) t=71.4 μs

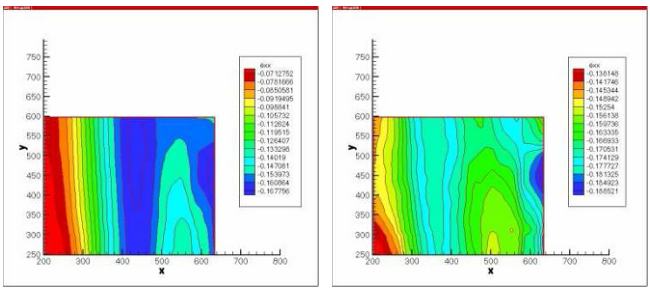

(c) t=107.1 μs (d) t=142.8 μs

Figure 1.27 An example of full-field strain measurement in a RTV630 specimen during a Kolsky bar experiment

Chapter 2. Testing Conditions in Kolsky Bar Experiments

In a material property characterization experiment, the specimen should deform uniformly under well-controlled testing conditions in order for the experimental results to be clearly documented and interpreted. In quasi-static experiments, testing conditions are monitored and adjusted in real time by closed-loop feedback control systems such that the specimen deforms under specified conditions throughout the test. In Kolsky-bar experiments, feedback control systems are not available. Furthermore, due to the relatively low stiffness of the bars, even under identical loading conditions, the testing conditions on the specimen depend on the specimen response. Therefore, it is challenging to subject the specimen to specified loading conditions in Kolsky-bar experiments. Both the loading processes in the specimen and their relations to the commonly defined testing conditions need to be carefully examined. In addition, the development of Kolsky bar and its data reduction scheme involves many idealized assumptions. However, in actual Kolsky-bar experiments, these assumptions are not satisfied automatically, which requires further efforts in experiment design. The valid testing conditions and necessary approaches to achieve specified conditions in the Kolsky-bar experiments are presented in this Chapter.

2.1 One-dimensional Planar Elastic Wave Propagation

In a Kolsky-bar experiment, the incident and transmission bars must remain linearly elastic so that the surface strains are linearly related to the stress waves inside the bars and the elastic wave theory can be employed for data reduction. A high-strength bar material such as alloy steel is therefore preferred. As indicated by (1.2), the upper limit of the striker impact speed is directly determined by the yield strength of the bar material.

The incident and transmission bars must also be sufficiently long to ensure one-dimensional wave propagation and to facilitate large deformation in the specimen when needed. Figure 2.1 shows an example of stress distribution in a cross section at a distance of half of the bar diameter (37 mm) to the impact end in a conventional Kolsky-bar experiment

W.W. Chen and B. Song, *Split Hopkinson (Kolsky) Bar: Design, Testing and Applications*, Mechanical Engineering Series, DOI 10.1007/978-1-4419-7982-7_2,

(Wang 2007). It clearly shows that the amplitude of axial stress decreases along the radial direction with the maximum at the center of the cross section and minimum at the bar surface. When the stress wave propagates to the distance of twice of the bar diameter, the axial stress distributes uniformly over the cross section, as shown in Fig. 2.2, but with significant oscillations. For the case shown in Fig. 2.1, the measured strain by the strain gages on the bar surface deviates from the actual bar strain. The strain gage locations thus should be far from the bar ends. In practice, they are mounted at least 10 bar diameters from both ends. Therefore, the bars should have a length-to-diameter (L/D) ratio of at least ~20. Most bars, particularly the incident bar, are typically much longer than this limit. To avoid wave overlapping at the strain gage location, the incident bar is at least twice as long as the striker.

When the Kolsky bar is used to conduct dynamic experiments on hard materials with a much smaller diameter than the bar diameter, the assumption of planar wave in the bars may be violated because of elastic or plastic indentation of the specimen into the bar ends. Such an indentation introduces a significant error in the strain measurements in the specimen particularly when specimen strain is small. The indentation can also cause premature failure in the specimen due to stress concentrations at the specimen edges. In order to avoid such an indentation, high-stiffness and high-strength platens such as tool steel and tungsten carbides are placed between the bars and the specimen. The wave impedance of the platens should match with that of the bars, $(\rho cA)_{platen} = (\rho cA)_{bar}$, to minimize the wave disturbances caused by the introduction of the platens. This issue will be further addressed in Chapter 3.

The oscillations in Fig. 2.2 are the result of wave dispersion. Since the bar material is free to move in the radial direction, the actual stress wave in the slender bars is still two dimensional in nature; however, it may be considered to be approximately one-dimensional when dealing with axial quantities. When a compressive wave propagates along the bar axis, the material is pushed forward, which is described by the axial kinetic energy, as well as sideways, which are the radial directions due to Poisson's effects. The material acceleration in the radial directions in turn causes inertia-induced stress in the axial direction. These two-dimensional effects result in wave dispersion when propagating along the bars. The effects of dispersion accumulate as the waves propagate over distance, and become more significant when bar diameter increases.

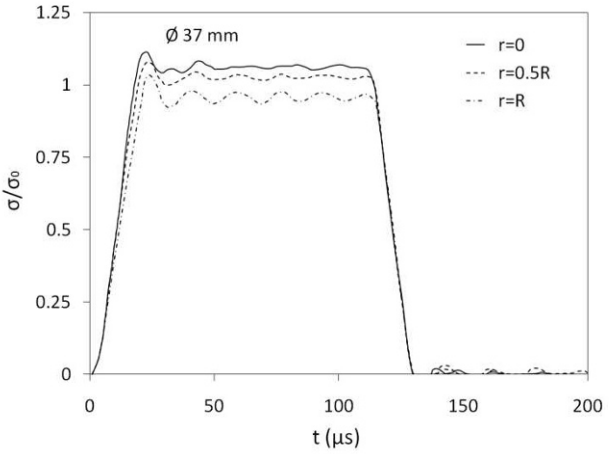

Figure 2.1 Axial stress distributions over the cross section 0.5D from the 37-mm-diameter bar end
(Reproduced from Wang (2007) with permission)

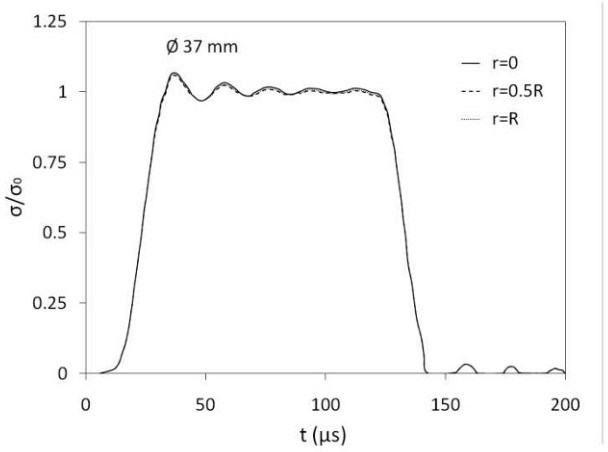

Figure 2.2 Axial stress distributions over the cross section 2D from the 37-mm-diameter bar end
(Reproduced from Wang (2007) with permission)

Wave dispersion has been extensively discussed starting from Pochhammer (1876) and Chree (1889). They independently solved the equation of motion for a sinusoidal wave propagating in an infinitely long cylinder. Figure 2.3 graphically shows the Pochhammer-Chree solution for wave dispersion, where Λ is the wave length (inversely proportional to the frequency), a is the radius of the circular cross-section of the bar in which the waves are propagating, $C_0 = \sqrt{E/\rho}$ is the elastic bar wave speed, and C_p is the elastic wave speed of wave components with various frequencies (Kolsky 1963). The Pochhammer-Chree solution reveals that the propagation velocity of a stress wave decreases with decreasing wavelength. In other words, a high-frequency stress wave travels slower than a wave which has a lower frequency.

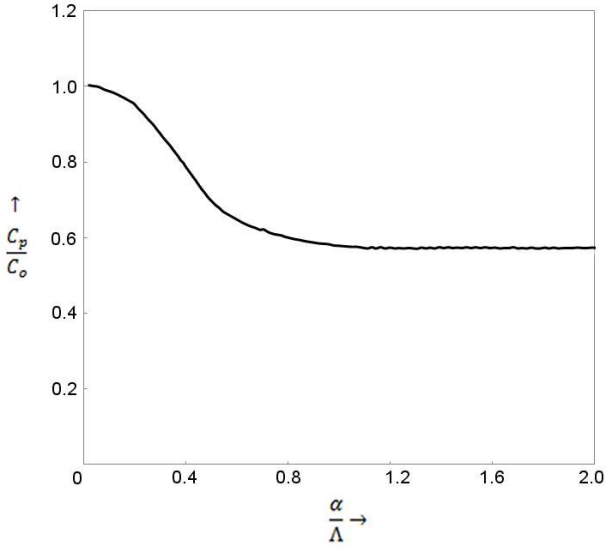

Figure 2.3 Pochhammer-Chree solution for wave dispersion ($\nu = 0.29$)
(Reproduced from Kolsky (1963) with permission)

In a Kolsky-bar experiment, the ideal rectangular pulse generated by the impact of the striker on the incident bar is composed of a spectrum of frequencies. Each frequency component has its own propagating velocity. The higher frequency components of the pulse lag behind the lower frequency components after traveling a distance, resulting in a distorted waveform, which is wave dispersion as discussed above. Figure 2.4 shows the wave dispersion in a Kolsky-bar experiment. The stress waves in Fig. 2.4 are the incident pulse and its reflection at the free end (no transmission bar was used). Both pulses were recorded by the same strain gages in the middle location of the incident bar, so that any difference between the two pulses was caused by wave dispersion in nature rather than by errors in the data acquisition system. As seen in Fig. 2.4, both incident and reflected pulses contain high frequency oscillations. A comparison of the two pulses shows that the reflected pulse differs from the incident pulse after propagating a distance of ~5700 mm, which is the result of wave dispersion.

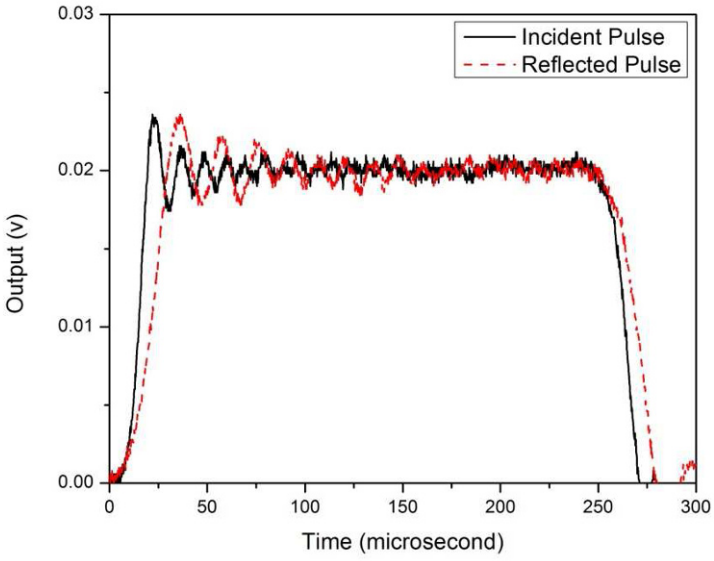

Figure 2.4. Wave dispersion in a Kolsky-bar experiment

The physics of wave dispersion has been analytically modeled. Therefore, correction for wave dispersion is possible and numerical corrections for wave dispersion have been extensively studied (Follansbee and Frantz 1983, Gorham 1983, Gong et al. 1990). Here we give an example of numerical correction through Fourier transform method originally published by Follansbee and Frantz (1983). The form of the Fourier transform of a wave $f(t)$ at the position, z, can be expressed as

$$f(t) = \frac{A_0}{2} + \sum_{n=1}^{\infty} D_n \cos(n\omega_0 t - \delta) \tag{2.1}$$

where A_0 and D_n are constants. The phase angel, δ, is given by

$$\delta = \frac{n\omega_0 z}{C_0}\left(\frac{C_0}{C_n} - 1\right) \tag{2.2}$$

where C_n is the propagation velocity of the frequency component $n\omega_0$. The dispersion can thus be corrected by adjusting the phase angle

$$\delta = \delta_0 + \frac{n\omega_0 \Delta z}{C_0}\left(\frac{C_0}{C_n} - 1\right) \tag{2.3}$$

where δ_0 is the phase angel at z_0; and δ is the phase angel at $z = z_0 + \Delta z$. The relationship between the phase velocity and wavelength is referred to Fig. 2.3.

Figure 2.5 shows the waves measured by the strain gages in the middle of the incident bar (a) and predicted at the incident bar/specimen interface (b) due to wave dispersion (Follansbee and Frantz 1983). In principle, the oscillations in all three pulses (incident, reflected, and transmitted pulses) should be corrected to the specimen/bar interfaces. When the specimen is a ductile material, the transmitted pulse is not as dispersive as the incident and reflected pulse because the specimen plays a role of filter. Dispersion correction reduces the oscillations in the resultant stress-strain curve so that the measurement of stress-strain response of the specimen becomes more accurate, particularly at small strains.

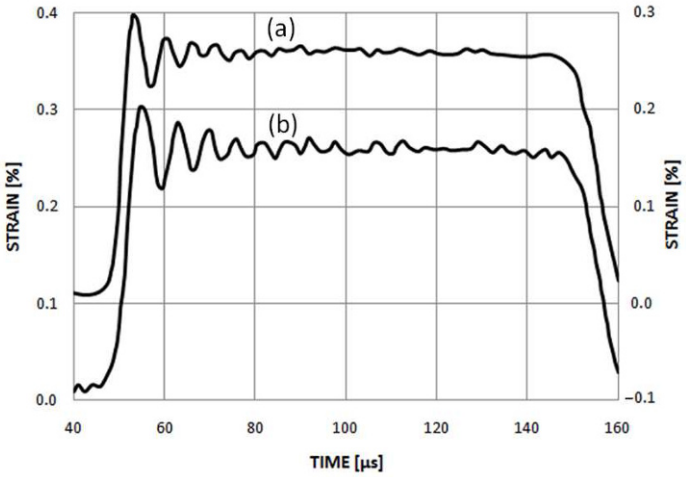

Figure 2.5 Comparison of incident wave measured by the strain gages in the middle of the incident bar (a) with that predicted at the incident bar/specimen interface (b)
(Reproduced from Follansbee and Frantz (1983) with permission)

The wave dispersion can be physically minimized in experiments through pulse shaping techniques where a small piece of material is placed on the impact end of the incident bar as the pulse shaper. The plastic deformation of the pulse shaper physically filters out the high frequency components in the incident pulse. Figure 2.6 shows the frequency spectrum comparison of a non-shaped pulse and a shaped pulse. The components with the frequencies above 40 KHz have been filtered out in the shaped pulse such that wave dispersion is significantly minimized, as evidenced in Fig. 2.7. Figure 2.7 shows that the incident pulse is exactly the same as its reflection from the free end, which is different from those shown in Fig. 2.4. Numerical correction of the wave dispersion is not necessary when the pulse shaper is used in a Kolsky-bar experiment. The use of the pulse shaping also extends the rise time in the incident pulse, which is necessary to achieve stress equilibrium in the specimen. Furthermore, proper design of the pulse shaping facilitates constant strain rate deformation in the specimen. The detailed pulse shaping technique is presented in Chapter 2.5.

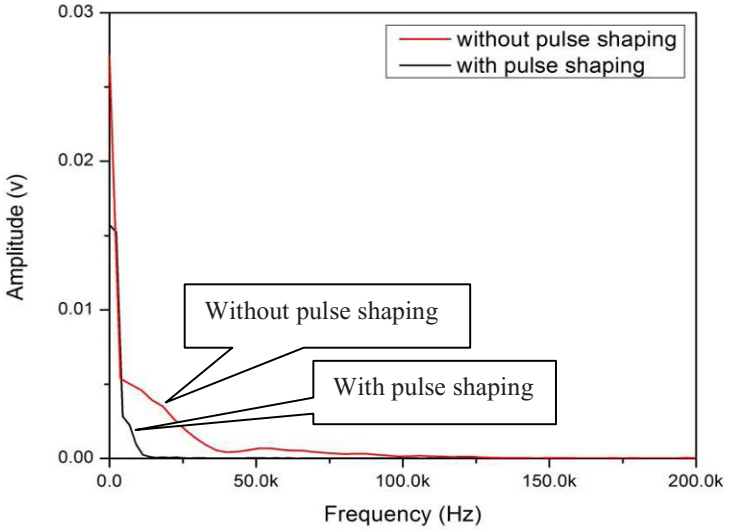

Figure 2.6 Frequency spectrums of the incident pulses produced without and with a pulse shaper

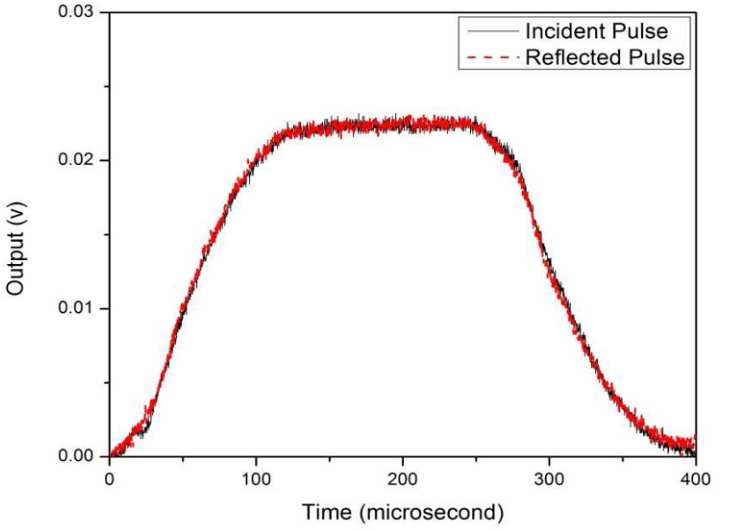

Figure 2.7 The incident and reflected pulses produced in a pulse-shaped Kolsky-bar experiment

2.2 Interfacial Friction

In a Kolsky-bar experiment, due to the short specimen required by dynamic stress equilibrium considerations, the interfacial friction between the specimen and the bar ends may lead the specimen to a three-dimensional stress state. The interfacial friction can significantly increase the measured strength in specimens with high lateral expansion because the friction limits the lateral expansion (Zenker and Clos 1998). For example, even a lubricant with a 0.05 friction coefficient produced an increase by 25% in the flow stress in a polyethylene specimen (Briscoe and Nosker 1984). Interfacial friction can also reduce the measured strength of brittle materials with small lateral expansion because the friction may result in multiaxial stress states at the specimen ends, causing premature failure.

Figure 2.8 shows a comparison of stress-strain curves for an alumina-filled epoxy without lubricant, with high vacuum grease and petroleum jelly as lubricants (Song et al. 2009c). All three stress-strain curves had similar elastic-perfectly plastic profiles with the same Young's modulus. However, the stress-strain curve without lubricant exhibits the highest apparent flow stress. Without lubricant, the interfacial friction restricted the specimen expansion laterally, which in turn increased the axial flow stress, particularly when the specimen is subject to large deformation. The elastic response was not significantly affected because the radial deformation in the specimen is relatively small during this stage. There is no significant difference in stress-strain response of the alumina-filled epoxy when using petroleum jelly or high vacuum grease as the lubricant.

Proper lubrication between the specimen and the bar interfaces is thus important. The lubricants may be different for different material characterization. Commonly used lubricants include high vacuum grease, petroleum jelly, polytetrafluoroethylene (PTFE), and molybdenum disulphide (MoS_2) (Trautmann et al. 2005). Vegetable oil has been used when characterizing some specific specimen materials, such as biological tissues (Hall and Guden 2003, Pervin and Chen 2009).

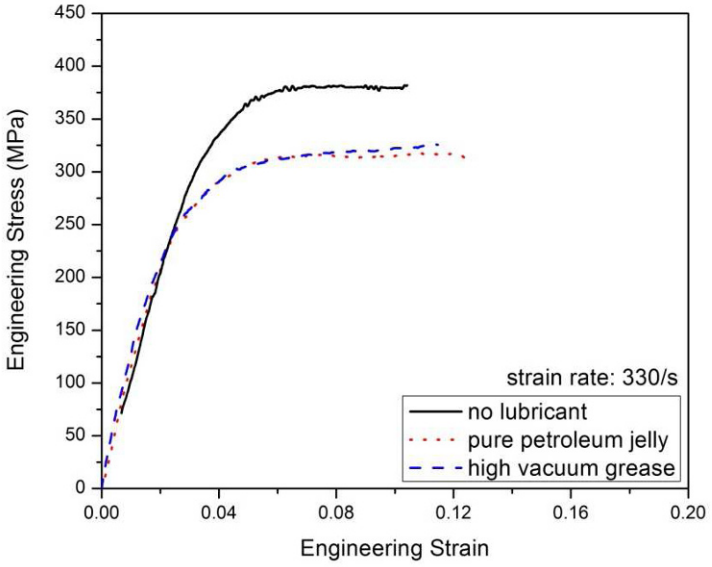

Figure 2.8 Lubrication effect on dynamic response of an alumina-filled epoxy
(Reproduced from Song et al. (2009c) with permission)

2.3 Inertia Effects in Specimen

Inertia effects are associated with most dynamic events. In a Kolsky-bar experiment, the specimen is initially at rest and is expected to deform at a desired rate. Acceleration, and thus inertia in both axial and radial directions, accompanies the strain rate change from zero to the desired level. However, the goal of the Kolsky-bar experiments is to determine the intrinsic material response. Inertia effects should be minimized through appropriate design of specimen geometry and experimental conditions.

In the analysis of the inertia effects in the specimen for Kolsky-bar experiments, Samanta (1971) corrected a previous analysis with the addi-

tional consideration of the rate of change of specimen energy in the convective part. The specimen stress was measured by the mean value of stresses at both ends with additional inertia terms.

$$\sigma = -\frac{1}{2}(\sigma_1 + \sigma_2) - \rho_0\left(\frac{l_0^{\,2}}{12} + \frac{a^2}{8}\right)\varepsilon - \rho\left(\frac{l_0^{\,2}}{12} - \frac{a^2}{16}\right)\varepsilon^2 \tag{2.4}$$

where ρ_0 and ν are density and Poisson's ratio of the specimen material, respectively; a is specimen radius; and ε is the time rate of change of strain rate in the specimen; σ_1 and σ_2 are the specimen stresses at the incident and transmission bar ends, respectively. Samanta's analysis indicates that the length-to-diameter ratio of $\sqrt{3}/4$ and a constant strain rate should be satisfied simultaneously to eliminate the inertia effect. The benefit of stress equilibrium from constant strain rate has also been confirmed by Gorham (1989). Gorham (1989) modified the inertia component of stress as

$$\Delta\sigma = \sigma_2 - \sigma_1 = \rho\frac{h^2}{2}\varepsilon \tag{2.5}$$

The axial acceleration is accompanied by the inertia (or acceleration) in the radial direction due to Poisson's effect. This effect becomes more significant for volume incompressible materials. Radial inertia has been recognized to produce extra axial stress in specimen. This extra axial stress due to radial inertia becomes a significant concern when characterizing very soft materials.

Kolsky (1949) used an energy method to calculate the extra axial stress caused by the radial inertia,

$$\sigma = \frac{\nu^2 a^2 \rho_0}{2}\varepsilon \tag{2.6}$$

Forrestal et al. (2006) presented a closed-form solution of the extra axial stress due to radial inertia based on linear elasticity. For incompressible materials ($\nu = 0.5$), the first order perturbation stress components at the radius of r in cylindrical coordinates are

$$\sigma_z = \sigma_\theta = \sigma_r = \frac{\rho_0(a^2 - r^2)}{4}\varepsilon \tag{2.7}$$

The extra axial stress produced by radial inertia has a parabolic distribution, which suggests the maximum value of the extra axial stress at $r = 0$ (specimen center) and zero at the specimen cylindrical surface ($r = a$). The average extra axial stress over the entire specimen cross section is obtained from

$$\overline{\sigma}_z = \frac{1}{\pi a^2} \int_0^a \int_0^{2\pi} \sigma_z r dr d\theta \tag{2.8}$$

which has been found to be consistent with Kolsky's analysis (2.6). Both (2.6) and (2.7) indicate the radial inertia effect is eliminated when the specimen is subject to constant strain-rate deformation. It is noted that (2.6) is derived from linear elasticity, which is usually used for linear response at small deformation, such as brittle material response.

Warren and Forrestal (2010) extended the analysis of radial inertia effect to large plastic deformation, which benefits more engineering materials and biological tissues capable of large deformation. For a specimen undergoing large plastic deformation, the extra axial stress produced by radial inertia is

$$\sigma_z = \frac{\rho_0}{4(1-\varepsilon)^2}\left[\frac{3\varepsilon^2}{2(1-\varepsilon)} + \varepsilon\right]\left(a_o^2 - r^2\right) \tag{2.9}$$

The extra stress induced by inertia and expressed by (2.9) also has a parabolic distribution in the radial direction. Similarly, the average axial stress, which is Cauchy stress, is

$$\overline{\sigma}_z = \frac{1}{\pi a^2} \int_0^a 2\pi r \sigma_z dr = \frac{3\rho_0 a_o^2}{16(1-\varepsilon)^3}\varepsilon^2 + \frac{\rho_0 a_o^2}{8(1-\varepsilon)^2}\varepsilon \tag{2.10}$$

Both strain and strain rate in (2.9) and (2.10) are in engineering measurements. In contrast to the linear elasticity analysis, the radial inertia will not be eliminated at large deformation even though the strain rate is constant. With increasing strains in the specimen, the radial inertia becomes more significant.

As indicated in (2.10), the amplitude of the extra axial stress produced by radial inertia depends on specimen density, radius, strain and strain rate. Within the strain rate range of Kolsky-bar experiment, the amplitude of the extra axial stress is approximately in the order of 1 MPa or below. Such a small amplitude is negligible for most engineering ma-

terials when the flow stress is on the order of 10^2 to 10^3 MPa. However, for very soft materials, such as soft rubbers, gelatins, and biological tissues, the stresses in which are often expressed in kPa, the radial inertia becomes a serious source of error. Since this radial inertia is not a part of the intrinsic material response of the specimen, it must be removed from experimental measurements. This issue will be further addressed in Chapter 4.2.

2.4 Constant Strain Rate Deformation

The Kolsky bar is designed to obtain families of stress-strain curves as a function of strain rate for the material under investigation. For each stress-strain curve, the strain rate is thus desired to be constant, particularly for those strain-rate-sensitive materials. As presented in the previous section, constant strain rate deformation also helps to validate the Kolsky bar testing conditions by minimizing inertia effects at small strains.

Unlike the quasi-static universal testing frames, the Kolsky-bar system is not sufficiently rigid in comparison to the specimen material. A constant velocity input, as generated in the form of the trapezoidal incident pulses in conventional Kolsky-bar experiments, does not necessarily produce constant-rate deformation in the specimen. Figure 2.9 illustrates typical strain-rate histories in an elastic-brittle and an elastic-plastic specimen from conventional Kolsky-bar experiments. Both strain rates are observed far from constant, particularly for the elastic brittle specimen. For a work-hardening material, the input stress level needs to progressively increase to deform the specimen at a constant rate. Otherwise, the engineering strain rate in the specimen decreases. The generation of an incident pulse with increasing amplitude in a Kolsky-bar experiment is an open loop control over the testing conditions on the specimen. Such control is a part of the Kolsky-bar experiment design.

Since the impact experiment does not allow real-time adjustment on the loading pulse based on the specimen feedback, the adjustment process on the control to achieve desired testing conditions on the specimen is iterative. In most cases, the conventional trapezoidal type of incident pulse does not satisfy the requirement of constant strain-rate deformation. However, the transmitted pulse from such a conventional experiment reveals information about the specimen response. Based on this response, the incident pulse is modified in the next experiment in order to

approach dynamic equilibrium and constant strain rate. The method to modify the incident pulse is pulse shaping technique.

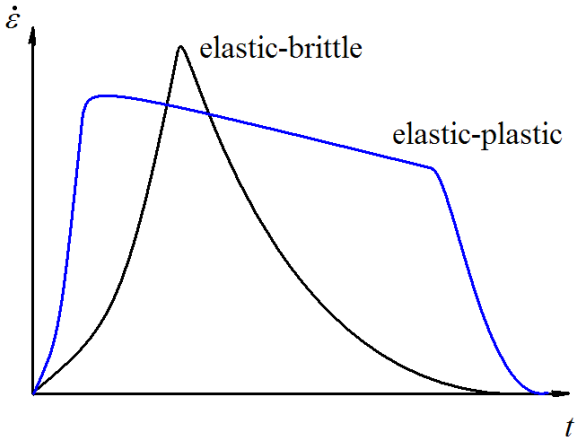

Figure 2.9 Illustration of strain rate histories for elastic-brittle and elastic-plastic materials in conventional Kolsky-bar experiments

2.5 Pulse Shaping Technique

Pulse shaping technique is used to facilitate stress equilibrium and constant strain rate deformation in the specimen through properly modifying the profile of the incident pulse based on specimen response in Kolsky-bar experiments.

Pulse shaping technique has been discussed and developed over the past three decades. Duffy et al. (1971) were probably the first authors to use pulse shapers to smooth pulses generated by explosive loading for the torsional Kolsky bar. Christensen et al. (1972) might be the first au-

thors to employ a pulse shaping technique in the compression version of Kolsky-bar tests to improve the accuracy and resolution of the initial portions of the stress-strain curves. They modified the incident pulse with a pulse shaping technique in Kolsky-bar experiments on rocks. A ramp incident pulse was found to be more appropriate than a square pulse in Kolsky bar experiments to obtain accurate compressive stress-strain response for rocks. In their study, they used conical strikers instead of the usual cylinders to partially accomplish ramp-like incident loading pulse. It is noted that the small end of the cone was fired as the impact end. The generated profile of the incident pulse corresponds to three loading regions: the initial impact of the truncated cone, the transition region determined by the cone angle, and the final region depending on the area of the cylinder joined to the cone. The profile of the input-stress wave can be varied over a considerable range with this technique through varying the area ratio of the cylinder and the cone, as shown in Fig. 2.10. A conical striker for pulse shaping technique is still being used for Kolsky-bar experiments on brittle materials (Lok et al. 2002). Figure 2.11 shows a schematic of currently used conical striker. Although the profile of incident pulse can be modified by varying the geometry of the striker, it brings difficulties to design and fabricate the specialized striker.

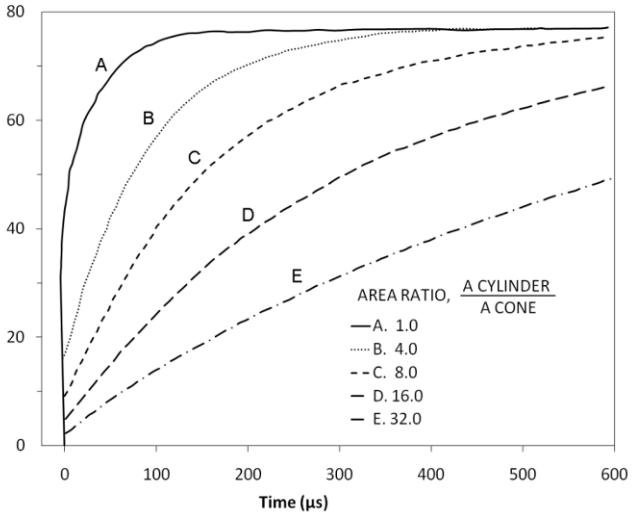

Figure 2.10 Incident pulses produced by varying the area ratio between the cylinder and the cone
(Reproduced from Christensen et al. (1972) with permission)

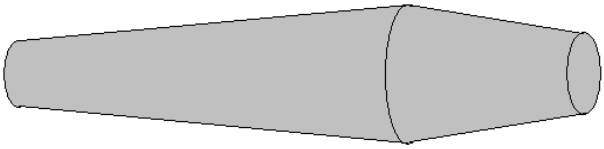

Figure 2.11 Schematic of conical striker

In order to facilitate constant strain-rate deformation in specimen, the incident pulse is generally required to possess a similar profile to the stress response of the tested specimen, which is represented by the transmitted signal. A three-bar technique for pulse shaping was developed to achieve this goal. Figure 2.12 illustrates the design of the three-bar technique (Ellwood et al. 1982). An additional pressure bar (preloading bar) and dummy specimen were implemented to the conventional Kolsky-bar configuration. The dummy specimen is recommended to be made of the same material as the tested specimen. The pulse transmitted through the dummy specimen becomes the actual incident pulse for the real specimen. Under this arrangement, the profile of the incident pulse is very similar to that of the transmitted pulse measured behind the specimen. This incident pulse produces a plateau in the reflected pulse, representing a constant strain rate in the specimen. Figure 2.13 shows typical incident, reflected, and transmitted pulses produced from the three-bar technique (Ellwood et al. 1982). The incident pulse was dictated by the dummy specimen's elastic-plastic response. This elastic-plastic response is very similar to that for the actual specimen because they are made of the same material. The actual specimen was thus subjected to a nearly constant strain-rate deformation, as indicated by the plateau in the reflected pulse in Fig. 2.13.

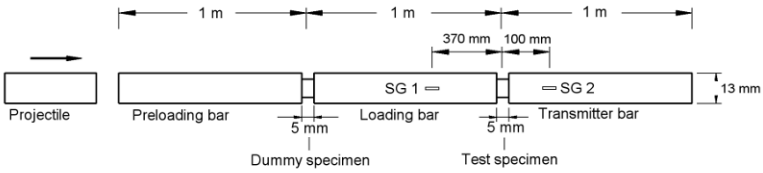

Figure 2.12 Three-bar technique
(Reproduced from Ellwood et al. (1982) with permission)

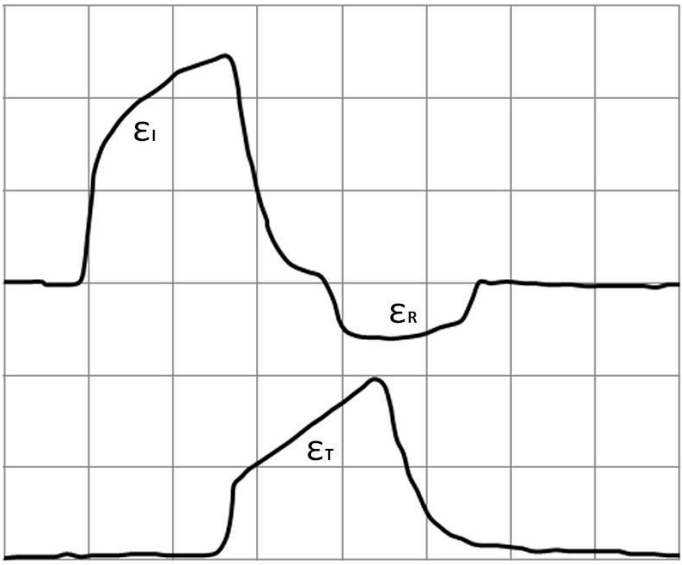

Figure 2.13 Pulse shaped Kolsky bar experiment
with the three-bar technique
(Reproduced from Ellwood et al. (1982) with permission)

The preloading bar in the three-bar technique was made from the same material as the incident and transmission bars. However, Parry et al. (1995) replaced the preloading bar with a lower-strength bar to minimize the stress wave dispersion. The reduction of the wave dispersion depends on the length of the pre-loading bar. A longer pre-loading bar minimizes the wave dispersion more efficiently.

As a simpler version of the three-bar technique, the pre-loading bar was removed. The dummy specimen was directly placed at the end of the incident bar and is subjected to the direct impact of the striker (Bragov and Lomunov 1995). Another alternative for controlling the incident pulse profile is to place a "tip" material between the striker and the incident bar, as illustrated in Figure 2.14. The tip material is usually called "pulse shaper" in Kolsky-bar experiments. The function of the pulse shaper in Kolsky-bar experiments includes minimizing wave dispersion, facilitating stress equilibrium and constant strain rate deformation in specimen.

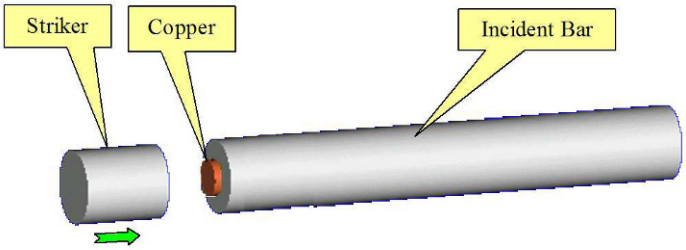

Figure 2.14 Pulse shaping technique with a copper "tip" material

This "tip" material is not necessarily the same as the specimen material under investigation. The tip material is commonly a disc made from paper, aluminum, copper, brass, stainless steel, and so on. Annealed copper discs have recently been extensively used as pulse shapers in Kolsky-bar experiments. Nemat-Nasser et al. (1991) might be the first authors to analytically model the pulse-shaping process using OFHC (oxygen-free, high-purity copper) as pulse shaper. Their analysis is based on the following constitutive response,

$$\sigma_c = \sigma_0 f(\varepsilon) \tag{2.11}$$

where the function $f(\varepsilon)$ is determined experimentally, σ_0 is a constant although it may depend on the strain rate in general. In (2.11), σ_c refers to true stress; whereas, ε is engineering strain. If the copper pulse shaper has an initial area A_1 and a thickness h_0, the axial strain ε in the pulse shaper as a function of time t can be calculated with

$$\left(\frac{h_0}{V_0}\right)\varepsilon + K\frac{f(\varepsilon)}{1-\varepsilon} = 1 \tag{2.12}$$

where

$$K \equiv \frac{A_1\sigma_0}{A_b\sigma_m} \tag{2.13}$$

$$\sigma_m \equiv \frac{1}{2}\rho_b C_b V_0 \equiv \frac{1}{2}\frac{E_b}{C_b}V_0 . \tag{2.14}$$

Equation (2.12) has the solution

$$t = \int_0^{\varepsilon}\left[1 - K\frac{f(x)}{1-x}\right]^{-1} dx \qquad t \le T \tag{2.15}$$

T is defined by (1.1). The strain and stress in the incident bar, ε_b and σ_b, are

$$\varepsilon_b = \frac{A_1\sigma_0}{A_b E_b}\cdot\frac{f(\varepsilon)}{1-\varepsilon} \tag{2.16}$$

$$\sigma = E_b\varepsilon_b \tag{2.17}$$

Assuming unloading of the pulse shaper occurs at $t = T_1$, the strain of the pulse shaper at $T \le t \le T_1$ is determined by integrating the following strain rate history,

$$\varepsilon(t) = \frac{V_0}{h_0}\left\{1 - K\left[\frac{f(\varepsilon(t))}{1-\varepsilon(t)} + \frac{f(\varepsilon(t-t_0))}{1-\varepsilon(t-t_0)}\right]\right\}, \quad T \le t \le T_1 \tag{2.18}$$

The strain and stress produced in the incident bar are then determined with (2.16) and (2.17), respectively.

Frew et al. (2002) presented a more extensive analysis to determine the strain of the pulse shaper. The pulse shaper deformation was derived as

$$\frac{h_0}{V_0}\varepsilon(t) = 1 - K'\left(\frac{1}{\rho_b C_b} + \frac{1}{\rho_{st} C_{st}}\right)\frac{f(\varepsilon)}{1-\varepsilon}, \quad \text{for } 0 \le t < T \tag{2.19}$$

$$\frac{h_0}{V_0}\varepsilon(t) = 1 - K'\left(\frac{1}{\rho_b C} + \frac{1}{\rho_{st} C_{st}}\right)\frac{f(\varepsilon)}{1-\varepsilon} - \frac{2K'}{\rho_{st} c_{st}}\sum_{k=1}^{n}\frac{f(\varepsilon(t-kT))}{1-\varepsilon(t-kT)},$$

$$\text{for } nT \le t < (n+1)T \tag{2.20}$$

where

$$K' = \frac{\sigma_0 A_1}{A V_0} \tag{2.21}$$

Equations (2.19) and (2.20) have the following solutions, respectively.

$$t = \frac{h_0}{V_0}\int_0^{\varepsilon}\left[1 - K'\left(\frac{1}{\rho_b C_b} + \frac{1}{\rho_{st} C_{st}}\right)\frac{f(x)}{(1-x)}\right]^{-1} dx, \quad \text{for } 0 \le t < T \tag{2.22}$$

$$t = nT + \frac{h_0}{V_0}\int_{\varepsilon^n}^{\varepsilon}\left[1 - K'\left(\frac{1}{\rho_b C_b} + \frac{1}{\rho_{st} C_{st}}\right)\frac{f(x)}{(1-x)} - \frac{2K'}{\rho_{st} C_{st}}\sum_{k=1}^{n}\frac{f(\varepsilon(t-kT))}{1-\varepsilon(t-kT)}\right]^{-1} dx$$

$$\text{for } nT \le t < (n+1)T \tag{2.23}$$

where ε^n is the strain in the pulse shaper at $t = nT$. The strain in the incident bar can be obtained from (2.16) after the pulse shaper strain is calculated from (2.22) and (2.23). Equations (2.22) and (2.23) are valid as long as the pulse shaper does not expand beyond the bar surfaces. The unloading response of the pulse shaper was also analyzed by Frew et al. (2002). As a practical reference in Kolsky-bar experiment design, a FORTRAN source code for the numerical solution of the pulse shaping equations is attached in Appendix A of this book, which was provided by Dr. Frew.

Using such a code, the shapes of the incident pulses can be predicted on the computer before pulse shapers are made, which improves the efficiency of the high-rate experiment design. As an example, if an annealed copper is used as the pulse shaper, its stress-strain response has been determined to have the following form,

$$\sigma_p = \frac{\sigma_0 \varepsilon_p^n}{1 - \varepsilon_p^m} \tag{2.24}$$

By curve fitting to experimental results on the pulse shaper material, the constants σ_0, n, and m are determined. Then the incident stress (or strain) histories can be predicted by the pulse-shaping models. Figure 2.15 shows experimental data and model predictions for incident stresses from a pulse shaped experiment with an annealed C11000 copper pulse shaper and Frew's model (Frew et al. 2002).

When a high-strength elastic-plastic material is to be characterized by the Kolsky-bar experiments with pulse shaping, the soft copper pulse shaper may not produce the desired incident pulse because of its low yield strength. In this case, a harder pulse shaper is necessary. However, the harder pulse shaper usually generates a high rate of loading even during initial loading stage, which is not desired for achieving early stress equilibrium. Stacking the soft and hard pulse shapers together forms dual pulse shaping technique that is illustrated in Fig. 2.16. The dual pulse shaper consists of a softer material, such as a copper, and a relatively harder material such as a steel. During the initial compression, the de-

formation of the soft shaper is much larger than that of the hard one. It is highly possible that the cross section of the soft shaper is beyond the hard shaper. In this case, a very rigid platen with a large diameter is placed between the soft and hard pulse shapers such that the soft shaper can continue to flow to larger strains. The major role of the soft pulse shaper is to produce a relatively low initial rate of loading so that the stress equilibrium is achieved early during an experiment. When the soft pulse shaper is compressed to very large strains, it eventually tends not to be further compressible. The hard pulse shaper starts to dominate the shape of incident pulse from this moment. The hard pulse shaper generates the majority of the incident pulse so that a constant strain rate is achievable.

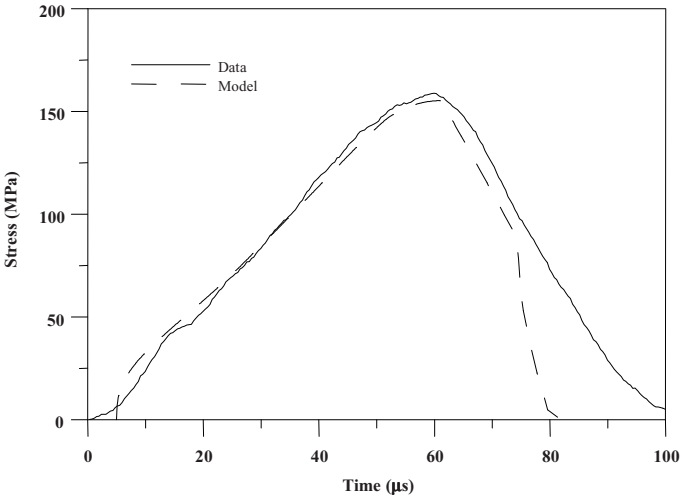

Figure 2.15 Incident pulse produced with annealed copper as pulse shaper
(Reproduced from Frew et al. (2002) with permission)

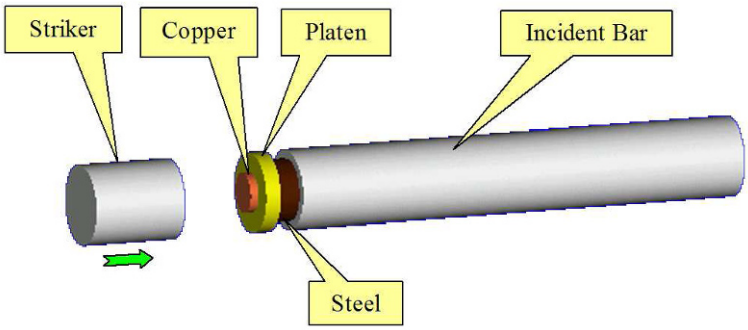

Figure 2.16 Dual pulse shaping technique

The dual pulse shaping technique for elastic-plastic material characterization has also been modeled by Frew et al. (2005). Both pulse shapers are assumed to have similar stress-strain response,

$$\sigma_\alpha = \sigma_{0\alpha} f(\varepsilon_\alpha) \tag{2.25}$$

$$\sigma_\beta = \sigma_{0\beta} g(\varepsilon_\beta) \tag{2.26}$$

where subscripts, α and β, refer to the soft and hard pulse shaper, respectively. The responses of both pulse shapers are correlated during compression,

$$\frac{g(\varepsilon_\beta)}{1-\varepsilon_\beta} = \frac{a_{0\alpha}}{a_{0\beta}} \cdot \frac{\sigma_{0\alpha} f(\varepsilon_\alpha)}{\sigma_{0\beta}(1-\varepsilon_\alpha)} \tag{2.27}$$

Very similar to the single pulse shaping analysis, the deformation of dual pulse shapers is determined by

$$\frac{h_{0\alpha}}{V_0}\varepsilon_\alpha(t)=1-K'_\alpha\left[\frac{1}{\rho_b C_b}+\frac{1}{\rho_{st}C_{st}}\right]\frac{f(\varepsilon_\alpha)}{1-\varepsilon_\alpha}-\frac{h_{0\beta}}{V_0}\varepsilon_\beta(t),\ \text{for } 0\le t<T \tag{2.28}$$

$$\begin{aligned}\frac{h_{0\alpha}}{V_0}\varepsilon_\alpha(t)=1-K'_\alpha&\left[\frac{1}{\rho_b C_b}+\frac{1}{\rho_{st}C_{st}}\right]\frac{f[\varepsilon_\alpha(t)]}{1-\varepsilon_\alpha(t)}\\&-\frac{2K'_\alpha}{\rho_{st}C_{st}}\left\{\frac{f[\varepsilon_\alpha(t-T)]}{1-\varepsilon_\alpha(t-T)}+\frac{f[\varepsilon_\alpha(t-2T)]}{1-\varepsilon_\alpha(t-2T)}\right.\\&+\quad+\left.\frac{f[\varepsilon_\alpha(t-nT)]}{1-\varepsilon_\alpha(t-nT)}\right\}-\frac{h_{0\beta}}{V_0}\varepsilon_\beta(t)\end{aligned}$$

$$\text{for}\quad nT\le t<(n+1)T \tag{2.29}$$

where

$$K'_\alpha=\frac{\sigma_{0\alpha}a_{0\alpha}}{A_b V_0} \tag{2.30}$$

Equations (2.28) and (2.29) are valid only when the pulse shapers remain in compression and do not expand beyond the cross sections of the striker and incident bar. It is obvious that the dual pulse shaper model is more complicated than the single pulse shaper model. The response of both pulse shapers are coupled together, which requires numerical solutions to the combination of (2.27), (2.28) and (2.29). Figure 2.17 shows an example of the dual pulse shaper modeling and corresponding data from an experiment by using annealed C11000 copper (α) and a 4340 R_c35 steel (β) as the pulse shapers (Frew et al. 2005). The detailed application of the dual pulse shaping technique is presented in Chapter 5.

Depending on the desired testing conditions on the specimens under investigation, the generation of incident pulse can be very diverse by varying the material, geometry, and dimensions of the pulse shaper(s) as well as the striking velocity, material, and geometry of the striker. Figure 2.18 shows a few dimensionless incident pulses generated with various pulse shaping designs (Chen and Song 2009). These pulses are designed for characterizing the materials with different characteristics in stress-strain response, in order to facilitate constant strain-rate deformation un-

der stress equilibrium. Detailed pulse shaping techniques for different material characterization is presented in the next several chapters. It is also noted that this solution of the pulse shaping design is not exclusive. Any design is acceptable as long as it produces an incident pulse that satisfies the requirements of constant strain rate deformation and stress equilibrium.

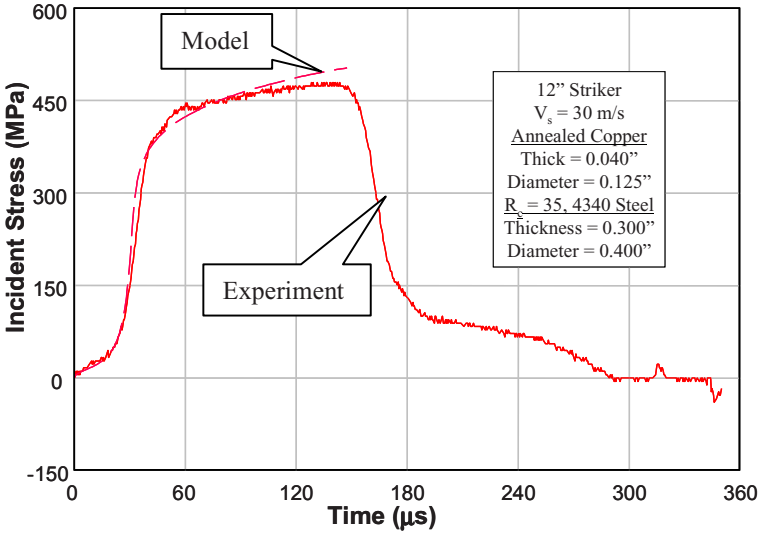

Figure 2.17 Incident pulse produced with dual pulse shaping technique
(Reproduced from Frew et al. (2005) with permission)

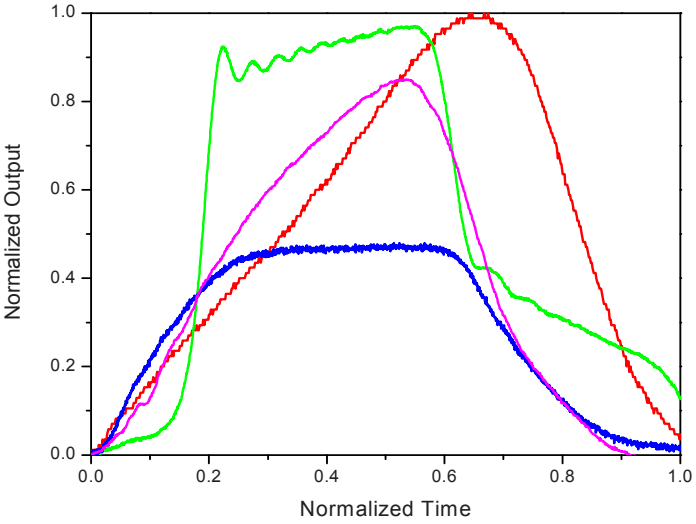

Figure 2.18 Various incident pulses produced with different pulse shaping designs
(Reproduced from Chen and Song (2009) with permission)

2.6 Single Loading and Unloading Control

When the striker impacts on the incident bar, the resulting stress wave propagates back and forth within the Kolsky-bar system. Figure 2.19 illustrates the stress waves measured with the strain gages in the middle of the incident bar in a typical Kolsky bar experiment. The corresponding displacement history of the incident bar end is also illustrated in Fig. 2.19. Figure 2.19 indicates that every time the stress wave reflects back from the specimen side, the bar end moves a small step. The stop-and-go response of the incident bar end has the specimen compressed progressively. Usually only the pulses associated with the first loading are recorded to calculate the stress-strain response of the specimen material; however, the specimen recovered after the experiment was actually subjected to multiple loading in a single Kolsky bar experiment. This causes

confusion in any attempt to correlate the mechanical response of the specimen with its microstructural change. If such correlation between the loading history and the microstructure evolution is desired, the specimen should be subjected to only a single loading. In other words, only the first loading goes through the specimen while the additional momentum after the first loading is trapped.

The concept of momentum trapping in Kolsky-bar experiments appeared as early as 1960s (Baker and Yew 1966), but different designs have been developed recently.

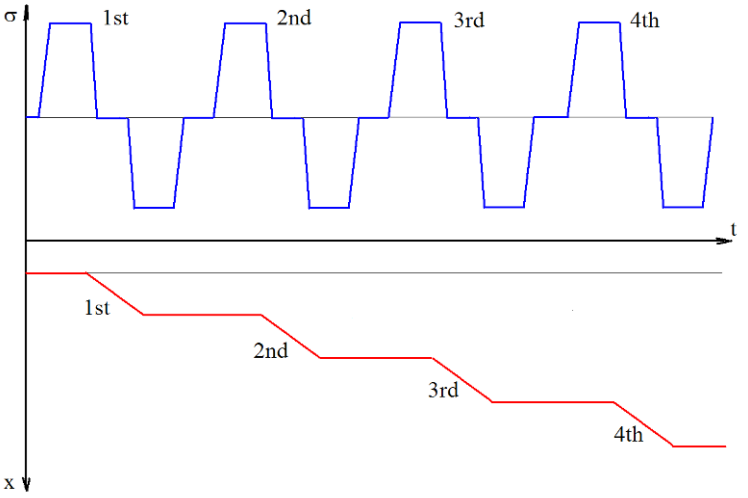

Figure 2.19 Multiple loading in Kolsky-bar experiment

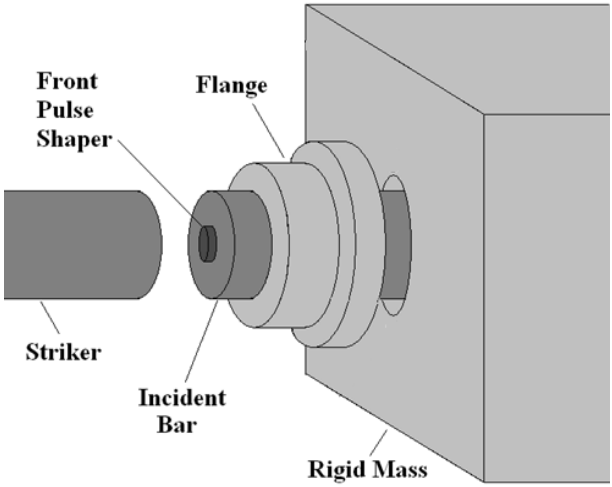

Figure 2.20 Modified momentum trap for Kolsky compression bar
(Reproduced from Song and Chen (2004c) with permission)

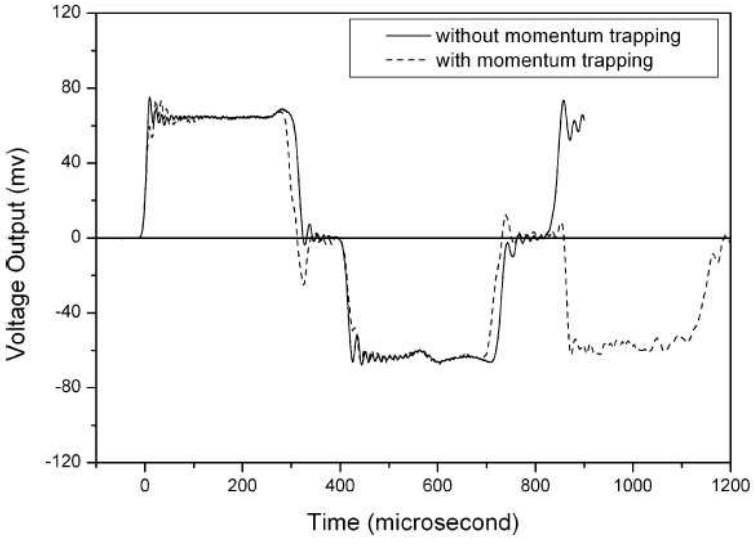

Figure 2.21 Comparison of pulses obtained with and without the momentum trap
(Reproduced from Song et al. (2006c) with permission)

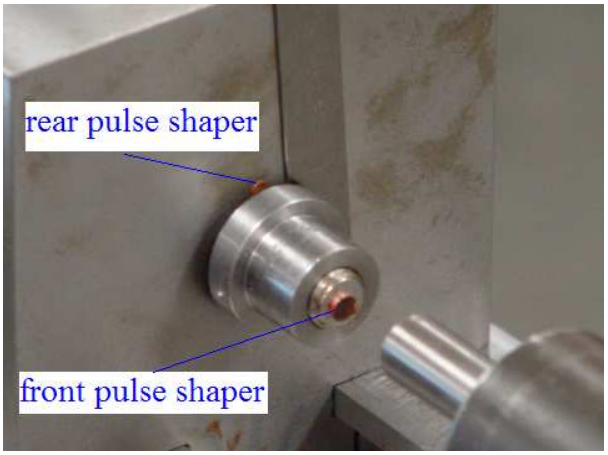

Figure 2.22 Rear pulse shaping technique

Song and Chen (2004c) modified a momentum trap concept and developed a single loading device for Kolsky compression bar which is illustrated in Fig. 2.20. As shown in Fig. 2.20, this momentum trap consists of a rigid mass and a flange attached to the impact end of the incident bar. The incident bar passes through the rigid mass that plays a role to trap the momentum (stop the bar system) after first impact. There exists a gap between the flange and the rigid mass that needs to be preset precisely. The necessary width of the preset gap, d, is determined with the incident strain history,

$$d = C_0 \int_0^T \varepsilon_I(t) dt \tag{2.31}$$

This gap allows only the first compressive pulse to pass into the incident bar before it is closed. The reaction mass then plays a role of rigid wall to block the incident bar from any further movement so that no more compression is loaded on the specimen. Figure 2.21 shows a comparison of the pulses with and without the momentum trap (Song et al. 2006c). It clearly shows that the secondary compression in the experiment without momentum trap is turned into a tensile pulse that pulls the incident bar back from the specimen when the single loading system is employed.

This new design of the momentum trap does not affect the application of the pulse shaping technique. Rather, it provides possibility of controlling not only the loading portion of the incident pulse but also the unloading portion through a reverse pulse shaping technique. The pulse shaping technique described so far in the book is to place the pulse shaper(s) on the impact surface of the incident bar to control the profile of the incident pulse. In this manner, only the loading portion is controllable. The unloading portion remains to be uncontrolled, which is not acceptable when the unloading cannot be random in the characterization of certain materials. For some materials with unique hysteretic stress-strain response such as shape memory alloys and viscoelastic or viscoplastic solids, it is desirable to understand their stress-strain response not only for loading but also for unloading. In some cases, understanding unloading stress-strain response is even more important than loading response. In order to obtain a valid loading-unloading stress-strain loop, the strain rate should be the same constant for both loading and unloading. The entire profile of the incident pulse including both loading and unloading needs to be under control.

The loading profile is controlled with the conventional pulse shaping technique while the unloading part is controlled through the reverse pulse shaping where pulse shapers are placed between the flange and reaction mass, as shown in Fig. 2.22. The rear pulse-shapers placed on the surface of the rigid mass initially has a preset gap from the flange. During an experiment, the front pulse-shaper is extensively compressed at first, generating a desired incident loading profile that deforms the specimen at a constant strain rate under dynamic stress equilibrium over the loading phase of the experiment. The gap between the flange and the rigid mass is then closed. The rear pulse-shapers on the surface of the rigid mass are thereafter compressed by the flange, changing the unloading profile of the incident pulse. This controlled unloading profile in the incident pulse ensures that the specimen recovers at the same constant strain rate during unloading. A compressive stress-strain hysteretic response for the material is thus obtained at a certain constant rate of both loading and unloading. The detailed applications of this technique are discussed in Chapters 4.5.1 (for PMMA) and 5.3.2 (for shape memory alloy).

The above momentum trap was designed following the general concept of the stress reversal Kolsky bar that was developed by Nemat-Nasser et al. (1991). The overall design of their setup is shown in Fig. 2.23. In addition to the conventional Kolsky-bar design, a transfer flange, a tube over the bar, and a reaction mass were implemented (Fig. 2.23). The incident tube is placed against the transfer flange at one end and against the reaction mass at the other end. When the striker impacts the

transfer flange, it imparts two common compression pulses traveling along the incident tube towards the reaction mass and along the incident bar towards the specimen. The compressive pulse in the incident tube is reflected from the reaction mass and travels back to the transfer flange also as compression. The compression is reflected from the flange as tension. This tension makes the particle velocity in the incident bar move in the reverse direction, avoiding the second compression on the specimen. The resultant incident pulse is thus a combination of compression-tension, as shown in Fig. 2.24 (Nemat-Nasser et al. 1991)

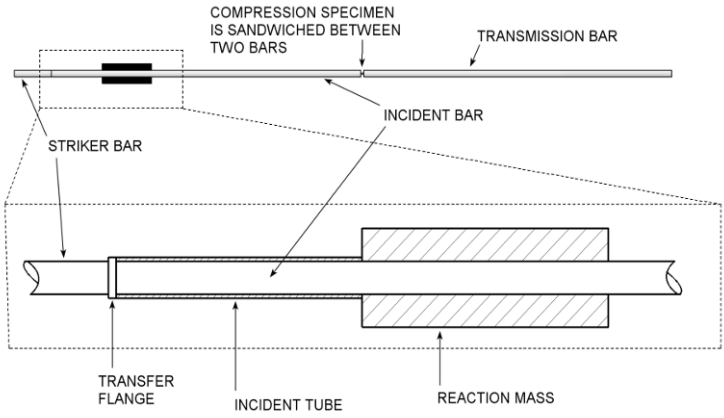

Figure 2.23 Stress reversal Kolsky bar
(Reproduced from Nemat-Nasser et al. (1991) with permission)

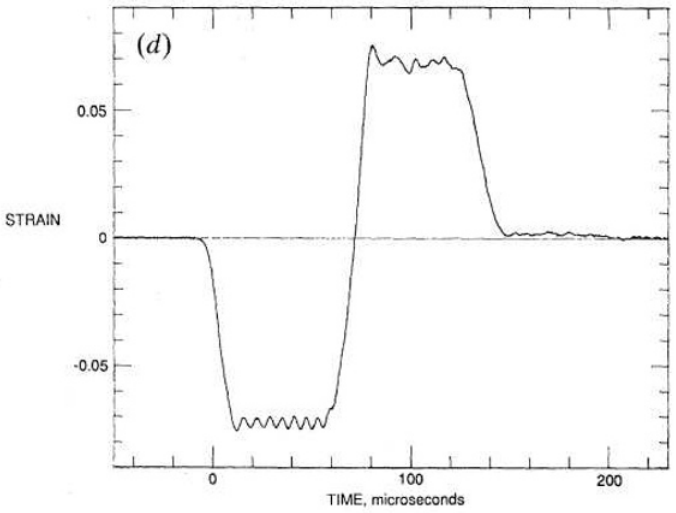

Figure 2.24 Incident pulse generated with the stress reversal Kolsky bar
(Reproduced from Nemat-Nasser et al. (1991) with permission)

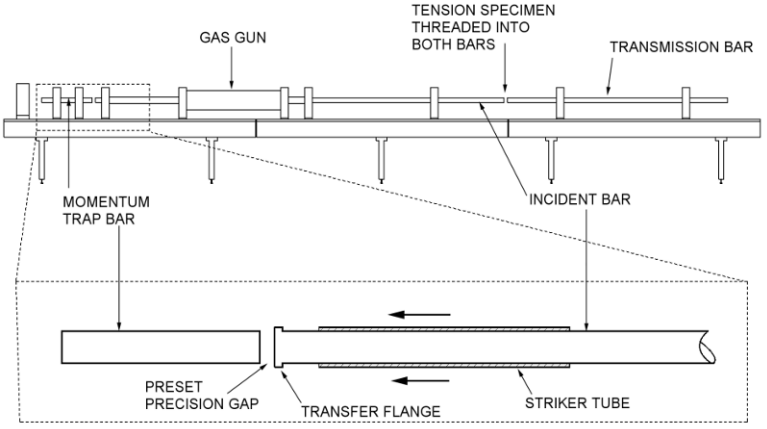

Figure 2.25 Momentum trapped Kolsky tension bar
(Reproduced from Nemat-Nasser et al. (1991) with permission)

Due to the additional incident tube, part of the external impact load is distributed to the incident tube, which is then reversed. This excessive stress may overwhelm the flange root when high stress levels are required for hard material characterization.

The momentum trap has also been developed for Kolsky tension bar with a very similar mechanism, as shown in Fig. 2.25 (Nemat-Nasser et al. 1991). A momentum trap bar is set aside the transfer flange on the incident bar with a preset gap. The gap needs to be precisely set such that the momentum trap bar starts to be in contact with the transfer flange surface once the first tensile pulse transfers into the incident bar through the transfer flange. The tensile pulse in the incident bar is reflected back at the incident bar/specimen interface, becoming compression. Without the momentum trap bar or with a wider gap between the momentum trap bar and the transfer flange, the compressive pulse turns back to the incident bar as the secondary tensile pulse, pulling the specimen in tensile deformation again. However, with the precisely preset gap between the momentum trap bar and the transfer flange, the compressive pulse directly transmits into the momentum trap bar, which will be reflected back at the far free end as a tensile pulse. This tensile pulse pulls the momentum trap bar off the incident bar as the contact interface with the transfer flange does not support tension. The pulse is thus trapped within the momentum trap bar; whereas, the incident bar remains at rest. Consequently the specimen is subject to only the first tensile loading.

2.7 Upper Limit of Strain Rate

In Kolsky-bar experiments for material property characterization, dynamic stress equilibrium and constant strain rate need to be achieved in the specimen. Since the specimen is initially at rest, the ideal testing conditions are not satisfied over the entire duration of the experiment. It takes time for the stress waves to bring the specimen into near equilibrium and the strain rate to a desired constant level. If the desired strain rate is very high, the specimen may fail as the strain rate is still rising. Therefore, there is a limit for the maximum strain rate for achieving dynamic stress equilibrium and constant strain rate simultaneously. Beyond this upper limit of strain rate, the specimen may deform under neither equilibrated stress nor constant strain rate. To estimate the validity range of the experimental results, it is necessary to know the upper limit

of strain rates that corresponds to certain strains where the material response drastically changes, such as plastic yielding or failure.

As mentioned earlier, stress wave takes several rounds of reflections back and forth in the specimen to approximately achieve dynamic stress equilibrium. The number of reflections required for dynamic stress equilibrium varies for different materials and different loading conditions. If we assume the required number of reflections is n, the corresponding time for the specimen to achieve stress equilibrium is

$$t = n\frac{L_S}{C_S} \tag{2.32}$$

If the specimen deforms at a constant strain rate, the strain accumulated before the specimen is in equilibrium is

$$\varepsilon = \dot{\varepsilon} \cdot t = n\dot{\varepsilon}\frac{L_S}{C_S} \tag{2.33}$$

In order to ensure the validity of the resultant data, any critical event, for example, either plastic yielding or failure, should not occur prior to this accumulated strain,

$$\varepsilon < \varepsilon_{cr} \tag{2.34}$$

where ε_{cr} is the critical strain for such an event. Hence, the strain rate is limited due to the requirement of stress equilibrium (Ravichandran and Subhash 1994),

$$\dot{\varepsilon} < \frac{\varepsilon_{cr} C_S}{nL_S} \tag{2.35}$$

The above strain-rate limit is derived from consideration of stress equilibrium. Another requirement is the achievement of constant strain rate, which turns out to be a more restrictive limit. In Kolsky-bar experiments, the strain rate has to increase from zero to a targeted value. It takes a finite amount of time for this process to take place, while the strain in the specimen is being accumulated. If the specimen fails or plastically yields during this process, the strain rate in the specimen during the entire loading process is not constant. Therefore, depending on the

failure strain in the specimen material, there is a limit on the achievable constant strain rate in the experiment.

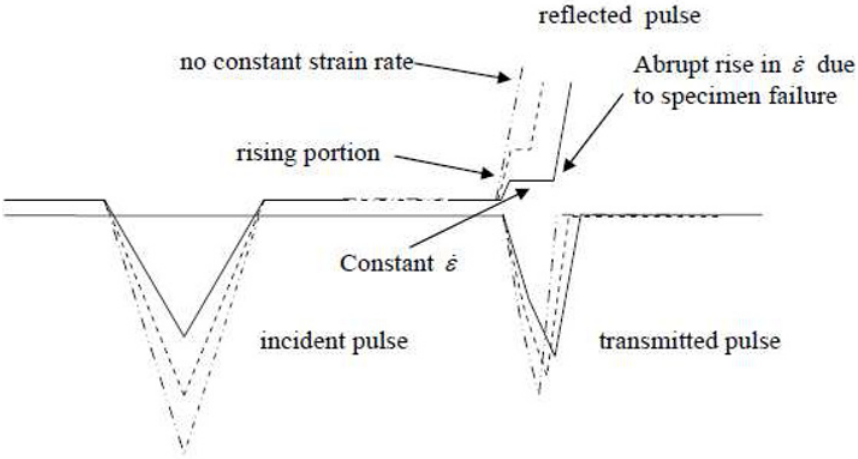

Figure 2.26 A schematic illustration of the upper limit of constant strain rate in a brittle specimen
(Reproduced from Pan et al. (2005) with permission)

Figure 2.26 illustrates the upper limit of constant strain rate in a brittle specimen (Pan et al. 2005). As will be discussed in detail in Chapter 3, it is necessary to generate a linear stress pulse to achieve a constant strain rate in a linear and brittle specimen,

$$\sigma_i = M \cdot t \tag{2.36}$$

where M is the loading rate of such a linear (ramp) pulse. The strain-rate history in the linear specimen, ε_S, can be analytically estimated by (Frew et al. 2002)

$$\varepsilon_S = \frac{A_B}{A_S} \cdot \frac{M}{E_S} \left[1 - \exp\left(- \frac{2C_S t}{L_S} \cdot \frac{\rho_S C_S A_S}{\rho_B C_B A_B} \right) \right] \tag{2.37}$$

The strain history is calculated by integrating (2.37) with respect to time,

$$\varepsilon_S = \frac{A_B}{A_S} \cdot \frac{M}{E_S} \left\{ t - \frac{A_B L_S}{2A_S C_S} \left[1 - \exp\left(- \frac{2C_S t}{L_S} \cdot \frac{\rho_S C_S A_S}{\rho_B C_B A_B} \right) \right] \right\} \tag{2.38}$$

The strain rate can be considered to be a constant from the instant $t = \tau$ until the specimen fails. The instant, τ, is determined by satisfying the following condition,

$$\xi = \left[\exp\left(- \frac{2C_S t}{L_S} \cdot \frac{\rho_S C_S A_S}{\rho_B C_B A_B} \right) \right]_{t=\tau} \to 0 \tag{2.39}$$

Hence,

$$\varepsilon_S = \frac{A_B}{A_S} \cdot \frac{M}{E_S} \eta \tag{2.40}$$

where

$$\eta = 1 - \xi \tag{2.41}$$

For a brittle material, a constant strain rate needs to be achieved prior to specimen failure or any other significant events under investigation,

$$\varepsilon_S \big|_{t=\tau} < \varepsilon_{cr} \tag{2.42}$$

or we have

$$\varepsilon_S < \frac{\beta}{\tau} \cdot \frac{\varepsilon_{cr}}{\alpha/\eta - 1} \tag{2.43}$$

where

$$\beta = \frac{2\pi C_S}{L_S} \cdot \frac{\rho_S C_S A_S}{\rho_B C_B A_B} \tag{2.44}$$

Hence, the upper limit of strain rate can be estimated with (2.43) for the consideration of constant strain-rate deformation.

Figures 2.27 and 2.28 show the strain rate histories from the pulse-shaped Kolsky-bar experiments on an S-2 glass/SC15 epoxy composite and a PMMA, respectively (Pan et al. 2005). In both figures, the solid dots indicate where the specimen starts to fail. The strain rate histories show that the critical strain rate for the composite is 1700 s^{-1}, beyond which non-constant strain rate is observed for the entire loading duration. When the desired strain rate is higher than 1700 s^{-1}, the specimen fails before a constant strain rate is achieved. In a very similar way, such a critical strain rate locates between 1910 and 2130 s^{-1} for the PMMA, as shown in Fig. 2.28. Table 2.1 presents a comparison of the upper strain-rate limit from theoretical estimates with (2.43) and experimental results for both materials, the result of which shows good agreement.

When estimating the upper limit of strain rate in Kolsky-bar experiments, both criteria of stress equilibrium and constant strain rate need to be satisfied simultaneously. The eventual upper limit of strain rate should be the minimum between the estimates from (2.35) and (2.43),

$$\varepsilon_{cr} = \min\left\{\frac{\varepsilon_{cr} C_S}{\alpha L_S}, \frac{\beta \varepsilon_{cr}}{\tau(\beta/\eta - 1)}\right\} \tag{2.45}$$

Using the above materials as examples again, the upper limits of strain rate for the composite and PMMA are estimated with (2.35) for dynamic stress equilibrium as 3950 and 9567 s^{-1}, respectively. These limits are much higher than those tabulated in Table 2.1 that are estimated from constant strain rate consideration. This indicates the requirement of constant strain-rate deformation is more restrictive than stress equilibrium requirement when estimating the upper limit of strain rates in Kolsky-bar experiments.

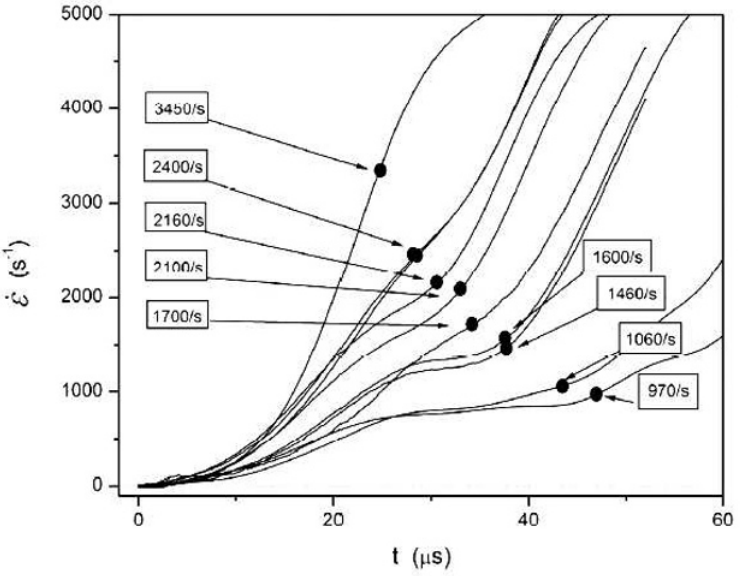

Figure 2.27 Strain-rate histories in composite specimens
(Reproduced from Pan et al. (2005) with permission)

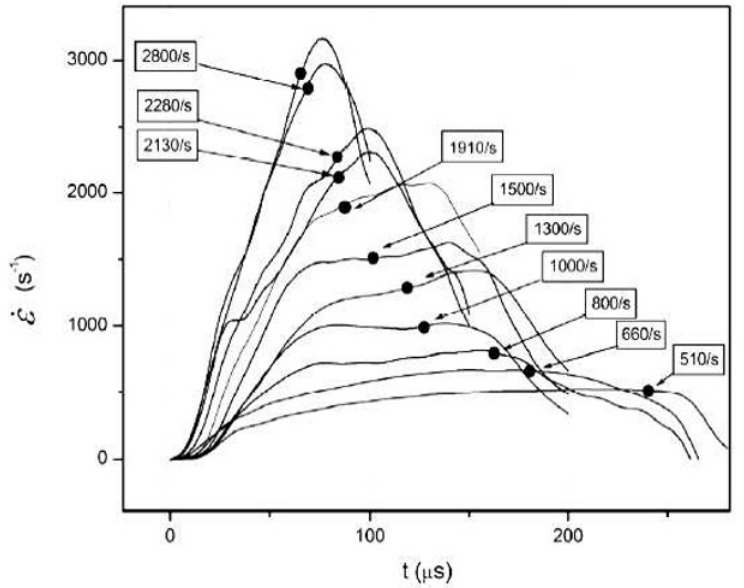

Figure 2.28 Strain-rate histories in PMMA specimen
(Reproduced from Pan et al. (2005) with permission)

Table 2.1 Comparison of upper strain-rate limit
from theoretical estimates and experimental results (Pan et al. 2005)

	PMMA	S-2 Glass/SC15 composite (in plane direction)
Theoretical estimate	1735 /s	1499 /s
experiments	~1910 /s	1600/s~1700 /s

Chapter 3. Kolsky Compression Bar Experiments on Brittle Materials

Many brittle materials deform in a manner of nearly linear elasticity until failure at small strains. As specimens in Kolsky-bar experiments, these materials are extremely sensitive to stress concentrations due to bar misalignment or non-parallel loading surfaces. To deform a linear elastic specimen at a constant strain rate, a loading pulse with constant stress rate is needed. This chapter describes the characteristics of brittle specimens, introduces the modifications to Kolsky bar necessary to achieve the desired and valid testing conditions on the specimen, and outlines the design of Kolsky compression bar experiments on brittle materials with step-by-step examples.

3.1 Brittle Specimens in Kolsky Bar

There is a wide range of materials that can be considered as brittle materials, such as ceramics, glass, ice, rocks, concrete, bricks, cortical bones, and some composites. Under compression, these materials deform in a nearly linear elastic manner and fail at small strain values, typically around 1% or less. This small strain-to-failure measurement makes measuring the deformation of the specimen with bar signals difficult. The linear nature of the specimen material requires a loading history of constant stress rate forconstant strain-rate deformation.

Brittle materials cannot yield locally, which make them susceptible to stress concentrations. There are three main sources of stress concentrations on brittle specimens: 1) Poor flatness and parallelism of the loading surfaces of the specimen, the machining tolerances on brittle specimens are much stricter; 2) Misalignment of the bars, which can cause the bar end faces to be unparallel and thus create stress concentrations at specimen edges even though the specimen has a high machining quality; and 3) Specimen indentation into the bar end faces caused by small diameter but stiffer brittle materials, such as tungsten carbide or aluminum nitride, under compression. The stiffer specimen indents into the more compliant bar end faces, generating stress concentrations around the edges of the specimen and causing premature failure.

W.W. Chen and B. Song, *Split Hopkinson (Kolsky) Bar: Design, Testing and Applications*, Mechanical Engineering Series, DOI 10.1007/978-1-4419-7982-7_3,

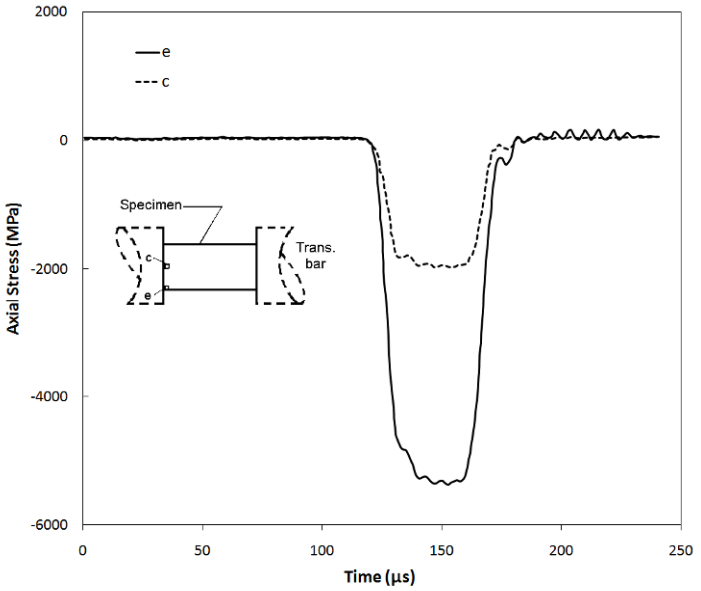

Figure 3.1 Stress concentration on the edges of a brittle specimen

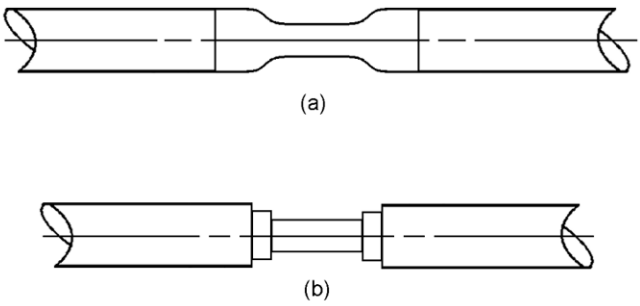

Figure 3.2 Brittle specimen configurations

Figure 3.1 shows the results from a numerical simulation of an aluminum nitride (AlN) specimen compressed elastically by a steel Kolsky bar (Chen et al. 1994). The solid line is the time history of the axial-stress in an element on the specimen edge, whereas the dashed line is the stress history at the center of the specimen end face. It is seen from Fig. 3.1 that the corner stress is 270% of the stress at the center. This situation becomes more severe as the specimen stiffness increases. Since brittle materials such as ceramics are unable to yield locally like ductile metals, this locally concentrated stress will cause the specimen to fail unevenly and thus prematurely. In order to obtain the failure strength of the brittle material under uniaxial stress conditions, the stress concentrations at the specimen edges must be minimized.

Two main types of specimen configurations have been proposed to reduce the stress concentration, as illustrated in Fig. 3.2 (Chen et al. 1994):

- Dumbbell shaped ceramic specimen (Fig. 3.2(a)).
- The specimen is sandwiched between platens made of hard materials (Fig. 3.2(b)).

Numerical analysis shows that the dumbbell shaped specimen design (Fig. 3.2(a)), with a diameter at ends matching the incident and transmission bar ends, is the best configuration to overcome the stress concentrations caused by indentation. It is noted that if the larger ends of the specimen are smaller than the bar ends, there will still be stress concentrations at the edges of the specimen ends. The specimen geometry should be carefully designed such that the larger ends are at least three times larger in cross-sectional area than the gage section. Consequently, the stress in the gage section is higher than the concentrated stress on the ends. Failure will occur in the gage section first. The disadvantage of this method is the cost to machine dumbbell specimens from ultra-hard brittle materials such as high-strength ceramics. Without stress concentrations, the strength of the ceramic material is affected by the quality of the surface finish of the specimens. To obtain statistically valid results from brittle materials, large quantities of specimens, up to 30 per condition, are often required (Greene, 1956). The demands on the quality and quantity of the dumbbell brittle specimens can often be cost prohibitive to a program.

Based on above considerations, a traditional right-circular-cylinder configuration of a brittle specimen with platens attached to both ends is more commonly used (Fig. 3.2(b)). The design of such platens will be discussed in the following section.

In order to determine the cylindrical specimen dimensions, the approximate specimen strength needs to be estimated either through quasi-

static experiments or by a preliminary Kolsky-bar experiment on the same or similar material. The specimen diameter should be calculated such that the stress in the transmission bar is less than 30% of the bar yield strength. The incident pulse stress will be higher than that of the transmission pulse. Therefore, even though the transmission bar is only loaded to 30% of its yield strength, care must be taken not to yield the incident bar. The incident pulse should terminate shortly after the specimen fails.

As an example, consider a ceramic specimen with a compressive strength of approximately 5 GPa that is to be tested with 19-mm-diameter maraging steel bars. Considering the rate effects and data scattering on ceramic samples, the specimen strength for experiment design purposes is estimated to be 6 GPa. The yield strength of the bar is at most 2.4 GPa. The maximum diameter of the specimen can be estimated to be

$$d_s = \sqrt{\frac{0.3\times 2.4}{6}} d_B = 0.346\times 19 = 6.57 \text{ mm} \tag{3.1}$$

where d_s and d_B are the specimen and bar diameters, respectively. It should be noted that the 2.4-GPa bar strength is from an ultra high-strength steel. If the bar material is weaker, the ceramic specimen diameter needs to be further reduced. On the other hand, if the brittle material has a low compressive strength as seen in many geological and construction materials, the specimen diameter should be the same as the bar diameter to avoid complications from stress concentrations.

With the specimen diameter determined, the other dimension is the specimen thickness. In quasi-static compression experiments on brittle specimens, the length-to-diameter ratio of the specimen is usually 2:1 as specified by ASTM standard C39 to minimize the end effects. In a Kolsky-bar experiment, the decision on specimen thickness is made by not only the end effects, but also the effects from dynamic stress equilibrium across the specimen, and the desired strain-rate level. The strain-rate achieved in a Kolsky bar experiment is inversely proportional to the specimen thickness. A short specimen is desired in order to achieve high strain-rates. For ceramics, a length-to-diameter ratio of 1.0 is more commonly used in Kolsky-bar experiments and even with a shorter length, as pointed out in Chapter 2.7, the achievable strain-rate is limited by the small failure strain of the specimen material. If the expected strain rate level is too high, brittle materials will fail during the strain acceleration stage before a constant strain rate can be reached.

For brittle materials with lower wave speeds, the specimen length is also restricted by the dynamic equilibrium requirement (Ravichandran

and Subhash 1994). Due to the small failure strains, a thick specimen will start to fail from impact end before the specimen is evenly loaded across its thickness.

Besides the overall dimensions of the specimen, the surface quality of brittle materials, such as glasses and ceramics, is critical to the strength measured in the experiments. The two end faces of a specimen should be flat and parallel. Figure 3.3 shows an example of a ceramic cylindrical specimen.

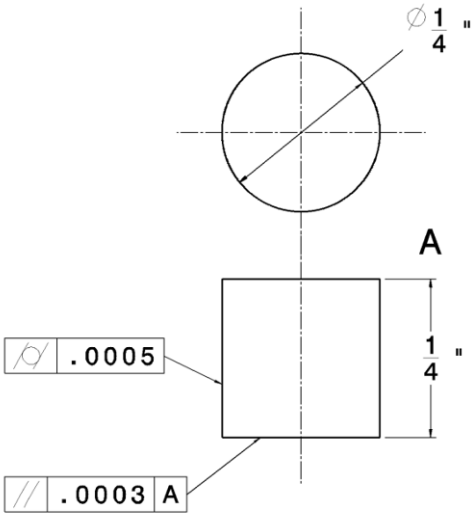

Figure 3.3 Geometry of a hard specimen

3.2 Platens to Minimize Stress Concentration

The typical characteristic of brittle materials is extremely small failure strain, however, the strength may be low or high, depending on the material under investigation. If the specimen strength is low, such as limestones or concretes, the diameter of the specimen should be the same as that of the bars to minimize stress concentrations on the specimen, as mentioned earlier. For specimens that are not as hard as ceramics, nor as weak as unconfined concretes, such as glasses, the steel bar end faces are the best fit material for lateral expansion. However, when the specimen fails, the sharp fragments of the specimen will damage the bar end faces after each experiment. In this case, hardened steel platens should be used to protect the bar end faces. When ultra high-strength materials, such as ceramics, are to be tested, the specimen section needs to be carefully designed. A pair of platens between the specimen and bars has been commonly used to minimize the indentation and stress concentration in Kolsky bar experiments.

There are two criteria in the selection of platen materials, along the axial and radial directions, respectively. In the axial, or thickness direction, the platens should be sufficiently stiff in terms of both material property and structural design. Tungsten carbide (WC) is a material commonly used as the platen material. The mechanical impedance (ρcA) of the platens is often made identical to that of the bars to minimize the effects of introducing platens on the one-dimensional wave propagation. This consideration determines the diameter of the platens as a function of the bar diameter and material. A thin platen can have significant equibiaxial bending when pressed by a hard specimen of small diameter. The platens thus require a certain thickness. If a steel bar diameter is 19 mm, the diameter of WC platens is about 12.7 mm to match the impedance with the bars. A thickness of 6.35 mm is commonly used (Chen and Luo 2004).

To ensure the integrity of the platens when testing very hard specimens, the hard platens are often confined by press-fit metal rings. The press-fit can be either a mechanical fit or a thermal expansion mismatch where a cold platen is fit into a hot ring. A schematic diagram of the ring-confined hard platen is shown in Fig. 3.4 (Chen and Ravichandran 1997). It is noted that the equivalent wave impedance due to the addition of the metal ring should match with that of the bars to minimize the disturbance to the one-dimensional stress wave propagation.

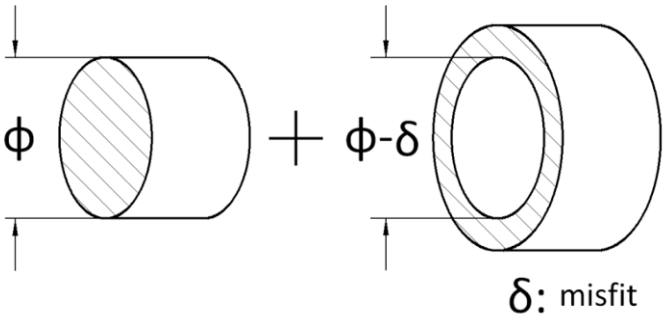

Figure 3.4 Hard platens confined by press-fit ductile rings
(Reproduced from Chen and Ravichandran (1997) with permission)

The hard platens can significantly reduce the stress concentration on the brittle specimen, but cannot eliminate it completely. A similar numerical simulation to the one shown in Fig. 3.1 discovered that when an AlN specimen is pressed against a thick WC platen, a stress concentration of nearly 150% is still in presence (Chen et al. 1994). Although this is much less than the 270% found in the case without a platen, the presence of stress concentration can still lead to premature failure with a measured failure strength below the actual material capacity. However, the platen method has been widely used because its affordability and simplicity.

Along the radial direction, the deformation of the platens should match that of the specimen. If the platens deform more than the specimen does, the specimen ends are torn apart by end friction, causing multiaxial stresses near the ends, as well as premature failure. On the other hand, if the platens deforms less than the specimen along the radial direction, the specimen ends are effectively confined, which suppresses failure initiation from the ends.

Take an example of experiments on glass specimens. Both the platen and specimen materials can be considered as isotropic linear-elastic materials. Under uniaxial loading, the lateral strains in both materials can be computed as

$$\varepsilon_{22} = \frac{1}{E}\left[\sigma_{22} - \nu\left(\sigma_{33} + \sigma_{11}\right)\right] \tag{3.2}$$

where σ_{11} is the axial stress, and σ_{22} and σ_{33} are the lateral stresses equal to zero for both materials. Table 3.1 gives a comparison of the mechanical parameters in (3.2) for steel and WC platens in characterizing a glass specimen.

Table 3.1 Mechanical parameters of platen materials and glass specimen

	Poisson's Ratio (ν)	Young's Modulus (E), GPa	$-\frac{\nu}{E}$, (m^2/N)
Glass	0.19	61	-3.11×10^{-12}
Steel	0.29	200	-1.45×10^{-12}
WC	0.20	566	-0.35×10^{-13}

As indicated in Table 3.1, under axial compressive loading, the lateral strains in both the steel and WC platens are less than that in the glass specimen. The WC platens constrain the specimen in the lateral direction more severely, resulting in higher axial peak stress achieved in the specimen. The lateral strain in the steel platens is closer to that in the specimen, which reveals more realistic failure initiation in the glass specimen under compression. However, in real Kolsky-bar experiments on brittle materials, the cross-sectional area mismatch between the platens and specimen should be considered when calculating the lateral strains.

3.3 Universal Joint

Due to the sensitivity of the specimen to stress concentrations, the precise linear and angular alignment of the striker, incident, and transmission bars is critically important in experiments on brittle materials. Since brittle materials fail at small strain levels, any misalignment of the Kolsky-bar system can result in inaccurate strain measurement.

Depending on the design of the bar supporting systems, there are a number of approaches to align the bars along a common axis. The laser

system presented in Section 1.4 is an excellent method for aligning the bar system. However, there still might be slight misalignment in the bar system that influences the measurement of stress-strain response for brittle materials. Unlike quasi-static testing machines that typically have universal joints for self-alignment, a conventional Kolsky bar does not have such a self-aligning device along its loading axis or gripping system to ensure that the specimen end faces are evenly loaded.

To correct the slight misalignment along the loading axis after the laser alignment, a simplified universal joint can be placed between the hardened platen and the transmission bar, as schematically shown in Fig. 3.5 (Meng and Hu 2003, Chen et al. 2007). The joint consists of a pair of disks with a spherical joining surface in between. The disks have the same diameter and material as the bars, thus introducing no impedance mismatching to the compressive transmitted pulse propagating along the loading axis and across the universal joint. In the gage section assembly procedure during an experiment, the spherical interface is the last to engage into contact, thus having any misalignment automatically corrected. Small amount of vacuum grease should be applied between the contacting surfaces along the loading axis to minimize friction and improve engagement. Figure 3.6 shows an example of using the universal joint in Kolsky-bar experiments on PMMA (Meng and Hu 2003). Four strain gages were attached at the same cross section but 90 degrees apart surrounding the cylindrical surface of the PMMA specimen. A slight misalignment of the bar system will result in non-uniform deformation in the specimen, as shown in Fig. 3.6 (a). However, the introduction of the universal joint subjects the specimen to uniform loading, which is indicated by the nearly same strain signals in Fig. 3.6 (b).

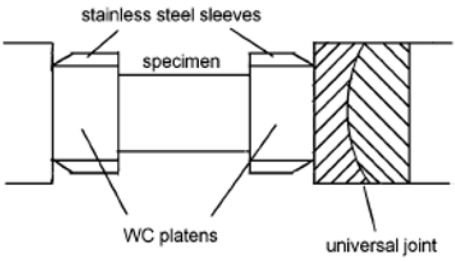

Figure 3.5 Universal joint in a specimen assembly
(Reproduced from Chen et al. (2007) with permission)

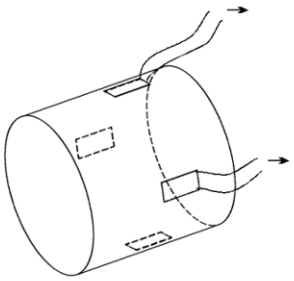

There are strain gages signed from for gages 90° apart on the sample.

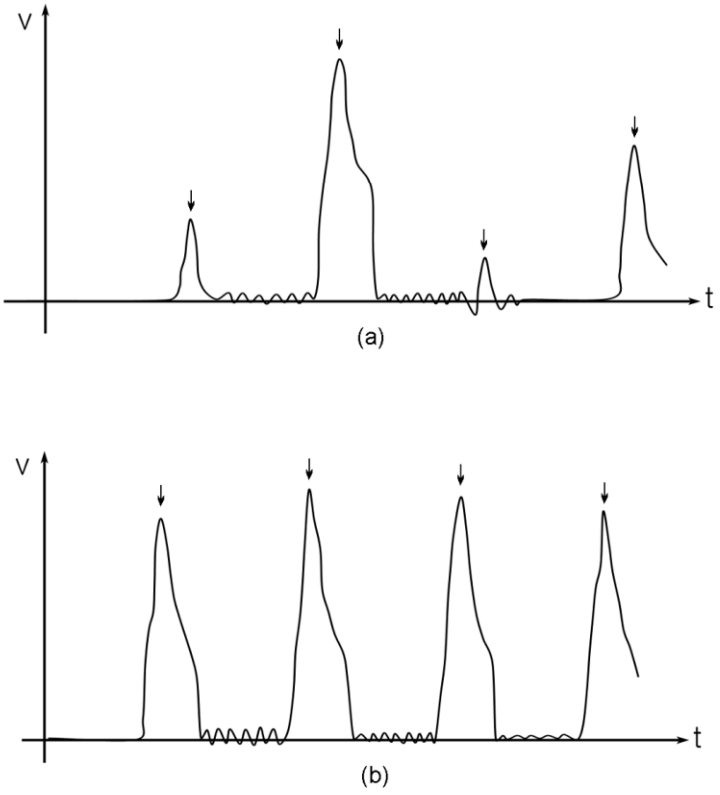

Figure 3.6 Comparison of axial strains in the PMMA specimen without (a) and with (b) the universal joint
(Reproduced from Meng and Hu (2003) with permission)

In Fig. 3.5, it is noticed that the stainless steel press-fit sleeves on the WC platens are tapered towards the bar-contacting surfaces. This is to minimize the disturbance, at the interface between the bars and the platens, by the introduction of the confining sleeves onto the platens that are already impedance matched with that of the bars.

3.4 Pulse Shaping

As outlined in Chapter 2, the specimen should be subjected to a particular stress-wave loading such that it deforms uniformly under a dynamically equilibrated stress state and at a constant strain rate. In most cases, the trapezoidal incident pulse does not facilitate the achievement of these experimental conditions. For example, the brittle specimen may fail at very early stage of loading, e.g., within the first 10 μs. Within such a short duration, the specimen may not be in dynamic equilibrium. Moreover, the specimen may deform at drastically decreased strain rates at the plateau of loading.

With the nearly linear response of the brittle specimens, the loading pulse needs to have a ramp history to deform the specimen at a constant strain-rate. This ramp history for the incident pulse also helps to quickly generate equilibrated stress state in the brittle specimen. Figure 3.7 illustrates the idealized incident pulse (i.e., loading history) and its relation with the transmitted pulse (stress history in the specimen). The constant gap between the incident and transmitted signals is the amplitude of the reflected signal, which indicates a constant strain rate during the experiment.

In order to produce a ramp incident pulse, the pulse shaping technique presented in Chapter 2.5 needs to be used. With respect to a variety of incident pulses that can be produced by the pulse shaping technique, the linear ramp type of pulse in Fig. 2.18 is needed for brittle material characterization. The ramp pulse also minimizes the wave dispersion. Examples will be given in the following sections.

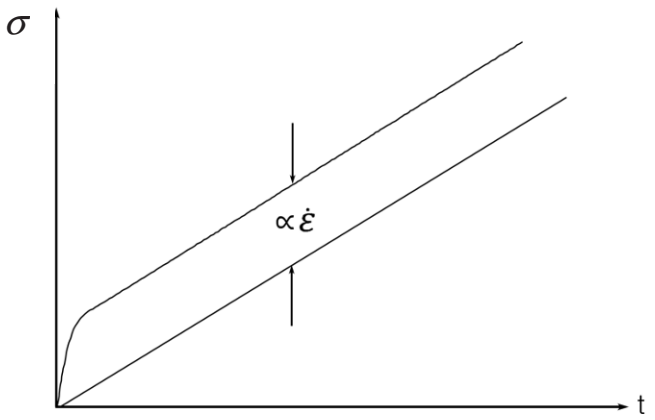

Figure 3.7 Desired incident pulse for brittle material testing

3.5 Experiment Design for Brittle Materials

The Kolsky-bar experiment design depends on the specimen response and the desired testing conditions. Without a feedback control system, the desired testing conditions in a Kolsky-bar experiment are typically achieved in an iterative manner. Due to the simplicity of the brittle material response, the number of iterations is minimal in brittle material characterization. We present several examples in this section to illustrate the Kolsky-bar experiment design for brittle materials.

3.5.1 Macor and Limestone

To demonstrate the basic characteristics of Kolsky bar experiments on brittle materials, we present results from two pulse shaped experiments with a machinable glass ceramic, Macor (Frew et al. 2002). We first

conducted a few quasi-static compressive stress-strain experiments with the material, and found that this material had relatively low strength and stiffness. This material easily fails in a localized manner.

Since the strength of the Macor is not high (relative to other ceramic materials), the specimen diameter is not a critical parameter in design. Considering the equilibrium requirement, the specimen was designed with a length of 9.53 mm and a diameter of 9.53 mm, making the length-to-diameter ratio as 1:1. Due to the localized failure at low strengths, no platens or universal joints were needed.

The striker, incident, and transmission bars were made from high strength, maraging steel and have density $\rho = 8100$ kg/m^3, Young's modulus E = 200 GPa, and bar wave velocity c = 4970 m/s. The incident and transmission bars had diameters of 19.05 mm and lengths of 2130 and 915 mm, respectively. Trial experiments revealed that it was necessary to generate a concave downward incident stress pulse similar to that shown in Fig. 2.15 to facilitate a nearly constant strain rate in the specimen under dynamic stress equilibrium over most of the loading duration.

An annealed C11000 copper disk with a diameter of 10.21 mm and a thickness of 0.79 mm was used as the pulse shaper for striking speed of 15 m/s in the Macor characterization. Figure 3.8 shows the pulse-shaping result of the incident pulse. The measured incident stress pulse and a prediction from our pulse shaping model presented in Chapter 2.5 are both shown in Fig. 3.8. Figure 3.9 shows axial stresses on the two end faces of the specimen, which were calculated with (1.8) and (1.9), respectively. Both interfacial stresses are in reasonably good agreement, which implies that the specimen is nearly in dynamic stress equilibrium. Under stress equilibrium, the strain rate in the specimen is calculated with (1.12), the result of which is shown in Fig. 3.10. The average strain rate is approximately 165 s^{-1} over 25 μs to 105 μs. Before 25 μs, the specimen is in the stage of strain acceleration. During this strain acceleration, the specimen has accumulated an axial strain (the area under the curve before 25 μs) of about 0.13%. The stress values for strains less than 0.13% were obtained when the strain rate varied from 0 to 165 s^{-1}. At about 105 μs, the specimen begins to fail with eventual catastrophic damage. The incident bar end no longer feels resistance from the specimen, as indicated by the fast rise in the reflected signal. This high-amplitude reflected signal is no longer an indication of the strain rate in the specimen, but of the free motion of the bar end face.

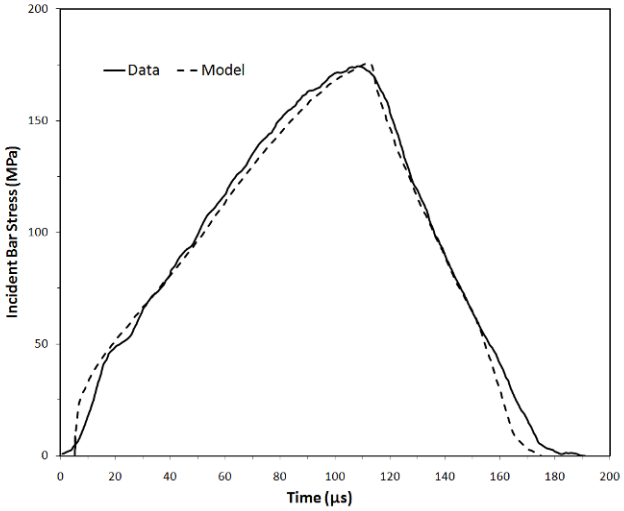

Figure 3.8 Incident pulse for characterizing Macor
(Reproduced from Frew et al. (2002) with permission)

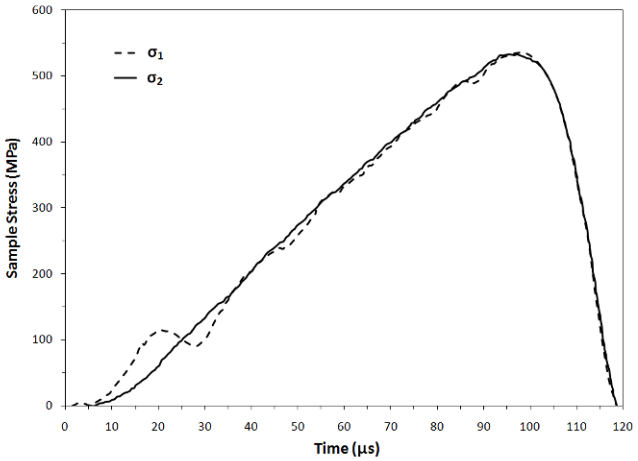

Figure 3.9 Equilibrium across the Macor specimen
(Reproduced from Frew et al. (2002) with permission)

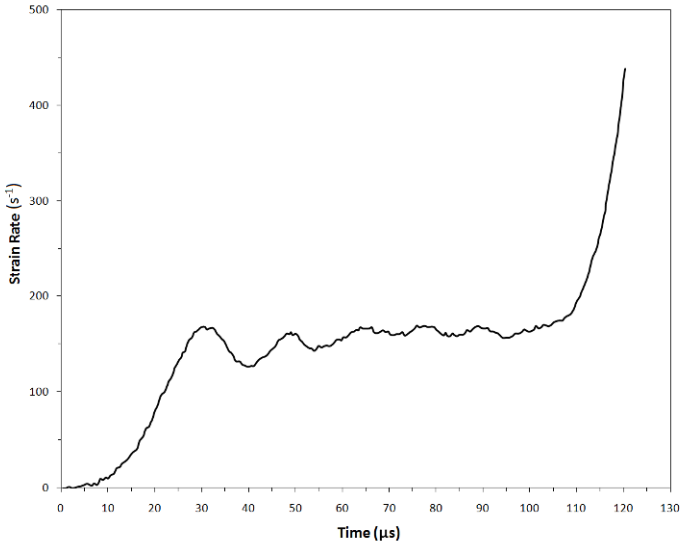

Figure 3.10 Strain-rate history in the Macor specimen
(Reproduced from Frew et al. (2002) with permission)

For the purpose of comparison, Figure 3.11 shows an average strain rate of 130 s^{-1} over 30 μs to 100 μs by using a shorter striker at a slightly lower impact velocity of 14.4 m/s. It is shown in Fig. 3.11 that, at 100 μs, the specimen was unloaded. Instead of a sudden rise of the reflected pulse shown in Fig. 3.10 at the catastrophic failure of the brittle specimen, the reflected signal in this experiment drops back down to zero, indicating an unloading process after the peak load. The specimen was recovered intact.

Figure 3.12 shows dynamic and quasi-static compressive stress-strain curves for the Macor. As explained earlier, the specimen with an average strain rate of $\dot{\varepsilon}_s$ = 165 s^{-1} failed catastrophically after peak stress. However, the specimen with an average strain rate of $\dot{\varepsilon}_s$ = 130 s^{-1} experienced strain beyond the elastic region and post-peak stress. Consequently, the stress-strain curve after the peak stress at 165 s^{-1} indicates the loss of load-bearing capability because of excessive damage; whereas, the curve at 130 s^{-1} turns back to zero indicating recovery without catastrophic failure. Specimens such as these can be retrieved for post-test microstructural evaluations. The recovery of the intact speci-

mens after a well-defined loading can also be achieved by the single-loading features discussed in Chapter 2.6.

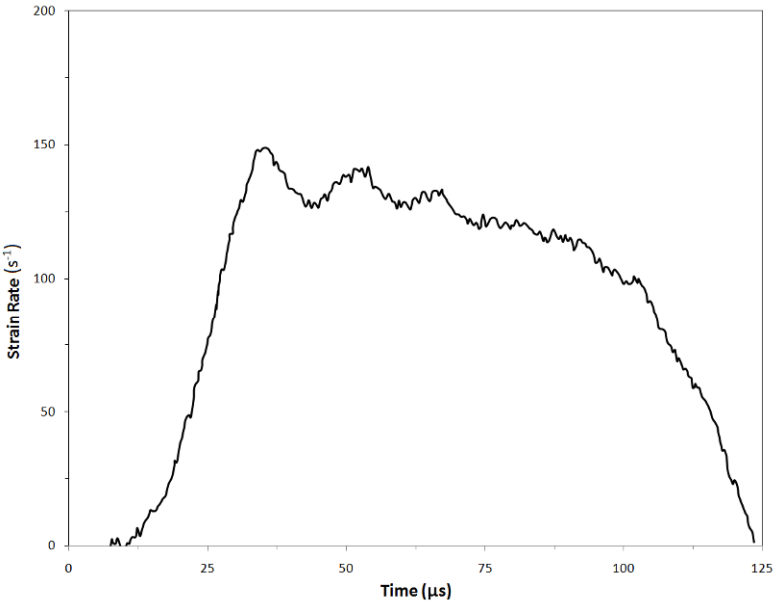

Figure 3.11 Strain-rate history in the Macor specimen at 130 s^{-1}
(Reproduced from Frew et al. (2002) with permission)

Similar pulse shaping techniques used to characterize the Macor ceramic material have also been applied in the dynamic compression testing of an Indiana limestone (Frew et al. 2001). Since the limestone has a stress-strain response more linear than the Macor, a nearly linear incident pulse needs to be used, as shown in Fig. 3.13. The steel bars had a common diameter of 12.7 mm. The incident and transmission bars were 2130 and 915 mm long, respectively. The incident pulse in Fig. 3.13 was generated by using a 3.97-mm-diameter, 0.79-mm-thick annealed C11000 copper disk as the pulse shaper with a striking velocity of 13.9 m/s. The

modified incident pulse produces a nearly constant strain-rate deformation in the limestone specimen under stress equilibrium, as shown in Fig. 3.14. Figure 3.15 shows the resultant compressive stress-strain curves for the limestone at two dynamic strain rates (100 and 120 s^{-1}) and one quasi-static strain rate (0.00001 s^{-1}). The failure strength for the limestone at the dynamic strain-rate levels is about double that obtained at the quasi-static strain rate. Figure 3.16 presents the strain-rate effect on the compressive strength of the limestone. In addition to the data obtained at different strain rates, the data for the specimens with different length-to-diameter ratios (L/D) and sizes are included as well. This Indiana limestone does not exhibit significant L/D or size effect. This is not unexpected. Due to the small Poisson's ratio and small axial failure strain, the lateral deformation of the specimen is very limited during axial compression, causing little effects on the axial response. On the other hand, the strain-rate effects on the axial behavior are clearly seen: the strength increases with increasing strain rate.

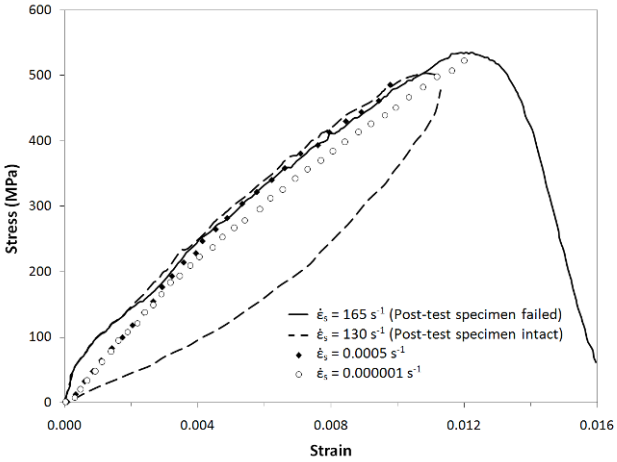

Figure 3.12 Compressive stress-strain curves for Macor
(Reproduced from Frew et al. (2002) with permission)

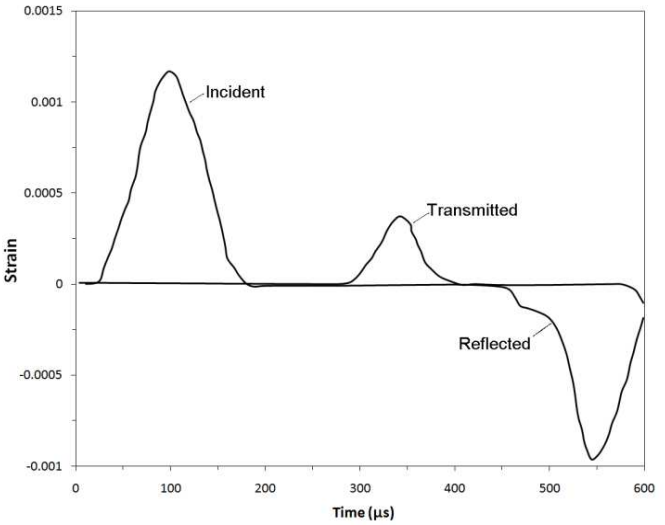

Figure 3.13 Incident, reflected and transmitted pulses in a pulse-shaped Kolsky bar experiment on an Indiana limestone *(Reproduced from Frew et al. (2001) with permission)*

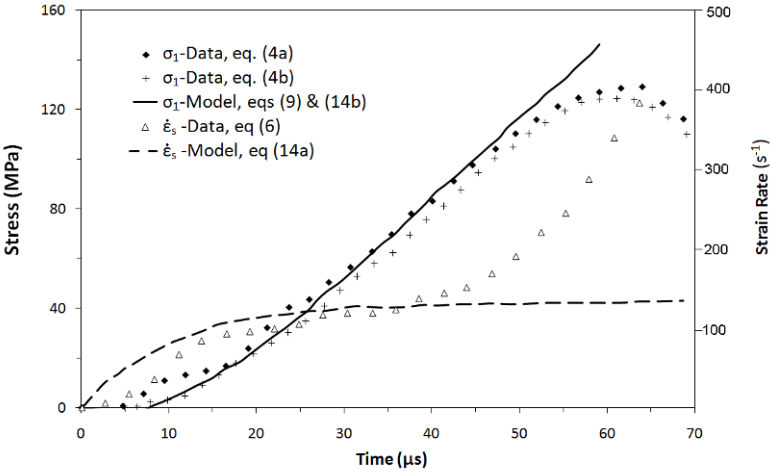

Figure 3.14 Stress equilibrium and strain-rate history in an Indiana limestone specimen *(Reproduced from Frew et al. (2001) with permission)*

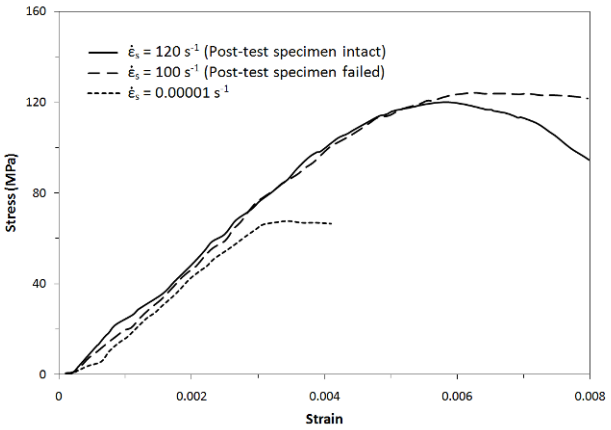

Figure 3.15 Dynamic and quasi-static stress-strain curves of an Indiana limestone
(Reproduced from Frew et al. (2001) with permission)

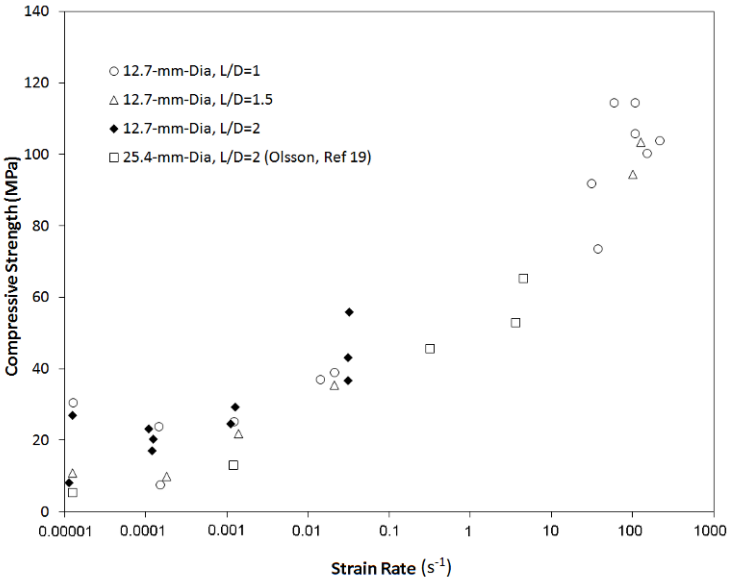

Figure 3.16 Compressive strain-rate sensitivity of an Indiana limestone
(Reproduced from Frew et al. (2001) with permission)

3.5.2 Loading-Reloading on Ceramics

In this example, we present the design of a set of experiments where an alumina ceramic is dynamically loaded by two consecutive stress pulses (Chen and Luo 2003, 2004, Luo and Chen 2004). The first pulse determines the dynamic response of the intact ceramic material while crushing the specimen, and the second pulse determines the dynamic compressive constitutive behavior of the crushed ceramic rubble. The purpose of this experimental design is to satisfy the needs for high-rate response of ceramics severely damaged by intensive mechanical loading.

In order to produce two consecutive stress pulses, a striker train of two elastic rods separated by pulse shapers is employed to replace the single striker bar in a conventional Kolsky-bar setup. A schematic illustration of the modified Kolsky bar used in this ceramic study is shown in Fig. 3.17 (Chen and Luo 2004), where two strikers are seen inside the barrel of the gas gun of a Kolsky-bar setup. For illustration purposes, the figure is not at scale of the actual experimental setup. The first striker is a maraging steel rod (ϕ19 mm $\times$ 152 mm), which creates the first stress pulse to crush the intact ceramic specimen after determining its response from an intact state. The second striker is either an aluminum bar or a steel bar with the dimension of ϕ19 mm $\times$ 203 mm to compress the crushed ceramic rubble at a different strain rate. As the case when testing any brittle material in a Kolsky device, careful pulse shaping is needed to ensure the specimen deforms at nearly a constant strain rate under dynamic stress equilibrium during both dynamic loadings. Pulse shaping also controls the amplitudes of the loading pulses, the values of strain rates, the maximum strains in the rubble specimens, and the proper separation time between the two loading pulses.

A C11000 annealed copper pulse shaper was used to control the first loading pulse to achieve the desired constant strain rate and amount of damage in the intact ceramic specimen. To control the profile of the second pulse such that the pulverized specimen deforms at an approximately constant strain rate under dynamic stress equilibrium, a 3003 aluminum tube was placed between the two strikers as the second pulse shaper (Fig. 3.17). The second pulse shaper also separates the second loading pulse from the first pulse. The combination of the second striker bar and the second pulse shaper determines the strain rate and maximum strain of the pulverized specimen during dynamic deformation. To ensure that the second loading pulse is transmitted smoothly from the second striker to the incident bar through the first striker, the first pulse shaper (the copper disk) needs to be sufficiently hardened during the first compression by the first steel striker.

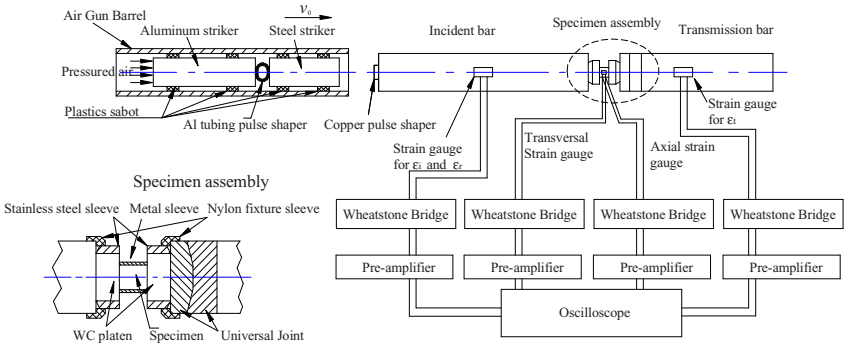

Figure 3.17 Kolsky bar set-up for loading and reloading experiments
(Reproduced from Chen and Luo (2004) with permission)

To minimize stress concentrations on the specimen that may result in uncontrolled premature failures, a pair of laterally confined WC platens (ϕ12.7 mm × 6.35 mm) were placed between the specimen and the bars (see Fig. 3.17). In addition, a simplified universal joint that consists of a pair of hard steel disks with a spherical joining surface was placed between the tungsten carbide platen and the transmission bar (Fig. 3.17) to avoid the specimen corners being loaded due to the possible slight misalignment in the bar system.

To prevent the ceramic specimen from shattering apart during the first loading, the cylindrical ceramic specimen is slightly confined by a thin-walled metal sleeve. The initial confining pressure is extremely small because the initial inside diameter of the sleeve is only 0.01 mm smaller than the specimen diameter. The sleeve was installed onto the specimen after being heated up. The pressure from this press fit will be further reduced during axial loading because the metal sleeve expands more in the lateral direction than the ceramic specimen due to mismatch in Poisson's ratios. The exact initial confining pressure is difficult to be estimated since there are machining tolerances on the already-small mismatch in diameters. However, during the fragment-flow stage of the

specimen deformation, the large lateral deformation and the relatively well-defined yield strength of the sleeve material makes it easier to estimate the confining pressure by assuming the sleeve as a thin-walled pressure vessel.

Due to the high stiffness of the intact ceramic specimen, the reflected signal during the first loading is typically small. A number of contacting surfaces in the testing section (Fig. 3.17) may bring additional contribution to the measured reflected signal, which is not representative of the specimen response. The contribution of all the contacting surfaces needs to be deducted from the measured reflected signal,

$$\varepsilon(t) = \frac{-2C_0}{L_s}[\varepsilon_R(t) - \varepsilon_{Rc}(t)] \tag{3.3}$$

where $\varepsilon_R(t)$ and $\varepsilon_{Rc}(t)$ are the reflected signals from experiments with a confined specimen and without the specimen, respectively. It is noted that this treatment on strain rate is only another approximation since the stress state in the sleeve with a sample inside is not clearly defined or evenly distributed.

A typical set of the incident, reflected, and transmitted pulses obtained from such a pulse shaped experiment are shown in the Fig. 3.18 (Chen and Luo 2004). The first pulse has a triangular shape with a loading duration of ~80 μs. The triangle has a linear ramp which is necessary to achieve a constant strain rate on the intact ceramic specimen possessing a linearly elastic brittle response. As shown in Fig. 3.18, the first reflected signal maintains at a constant level for ~80 μs starting from the instant of 620 μs.

Approximately 30 μs after the first pulse is completed; the second pulse produced by the second striker in association with the tube pulse shaper arrives. This nearly flat reflected signal over the entire first loading period indicates that a nearly constant strain-rate has been achieved in the intact specimen. The amplitude of the first reflected signal then increases drastically, indicating that the damaged specimen has a reduced resistance to the motion of the incident bar end. Now, the specimen has been crushed but still remains in the testing section of the Kolsky bar setup because gravitational force is unable to drop the specimen for a noticeable distance within only a few dozens of microseconds before the second loading pulse arrives.

Through proper control over the shape of the second incident pulse, the second reflected signal also exhibits a nearly flat portion that corresponds to the constant strain-rate deformation in the specimen. Consequently, the transmitted signal contains two pulses corresponding to the

two loading periods. The first portion shows a typical brittle specimen response, where the load increases nearly linearly until a sudden drop due to the crushing of the specimen. The load does not immediately drop to zero because the specimen is crushed but not shattered due to the confining metal sleeve. The second portion of the transmitted signal shows a flow-like behavior of the pulverized specimen.

Figure 3.19 shows the axial stress histories recorded on both ends of the specimen (Chen and Luo 2004). The axial stresses on the front end of the specimen are observed nearly the same as that on the back-end during the loading phase of the first loading pulse and over nearly the entire duration of the second loading pulse. However, when the specimen is being crushed near the end of the first loading pulse, the dynamic equilibrium does not exist.

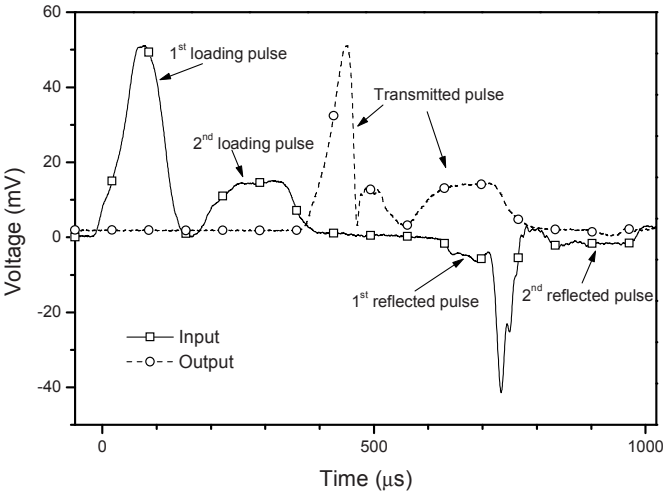

Figure 3.18 Oscilloscope records of a loading/reloading experiment on an alumina
(Reproduced from Chen and Luo (2004) with permission)

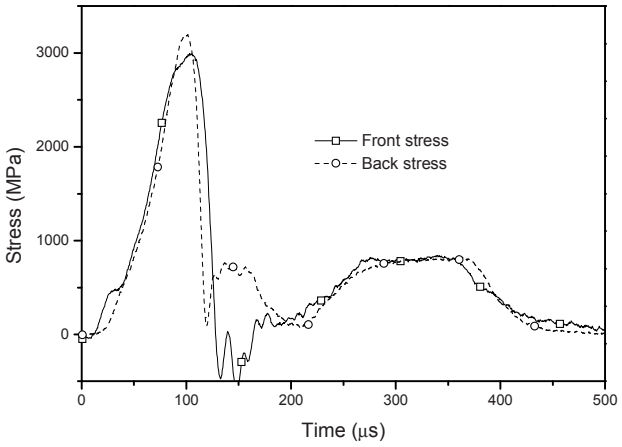

Figure 3.19 Dynamic equilibrium check during loading and reloading
(Reproduced from Chen and Luo (2004) with permission)

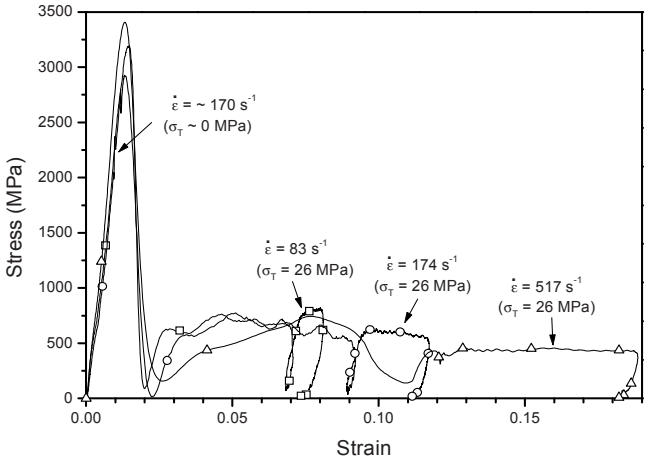

Figure 3.20 Stress-strain curves from loading/reloading experiments on AD995
(Reproduced from Chen and Luo (2004) with permission)

The analysis of the results from Figs. 3.18 and 3.19 indicates that the specimen deforms at nearly constant strain rates under dynamic stress equilibrium during both loading periods. Such an experiment is considered as a valid dynamic experiment. After checking for dynamic stress equilibrium and constant strain rate, the data are reduced to obtain the dynamic stress-strain histories in the specimen.

Three resultant dynamic compressive stress-strain curves of AD995 ceramic are shown in Fig. 3.20 (Chen and Luo 2004). As described previously, the confining pressure from the metal sleeve on the ceramic specimen can initially be neglected when the specimen is under elastic deformation. After damage, the sleeve confines the pulverized specimen at an estimated pressure of 26 MPa through the plastic deformation of the thin metal sleeve. The strain rates are commonly ~170 s^{-1} for the intact alumina and 83, 174, and 517 s^{-1} for the damaged specimen from three experiments. The variation in the strain rates in the crushed specimens is achieved by changing the second striker material (aluminum or steel) and the second pulse shaper. As shown in Fig. 3.20, the ceramic specimen initially behaves as a typical brittle material exhibiting a linear stress-strain response with peak stresses in the range of 2.8-3.4 GPa. As the specimen is being crushed, the lateral confinement from the thin metal sleeve causes an axial stress increasing from nearly zero at the beginning of crush to 500-700 MPa near the unloading of the first pulse. The incident pulse was controlled such that unloading started shortly after the peak load when the specimen was crushed to a desired level. It should be noted that the stress-strain behavior obtained during this crushing phase of the experiment may not be realistic since the specimen was not in dynamic stress equilibrium. The second pulse came after the end of the unloading from the first stress pulse. During the dynamic compression from the second pulse, the specimen stress ascends to a "flow" stress of about 500-700 MPa. This portion of stress-strain curve in each of the three experiments represents the dynamic compressive response of the crushed ceramic specimen to impact loading.

The same procedure has also been exercised on another ceramic material, SiC-N (Luo et al. 2006, Chen et al. 2007). Figures 3.21 shows oscilloscope records of the incident bar signals from a series of four experiments attempting to reveal the damage effects on the compressive stress-strain response of the SiC-N ceramic. As shown in Fig. 3.21, the amplitude of the first loading pulse was slightly adjusted to compress the ceramic specimens to different damage levels, while the second pulse remained nearly identical. The confining pressure was estimated to be approximately 104 MPa. The peak load of the first pulse does not appear to vary significantly. However, the small variations produced vastly different responses. Figure 3.22 shows the corresponding dynamic com-

pressive stress–strain curves and the effects of specimen damage on the compressive mechanical responses. The results in Fig. 3.22 show that when the ceramic specimen is not damaged above a critical level, the specimen is not crushed and remains nearly elastic under the second loading (#1 in Fig. 3.22). When the specimen is damaged beyond the critical level, the specimen is crushed and the flow curves under the second loading pulse represent the stress-strain response of the pulverized ceramic material. The results indicate that the effects of damage on the mechanical response of the ceramic are not gradual. Instead, the effects have an abrupt behavior. A critical damage state in the sample divides the response: either nearly intact or granular flow.

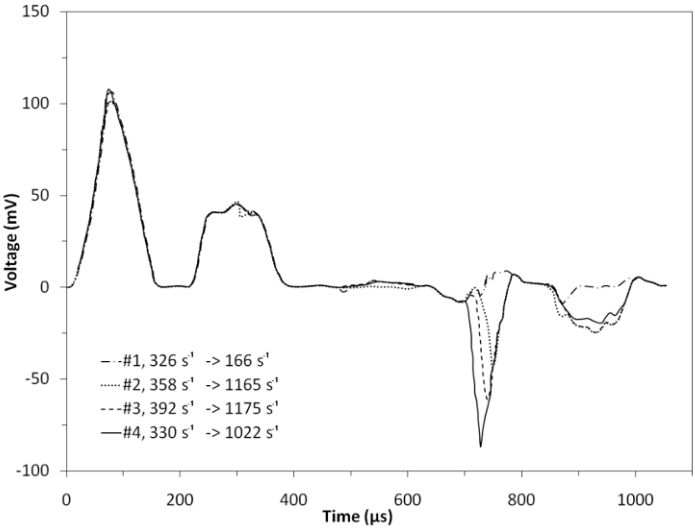

Figure 3.21 Incident bar pulses producing different damage levels in SiC-N specimens
(Reproduced from Chen et al. (2007) with permission)

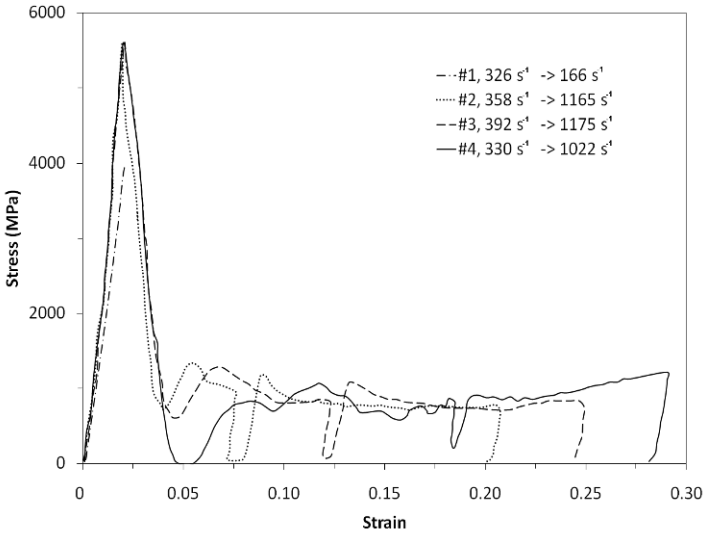

Figure 3.22 Dynamic stress-strain curves of SiC-N
(Reproduced from Chen et al. (2007) with permission)

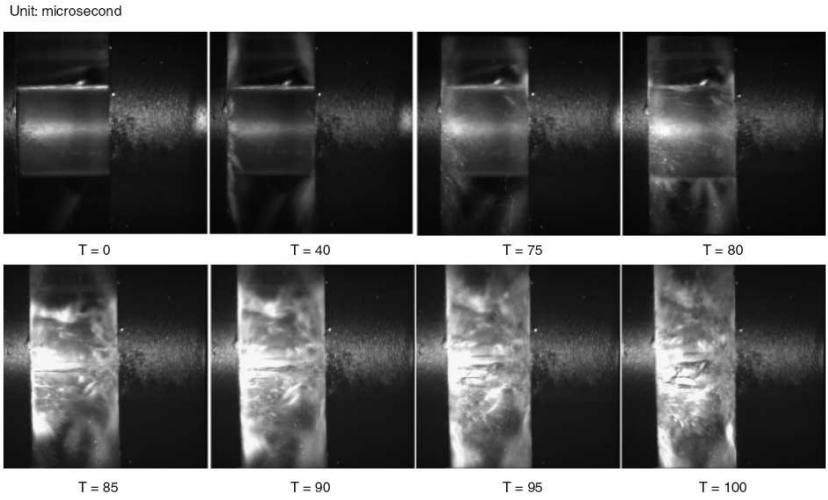

Figure 3.23 Dynamic fracture and failure process
of a nearly perfect SiC-N specimen
(Reproduced from Chen et al. (2007) with permission)

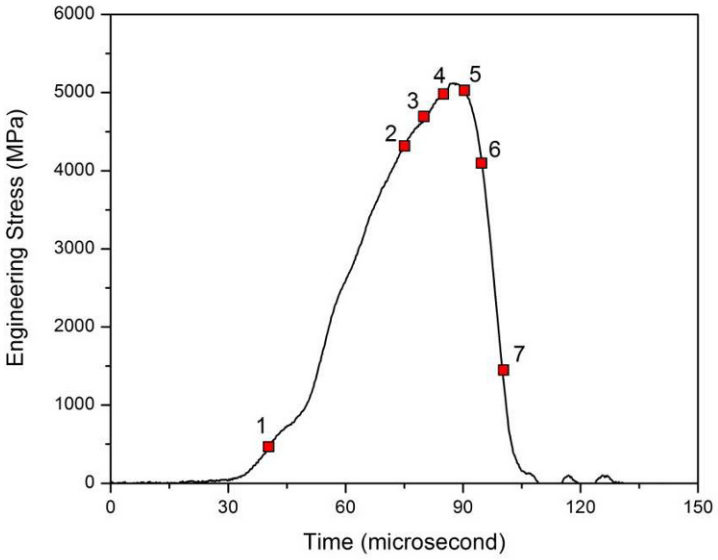

Figure 3.24 Corresponding stress history in the SiC-N specimen
(Reproduced from Chen et al. (2007) with permission)

The ceramic specimen may still maintain an extremely high load-bearing capacity even when already damaged. The capacity suddenly declines when damage reaches a critical level. The three stress–stain curves (#2, 3, 4) in Fig. 3.22 for extensively damaged specimens also indicate that, once beyond a critical damage level, further damage to the ceramic does not significantly affect the crushed material's load-bearing capacity.

Damage is critical to the response of ceramic materials, particularly to the maximum stress in the stress-strain behavior. To demonstrate the effect of damage on the dynamic compressive response of ceramics, we present two experiments conducted under identical loading conditions (Chen et al. 2007). The cylindrical specimens are made of the same material (SiC-N) with the same dimensions (Φ6.35×6.35 mm), the only difference between the two specimens is their initial surface conditions. The first specimen condition is nearly perfect; whereas, the second specimen has a small pre-existing surface defect.

Figure 3.23 shows the sequential high-speed images of the fracture and failure processes of the nearly perfect specimen; while the loading history in correspondence to the high-speed images is shown in Fig. 3.24. The first image shows the SiC–N specimen before dynamic testing. The second image was taken 40 μs after initiation of dynamic loading. The load was observed to be only about 10% of the maximum stress (position 1 in Fig. 3.24). Fine ceramic particles mixed with some lubricant were ejected from the edges of both ends of the cylindrical specimen. The locally concentrated and multi-axial stresses pulverized the ceramic materials to the fine particles at the specimen edges. Visible cracks were observed to initiate from the specimen edges at 75 μs after load initiation, as shown in the third image in Fig. 3.23, however, the stress at this time has reached only about 83% of the eventual peak value (Fig. 3.24).

Such cracks along the specimen axial direction quickly populated the specimen, as shown in the fourth image in Fig. 3.23. Fine particles were ejected in the radial directions from the middle of the specimen, in addition to those ejected from the edges. As the cracks propagated in the axial direction, the specimen was divided into thin axial columns. Some of the columns started to collapse near both ends of the specimen by the continued increase of axial load. The axial compressive stress reached its peak value (position 5 in Fig. 3.24) just before the columns collapsed.

Figure 3.25 shows the images of the fracture and failure processes in the specimen with a pre-existing surface flaw, while Fig. 3.26 shows the corresponding stress history in this specimen. By contrast to the nearly perfect specimen in Fig. 3.23, an inclined surface crack became visible, as shown in the left middle portion of the second image in Fig. 3.25, 15 μs after dynamic loading began. This inclined crack was considered to initiate from a pre-existing surface defect on the specimen and grew as the loading was increased until turning into the axial direction at 45 μs. This crack tip behavior is similar to the well-documented wing cracks observed under quasi-static loading conditions (Brace and Bombolakis 1963, Nemat-Nasser and Horii 1982, Horii and Nemat-Nasser 1985). At the moment of 45 μs, other axial cracks also initiated and propagated in the axial direction, as seen in the following images of Fig. 3.25. Similar to Fig. 3.23, numerous axial columns were formed and then started to collapse at the maximum stress (Fig. 3.26). Because of the small surface defect, the maximum stress of this specimen was much lower than the previous case (3.3 vs 5.3 GPa). Results from these experiments clearly demonstrate surface effects on the failure strength of ceramic materials.

The results presented above indicate that the ceramic specimen is still able to bear further increased axial load even when cracked extensively. The external load is distributed to the formed axial columns until

they are collapsed by further loading where the maximum stress or buckling load is reached. After the maximum stress, the ceramic specimen loses its load-bearing capacity in a rapid drop to zero in the specimen stress.

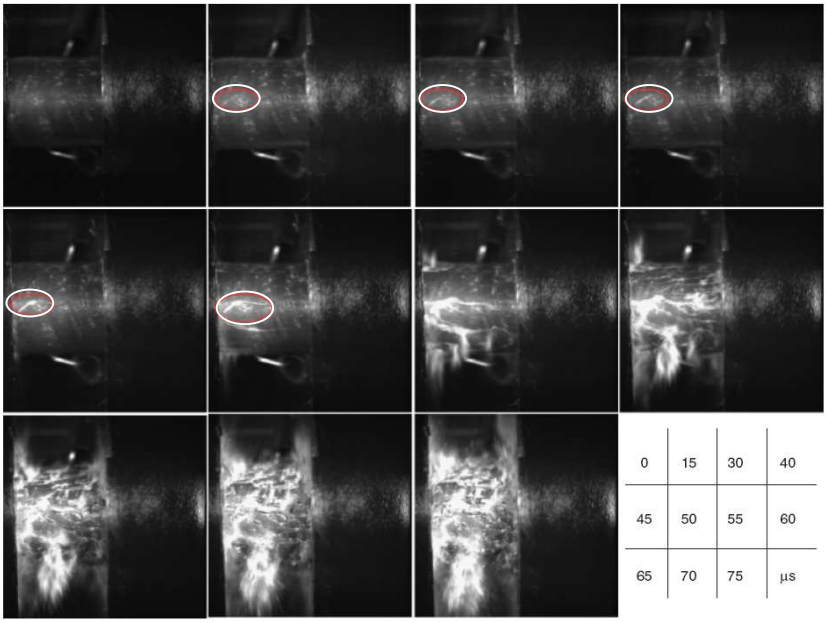

Figure 3.25 Dynamic fracture and failure process of a SiC-N specimen with a pre-existing surface damage
(Reproduced from Chen et al. (2007) with permission)

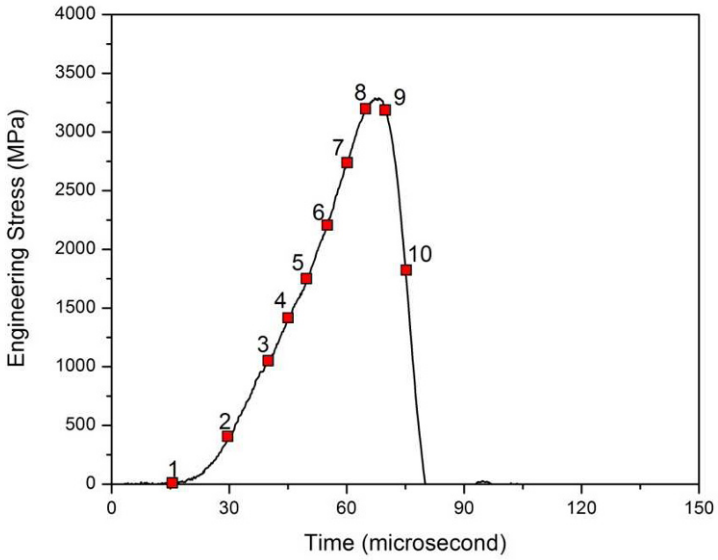

Figure 3.26 Corresponding stress history in the SiC-N specimen
(Reproduced from Chen et al. (2007) with permission)

3.5.3 S-2 Glass/SC15 Composite

In this example, a S-2 glass/SC15 composite material which has 55–60% in volume of S-2 glass fibers woven evenly along the 0 and 90° directions. The resin in the composite is SC15 epoxy. The composite contained 58 plies through a thickness of 38.1 mm (Song et al. 2003). Table 3.2 lists the description of the composite material. Although fiber-reinforced composites are not typically considered brittle materials, the nearly linear stress-strain compressive response of the composite presented here makes the experimental procedure similar to that for brittle materials.

Table 3.2 Material description of S-2 glass/SC15 composite
(Reproduced from Song et al. (2003) with permission)

Composite Density	Fiber Volume Fraction	Resin Volume Fraction	Void Volume Fraction	Fiber Density	Resin Density	Per-ply Areal Density
1.87×10^3 kg/m^3	0.50	0.48	0.02	2.485×10^3 kg/m^3	1.139×10^3 kg/m^3	1.15 kg/m^2/ply

The cylindrical composite specimens were 12.70 mm in diameter and 6.35 mm in thickness, which were characterized using a 19.05-mm C350 maraging steel Kolsky compression bar. The loading direction was either perpendicular to the ply-plane (through thickness) or along the direction of one group of fibers, 0 or 90°, in the ply-plane (in-plane). Annealed C-11000 copper disks were used as pulse shapers to generate incident pulses such that the specimen deformed at a nearly constant strain rate under a dynamically equilibrated stress state. Petroleum jelly was applied to the interfaces between the specimen and the bars to minimize the interfacial friction.

Figure 3.27 shows a typical set of incident, reflected, and transmitted signals for the composite specimen loaded in the through-thickness direction at a strain rate of 800 s^{-1}. Dynamic stress equilibrium in the specimen was checked with the following equation (Ravichandran and Subhash 1994),

$$R(t) = \left| \frac{\Delta\sigma(t)}{\sigma_m(t)} \right| = 2 \left| \frac{\sigma_1 - \sigma_2}{\sigma_1 + \sigma_2} \right| \tag{3.4}$$

In (3.4), σ_1 and σ_2 are defined with (1.8) and (1.9), respectively. The stress is considered in equilibration when $R(t) \le 0.05$ (Ravichandran and Subhash 1994).

The dynamic stress equilibrium represented with (3.4) in the composite specimen is shown in Fig. 3.28. The specimen was observed in stress equilibrium over the entire duration of loading event except for the first 15 μs. Under stress equilibrium the strain rate was calculated with (1.12) and shown in Fig. 3.29. The strain-rate history had a nearly constant amplitude for the first 125 μs, then takes a sharp rise, indicating that

the specimen has been extensively damaged or has failed, as discussed in Chapter 3.5.1.

Following the same procedure, the compressive stress-strain curves for this composite material along the in-plane and through-thickness directions were obtained, the results of which are shown in Figs. 3.30 and 3.31, respectively. When loaded in the through thickness direction, the dynamic stress–strain curves initially show a nearly linear behavior at small strains and then become nonlinear as the strain increases due to accumulated stress-induced damages in the specimen. At certain strain levels, the compressive stresses are sensitive to strain rate, particularly when the strain rate changes from quasi-static to dynamic levels. All the specimens failed during loading in both the quasi-static and dynamic loading, except for the one at a strain rate of 330 s^{-1} due to early unloading.

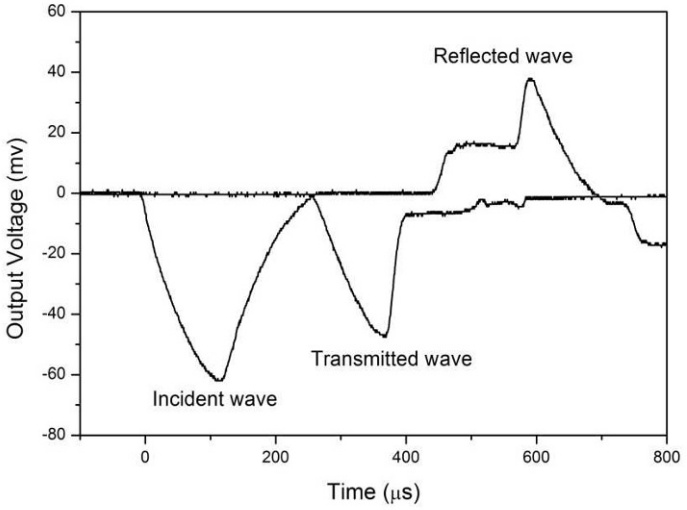

Figure 3.27 Oscilloscope records in the Kolsky bar experiment on a composite specimen through thickness direction
(Reproduced from Song et al. (2003) with permission)

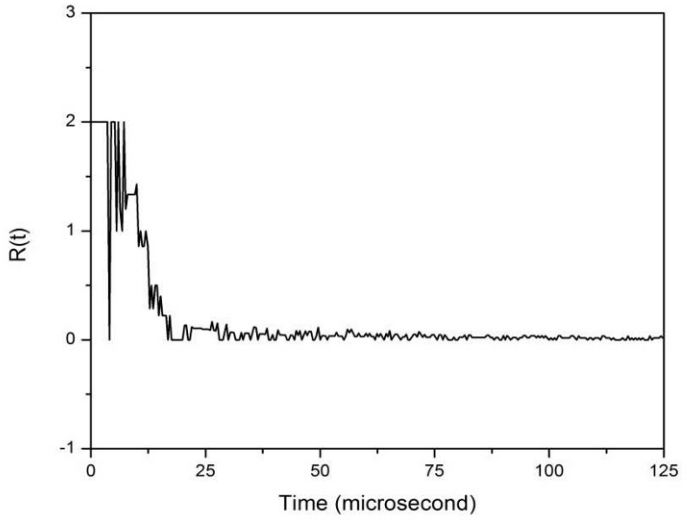

Figure 3.28 Dynamic stress equilibrium process
(Reproduced from Song et al. (2003) with permission)

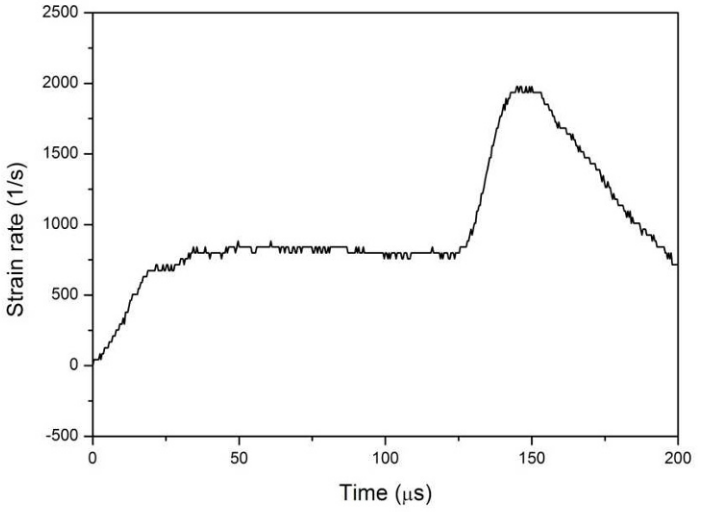

Figure 3.29 Strain rate history
(Reproduced from Song et al. (2003) with permission)

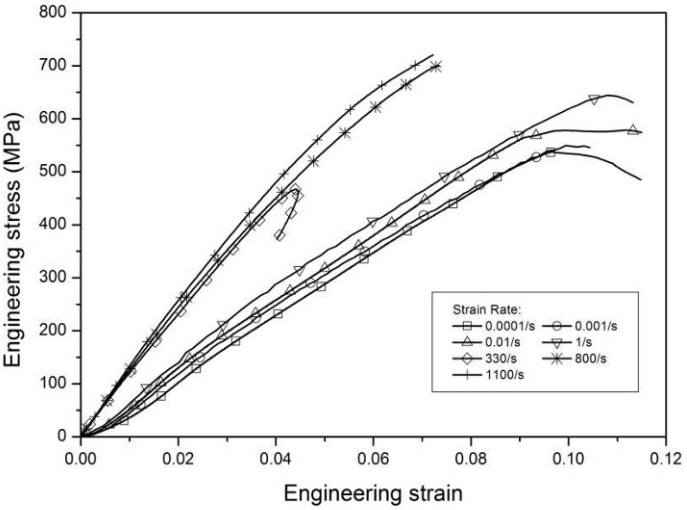

Figure 3.30 Compressive stress-strain curves of the composite through thickness direction
(Reproduced from Song et al. (2003) with permission)

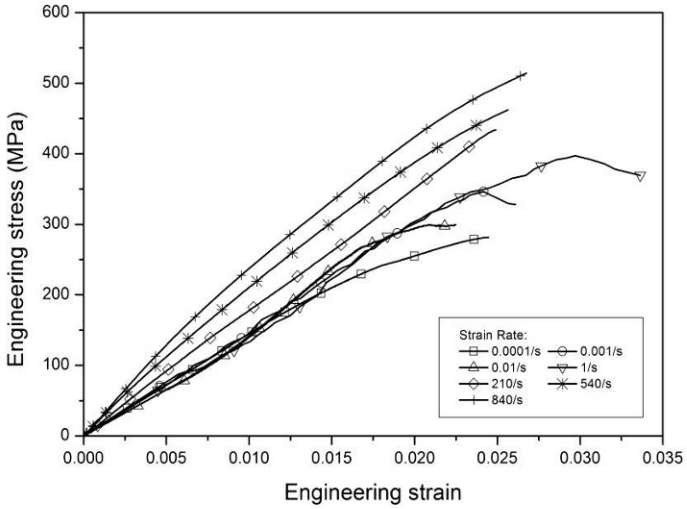

Figure 3.31 Compressive stress-strain curves of the composite along in-plane direction
(Reproduced from Song et al. (2003) with permission)

The compressive stress–strain curves of the composite material along its in-plane direction present nearly linear behavior at both low and high strain rates, except for the case at the highest strain rate (840 s^{-1}) where nonlinear behavior due to damage accumulation in the specimen becomes apparent (Fig. 3.31). The results in Fig. 3.31 also indicate that the strain-rate sensitivity is quite different when the rate is in the quasi-static or dynamic range. The compressive stress–strain curves exhibit strong sensitivity to strain rate at high levels, but do not show a clear rate sensitivity at low strain rates. Comparing the results shown in Figs. 3.30 and 3.31, the failure strain and stress for the composite along its in-plane direction are much less than that in the through-thickness direction due to different failure modes.

Figures 3.32 and 3.33 show typical pictures of the fractured specimens dynamically loaded along the through-thickness and in-plane directions, respectively. After the composite specimen is loaded through its thickness direction (or perpendicular to fiber direction), it fractured through extensive delamination, as well as fiber fracture due to the combined local tension and shear loading, as shown in Fig. 3.32. However, when the load is along fiber direction (or in-plane direction), the specimen was mostly damaged by delamination between the fibers and resin (Fig. 3.33), indicating low interfacial strength between the fiber and the resin. Most fibers were not fractured in this case, as also shown in Fig. 3.33. The specimen splits along the loading direction, which was aligned with the direction of one set of fibers.

Figure 3.32 Composite specimen after mechanical loading along through-thickness direction
(Reproduced from Song et al. (2003) with permission)

Figure 3.33 Composite specimen after mechanical loading along in-plane direction
(Reproduced from Song et al. (2003) with permission)

3.5.4 Glass Failure under Compression/Shear

In this example, the dynamic response of a borosilicate glass at an average strain-rate of 250 s^{-1} is explored using a modified 19-mm maraging steel Kolsky bar under multiaxial loading conditions (Nie et al., 2007). Instead of applying confining pressure that would result in a multiaxial compression stress state, cuboid specimens with the material axis inclining to the loading direction at different angles were used to generate higher shear stresses. The specimens are in compression/shear during dynamic loading. A high-speed digital camera, synchronized with the loading stress pulse, was used to record the dynamic crack initiation and propagation in the glass specimens at a rate of 200,000 frames per second (FPS). The annealed copper disc pulse shapers used were 9 mm in diameter and 1.7 mm in thickness to generate a linear incident ramp at the stress rate of approximately 4.2×10^6 MPa/s.

The borosilicate glass is in the form of 8.9-mm thick flat plates with a 80/50 scratch/dip polished surface finish. The chemical composition of

the glass is summarized in Table 3.3. Other physical and mechanical properties of interest are: density $\rho = 2.21$ g/cm^3, Young's modulus E = 61 GPa, Poisson's ratio $\nu = 0.19$, longitudinal wave speed $C_L = 5508$ m/s, shear wave speed $C_S = 3417$ m/s. Specimens were cut and ground to 8.9×8.9 ± 0.01 mm in cross section and 12.5 ± 0.01mm in length. The tolerance on the parallelism of the end surfaces was within 0.001 mm. The cuboid specimen geometry, with the tilting angles of 0°, 3°, 5° and 7°, is shown in Fig. 3.34. All the specimens were polished to the surface finish of 1.27 micrometers Ra to minimize the influence of surface flaws on the measured glass strength. As mentioned in Chapter 3.2, polished steel platens were placed in between the glass specimen and bar end faces. The interfaces between the specimen and bar ends were also lubricated by light high-vacuum grease to minimize friction.

Table 3.3 Chemical composition of the borosilicate glass

Composition	SiO_2	B_2O_3	Na_2O	Al_2O_3
Percentage (%)	80.5	12.7	3.5	2.5

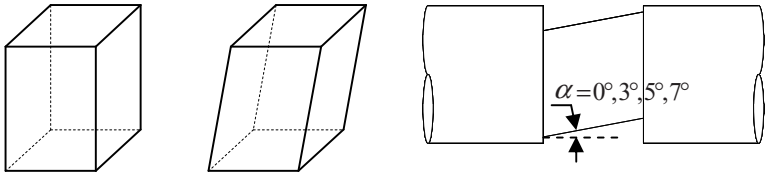

Figure 3.34 Cuboid specimen geometry for compression/shear experiments. *(Reproduced from Nie et al. (2007) with permission)*

A typical set of original oscilloscope recordings of the incident, reflected, and transmitted signals from the Kolsky compression bar experiment are shown in Fig. 3.35. Comparison of the force histories in the front and back of the specimen concludes that the glass specimen was under dynamic equilibrium until failure. Recall that when the specimen is under dynamic equilibrium, the reflected signal is proportional to the strain rate in the specimen. The plateau on the reflected signal indicates that this specimen experienced a constant strain rate before failure.

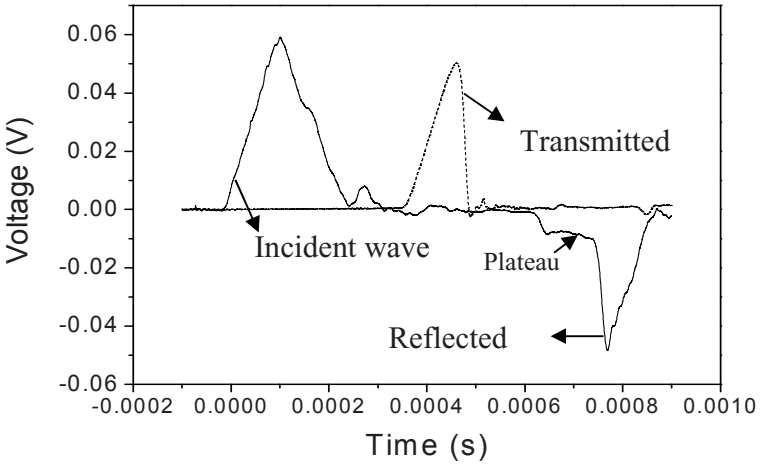

Figure 3.35 Typical set of experimental records for glass
(Reproduced from Nie et al. (2007) with permission)

Figure 3.36 shows the sequential high-speed images for the 0° specimen. The associated axial stress-time history is also shown in Fig. 3.36. The six numbered-points on the stress-time history are corresponded to the six images in Fig. 3.36. In the experiments, flash lights were placed on the same side as the high-speed camera. Under this lighting condition, the initial images of the transparent specimen appeared to be dark. When cracks are initiated, the damaged glass reflects light, thus

becomes visible. A time interval between all of the images is 5 μs. Images prior to image #1 did not show any feature that reflected light, revealing a uniformly deforming specimen. Images after #6 show widespread damage in the specimen. The images in between, as shown in Fig. 3.36, reveal the time sequence of the damage process under dynamic ramp loading. The circled area in frame #2 contains a small crack extremely close to the end of the transmission bar, which is a sign of damage initiation. In frame #3, nearly one-third of the specimen was damaged by axial cracks emanating from the transmission bar side. However, another group of cracks initiated from either inside of the specimen or on the farther side of the specimen surface. In frame #4, the cracks initiated from left side are propagating through the specimen in axial direction; and the internal cracks initiated in frame #3 remain stationary. However, a new internal crack appears just above the stationary group. More cracks are observed being initiated and coalesced in frame #5. Finally, the damage in the specimen is nearly saturated as shown in frame #6. It is seen that the cracks, once initiated, propagate roughly along the specimen axis, which coincides with the loading axis of this specimen. Before any dominant crack can propagate through the entire specimen, other cracks initiate and propagate in the specimen. From the inter-frame rate of the consecutive images, the axial cracks are estimated to propagate at a speed of approximately 560 m/s.

The results shown in Fig. 3.36 illustrate that the onset of damage in the glass specimen can be accurately determined from the high-speed camera images. When the specimen axis is positioned at an angle from the loading axis, the damage always initiates from the stress-concentrated corners. The capability of damage initiation determination in angled specimens facilitates the calculation of dynamic strength of the borosilicate glass under compression/shear loading. In order to identify the failure stress that corresponds to damage initiation in the specimen, local stress state at the corners, rather than average stress, needs to be used. A finite element analysis (FEA) with a commercial code, ABAQUS, together with the Kolsky-bar stress-history data and the high-speed images, was conducted to determine the stress state in the specimen when damage initiates. The trend shown in Fig. 3.37 indicates that the failure strength, in terms of equivalent stress, of the borosilicate glass is sensitive to the imposed shear component. The equivalent stress at failure initiation decreases with increased shear.

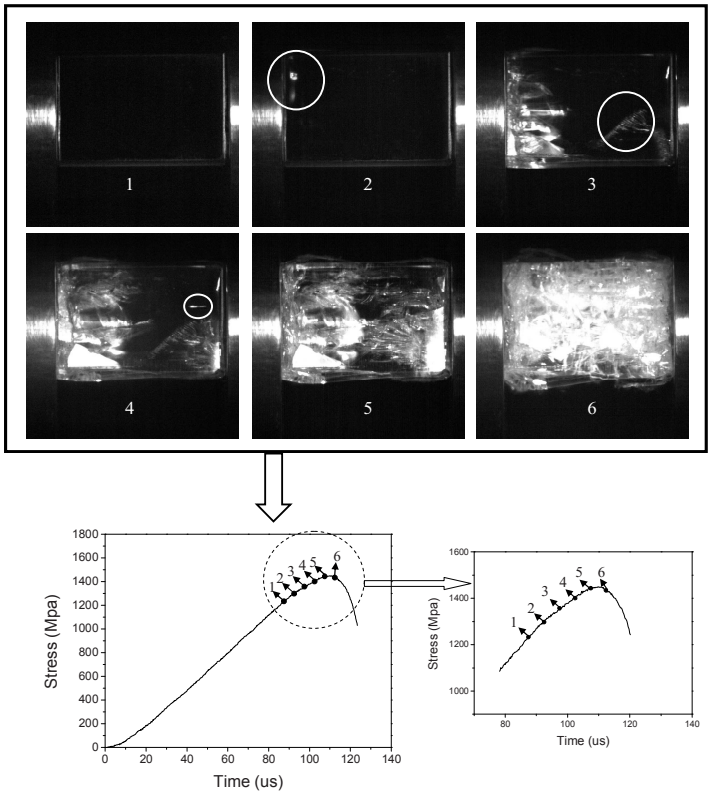

Figure 3.36 Damage process in a right glass specimen
(Reproduced from Nie et al. (2007) with permission)

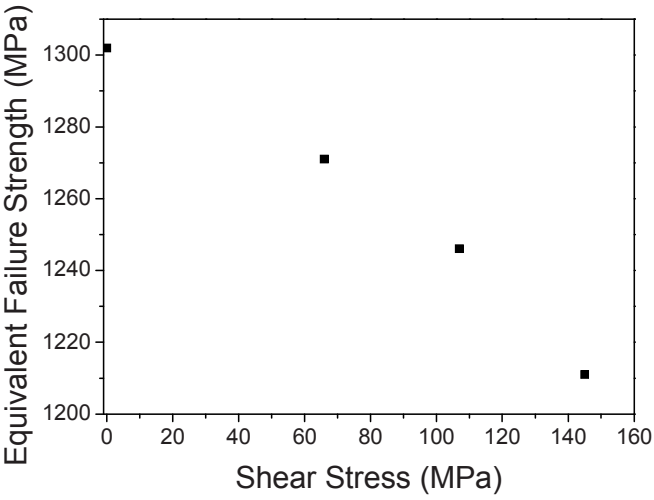

Figure 3.37 Effect of shear stress on the failure initiation in the glass specimen
(Reproduced from Nie et al. (2007) with permission)

Chapter 4. Kolsky Compression Bar Experiments on Soft Materials

In this chapter, we present Kolsky-bar techniques modified for soft material characterization in compression. Soft materials typically have low strength, stiffness, and wave impedance, which make it challenging to obtain accurate stress-strain responses at high strain rates. The challenges in characterizing soft materials are introduced in this chapter. Solutions in regard to achieving stress equilibrium, generating proper pulse shapes and sensing low-amplitude forces are then presented. Experimental design for soft material characterization is illustrated with example materials that include PMMA, rubber and rubber-like polymers, brittle and elastic-plastic polymeric foams, and biological tissues.

4.1 Challenges in Characterizing Soft Materials

Typical soft materials include elastomers, foams, gels, and soft biological tissues. These soft materials have common characteristics of low strength, stiffness, and wave impedance. The mechanical response of soft materials is sensitive to loading conditions such as the rate and state of loading. The low wave speeds in the soft specimens make stress equilibrium, a necessary condition for uniform deformation, much more difficult. The low strength makes the amplitude of the transmitted pulse too weak to be precisely measured. The sensitivities to strain rate and stress state make the requirement on the control over testing conditions much more strict.

The most challenging issue is to facilitate uniform deformation in a soft specimen when conducting Kolsky compression bar experiments because of the nature of low wave speeds in the soft specimens. In Kolsky-bar experiments, it is assumed that the specimen deforms uniformly so that the measurement of deformation averaging over the specimen length may represent any point-wise deformation. However, this assumption may not be satisfied automatically in soft material testing. Figure 4.1 shows the high-speed deformation images of an RTV630 rubber specimen (Song and Chen 2005). The specimen has the same diameter and thickness of 12.6 mm. The incident and transmission bars are at the right and left hand sides, respectively, in Fig. 4.1. The incident bar end moved in and then compressed the rubber specimen from the right side. At the very beginning of the loading ($t = 49.5$ μs), only the portion of specimen in contact with the incident bar was compressed as indicated in Fig. 4.1. With increasing time, the deformation propagates towards the other side,

W.W. Chen and B. Song, *Split Hopkinson (Kolsky) Bar: Design, Testing and Applications*, Mechanical Engineering Series, DOI 10.1007/978-1-4419-7982-7_4,

indicating stress wave propagation. At $t = 198.0\,\mu s$, the deformation of the rubber specimen at the transmission bar end becomes larger than that at the incident bar end. The specimen eventually achieves nearly uniform deformation ($t = 247.5\,\mu s$) due to the stress wave propagation back and forth in the specimen. In hence, the images in Fig. 4.1 clearly show that the rubber specimen does not deform uniformly over the most duration of loading.

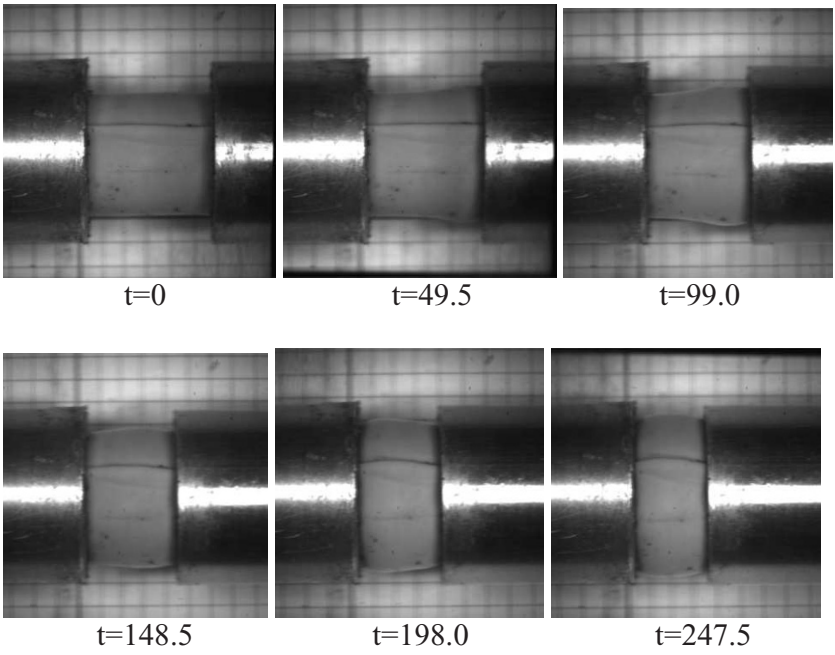

Figure 4.1 High speed deformation of an RTV630 rubber

Due to the characteristic of stress wave propagation in the specimen, the specimen will never achieve a state of ideal uniform deformation. However, the stress distribution can be considered uniform after several rounds of ringing up of stress waves inside the specimen. Ideally, this initial ringing-up process of stress wave inside the specimen should lead to stress equilibrium at the very early stages of dynamic loading.

The time for the elastic wave to propagate a single trip through the specimen is a critical parameter in the achievement of uniformity in stress distribution over the specimen length. Assuming the one-dimensional elastic wave speed in the specimen material is a constant, the time required for a single trip is

$$t_0 = \frac{l_0}{C_0} \tag{4.1}$$

where l_0 and C_0 are specimen length and elastic wave speed of the specimen material. The one-dimensional elastic wave speed is usually a characteristic constant for a certain material, making the specimen length as a critical variable to achieve uniform deformation. A thinner specimen clearly facilitates stress equilibrium sooner. A thin specimen also mitigates the possible stress wave attenuation in the specimen particularly when characterizing polymers possessing significant viscoelastic nature. However, a thin specimen makes the effect of interfacial friction between the specimen and bar ends more serious. In some cases, the entire specimen may not be under uniaxial stress loading at all, challenging appropriate data interpretation. The specimen length thus needs to be properly optimized while the interfaces between the specimen and bar ends are properly lubricated.

The non-uniform deformation in the axial direction also refers to axial inertia that produces stress and strain gradients along the axial direction. It is noted that, for some material like foams, the specimen deformation deviates from uniformity even though the stress may be consistent at both ends of the specimen because of their unique cell-collapse response. Figure 4.2 shows high-speed deformation process of an epoxy foam column with a 10×10 mm^2 cross section and a 19 mm length (Song and Chen 2005). It is observed that the failure (cell collapse) started from the incident bar end and then propagated to the other end (the transmission bar end). The propagation of such a failure front was defined as compaction wave, the speed of which is much slower than the elastic wave speed (Song et al. 2006c). The compaction wave divides the specimen into two different characteristic zones: compacted and uncompacted. The propagation of the compaction wave demonstrates the existence of drastic non-uniform deformation in the specimen, even though the stress in the specimen is globally uniform. The specimen stress during this process is represented with the plateau stress in the stress-strain curve (Fig. 4.3) (Song et al. 2006c). The unique deformation characteristic of the foam specimen makes it impossible to achieve uniform deformation under dynamic loading. However, in Kolsky-bar experiments on

soft materials, measures should be taken for the stress distribution in the specimen to be as uniform as possible.

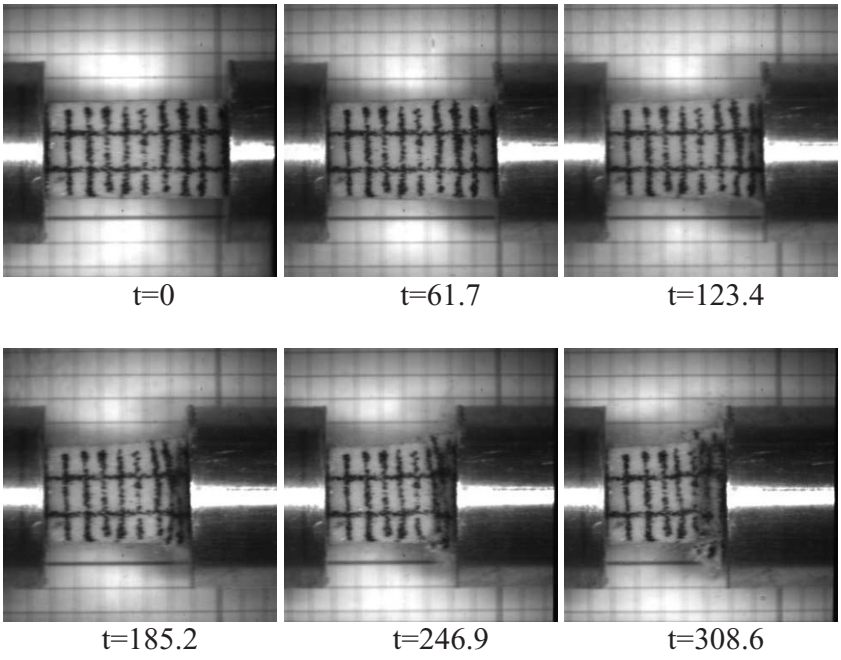

Figure 4.2 High speed deformation of an epoxy foam column

The non-uniform deformation presented in Figs. 4.1 and 4.2 is related to axial inertia encountered in dynamic loading. The axial inertia (or acceleration) also results in inertia along radial directions due to Poisson's effect. The radial inertia in turn produces extra axial stress on the specimen. The extra axial stress from radial inertia takes the form of a spike in the specimen stress measurement during the acceleration state of the dynamic deformation, as shown in Fig. 4.4 (Song et al. 2007e). The amplitude of this spike stress is in the order of 1 MPa, which could be neglected when characterizing many engineering materials. However, this amplitude is comparable to the strength of soft materials, and even higher than the strength of extra-soft materials. Since this spike is not

material intrinsic response, it should be removed from the stress measurement in dynamic characterization of soft materials, particularly extra-soft materials. The inertia-induced extra stress also takes a form of a downward spike during deceleration in axial direction.

As discussed in Chapter 2.3, the specimen aspect ratio (length-to-diameter ratio) determines the severity of both axial and radial inertia. An appropriate determination of specimen dimensions is required in the specimen design for Kolsky-bar experiments. This is applicable not only to the soft materials but also to all materials characterized with Kolsky bar since the inertia issue is independent of material strength. However, due to the low mechanical strength of soft materials, the inertia issue becomes much more severe that has to be taken care of in soft material characterization. The inertia in both axial and radial directions is related to the geometry and dimensions of the specimen and the acceleration the specimen experiences. Minimizing both axial and radial inertia in specimen can therefore be approached in both specimen design and loading-condition control.

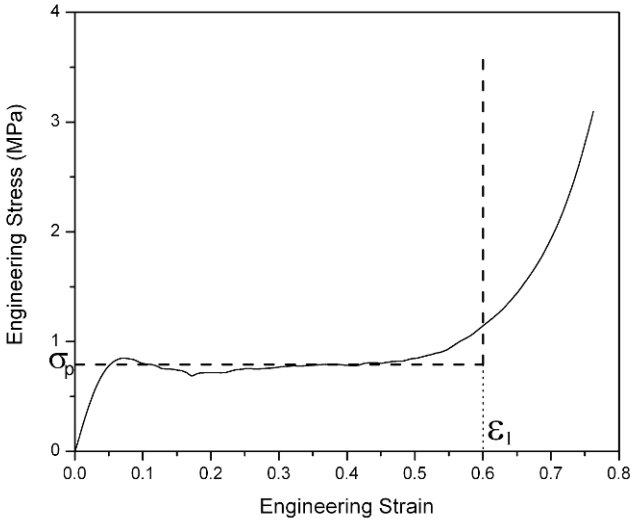

Figure 4.3 Typical stress-strain response of foam material
(Reproduced from Song et al. (2006c) with permission)

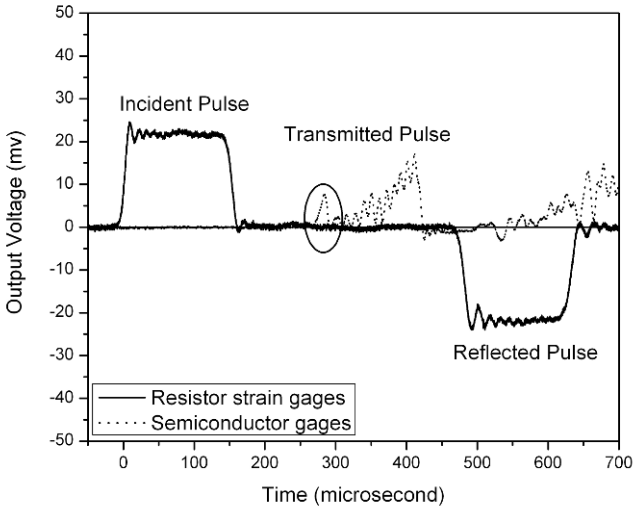

Figure 4.4 Stress spike in the transmitted pulse for soft material characterization *(Reproduced from Song et al. (2007e) with permission)*

The low strength of soft materials requires new techniques to detect the weak transmitted signals in Kolsky-bar experiments. Regular resistor strain gages are not sufficiently sensitive to measure the weak signals with a reasonable signal-to-noise ratio. Highly sensitive transducers are needed to record the weak signals transmitted through the soft specimen. The much lower wave impedance of the soft materials than the bar material makes a nearly full reflection of the incident pulse. Significant noise occurs when using (1.8) to calculate the stress at the incident bar/specimen end. This makes stress equilibrium verification nearly impossible. New techniques are needed to monitor the stress equilibration during dynamic loading.

Many soft materials are sensitive to strain rates. The strain rate in an experiment is not well defined if it varies during an experiment after the initial acceleration stage. Furthermore, the variation in strain rate also changes the stress-strain response for strain-rate-sensitive materials. Therefore, the strain rate is desired to be constant in a Kolsky-bar experiment. In a conventional Kolsky-bar experiment with a roughly con-

stant incident pulse amplitude, the strain rate that is proportional to the reflected pulse typically decreases as the deforming specimen transmits more and more load into the transmission bar. The profile of the incident pulse thus needs to be controlled to ensure constant strain-rate deformation in the specimen.

4.2 Specimen Design

As discussed in Chapter 2.3, to minimize both axial and radial inertia, both specimen length and diameter should be properly designed. When characterizing soft materials with Kolsky bar, the inertia becomes more severe due to the low strength of the soft materials.

Many soft materials are capable of large deformation under axial compression while large expansion along radial directions occurs. In a Kolsky-bar experiment, the specimen cross-sectional area (or diameter) should not exceed that of the bars. With the known bar diameter, the initial specimen diameter is limited for a desired axial compressive strain, or vice versa. For example, a specimen with an initial diameter of 12.7 mm loaded with 19-mm diameter bars will generate valid data up to an axial engineering strain of 55%. The assumption of incompressibility is usually used to approximate the little volume change in a specimen, i.e.,

$$\frac{\pi}{4} d_0^{\,2} l_0 = \frac{\pi}{4} d^2 l \tag{4.2}$$

where d_0 is the original specimen diameter and thickness, respectively; d and l are the current diameter and thickness, respectively, of the soft specimen during deformation; and in the case of compression experiments,

$$\frac{l}{l_0} = 1 - \varepsilon_E \tag{4.3}$$

where ε_E is the engineering strain of the specimen (positive in compression). The maximum allowable specimen diameter during deformation is the bar diameter to ensure the rubber specimen stays within the bar end faces. The corresponding maximum original specimen diameter, d_0, for

a desired specimen strain, ε_E, and a given bar diameter, d_{bar}, can thus be calculated as

$$d_0 = d_{bar}\sqrt{1-\varepsilon_E} \tag{4.4}$$

For example, if the desired largest engineering strain is 0.7 when tested with 19.05-mm diameter bars, the corresponding maximum original diameter of the rubber specimen should be less than 10.43 mm.

Figure 4.5 shows the high-speed backlight images of an EPDM rubber specimen edge (~12.70-mm diameter, 1.60-mm thick) during dynamic compression (Song and Chen 2003). The apparent concave edge is actually the lubricant on the specimen/bar interfaces that is squeezed out by the laterally expanding specimen. When the engineering strain is larger than 0.6 ($t > 164.5\mu s$), the cross-sectional area of the rubber specimen exceeds that of the bars.

After the specimen diameter is determined, the specimen thickness could be optimized to minimize the inertia effects. However, when the Kolsky bar is employed to characterize soft materials, particularly extra soft materials, the general optimization of length-to-diameter ratio described in Chapter 2.3 may not be appropriate because of the low wave speed in the materials. Thinner specimen is desired to facilitate dynamic stress equilibrium.

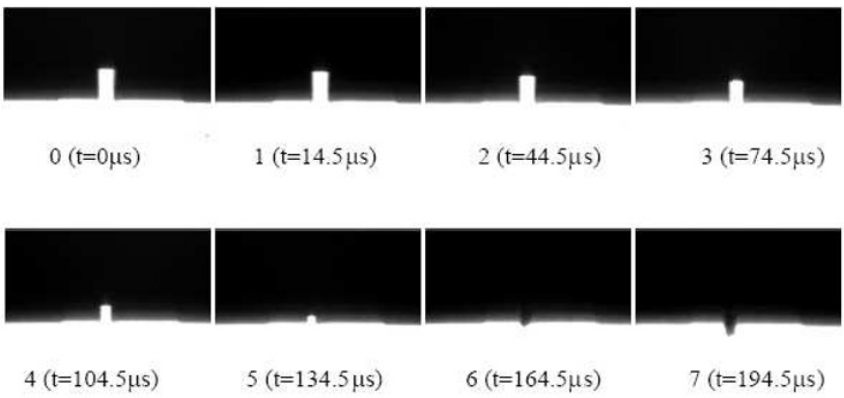

Figure 4.5 High-speed deformation of the EPDM rubber specimen
(Reproduced from Song and Chen (2003) with permission)

On the other hand, the thin specimen makes the interfacial friction between the specimen and the bar ends significant, necessitating sufficient lubrication. In the case of characterizing a foam specimen, a thin specimen may have few cell structures along the axial loading direction. The mechanical response obtained from such a thin specimen may thus be deviated from the actual response of the bulk foam. Therefore, in experiment design, trade-offs are made among the optimized length-to-diameter ratio, dynamic stress equilibrium, friction effects, and representative volume size.

Due to the nature of stress wave propagation, the stress equilibrium is not possible to be achieved perfectly in experiments. It is convenient to have an evaluation criterion for assessing stress equilibrium. One proposed criterion is that described in Chapter 3.5.3: the specimen is considered under uniform loading (dynamic stress equilibrium) when the ratio ($R(t)$) of stress difference ($\Delta\sigma(t)$) between both specimen ends to the mean value ($\sigma_m(t)$) within the specimen is less than 5%,

$$R(t)=\left|\frac{\Delta\sigma(t)}{\sigma_m(t)}\right|\le 0.05 \tag{4.5}$$

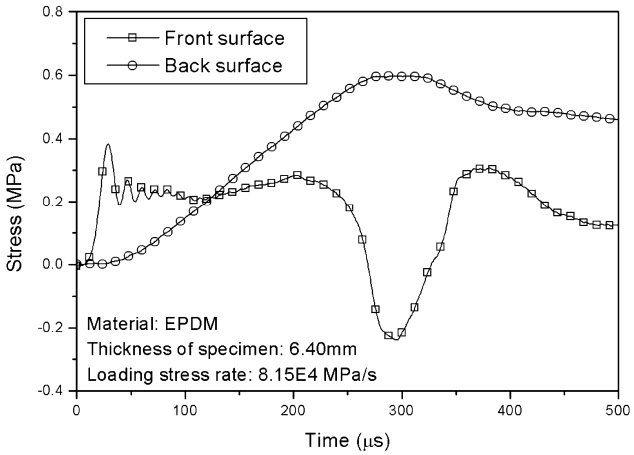

Figure 4.6 Comparison of stress at both ends of a 6.40-mm-thick EPDM rubber specimen
(Reproduced from Song and Chen (2004b) with permission)

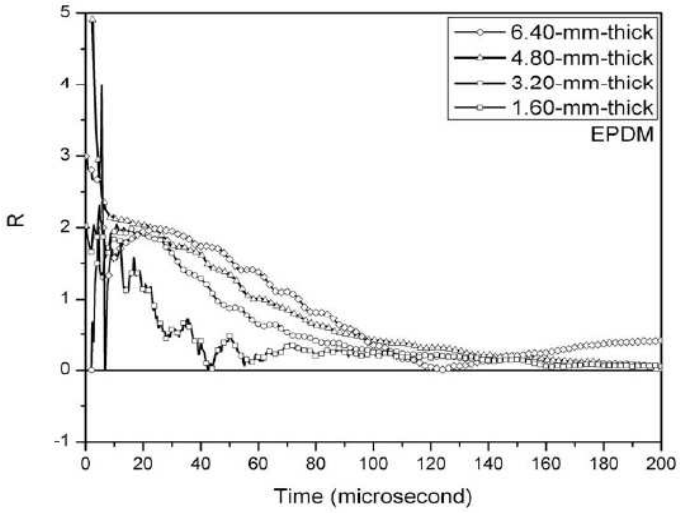

Figure 4.7 Effect of specimen thickness on dynamic stress equilibration

Once the stress equilibrium is defined, the optimized specimen thickness can be developed by judging the time to equilibrium. Figure 4.6 shows the stress histories at both ends of a 6.40-mm-thick EPDM rubber specimen loaded by a conventional Kolsky-bar incident pulse (Song and Chen 2004b). It is clearly shown that the specimen was far from stress equilibrium over the entire loading duration. The stress equilibration factor $R(t)$ is shown in Fig. 4.7 (Song and Chen 2005). Figure 4.7 also shows the comparison of the stress equilibration factor when the specimen thickness is reduced from 6.40 mm to 1.60 mm. The specimen becomes closer to stress equilibrium with reduced specimen thickness. Even though the specimen thickness is reduced to 1.60 mm, the stress in the specimen is still not in equilibrium. Therefore, a thin specimen is one of the requirements in Kolsky-bar experiments on soft materials but is not sufficient to achieve dynamic equilibrium. Further modifications, such as control of initial loading rate, are required. Lower rates of initial loading facilitate early stress equilibrium in the specimen. Constant strain-rate deformation minimizes the specimen inertia in Kolsky-bar experiments. Both initial loading rate and strain rate can be controlled with proper pulse shaping technique, as described in Chapter 2.5.

In addition to axial inertia, radial inertia in a soft specimen becomes significant at high rates of loading. When the specimen is subjected to dynamic axial compression, the axial acceleration also generates inertia (or acceleration) in the radial directions due to Poisson's effect, particularly when the specimen being characterized is nearly incompressible. This radial inertia, in turn, produces an extra axial stress in the specimen. This extra axial stress is not associated with the intrinsic mechanical properties of the material. As indicated in (2.8), the amplitude of the radial-inertia-induced axial stress depends on the specimen material density, the strain acceleration, and the specimen radius. In a typical Kolsky-bar experiment, this radial inertia-induced axial stress is in the order of 1-2 MPa. This amplitude is negligible for most engineering materials with two orders higher amplitude of strength. Therefore, specimen radial inertia issue is typically not mentioned in most Kolsky-bar experiments. However, for the soft materials with strength in the same or even lower order of amplitude, this radial-inertia-induced axial stress is no longer negligible. For example, the strength of brain tissues is only in the order of kPa, the extra stress of 1-2 MPa can easily overshadow the specimen's intrinsic mechanical response (Pervin and Chen 2009). Therefore, when testing soft materials in Kolsky-bar experiments, it is necessary to minimize the inertia effects through proper design of the experiments.

For an incompressible material under small elastic deformation, the extra stress caused by radial inertia is determined by closed-form solution,

$$\sigma_z = \sigma_\theta = \sigma_r = \frac{\rho_0 (a^2 - r^2)}{4} \varepsilon \tag{2.7}$$

The distribution of this extra stress σ_z in the radial directions of the cylindrical (or disk) specimen is illustrated with solid line in Fig. 4.8 (Song et al. 2007e). The specimen has a radius of 5 mm. The distribution shows that the amplitude of the inertia-induced axial stress reaches the maximum at the specimen center but vanishes at the specimen edge. The averaged extra axial stress over the specimen cross section has been found consistent with Kolsky's original energy-based analysis (2.6). According to (2.6), if the strain rate is constant, the inertial term vanishes when the specimen deformation is small. However, it takes time for the strain rate to accelerate from zero to a desired constant level. The acceleration-induced inertia is inevitable during the initial stages of loading, even though the inertia may be reduced through the control over the initial acceleration. A reduced initial acceleration is also desirable for the soft

specimen to achieve stress equilibrium. A loading pulse with an extended rise time is commonly used to satisfy these experimental requirements.

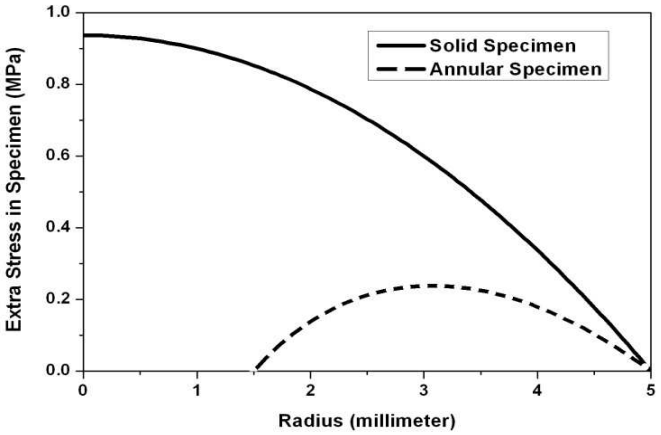

Figure 4.8 Extra axial stress distribution along radial direction in solid and annular specimens
(Reproduced from Song et al. (2007e) with permission)

Since the maximum stress induced by radial inertia incurs its maximum at the center of specimen (Fig. 4.8), an effective approach to minimize the inertia effects is to use a hollow specimen for Kolsky-bar characterization. An analysis has shown that the radial-inertia-induced stress can be significantly reduced when the central portion of the specimen is removed (Song et al. 2007e). The dashed line in Fig. 4.8 shows the distribution of the radial inertial stress induced axial stress along the radial direction of the specimen with a hole of 1.5 mm in radius cut at the center. As shown in Fig. 4.8, the extra stress is zero at both the inner and outer edges of the hollow specimen. The peak value of the inertia-induced stress is only 25% of that in a solid specimen. Parametric studies indicate that the radial inertia becomes insignificant when the inner diameter approaches to the outer diameter. However, in practical experi-

ments, when the initial acceleration is reduced, the 1.5-mm radius hole in a 5-mm radius specimen has been found to reduce the acceleration-induced extra stress to below experimental error level. Furthermore, with the quantitative analysis tool available, it is also feasible to numerically correct the acceleration-induced inertia effects when it is impractical to make hollow specimens or to reduce initial acceleration.

As indicated by (2.10), even after eliminating the acceleration induced extra stress, high strain rate itself can also produce inertia-induced stresses, especially when the strain in the specimen is large. For instance, when the engineering strain in the specimen approaches 1, the inertia-induced stress can overshadow the mechanical response in the specimen. Therefore, one needs to be cautious when interpreting experimental results from Kolsky bar experiments on a soft material deforming to large strains at high rates.

In summary, when the Kolsky bar is used to characterize soft materials, both specimen geometry and dimensions should be carefully designed to reduce the effects of both axial and radial inertia. In addition, the specimen should be under dynamic equilibrium and the strain rate needs to be constant. Before the strain rate reaches constant, the acceleration process in strain rate should be extended such that the inertia effects are minimized and the equilibrium is able to be achieved. When the soft specimen deforms to large strains at high rates, the data need to be carefully examined since a significant portion of the transmitted signal may come from inertia effects, even though the strain rates are maintained at constant levels after initial acceleration.

4.3 Pulse Shaping

In Kolsky-bar experiments, besides the design of specimen geometry, the profile of the incident pulse is the only controllable parameter to subject the specimen to desired testing conditions. The shape of the incident pulse is controlled through pulse shaping techniques. During the initial stages of the dynamic loading on a soft specimen, the incident pulse should have a relatively low rate of loading to achieve stress equilibrium in the specimen and to minimize acceleration-induced inertia. The continuing portion that follows the initial loading is properly modified according to the specimen response to facilitate constant strain rate deformation.

Compared to that in conventional Kolsky bar experiments, the rise time of the incident pulse should be significantly increased through pulse shaping. For example, at least 100 microsecond rise time, nearly an order of magnitude longer than that in conventional Kolsky-bar experiments, of the incident pulse is required for stress equilibrium in a rubber specimen (Song and Chen 2004b). After the initial rising, the profile of the incident pulse is altered to maintain a constant strain rate deformation in the specimen, as indicated by a reflected pulse with a plateau according to (1.12). Under stress equilibrium, the incident pulse is the sum of reflected pulse and transmitted pulse. The transmitted pulse is proportional to the stress history in the specimen under investigation. The desirable profile of the incident pulse is the transmitted pulse plus a constant reflected pulse. Different constant levels of the reflected pulse represent different constant strain rates in the soft specimen. When the transmitted pulse is comparable to the reflected pulse, the incident pulse is desired to have a similar profile but with higher amplitude in comparison to the transmitted pulse, as illustrated in Fig. 4.9. However, when the specimen material is very soft, the amplitude of the transmitted pulse may be negligible as compared to the reflected pulse. In this case, the desired incident pulse is a plateau with a long rise time prior to the plateau, which is illustrated in Fig. 4.10. Since the profile of the transmitted pulse of a soft specimen is not known under a specific set of testing conditions, the generation of a proper incident pulse profile is iterative in nature.

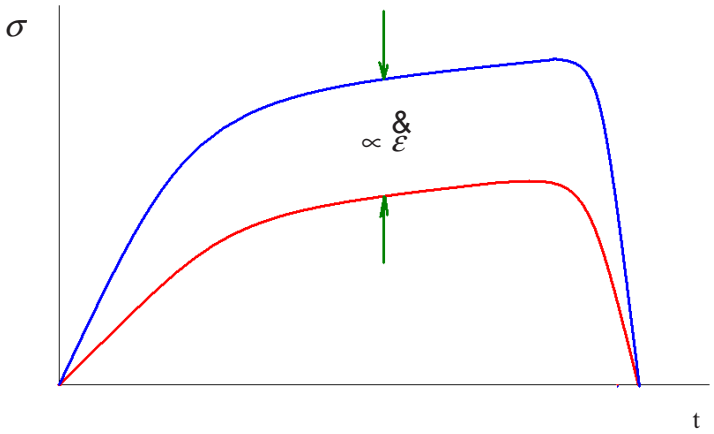

Figure 4.9 Illustration of incident pulse design for soft materials

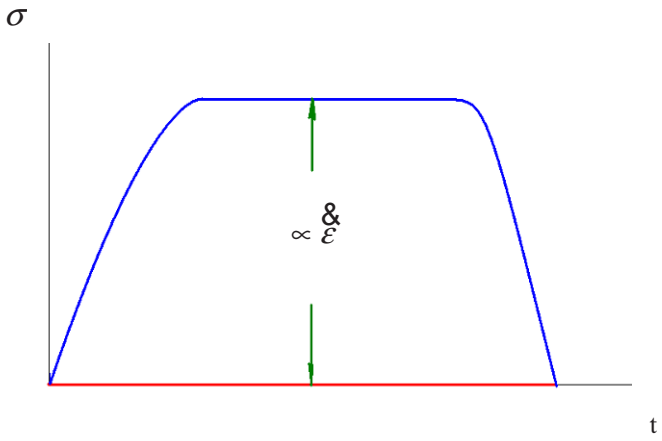

Figure 4.10 Illustration of incident pulse design for extra-soft materials

In order to generate the desired incident pulse, pulse shapers are generally employed. However, the selection of pulse shaper is quite diversified for different soft materials. In addition to the copper pulse shaper that has been analytically modeled, paper, copper tubes, and even foam disks are also commonly used as pulse shapers for soft material characterization. In Chapter 4.5, we will give examples for soft material characterization including pulse shaping techniques.

4.4 Force Sensing

Force sensing becomes more challenging in Kolsky-bar characterization of soft materials, such as biological tissues, which possess strengths in the order of kPa. In Kolsky-bar experiments, the specimen stress is calculated from the amplitude of transmitted pulse (1.14). The high stiffness of the bar material is desired to maintain a high wave impedance mismatch between the specimen and the bars for early dynamic equilibrium. In such a system, each reflection of the stress wave at the specimen/bar interface nearly doubles the stress amplitude in the specimen. It is desir-

able to build up the stress amplitude as much as possible from each reflection in the soft specimen quickly since the number of stress wave reflections is limited during an experiment due to the low wave speed. However, the low stress in the specimen produces extremely low strain in the stiff transmission bar. For instance, the stress of 1 MPa in the specimen with 10 mm in diameter transits into 0.25 MPa in a 20-mm-diameter transmission bar. This 0.25 MPa stress produces only 1.25 microstrain in a steel transmission bar. It is very difficult to clearly detect such a small strain by regular strain gages mounted on the steel bar surface. The force sensing components in conventional Kolsky-bar systems need to be improved to obtain a high signal-to-noise measurement in specimen stress.

According to (1.14), under a constant stress level on the left side of the equation, there are two approaches to increase the amplitude of the transmitted strain signal, ε_T. One is to reduce the bar material stiffness, E; and the other is to reduce the bar cross-sectional area, A_B. To examine the possibilities in bar material selection, Table 1 lists the modulus of elasticity, density, and mechanical impedance (ρC or $\sqrt{\rho E}$) for different metallic and polymeric materials in comparison to steel that is used in conventional Kolsky bars. It is shown that the aluminum alloy has a modulus of approximately one-third of steel, which means that the strain signal will be amplified by three times in amplitude for a certain transmitted stress if using aluminum as the bar material. In fact, the aluminum alloy has been very popularly used as the bar material in Kolsky-bar experiments on soft polymers and polymeric foams (Chen et al. 2002b). Other metallic materials including titanium and magnesium have also been recommended as the bar material for soft material characterization (Gray et al. 1997, Gray and Blumenthal 2000, Shergold et al. 2006). These materials have even much lower Young's moduli than aluminum, and are capable of sensing weaker transmitted signals. However, the relatively low yield strengths limit their application to materials characterization.

Table 4.1 Mechanical Parameters of Various Materials

Material	Density, ρ, (kg/m^3)	Elastic Wave Speed, C, (m/s)	Young's Modulus, E, (GPa)	Wave Impedance, ρC or $\sqrt{\rho E}$, ($kg/m^2/s$)
C350 Maraging Steel	8000	5000	200	4×10^7
7075-T6 Aluminum	2810	5051	71.7	1.42×10^7
CA-1000-1 PMMA	1160	1313	2.0	1.52×10^6
Rubber	930	46	0.002	4.28×10^4

Due to their much lower stiffness, polymeric materials have been used as bar materials for characterization of soft polymers and polymeric foams. Common polymers used as the bar materials include polymethyl methacrylate (PMMA), nylon, and polycarbonate (PC). The low Young's moduli of these materials yield higher sensitivities than the metallic materials. However, the gains in sensitivity are limited. One limitation is the heat conductivity of the polymeric materials. When a strain gage is mounted on the bar surface, heat is generated when the electric current passes through the gages. When the gages are on metallic bar surfaces, the heat is easily dissipated through the bars, leaving the strain gages at nearly the same temperature as the bars. Furthermore, the temperature is nearly constant after the warm-up of the data acquisition system. When the gages are on the polymer bar surfaces, the poor heat conductivity of the polymers leads to temperature rise in the gages. To avoid excessive temperature in the gages, the exitation voltage to the Wheatstone bridges is severely limited, typically lowered by an order of magnitude. As expressed by (1.42) or (1.48), at a given strain, the amplitude of the output signal is directly proportional to the excitation voltage. An excitation voltage of an order of magnitude lower offsets most of the potentials gained from the lower stiffness of the polymeric bars.

In addition to the limited excitation voltage, the nature of viscoelasticity of the polymeric bars further limits their utilization as the bar material in Kolsky-bar experiments. The viscoelasticity brings dispersion and attenuation of stress waves in propagation. Dispersion distorts the profile of a stress wave while attenuation decreases its amplitude. Therefore, the stress wave measured at the strain gage location is no longer representative of the stress wave at the interface between the specimen and bar ends. The stress wave signal measured at the strain gage location must be corrected back to the specimen/bar end interface. The typical viscoelastic response of the polymeric materials makes the relationship between the surface strain measurements and the axial stresses in the bars depend on strain rate, temperature, humidity, and aging. All these increase uncertainties in the mechanical response of the specimen material obtained using the polymeric bars. Therefore, the use of polymer bars is mostly limited to special situations where metallic bars are not applicable such as in microwave environments.

The other approach to increase the bar sensitivities but still using metallic bars is to use hollow bars. Bar sensitivity can be increased when the bar cross-sectional area is reduced, for example, by employing hollow tubes as bars. A common bar combination in soft material characterization is to use a solid aluminum bar as the incident bar and a hollow bar with the same material as the transmission bar. In this case, the hollow transmission bar works as a linear elastic stress/strain amplifier.

Since the axial stress in the tube is also related to the surface axial strain by the bar material's Young's modulus, no further complication is introduced by the incorporation of hollow transmission bars except for possible issues associated with elastic wave propagation in tubes. Since the incident and transmission bars are different in cross-sectional areas, the classic data reduction equations for calculation of strain rate and strain (Eqs. (1.12) and (1.13)) are no longer applicable, which need to be modified (Chen et al. 1999),

$$\varepsilon(t)=\frac{C_0}{l_0}\left(1-\frac{A_i}{A_t}\right)\varepsilon_I(t)-\frac{C_0}{l_0}\left(1+\frac{A_i}{A_t}\right)\varepsilon_R(t) \tag{4.6}$$

$$\varepsilon(t)=\frac{C_0}{l_0}\left(1-\frac{A_i}{A_t}\right)\int_0^t\varepsilon_I(\tau)d\tau-\frac{C_0}{l_0}\left(1+\frac{A_i}{A_t}\right)\int_0^t\varepsilon_R(\tau)d\tau \tag{4.7}$$

where A_i and A_t are cross-sectional areas of the solid incident and the hollow transmission bars, respectively. Unlike Eq. (1.12), the strain rate is not proportional to the amplitude of reflected pulse when the hollow transmission bar is used. This may bring difficulties in experimental design to obtain constant strain rate in the specimen. Equations (4.6) and (4.7) yield to Eqs. (1.12) and (1.13), respectively, when the transmission bar has the same diameter and material as well, as the incident bar.

Besides working with the bar material and cross-sectional area to increase the amplitude of the transmitted pulses, another direct solution is to utilize highly sensitive transducers. The commonly used resistor strain gage on the bar surface has a gage factor of approximately 2.0. However, the semiconductor strain gage factor is approximately 150. The over 70 times higher sensitivity of the semiconductor strain gage is able to satisfy the measurement requirement for most soft materials. A combination of semi-conductor strain gages and hollow bars satisfies most needs in transmitted signal sensing except for some extreme cases. Another approach to precise force measurements is direct force (or stress) measurement using highly sensitive force transducers. X-cut circular piezoelectric quartz crystal force transducers have been applied to Kolsky-bar experiments on soft materials. These force transducers have been used to measure dynamic force profiles for many years. The 0.254±0.025 mm thick quartz crystal force transducer used by Chen et al. (2000) has a piezoelectric constant of 2.30 pC/N. The quartz crystal has an excellent linearity up to the pressure where dielectric breakdown occurs and is not very sensitive to environmental temperatures. The quartz crystal also has a mechanical impedance (ρC_o) of approximately

1.394×10^7 kg/m^{2}s, which is very close to the impedance (1.350×10^7 kg/m^{2}s) of aluminum alloy. Therefore, when the quartz crystal force transducers are embedded into aluminum bars, the disturbance to the one-dimensional stress wave propagation in the bar system is minimal.

The quartz crystal force transducer is able to directly measure the force (or stress) of the specimen not only on the transmission bar side but also on the incident bar side. When the specimen material is soft, it is difficult to measure the force (or stress) at the front side of specimen to verify the force (or stress) equilibration process because the amplitudes of the incident and reflected pulse are very close. The difference between the two large-amplitude pulses is noisy and hard to be compared to the low-amplitude transmitted signal. When the quartz crystal is attached to the interface between the incident bar and the specimen, the force at this interface can be measured directly instead of taking the difference between the incident and reflected signals.

The quartz crystal force transducer is glued with conductive epoxy on the bar end. In order to protect the quartz crystal force transducer, a thin aluminum disc is usually glued on the other side of quartz crystal. However, the thin aluminum disc may bring additional axial inertia force, particularly when it is subjected to significant acceleration generated by the high-amplitude incident pulse. This axial inertia force makes the measurement from the quartz crystal force transducer different from the actual force history on the specimen (Casem et al. 2005),

$$F_{1m} = F_1 + m_e a_1 = F_1 + m_e C_0 \frac{d\left(\varepsilon_i - \varepsilon_r\right)}{dt} \tag{4.8}$$

$$F_{2m} = F_2 - m_e a_2 = F_2 - m_e C_0 \frac{d\varepsilon_t}{dt} \tag{4.9}$$

where F_{1m} and F_{2m} are forces directly measured by the quart crystal force transducers at the front and back ends of the specimen, respectively; m_e is the effective mass that carries the additional axial acceleration,

$$m_e = \frac{1}{2} m_g + m_1 \tag{4.10}$$

In (4.10), m_g and m_1 are masses of the quartz crystal transducer and the aluminum disc; respectively. The last terms in both (4.8) and (4.9) represent the additional axial inertia forces brought by the additional alumi-

num discs and the quartz crystals themselves at both ends of the specimen. When testing soft materials, the transmitted signal is so weak that the acceleration at the specimen back end can be neglected. However, at the front end of the specimen, the acceleration is too significant to be negligible. Note that the incident and reflected strains have opposite signs.

This axial inertia force at the front end needs to be corrected or compensated. A numerical correction can be performed according to (4.8) after measurement of the masses of the quartz crystal and the aluminum disc as well as both incident and reflected pulses. Alternatively, a so-called "three-quartz technique" has been developed to experimentally compensate the axial inertia force, which is illustrated in Fig. 4.11 (Casem et al. 2005). When m_s and m_p satisfy the following relationship,

$$m_s = m_p - \frac{1}{2} m_g \tag{4.11}$$

the additional inertia force is automatically compensated. Figure 4.12 shows the comparison of Kolsky-bar experiments on a polymeric foam with the single quartz crystal and the "three-quartz crystal" technique (Casem et al. 2005). The records clearly show that, without the compensation of the additional axial force, the stress equilibration could be assessed at fault. Since the inertia is related to acceleration, the axial inertia force vanishes under constant-speed loading. In Kolsky-bar experiments, the initial acceleration is of high amplitude and inevitable. In hence, the axial inertia force brought by introducing the quartz crystal and attached aluminum disc should be corrected or compensated when testing soft materials.

Another possible transducer for direct force sensing is polyvinylidene fluoride (PVDF). This thin-film type of force transducer has approximately one order of magnitude higher sensitivity than the quartz crystal force transducers. However, the possible nonlinearity of the sensitivity of the PVDF requires accurate calibration within the full range of application, which is not yet available (Ueberschlag 2001).

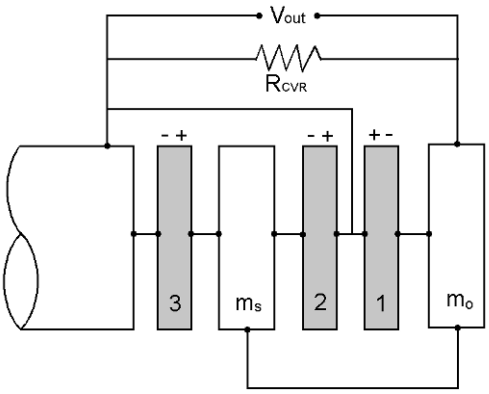

Figure 4.11 Three-quartz technique
(Reproduced from Casem et al. (2005) with permission)

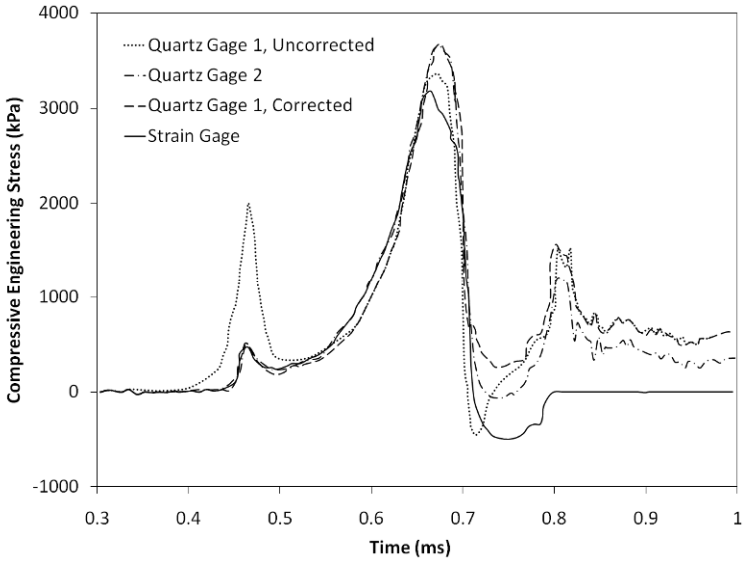

Figure 4.12 Comparison of single-quartz and three-quartz techniques
(Reproduced from Casem et al. (2005) with permission)

4.5 Experiment Design

As described in previous sections, considerations for valid Kolsky-bar experiments should be focused on specimen design, force sensing, and pulse shaping design with the goal of achieving uniform deformation/stress equilibration and constant strain rate deformation in the specimen.

Due to different mechanical responses of different soft materials to high-rate loading, the detailed experiment designs for these materials are diversified. Figure 4.13 illustrates a general layout of the Kolsky-bar setup modified for soft material characterization. The bars are usually solid rods being made of low-stiffness alloys such as aluminum alloy. In the cases where the transmitted signal is too weak, the transmission bar is hollow, and/or with highly sensitive strain gages, such as semiconductor strain gages. As compared to the conventional setup in Fig. 1.6, the Kolsky bar is modified with the employment of the pulse shaper that is placed on the impact end of the incident bar, and quartz-crystal force transducers that are attached to the specimen ends of the incident and transmission bars, respectively. Again, the transmission bar may be hollow. In addition, to preserve the deformed state in the specimen after high-rate loading, the incident bar can be modified to single-loading type, as described in Chapter 2.6, to ensure single loading on the soft specimen.

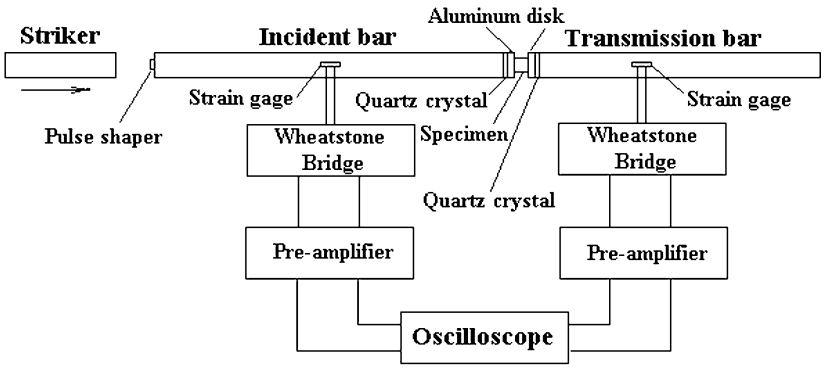

Figure 4.13 Kolsky-bar setup for soft material characterization

Most soft materials can deform to large strains, the bars thus need to be sufficient long to enable the needed long duration of loading to the specimen. When long bars are used, stress wave dispersion, as described in Chapter 2.1, during propagation may become significant due to two-dimensional effect (Poisson's effect) of the bars. One purpose of the pulse shaping is to efficiently minimize the stress wave dispersion as a physical low-pass filter that eliminates dispersive high-frequency wave components. The pulse shaper also needs to be properly designed to produce a desired profile of the incident pulse facilitating stress equilibration and constant strain-rate deformation in the specimen, depending on the mechanical response of the specimen material.

The quartz-crystal force transducers are used to monitor the process of stress equilibrium in specimen during high-rate loading. Since the existence of quartz-crystal transducers should not influence the stress wave propagation, the quartz-crystal force transducers are ideally very thin circular discs with the same diameter as the bars. The mechanical impedance of the quartz-crystal force transducers should be as close as the bar material, which limits the material to be aluminum alloys. The axial inertia brought by the additional disc at the incident bar end needs to be compensated numerically or by using three-quartz technique. Such a compensation of axial inertia on the transmission bar side is usually not necessary due to the low transmitted pulses through the soft specimens.

Even though the specimen dimensions and geometry may vary from material to material, the soft specimen always needs to be thin as a general principle for specimen design. Such a thin specimen may increase the influence of interfacial friction between the soft specimen and the bar ends. Significant interfacial friction makes the specimen in multiaxial stress state, which will erroneously increase the strength of the specimen material. A barrel shape of the specimen during high-rate deformation is a typical indicator of insufficient interfacial lubrication. The effect of lubrication on specimen response in Kolsky-bar experiments has been investigated (Briscoe and Nosker 1984, Zenker and Clos 1998, Trautmann et al. 2005). Petroleum jelly has been recognized as a good lubricate for most soft materials (Trautmann et al. 2005). However, for some special materials, e.g., biological tissues, the petroleum jelly is too viscous to provide sufficient lubrication for such extra-soft materials. Vegetable oils have been successfully used for biological tissues and gelatins in Kolsky-bar experiments (Moy et al. 2006, Song et al. 2007b, Pervin and Chen 2009).

In the following sections, we give several examples of Kolsky-bar experiment designs for different soft materials, which may be used for references when characterizing different materials but with similar characteristics.

4.5.1 Polymethyl Methacrylate (PMMA)

The PMMA specimens were machined into cylinders with a diameter of 12.70 mm and a thickness of 6.35 mm, making a length-to-diameter ratio of 0.5, from a commercially available rod. In order to relieve the residual stress in the specimens due to material handling and machining, all PMMA specimens were heat-treated in a sealed furnace to 110˚C for 4 hours, and then cooled down to room temperature overnight.

7075-T651 aluminum alloy was selected as the bar material. The bars had a common diameter of 19.05 mm. Since the yield strength of the PMMA is a significant fraction of that of the bar material, the transmitted signal could be easily detected with regular resistor strain gages mounted on the solid aluminum transmission bar. In addition, the quartz-crystal force transducers in Fig. 4.13 are not necessary because the stresses at both ends of the specimen can be calculated with (1.8) and (1.9) without ambiguity for stress equilibrium evaluation. The specimen ends were lubricated with petroleum jelly.

As a typical viscoelatic material, both loading and unloading response of the PMMA are of interest. However, the experimental conditions, such as strain rate, during loading and unloading should be maintained the same to obtain the dynamic hysteretic response of the material. In this case, a special pulse shaping design is required because not only the loading profile but also the unloading profile of the incident pulse is in need of precise control to subject the specimen to desired testing condition during the experiment.

A pulse shaping technique, shown in Fig. 2.22, has been used for the PMMA characterization. The front pulse shaper is used to generate a desired incident loading profile for stress equilibrium and constant strain rate over the loading phase of the experiment. The rear pulse shapers on the surface of the rigid mass start to play the role, after the gap between the flange and the rigid mass is closed, to modify the unloading path of the incident pulse appropriately for stress equilibrium and the same constant strain rate over the unloading phase of the experiment.

In this case, a 3.97-mm-diameter, 1.57-mm-thick C11000 half-hardened copper disk was employed as the front pulse-shaper and two 2.38-mm-diameter, 0.51-mm-thick annealed C11000 copper disks were selected as the rear pulse-shapers. The gap between the flange and the rigid mass was preset at 0.89 mm. The incident pulse generated through such a special pulse shaping technique, and consequent reflected, and transmitted pulses for the PMMA at a strain rate of 360 s^{-1} are shown in

Fig. 4.14 (Song and Chen 2004c). Figure 4.14 also shows that both dynamic stress equilibrium and constant strain rates were achieved in both loading and unloading portions. In addition, the unloading strain rate is maintained to be the same as the loading strain rate. The same strain rate for loading and unloading makes the resultant stress-strain loop at a common constant strain rate for strain-rate-effect investigation.

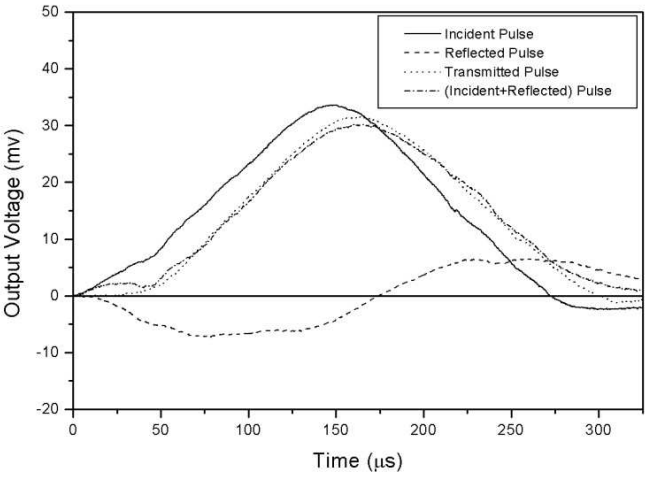

Figure 4.14 Kolsky-bar experiment on PMMA
(Reproduced from Song and Chen (2004c) with permission)

Figure 4.15 shows the stress-strain loops at one dynamic strain rate of 360 s^{-1} and two quasi-static strain rates of 0.0001 s^{-1} and 0.01 s^{-1} (Song and Chen 2004c). All stress-strain curves exhibit similar characteristics: a nearly linear behavior at small strains (<3%) followed by a non-linear behavior in both loading and unloading portions. The unloading stress is lower than that of loading at a certain strain, making the stress-strain loop with a residual strain, or permanent set. The non-linear behavior and the residual strains after mechanical tests may indicate the presence of damage to the microstructures of the materials. Moreover, the residual

strain was found to depend on the maximum loading strain in the specimen: a larger maximum loading strain leads to a larger residual strain. Figure 4.15 also shows that the stress-strain loops are significantly sensitive to strain rate. The strong rate-sensitive hysteretic stress-strain loops verify the viscoelastic nature of the material.

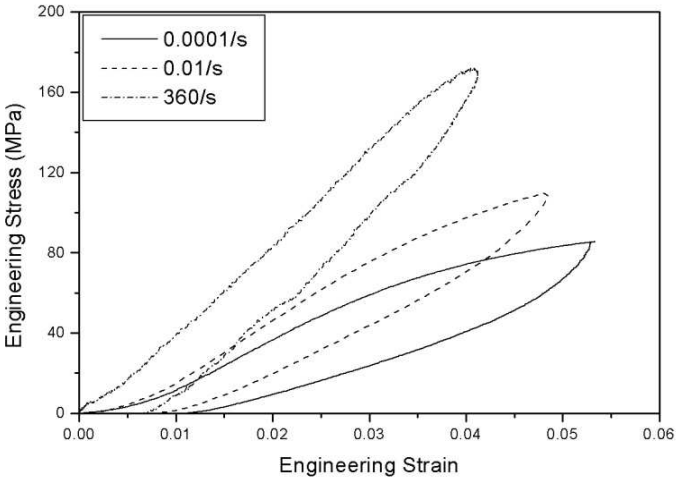

Figure 4.15 Loading and unloading stress-strain curves of PMMA
(Reproduced from Song and Chen (2004c) with permission)

4.5.2 Rubbers

Rubbers typically exhibit characteristics of nonlinear large deformation and significant sensitivity to strain rate and stress state. The low stress wave speed makes it challenging to achieve uniform deformation and stress equilibrium under high-rate loading, as shown in Fig. 4.1. The

rubber specimen needs to be thin and requires a low-rate initial loading to achieve stress equilibrium. As a role of thumb, a 3-mm-thick specimen is perhaps appropriate for achieving stress equilibrium after proper pulse shaping technique is used to produce low rate in the initial loading (or relatively long rise time in the incident pulse). The incident pulse has a rise time of as long as 100 μs which is approximately 10 times longer than that in conventional Kolsky-bar experiments. Petroleum jelly has also been found to provide sufficient lubrication for rubber testing.

4.5.2.1 Soybean-Oil Based Polymers

In this section, we present Kolsky compression bar experiments on soybean-oil based polymers, which have similar characteristics as other engineered rubbers. The materials are polymers made through the reaction of epoxidized soybean oil (ESO) with diamine compounds. The ESO was mixed thoroughly with the curing agent, triethylenetetramine (TETA) or diethylenetriamine (DETA), with different fractional amounts, as tabulated in Table 4.2 (Song et al. 2006b).

Table 4.2 Composition of soybean-oil based polymers
(Reproduced from Song et al. (2006b) with permission)

Sample code	ESO (g)[a]	Curing agent (g)[a]			T_g (°C)
		TETA	DETA	TETA	
ESOT-I	140.6 (0.141)	40.3 (0.28)			7.84
ESOD	149.1 (0.149)		30.3 (0.29)		1.51
ESOT-II	152.3 (0.152)			27.5 (0.19)	0.22

[a] Values in parentheses indicate moles.

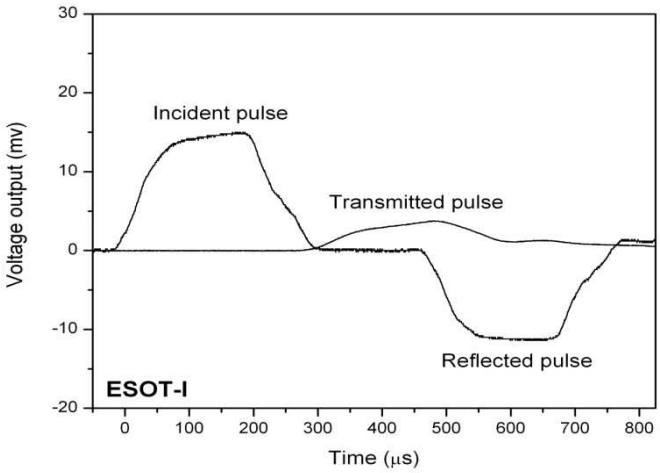

Figure 4.16 Kolsky bar experiment on ESOT-I
(Reproduced from Song et al. (2006b) with permission)

Figure 4.16 shows typical incident, reflected, and transmitted pulses in a Kolsky-bar experiment on the ESOT-I polymer listed in Table 4.2 (Song et al. 2006b). An annealed C11000 copper disk was employed as the pulse shaper in the experiment. The incident pulse had a rise time of about 100 μs. This long rise time during the initial portion of the incident pulse was generated for achieving stress equilibrium in the specimen. The dynamic stress equilibrium process in the ESOT-I rubber, which was monitored by the quartz transducers, is shown in Fig. 4.17. Figure 4.17 clearly indicates that the specimen was in dynamic stress equilibrium over the entire loading duration. As shown in the transmitted pulse, the stress in the specimen continuously increases under continuous compression. This type of specimen response requires more input energy to maintain constant strain rate in the specimen. Accordingly, the amplitude of incident pulse needs to be increased with time for this purpose. The increase rate for the amplitude of this incident stress needs to be carefully designed. If the rate is not sufficiently high, the strain rate in the specimen will still decrease even though the decrease rate may be slowed down by the pulse shaping. On the other side, if the incident stress is over supplied, the specimen will be compressed in acceleration. In this

set of experiments, the nearly linear portion in the incident pulse was generated for constant strain rate deformation in the specimen, which is shown in Fig. 4.16. However, the strain rate was not achieved to a constant until 100 μs after initial loading due to the long rise time in the incident pulse and the resultant strain rate acceleration from zero to the desired level. Strictly, the data obtained during the first 100 μs are not accurate, even though the stress may have been equilibrated by the end of this stage, because the strain rate has not achieved a constant yet. It is noted that the deformation produced in the first 100 μs may not be large due to the low strain rate before achieving the constant value. However, the accumulated strain in the specimen during the first 100 μs serves as a dividing point on the stress-strain curve that separates the valid and invalid portions of the dynamic stress-strain curve.

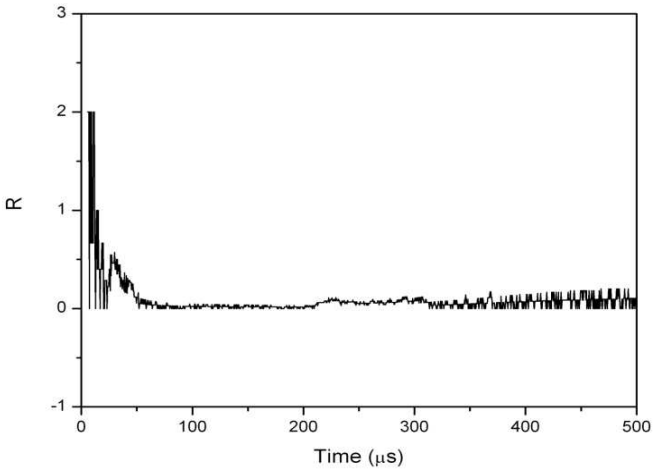

Figure 4.17 Dynamic stress equilibrium in the ESOT-I specimen
(Reproduced from Song et al. (2006b) with permission)

Figure 4.18 shows the engineering stress-strain curves for the ESOT-I at various dynamic strain rates from 230 to 1650 s^{-1} (Song et al. 2006b). In order to study the strain-rate effect over a wide range, quasi-static stress-strain curves are also plotted in the same figure. Following the same procedure, the stress-strain curves for the other two materials

(ESOD and ESOT-II) listed in Table 4.2 are obtained and shown in Figs. 4.19 and 4.20, respectively. Significant strain-rate effects were found on all three materials, which also exhibit similar shapes in stress-strain curves. Not only stress amplitudes at certain strains but also the shapes of the stress–strain curves change due to strain rate effects when comparing the dynamic stress-strain curves to their quasi-static counterparts. An initial nearly linear behavior followed by a transitional nonlinear response and then a strain-hardening behavior is typical characteristic for the dynamic stress–strain curves. However, the initial linear behavior in quasi-static stress–strain curves is not significant when strain rate is below 1.0 s^{-1}. The tangential moduli in the quasi-static stress–strain curves increase with increasing strains.

The unloading part for the stress-strain curve of ESOT-I at 1650 s^{-1} is plotted in Fig. 4.18. This is a typical unloading curve obtained from Kolsky-bar experiments on rubber or rubber-like materials. However, this measured unloading response may not represent the actual unloading process in the specimen material. When the specimen is unloaded, the viscoelastic nature makes it recover but with very low stress amplitude. This small stress produced by the specimen recovery may not be sufficiently high to push the compression bars back so that the specimen keeps being deformed but the stress is relaxed due to the nature of viscoelasticity.

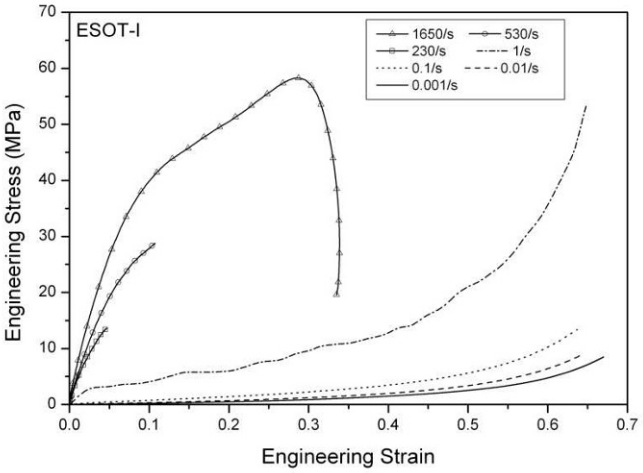

Figure 4.18 Compressive stress-strain curves of ESOT-I
(Reproduced from Song et al. (2006b) with permission)

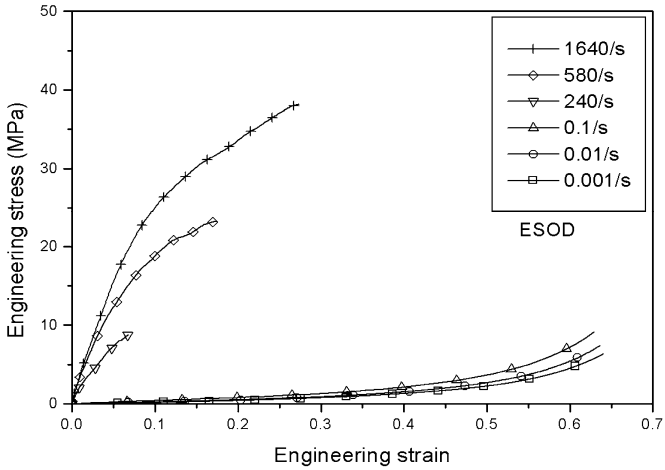

Figure 4.19 Compressive stress-strain curves of ESOD
(Reproduced from Song et al. (2006b) with permission)

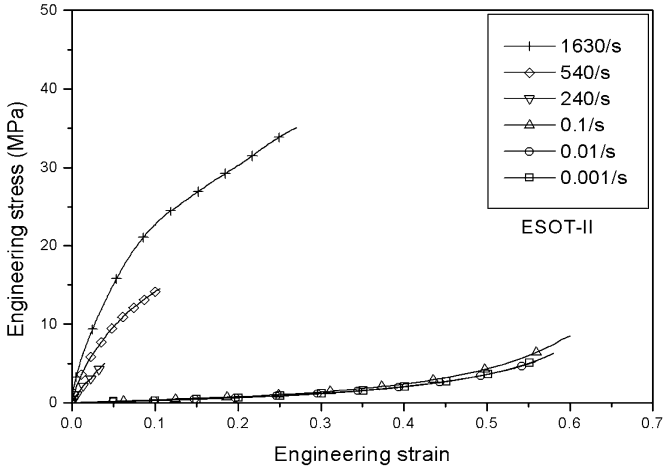

Figure 4.20 Compressive stress-strain curves of ESOT-II
(Reproduced from Song et al. (2006b) with permission)

4.5.2.2 ESO-NanoClay Composites

The composites with the ESO polymers as matrix and nanoclay (Closite 30B particles: montmorillonite modified with alkyl quaternary ammonium montmorillonite) as fillers exhibit very similar mechanical response as the base ESO polymers. However, the stresses at certain strains may either increase or decrease in comparison with the matrix material, depending on the weight of nanoclay and strain rate. The stress-strain curves of the three materials with 0, 5%, and 8% nanoclay in weight, respectively, were obtained using the same procedure for the ESO copolymer characterization and are shown in Figs. 4.21, 4.22, and 4.23, respectively (Song et al. 2006a).

The effects of strain rate and nanoclay-weight are summarized in Table 4.3. Consistent strain-rate hardening was observed for the composite with 5% nanoclay in weight. However, for the composite with 8% nanoclay in weight, the stress at the strain of 5% at the strain-rate of 2540 s^{-1} is slightly lower than that at the same strain but at a lower strain rate of 700 s^{-1} (Table 4.3). The disappearance of strain-rate hardening at this nanoclay weight may be caused by interface decohesion between the nanoclay and the ESO material due to too high load of nanoclay.

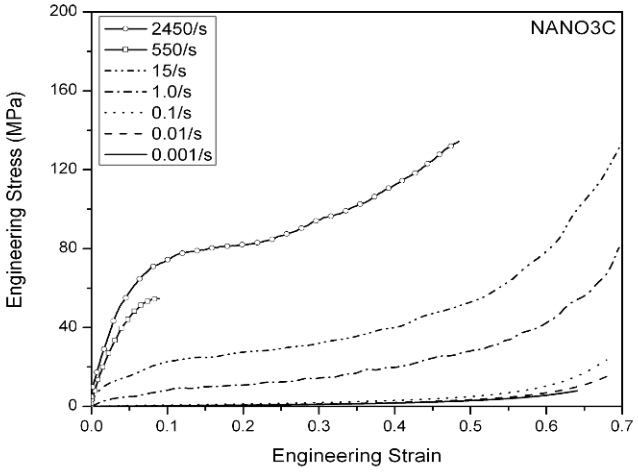

Figure 4.21 Compressive stress-strain curves of ESO/Clay-0
(Reproduced from Song et al. (2006a) with permission)

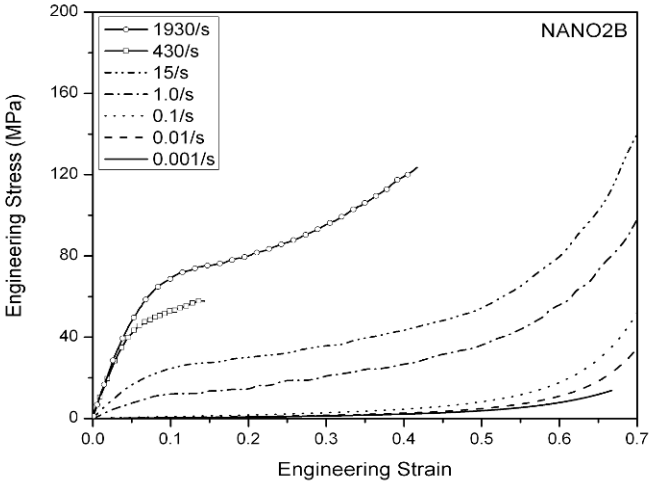

Figure 4.22 Compressive stress-strain curves of ESO/Clay-5
(Reproduced from Song et al. (2006a) with permission)

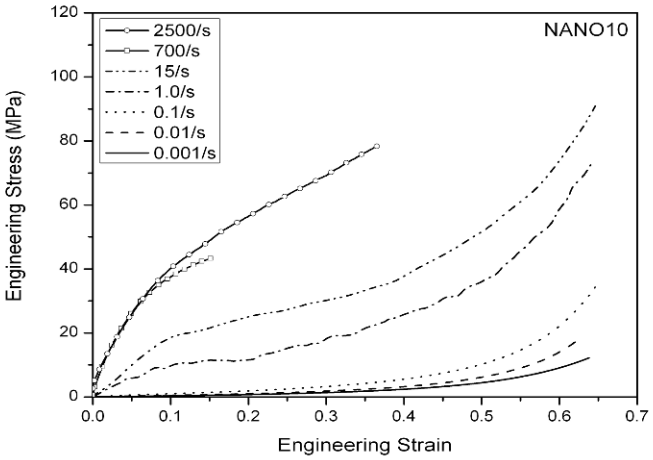

Figure 4.23 Compressive stress-strain curves of ESO/Clay-8
(Reproduced from Song et al. (2006a) with permission)

The effects of nanoclay on the strength of the nano-composite materials were found to be mixed. The nanoclay is shown to enhance the strength of the nanocomposites only at low strain rates. The addition of nanoclay has little or negative effects on the material stress at a certain strain and at high strain rates. When strain rate is below 1.0 s^{-1}, the stress at a certain strain increases with increasing nanoclay weight. At the strain rate of 1.0 s^{-1}, the stresses for both nanocomposites were still enhanced in comparison with that for the material without nanoclay. However, the stress for the composite with 5% nanoclay is superior to that for the composite with 8% nanoclay at this strain rate. When the strain rate is increased to 15 s^{-1}, the stress increases when the nanoclay addition up to 5% in weight. However, when more nanoclay (8%) is added, the stress becomes even lower than that for the material without nanoclay. At further higher strain rates, the material without nanoclay has the highest stress at small strains. At a certain strain level, the stress decreases with increasing weight of nanoclay. At large strains, the dynamic stress increases slightly when 5% weight nanoclay is added, but significantly decreases when more nanoclay (8%) is added. The experimental results indicate that the material containing too much nanoclay without special treatment damages its strength due to possible aggregation of the clay layers.

Table 4.3 Strain-rate and nanoclay-weight effects
(Reproduced from Song et al. (2006a) with permission)

	ESO:H = 1:1.37					
Components	ESO/clay-0		ESO/clay-5		ESO/clay-8	
Nanoclay weight	0		5%		8%	
Strain	Strain rate (s^{-1})	Stress (MPa)	Strain rate (s^{-1})	Stress (MPa)	Strain rate (s^{-1})	Stress (MPa)
5%	10^{-3}	0.12	10^{-3}	0.15	10^{-3}	0.16
	10^{-2}	0.19	10^{-2}	0.23	10^{-2}	0.26
	10^{-1}	0.37	10^{-1}	0.53	10^{-1}	0.60
	15	15.62	15	16.60	15	10.07
	550	44.96	430	41.72	700	26.24
	2450	58.13	1930	48.22	2540	26.01
10%	10^{-3}	0.25	10^{-3}	0.30	10^{-3}	0.33
	10^{-2}	0.34	10^{-2}	0.43	10^{-2}	0.48
	10^{-1}	0.63	10^{-1}	0.88	10^{-1}	1.02
	15	22.63	15	24.76	15	18.65
	550	/	550	52.95	550	37.52
	2450	74.36	1930	68.93	2540	40.22
40%	10^{-3}	1.72	10^{-3}	2.13	10^{-3}	2.42
	10^{-2}	1.94	10^{-2}	2.62	10^{-2}	3.22
	10^{-1}	3.05	10^{-1}	4.66	10^{-1}	5.51
	15	39.83	15	43.35	15	37.72
	550	/	550	/	550	/
	2450	112.28	1930	119.02	2540	79.65

4.5.2.3 EPDM Rubber

An ethylene-propylene-diene monomer copolymer (EPDM) rubber was characterized with the same procedure in Kolsky compression bar experiments. Here we present the resultant stress-strain behavior for the EPDM rubber at various strain rates.

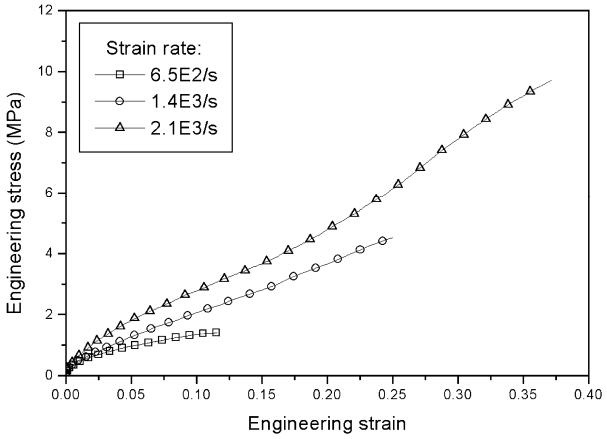

(a)

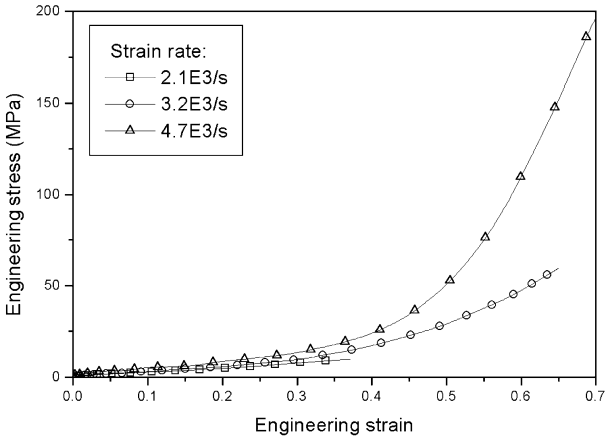

(b)

Figure 4.24 Compressive stress-strain curves of EPDM rubber
(Reproduced from Song and Chen (2003) with permission)

Figure 4.24 shows the compressive engineering stress-strain curves for this EPDM rubber, which are grouped into two graphs due to the drastic stress amplitude differences at different strain rates. The dynamic stress-strain behavior of the EPDM rubber is highly nonlinear with significant strain-rate effects. For each stress-strain curve, the slope increases significantly with increasing strain at large strains (>5%), which is different from that at small strains (<5%). The strain rate sensitivity also depends on the amplitude of strain. The strain rate effect on the nonlinear mechanical response of the EPDM rubber has been quantitatively studied and modeled (Song and Chen 2003, Song et al. 2004a).

4.5.3 Foams

Foam materials exhibit unique mechanical response to external loading. Changes in the matrix material or cell structures (open or closed cell structures) can consequently result in significant change in their global material response. Generally, the foam materials may be classified into two groups: elastic-brittle foams and elastic-plastic foams according to their mechanical responses. Different types of foams may require different designs in Kolsky-bar experiments. In this section, we present the Kolsky-bar experiment designs for brittle and elastic-plastic foams, respectively.

4.5.3.1 Brittle Foams

The material we present here is an epoxy syntactic foam, which is made of an epoxy resin as binder and hollow glass microspheres with a maximum diameter of 50 μm as fillers. This syntactic foam has a density of 0.77×10^3 kg/m^3, a glass transition temperature of 70°C, and an ultrasonic longitudinal wave speed of 2700 m/s. This longitudinal wave speed may not necessitate thin specimens for achieving stress equilibrium. The specimen has a thickness of 6.35 mm and a diameter of 12.70 mm, producing a length-to-diameter ratio of 0.5.

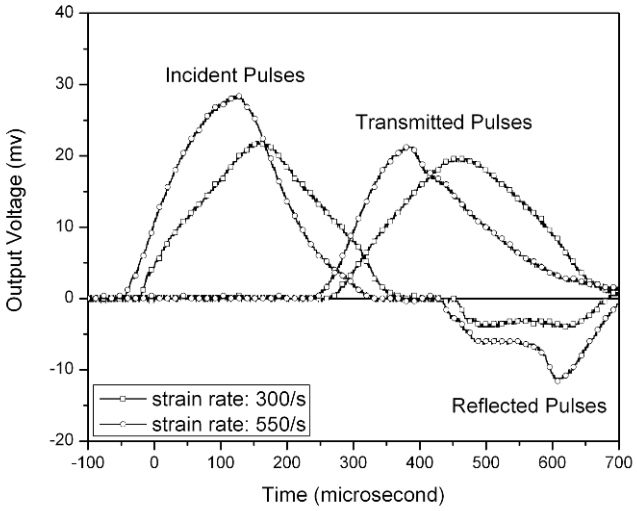

Figure 4.25 Kolsky bar experiments on epoxy syntactic foam

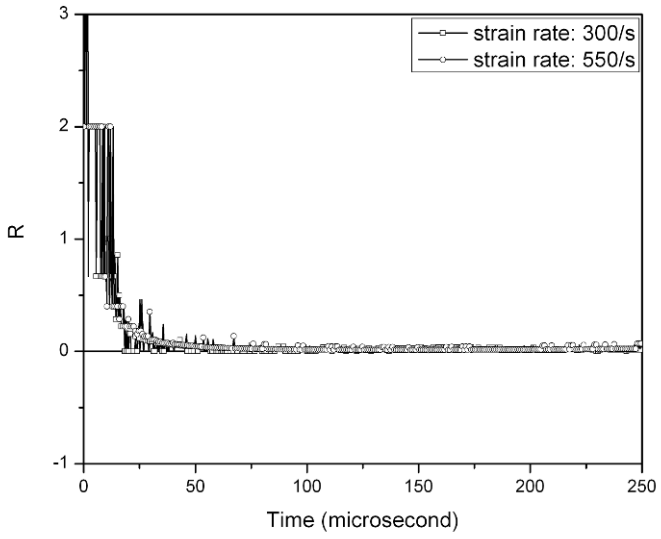

Figure 4.26 Dynamic stress equilibrium processes

The Kolsky bar schematically shown in Fig. 4.13 was employed for dynamic compression experiments. To facilitate a constant strain-rate deformation in such a nearly linear elastic material, a ramp loading pulse with a constant slope is necessary. This ramp slope determines the strain rate in the specimen. The ramp incident pulses with different slopes were produced with annealed C11000 copper disk pulse shapers of various dimensions associated with different striking velocities.

Figure 4.25 shows two sets of incident, reflected, and transmitted signals at the strain rates of 300 and 550 s^{-1} (Song and Chen 2005). It is observed that, such nearly linear profiles of the incident pulses produced plateaus in the reflected pulses, which represent constant strain rates if the stress is proven to be in dynamic equilibrium. Figure 4.26 shows the processes of dynamic stress equilibrium by means of (4.5). The forces at both ends of the specimen were directly measured with the quartz-crystal force transducers (Fig. 4.13). The axial inertia force brought by the aluminum disk at the incident bar end is insignificant as compared to the strength of the syntactic foam, making it unnecessary to compensate this axial inertia force. Only single quartz crystal was used. It is observed that the specimens were in stress equilibrium within most of loading durations at both strain rates due to the modified loading profiles through pulse-shaping. The strain-rate histories in specimens are shown in Fig. 4.27. The strain rate does not reach constant values until ~50 μs after the specimen is loaded. When the strain rate is high, i.e., 550 s^{-1} in Fig. 4.26, it may have a sharp rise following the constant part due to the sudden failure of the brittle specimen. This is similar mechanism to the brittle material characterization described in Chapter 3.

Figure 4.28 shows the dynamic compressive stress-strain curves of the epoxy syntactic foam over a range of strain rates from 300 to 1900 s^{-1} (Song et al. 2004b). The elastic recovery in the stress-strain curve at 300 s^{-1} is the result of unloading before reaching the failure of the specimen. The maximum stress shown in this curve does not represent the specimen failure strength. However, for the other stress-strain curves in Fig. 4.28, the peaks indicate the failure strength of the material. The sudden increase in the reflected signals in those experiments indicates that the specimens fail catastrophically during the first pass of the loading pulse. Both Young's modulus and failure strength increase when the strain rate increases from 300 to 550 s^{-1}. However, little change in both modulus and failure strength was observed when the strain rate further increases to 1030 s^{-1}. Moreover, both modulus and failure strength decrease when the strain rate reaches a higher level at 1900 s^{-1}. This puzzling phenomenon has been concluded as a result of mixture of strain-rate strengthening and damage softening in the specimen under dynamic loading. A strain-

rate- and damage-dependent material model has been developed to describe the phenomenon (Song et al. 2004b).

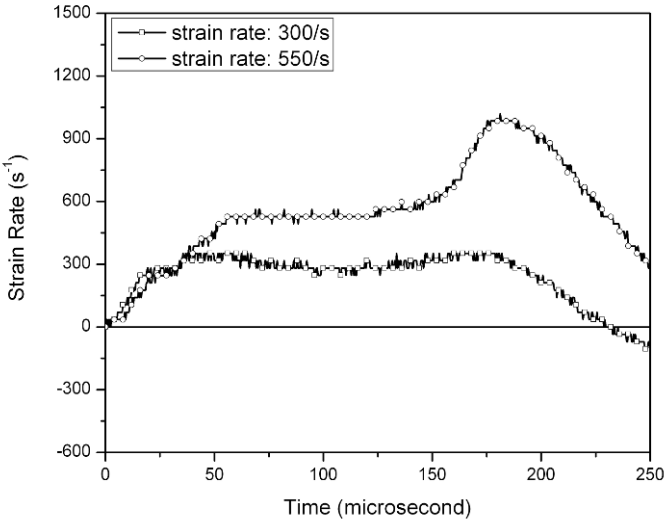

Figure 4.27 Strain-rate histories

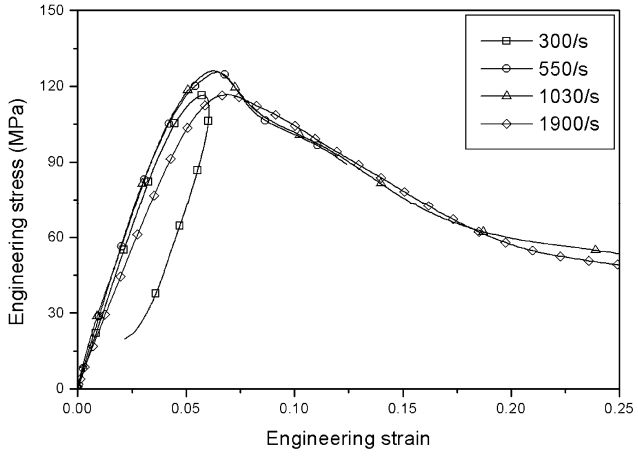

Figure 4.28 Compressive stress-strain curves of epoxy syntactic foam
(Reproduced from Song et al. (2004b) with permission)

4.5.3.2 Elastic-plastic Foam

Due to the significant differences in the transmitted signals between brittle foams and elastic-plastic foams, the pulse shaping design for testing elastic-plastic polymeric foams is different from that for testing brittle foam described above.

Elastic-plastic polymeric foams are unique in their compressive stress-strain curves: elastic, cell collapsing, and densification stages. In addition, the low mass density and slow wave speed in the elastic-plastic polymeric foams result in drastically reduced wave impedance. Consequently, nearly all of the incident pulse is reflected back and the transmitted pulse is hardly recorded by regular resistor strain gages. In other words, the transmitted pulse has a negligible amplitude as compared to the incident pulse. In this case, a trapezoidal incident pulse is needed to produce constant strain rate on the specimen. The rise time of the trapezoidal pulse should be sufficiently long to allow the specimen to achieve stress equilibrium. In Kolsky-bar experiments on low-density polymeric foams, stress equilibrium becomes a more challenging condition to meet than constant strain-rate deformation. The foam specimen could collapse progressively from one end to the other end if the pulse shaping and specimen length are not carefully designed (Song et al. 2006c). The low initial loading slope (or long rise time) allows the specimen to have sufficient time to achieve uniform stress during the early stages of loading, thereby giving the specimen a chance for uniform deformation. To facilitate such a trapezoidal incident pulse with a low initial slope, both copper tubes and copper disks have been found to be effective serving as pulse shapers. In addition, the foam specimen is required to be thin but still needs to contain several cells along the thickness direction to make an effective representative volume. Due to small Poisson's ratios in such foams before the deformation reaches densification stage, the effects of radial inertia and interfacial friction are negligible in the dynamic compression experiments on these foams.

Figure 4.29 shows the typical pulses obtained from a Kolsky compression bar experiment on a 3.3-mm-thick, 12.2-mm-diameter rigid polyurethane foam specimen using a copper tube as pulse shaper (Song et al. 2005b). The 0.24×10^3 kg/m^3 foam material has an average closed-cell size of 200 μm, possessing at least 16 cells along the 3.3-mm-thick direction. As shown in Fig. 4.29, the rise time of the modified incident pulse is approximate 50 μs which is about five times longer than that (~10 μs) in a conventional Kolsky-bar experiment. In addition, the weak

transmitted signal was sensed by semiconductor strain gages (Fig. 4.29). Note that the transmitted signal shown in Fig. 4.29 is measured with semiconductor strain gages that are about 70 times higher in sensitivity than resistor strain gages. The actual amplitude of the transmitted signal is much lower than the incident pulse. In hence, the hardening portion behind the stress plateau in the transmitted signal does not significantly affect the design of incident pulse for the purpose of achieving constant strain-rate deformation. The dynamic stress equilibrium process monitored with quartz-crystal force transducers is shown in Fig. 4.30. Even though the pulse shaper was employed to reduce the initial incident loading rate, the stress in the specimen was not equilibrated until 50 μs after initial loading, resulting in unreliable stress-strain data for the first 50 μs. The first 50 μs period produces approximate 12% strain at this strain rate (4100 s^{-1}), which is beyond yield strain for the foam.

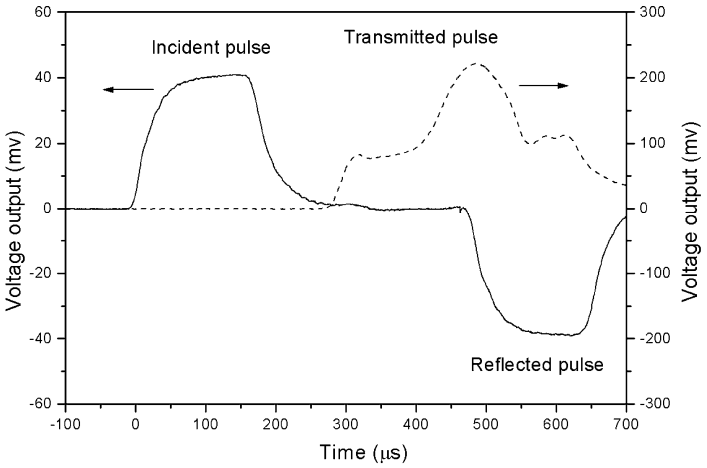

Figure 4.29 Kolsky bar experiment on a rigid polyurethane foam
(Reproduced from Song et al. (2005b) with permission)

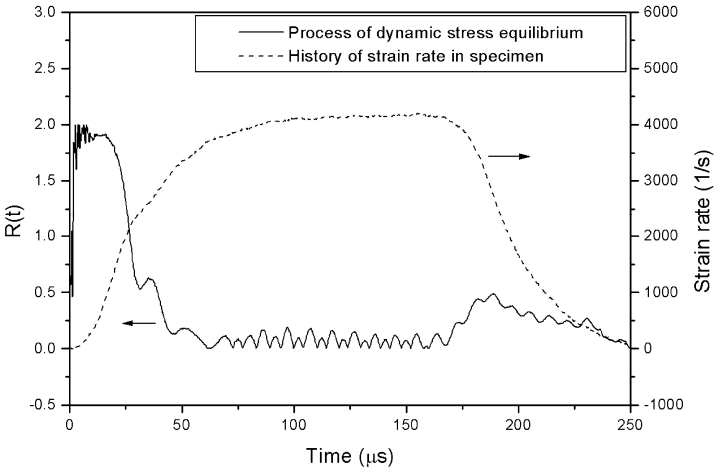

Figure 4.30 Dynamic stress equilibrium at the strain rate of 4100 s^{-1}
(Reproduced from Song et al. (2005b) with permission)

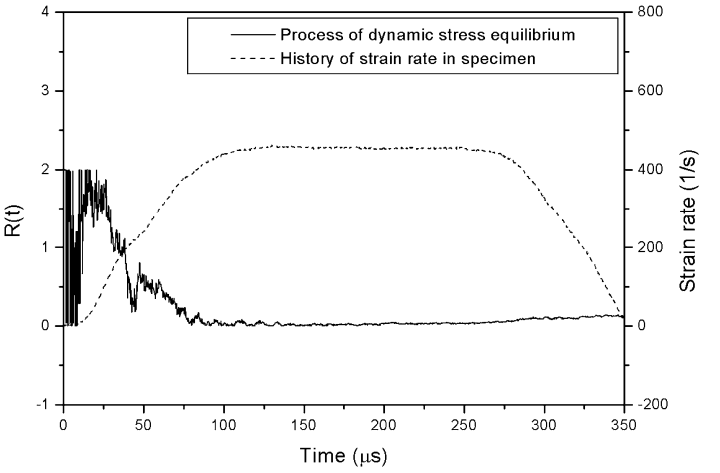

Figure 4.31 Dynamic stress equilibrium at the strain rate of 450 s^{-1}
(Reproduced from Song et al. (2005b) with permission)

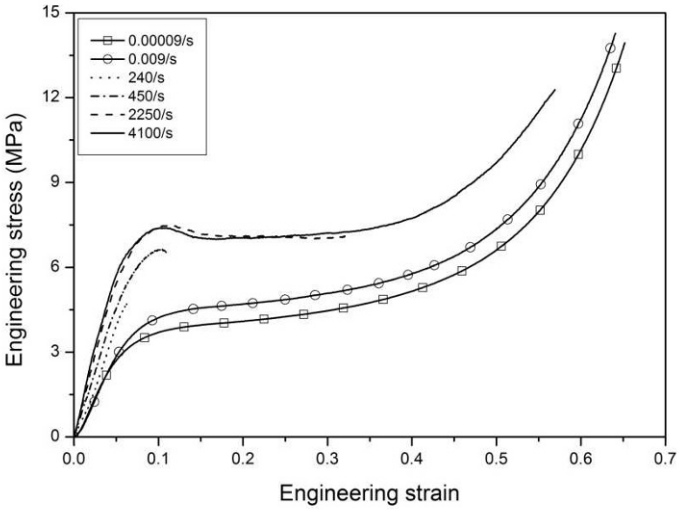

Figure 4.32 Compressive stress-strain curves of rigid polyurethane foam
(Reproduced from Song et al. (2005b) with permission)

In order to investigate the initial elastic and early collapse behavior of the material, the loading rate of the incident pulse needs to be further lowered. Under such loading pulses, the stress equilibrium in the specimen can be achieved at much earlier stages of the deformation, i.e., at strains much smaller than the 12% in the experiments described above. However, due to the focus on the initial stages of the experiment in design, the strain rate level will have to decrease inevitably such that the experiment does not rush through the initial states in the attempt to approach a higher strain rate. Figure 4.31 indicates that the stress equilibrium was achieved at 85 μs after initial loading, which corresponds to only 1.7% strain at the strain rate of 450 s^{-1}. As a result, most of the elastic portion and early collapse portion in the stress-strain curve for the foam material were obtained accurately under controlled testing conditions, but at relatively low strain rates.

Figure 4.32 shows the stress-strain curves of the polyurethane foam at various strain rates. The initial elastic and early cell-collapse data are not reliable for the experiments at the strain rates of 2250 and 4100 s^{-1} but are accurate when the strain rate is down to 240 or 450 s^{-1}.

The elastic and early cell collapse response has also been investigated for a polystyrene foam with the Kolsky-bar techniques (Song et al. 2005a). The polystyrene foam material was manufactured under precise control of processing parameters to produce relatively uniform microstructures (Wischmann and Assink 1977). The global foam material had fused hexagonal interfaces among the conjoint polystyrene beads with open cells approximately 50-60 μm in diameter inside the closed foam beads. The 0.4×10^3 kg/m^3 density foam material was made into cylindrical specimens with a diameter of 12.70 mm, but 3.0 and 6.0 mm in thickness for Kolsky-bar and quasi-static experiments, respectively. The compressive stress-strain curves of the polystyrene foam are shown in Fig. 4.33. As presented in Chapter 2.7, there is an upper limit of constant strain rate to obtain reliable stress-strain response for elastic specimens including the elastic-brittle foams as well as the early elastic and cell-collapse response for the elastic-plastic foam.

Due to very similar elastic-plastic characteristic, the above Kolsky compression bar technique is applicable to many other polymeric foam materials. The mechanical response, however, may quantitatively differ from material to material because of variations in the matrix material, cell structure, density, and so on.

Figure 4.34 shows the compressive stress-strain curves of a removable epoxy foam with a low density of 0.12×10^3 kg/m^3 at various strain rates (Song et al. 2007c). This removable epoxy foam is designed to be cast in molding applications but can be removed with mild solvent at 90ºC to allow for recovery of potted components when used as a potting material. The epoxy foam has a closed cell structure with an average cell size of ~200 μm in diameter. The epoxy foam specimen for Kolsky compression bar experiments had a diameter of 13.80 mm and a thickness of 2.70 mm. The high-rate stress-strain curves were experimentally obtained with the Kolsky-bar experiments following the same procedure as above. This removable epoxy foam exhibits similar stress-strain response of elasticity-plastic plateau-densification hardening stages, but with a lower cell-collapsing stress (plastic plateau) of approximately only 1 MPa. The plateau stress increases with increasing strain rate.

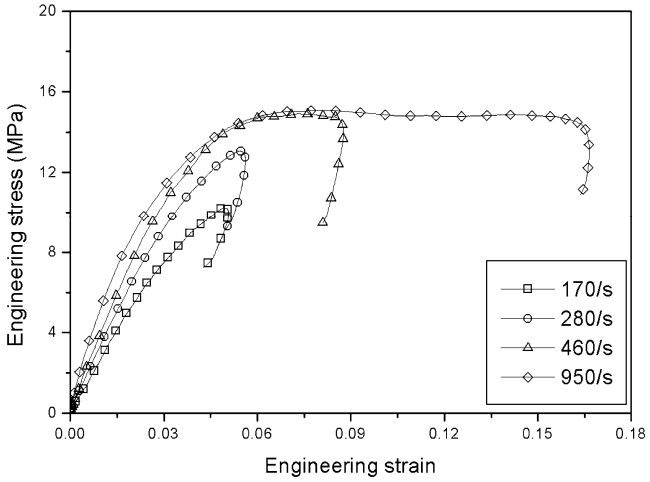

Figure 4.33 Elastic and early collapse response of polystyrene foam
(Reproduced from Song et al. (2005a) with permission)

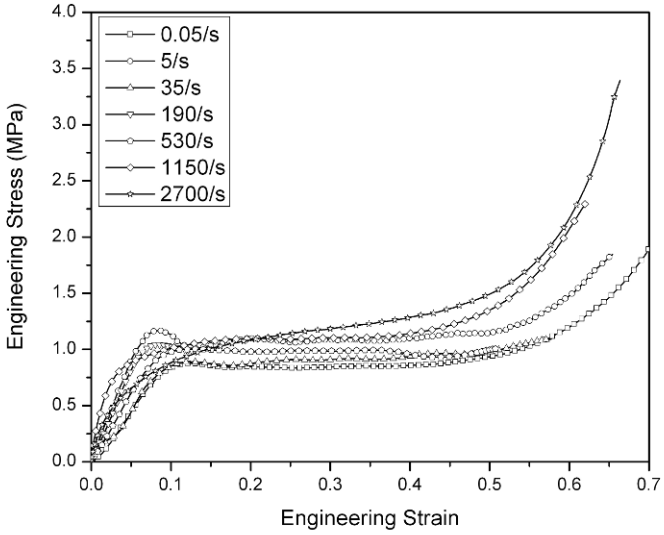

Figure 4.34 Compressive stress-strain curve of 0.12×10^3 kg/m^3 epoxy foam
(Reproduced from Song et al. (2007c) with permission)

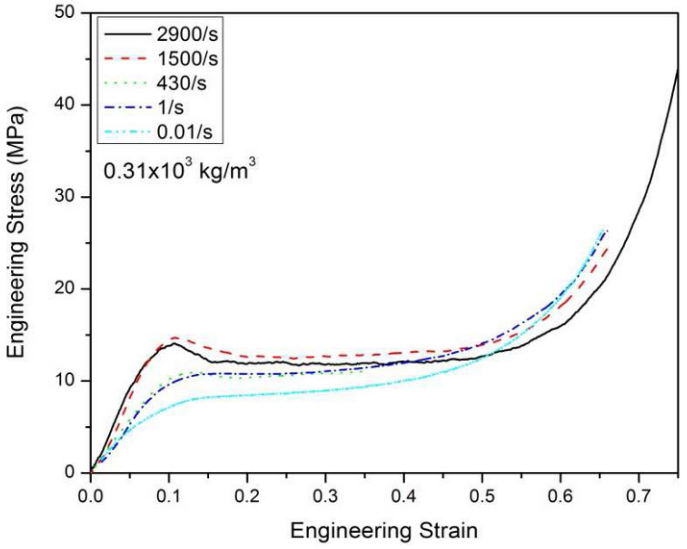
2900/s
1500/s
430/s
1/s
0.01/s
0.31x10^3 kg/m^3
Engineering Stress (MPa)
Engineering Strain
0
10
20
30
40
50
0.0
0.1
0.2
0.3
0.4
0.5
0.6
0.7

(a)

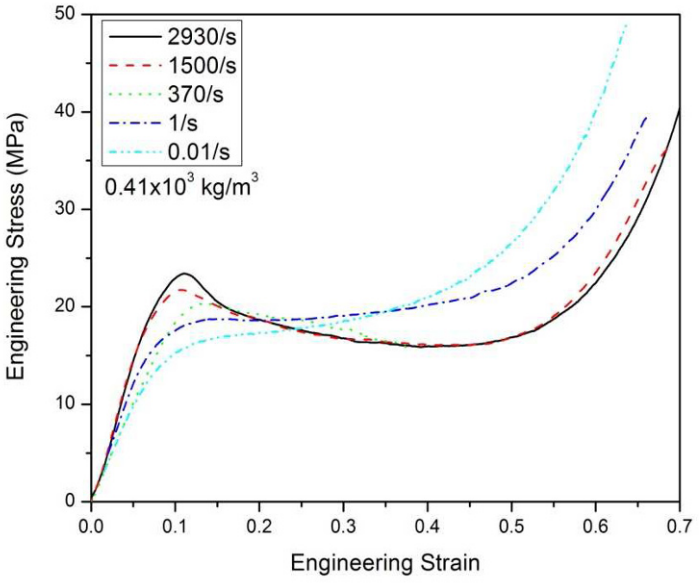
2930/s
1500/s
370/s
1/s
0.01/s
0.41x10^3 kg/m^3
Engineering Stress (MPa)
Engineering Strain
0
10
20
30
40
50
0.0
0.1
0.2
0.3
0.4
0.5
0.6
0.7

(b)

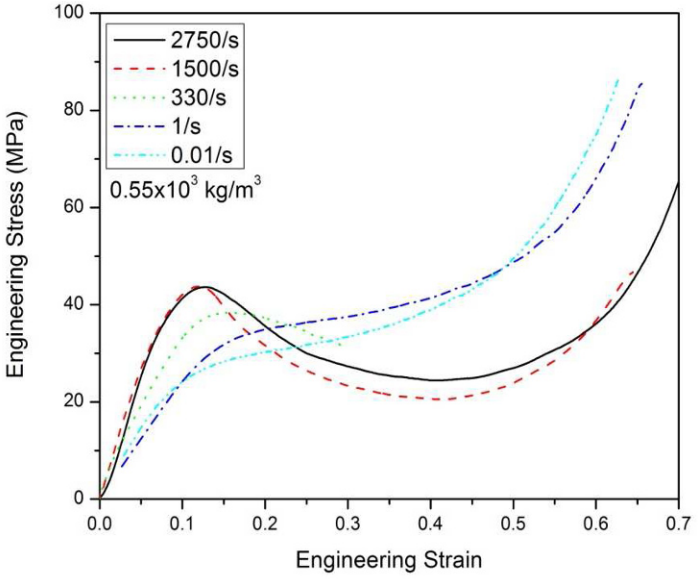

(c)

Figure 4.35 Compressive stress-strain curves of PMDI foam
(Reproduced from Song et al. (2009d) with permission)

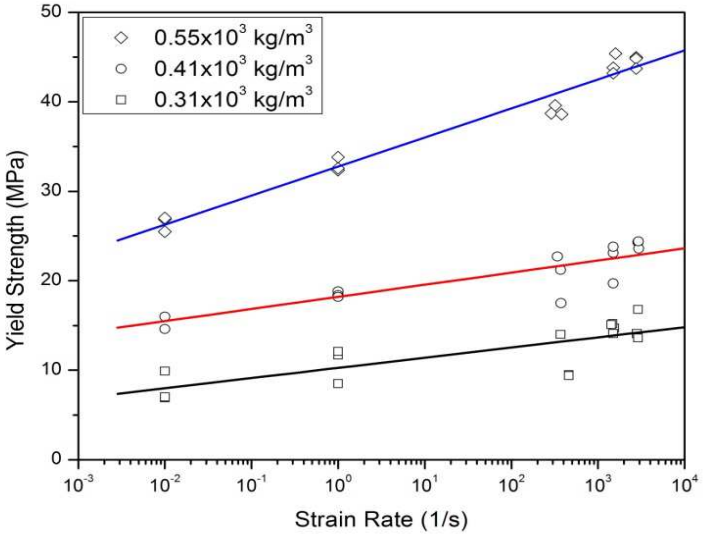

Figure 4.36 Effects of strain rate and density on compressive response of the PMDI foam
(Reproduced from Song et al. (2009d) with permission)

Foam density has been found to be a key parameter dominating the mechanical response. Figure 4.35 shows the compressive stress-strain response of a polymethylene diisocyanate (PMDI) based rigid polyurethane foam with three different densities (0.31×10^3, 0.41×10^3, and 0.55×10^3 kg/m^3) at various strain rates (Song et al. 2009d). The PMDI foam materials have a closed-cell structure with a cell diameter varying from 100 to 200 μm. The foam densities were produced by controlling the volume fraction of the cells. Besides the strain-rate effect, density also significantly affects the mechanical response, i.e., yield strength, of the foam materials, as shown in Fig. 4.36. For a foam material with a certain density, the yield strength linearly increases with the logarithm of strain rate. Furthermore, at a certain strain rate, the yield strength significantly increases with increasing foam density.

4.5.4 Biological Tissues

The Kolsky bar experimental technique for the engineered soft materials presented in previous sections has also been applied for dynamic characterization of soft biological tissues. In this section, we present experiments on muscles and brain tissues.

4.5.4.1 Porcine Muscles

Porcine muscles have similar issues as other soft materials under Kolsky bar loading in terms of inertia effects, interfacial friction and dynamic equilibrium. Therefore, thin specimens are necessary for axial stress equilibrium, hollow geometry is necessary to minimize radial inertia effects, the interfaces between the specimen and the bar ends need to be properly lubricated, and pulse shaping is needed to facilitate constant strain rate under dynamic equilibrium.

Unlike working with engineered materials, attention is paid to the specimen conditions when the biological tissues are subject to mechanical loading. For example, in order to closely simulate the actual response of “live” tissues in applications, the biological tissues need to remain “fresh” when subjected to mechanical loading. To preserve the tissues investigated in the porcine muscle examples given here, a modified Kreb

solution (136 m*M* NaCl, 4 m*M* KCl, 2.35 m*M* $CaCl_2$, 1 m*M* NaH_2PO_4, 0.85 m*M* $MgCl_2$, 12 m*M* $NaHCO_3$, 5 m*M* glucose, PH=7.4) bubbled with 95% O_2 and 5% CO_2 at the temperature of 39.2°C (López et al. 1988) was used.

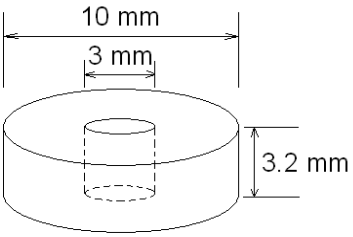

(a)

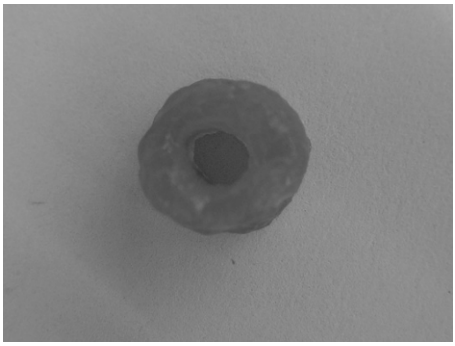

(b)

Figure 4.37 Schematic and photograph of annular porcine muscle tissue
(Reproduced from Song et al. (2007b) with permission)

The muscle tissues from a ham of a 5-month-old female swine have been characterized with the loading direction along and perpendicular to the fiber direction by using the Kolsky-bar techniques modified for soft material characterization (Song et al. 2007b). Immediately after the slaughter, the ham of the swine was marinated in the modified Kreb solution and then sliced into 3.2-mm-thick flat sheets along and perpendicular to fiber directions. The flat sheets were cut with 10.0-mm- and 3.0-mm-diameter trephine blades with sharp edges (to minimize damage to the neighboring tissues during cutting) to make annular tissue specimens with 10.0-mm outer diameter and 3.0-mm inner diameter for dynamic experiments. Figure 4.37 shows the schematic and photograph of the annular specimen. The annular specimen is not necessary for quasi-static experiments because the radial inertia is negligible when the loading rate is low. Conventional solid disk specimens with 3.2-mm in thickness and 10.0-mm in diameter were used for quasi-static experiments. The low strength of the soft tissue requires sufficient lubrication on the specimen ends. Vegetable oil was found to be excellent in lubricating soft biological tissues.

Due to extremely low strength in the biological tissues, the trapezoidal incident pulse is capable of producing constant strain rate deformation. However, the rise time should be sufficiently long to achieve dynamic stress equilibrium in such soft tissue specimens. In addition, the high-frequency oscillations that usually appear in conventional incident pulses should be eliminated. Such oscillations are significant enough to disturb the loading conditions on the tissue specimen with a very low strength. Either annealed copper disk or tube can serve as an effective pulse shaper.

The incident, reflected, and transmitted pulses from a typical high-rate experiment on the porcine muscle are shown in Fig. 4.38. It is observed that the spike appeared in the transmitted pulse in Fig. 4.4 disappeared in Fig. 4.38 after annular specimen geometry and proper pulse shaping were employed. The radial inertia has been minimized. This pulse shaping also minimizes the axial inertia, which was verified by comparing the forces measured with the quartz crystal force transducers at both ends of the specimen (Fig. 4.39). The axial inertia in the aluminum disk on top of the quartz crystals has been compensated by using three quartz transducers. The stress measurement by the quartz crystals may still contain noise-like oscillations in the loading histories due to the small amplitudes of the pulses. Figure 4.40 shows the strain rate and strain histories in the specimen indicating that the specimen deformed at a nearly constant strain rate of 3650 s^{-1}.

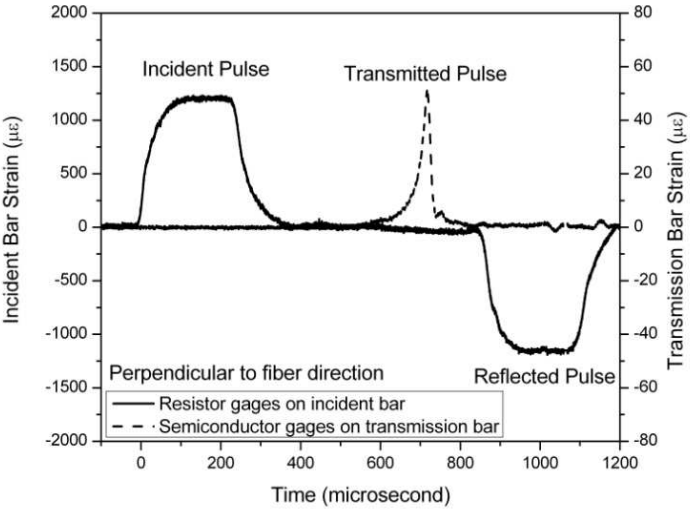

Figure 4.38 Kolsky bar experiment on porcine muscle tissue
(Reproduced from Song et al. (2007b) with permission)

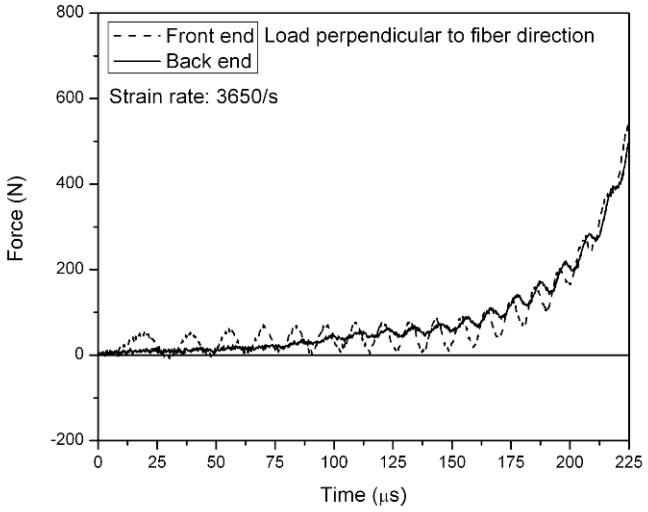

Figure 4.39 Stress equilibrium in the porcine muscle tissue specimen
(Reproduced from Song et al. (2007b) with permission)

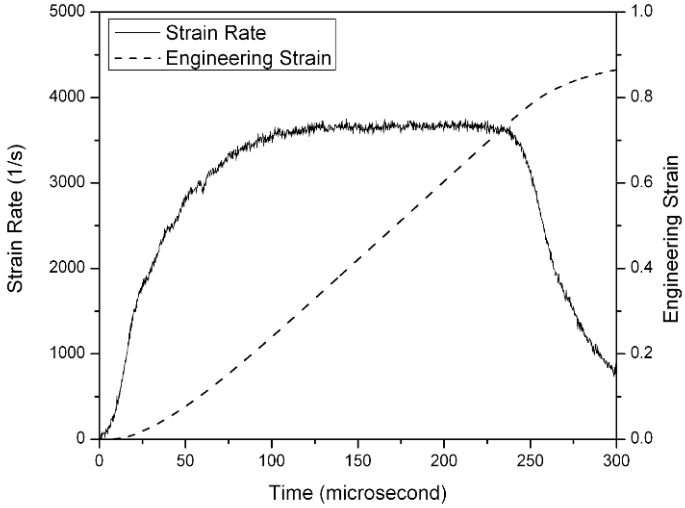

Figure 4.40 Strain rate and strain histories in the porcine muscle tissue specimen
(Reproduced from Song et al. (2007b) with permission)

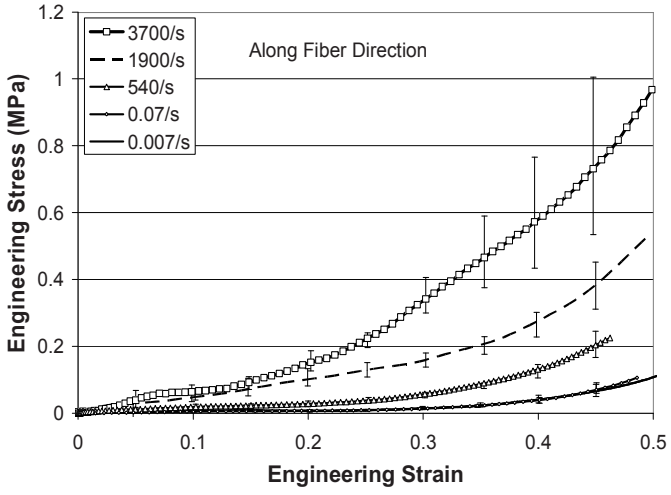

Figure 4.41 Compressive stress-strain curves of the porcine muscle tissue where loading is perpendicular to the fiber direction
(Reproduced from Song et al. (2007b) with permission)

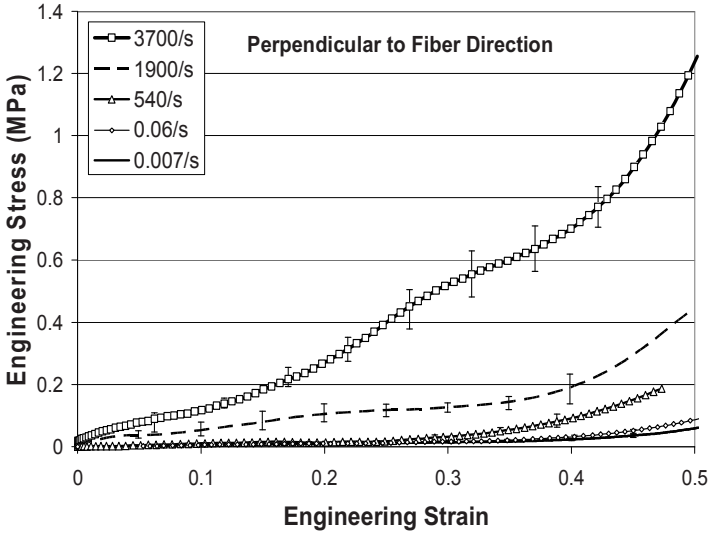

Figure 4.42 Compressive stress-strain curves of the porcine muscle tissue where loading is along the fiber direction
(Reproduced from Song et al. (2007b) with permission)

Figures 4.41 and 4.42 show the resultant compressive stress-strain curves of the porcine muscle tissues where the loading direction is along and perpendicular to the muscle fiber direction, respectively. In both Figs. 4.41 and 4.42, error bars were plotted on the mean stress-strain curves from several repeated experiments to show the level of data scatter under identical testing conditions. Regardless of loading direction, the stress-strain curves exhibit rubber-like mechanical characteristic: a toe region at the beginning, followed by a transitional non-linear response and then a strain-hardening behavior. Strain-rate effects are apparent in the porcine muscle tissue. However, the strain-rate sensitivity depends on the loading direction. The strain-rate sensitivity along the perpendicular direction is more significant than that along the fiber direction.

4.5.4.2 Brain Tissues

Similar experimental setup for the porcine muscle experiments was used to determine the dynamic responses of brain tissues (Pervin and Chen 2009). Using a similar experimental facility, the gray and white matters of fresh bovine brain tissues were characterized under compression to large strains over a strain rate range from 0.01 to 1800 s^{-1}. The white matter was examined both along and perpendicular to the coronal section for anisotropy characterization. Similar to the practice in porcine muscle experiments, a pulse shaper at the impact end of the incident bar is attached with vacuum grease to generate an initial ramp followed by a plateau to facilitate early dynamic stress equilibrium and constant strain rate in the specimen. However, the impact of the striker is at much lower velocities. In order to increase the amplitude of the transmitted signal from soft brain tissues, a hollow aluminum transmission bar was used, together with semiconductor strain gages on the transmission bar. Quartz-crystal force transducers were used to verify the dynamic equilibrium in the specimen. The transducer on the incident bar end has a three-quartz configuration to compensate the inertia brought by the introduction of the aluminum disk.

The experiments for this study were performed *in vitro* on bovine brain. The brain from a twenty-one-months-old steer was collected from a slaughter house a few minutes after the death of the animal. The tissue was preserved in artificial cerebrospinal fluid at 37°C. All the experiments were completed within eight hours postmortem. Annular specimens of outer diameter 10 mm, inner diameter 4.7 mm and thickness 1.7 mm were excised from sections of gray matter (frontal and parietal lobe) and white matter (corona radiata). The geometry of the specimens is the same as the muscle specimen shown in Fig. 4.37 except for the dimensional differences in thickness and inner radius. A thin layer of vegetable oil was applied on the interface between the specimen and bar end face to minimize friction. A thickness gage was used to set the specimen initial thickness individually to eliminate pre-stressing the specimen before dynamic loading.

The incident, reflected, and transmitted strain signals of a typical Kolsky-bar experiment on brain tissues at a strain rate of 1800 s^{-1} are shown in Fig. 4.43. The stress histories at the both end faces of the tissue specimen were measured by the quartz-crystal force transducers and compared for each experiment. The force histories were found to overlap

each other indicating dynamic equilibrium across the specimen thickness, as shown in Fig. 4.44.

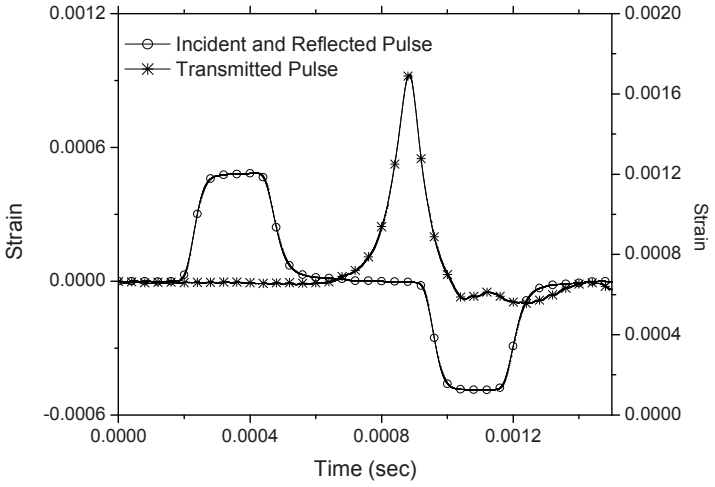

Figure 4.43 Strain signals from a Kolsky bar experiment on a brain tissue specimen
(Reproduced from Pervin and Chen (2009) with permission)

The resultant compressive stress-strain curves obtained on both gray and white matters are shown in Fig. 4.45. Due to significant difference in stress amplitude under quasi-static and dynamic loading, Fig. 4.45(a) shows the quasi-static stress-strain curves while dynamic stress-strain responses for both gray and white matters are shown in Fig. 4.45(b). Figure 4.45(a) also presents previous data for swine brain obtained by Miller and Chinzei (1997) for comparison purpose. For each strain rate, five experiments were repeated under the identical testing conditions. The results presented in Fig. 4.45 are mean data from 15 resultant data under identical testing conditions. Both gray and white matters exhibit similar characteristics: non-linear response with significant strain rate effects.

The stiffness significantly increases with increasing strain-rate. The mechanism behind the apparent rate effects is not completely understood. One possible factor is the change in damage/failure modes as the strain rate increases. Another possibility is the change in stress state under high rate loading due to the restrictions to the lateral motion of the soft brain tissue by radial inertia and/or friction. More experiments under other loading conditions need to be conducted to develop a comprehensive understanding of the behavior.

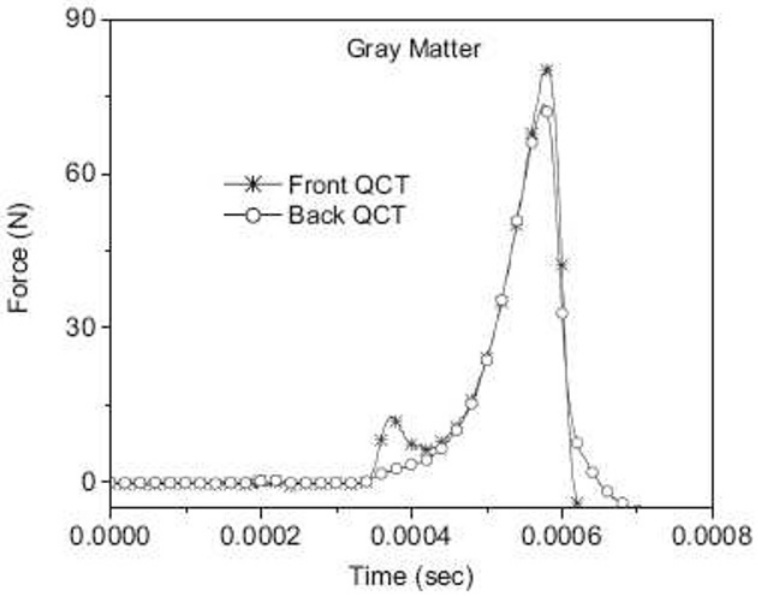

Figure 4.44 Dynamic stress equilibrium
(Reproduced from Pervin and Chen (2009) with permission)

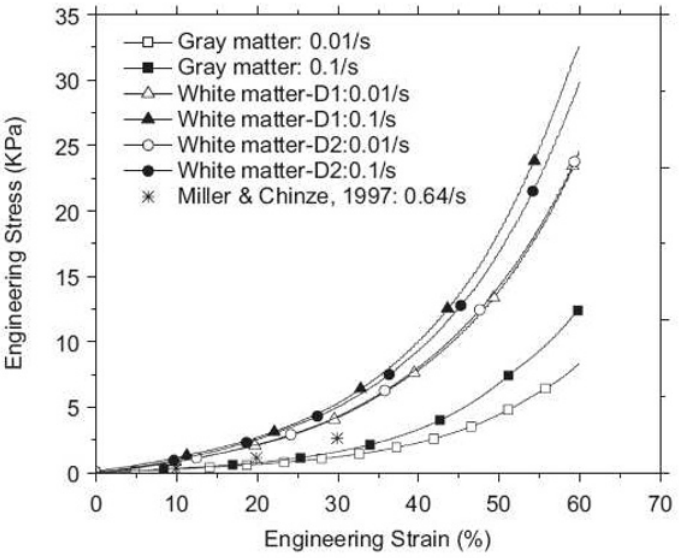

(a)

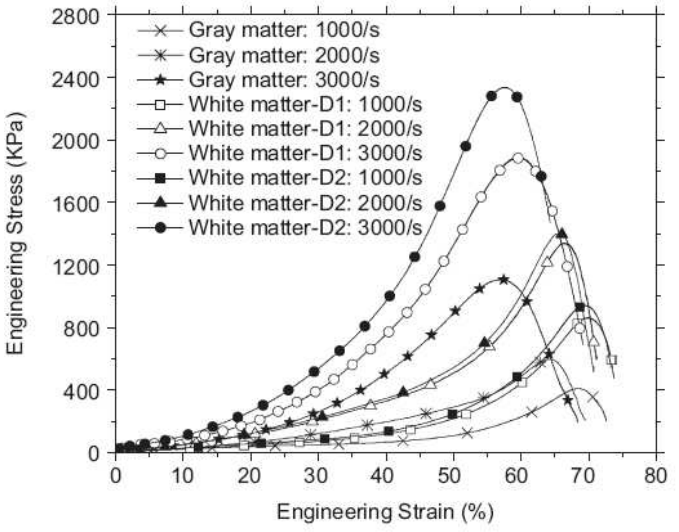

(b)

Figure 4.45 Compressive stress-strain curves of bovine brain tissues under (a) quasi-static and (b) dynamic loading conditions
(Reproduced from Pervin and Chen (2009) with permission)

Chapter 5. Kolsky Compression Bar Experiments on Ductile Materials

Ductile materials initially deform elastically and then plastically to large strains. The material stiffness is quite different in elasticity and plasticity. Experiment design may be focused on the response in either elasticity or plasticity, but mostly in the latter. This chapter describes the distinct characteristics of ductile materials, introduces a compound pulse shaper to maintain constant plastic strain rates. Examples are then given with the specimen materials being metals, a shape-memory alloy, an alumina particle-filled epoxy, and a lead-free solder.

5.1 Issues in Kolsky-Bar Experiments on Ductile Materials

Traditionally, the Kolsky bar has been widely used to characterize the high-rate flow behavior of ductile metals. When the specimen enters plastic deformation, it can deform to large strains at high strain rates. However, it has been recognized in the past decades that the Kolsky bar cannot obtain valid elastic response of ductile materials (Gray 2000). For example, the rate-independent moduli of elasticity of alloys measured from Kolsky-bar experiments are usually only 30% to 50% of the values obtained from quasi-static experiments. The reason for the erroneous elasticity measurement is due to the inaccurate measurement in specimen deformation. In Kolsky-bar experiments, it is typically more challenging to measure the specimen deformation than the stress, particularly when the specimen is subjected to small deformation. Many traditional alloys have been recognized that their elastic moduli are independent of strain rate. The inaccurate measurement in elastic response may not be serious for these materials. However, more attention should be paid to the ductile materials that exhibit significant strain-rate sensitivities even in elastic response, for example, shape memory alloys. Moreover, the elastic response is required to be accurately measured for those materials whose responses are not known yet.

There are three sources that may lead to inaccurate measurements in specimen deformation. The first one is wave dispersion. As discussed in Chapter 2.1, the stress wave dispersion results in different signals at the specimen/bar end interfaces from those recorded by the strain gages in the middle of the bars. Without dispersion correction, the specimen strain

W.W. Chen and B. Song, *Split Hopkinson (Kolsky) Bar: Design, Testing and Applications*, Mechanical Engineering Series, DOI 10.1007/978-1-4419-7982-7_5,

directly calculated with the signals from the strain gages deviates from the actual strain to which the specimen is subjected. The deviation is so significant, in comparison to the elastic strain in the specimen, that the measured modulus is erroneous, usually smaller, even though the stress measurement is accurate (Zhao and Gary 1996). Correcting the stress wave dispersion with either numerical method or physical pulse shaper can improve the accuracy of the elastic response for ductile materials. However, wave dispersion correction alone is not sufficient to accurately determine the elastic moduli. At the beginning stages of the high-rate loading, more complications are encountered in the accurate determination of strain history.

In a Kolsky-bar experiment, it takes only a few microseconds for the ductile specimen to yield due to its small yield strain. The stress may not be in equilibrium yet within such a short duration, particularly when the initial rate of loading is high. The non-equilibrated stress state in the specimen results in non-uniform deformation through its thickness direction. Taking an average in both stress and strain over the specimen length, as expressed by (1.7) and (1.15), may yield smoother results. However, this is artificial and does not reflect the actual loading and deformation states in the specimen. In order to achieve the specimen stress equilibrium when the strain is still low, the initial rate of loading must be low. A trade off of this low rate of initial loading is to sacrifice the strain rate. For example, the strain rate in elasticity is below 100 s^{-1} to obtain accurate elastic response for elastic-plastic alloys (Chen et al. 2003).

As presented in Chapter 2.5, pulse shaping makes Kolsky-bar experiments more controllable for not only stress equilibrium but also constant strain-rate deformation in specimen. The constant strain-rate deformation is desired for the specimen even under elastic deformation, particularly when the specimen material is highly strain-rate sensitive, such as shape memory alloys. Similar to the brittle material characterization discussed in Chapter 3 where there is a limit in achievable constant strain rate, the ductile specimen may yield before the strain rate reaches a constant because it takes time for the specimen to accelerate from rest to the high strain rate. Strain is accumulated in the specimen during this acceleration process. This also limits the maximum achievable elastic strain rate in Kolsky-bar experiments on ductile materials. When the specimen deforms beyond its elastic limit, its stiffness decreases drastically. This results in a sudden increase in strain rate. When ductile materials are investigated at high rates, the “strain rate” is usually referred to the later plastic strain rate, which is typically 1-2 orders higher in amplitude than elastic strain rate achieved in the same experiment.

Another source for erroneous measurement in elastic response is the possible indentation to the bar ends by a stiff specimen (Safa and Gary

2009). This indentation results in severe non-planar stress waves. Furthermore, the particle velocity at the incident bar/specimen interface is higher; whereas, the particle velocity at the specimen/transmission bar is lower, than those the specimen actually experiences. Consequently, the calculated strain rate and strain in the specimen becomes higher, which leads to lower modulus of elasticity. In order to prevent such an indentation when characterizing high-strength ductile materials, stiff platens are needed, as discussed in Chapter 3.

Before yielding, most ductile materials behave in the same manner as brittle materials with high stiffness. The Kolsky bar method for brittle material characterization is applicable in the characterization of the elastic response of ductile materials. After yielding, the tangential modulus in the stress-strain curves for ductile materials drops sharply in plastic deformation. The linear ramp pulse for brittle materials is not applicable any longer. Instead, the profile of the incident pulse needs to be further modified according to the work hardening response of the ductile material under investigation. If the material possesses significant work hardening response, the traditional flat-top loading pulse is typically unable to maintain a constant strain rate at large strains. A typical set of oscilloscope records from conventional Kolsky-bar experiment on a work hardening ductile material are shown in Fig. 5.1 (Chen et al. 2003). The incident pulse needs to increase with time to maintain a constant engineering strain rate in the plastically deforming specimen. In addition to the modification to the shape of the incident pulse, the amplitude of the incident pulse needs to be sufficiently high to compress the ductile specimen at high strain rates. This brings another challenge in pulse-shaping design where a soft material such as annealed copper is usually employed as the pulse shaper.

If, in addition to the loading stage, the unloading process needs to be controlled, the pulse in the unloading part must be shaped accordingly. A typical example of this class of experiments is the characterization of the dynamic stress-strain loops of shape-memory alloys. As can be imagined, these experiments are more challenging to perform.

Since ductile materials are capable of large deformation, the specimen will significantly expand along lateral directions when it is subjected to large deformation under axial compression. At large deformation, the interfacial friction at the bar end/specimen interfaces may restrict the lateral expansion of the specimen. In this case, the specimen under large deformation is in a shape of barrel, revealing three-dimensional stress state at the specimen ends. Therefore, the interfacial friction should be minimized in Kolsky-bar experiments on ductile materials to large deformation.

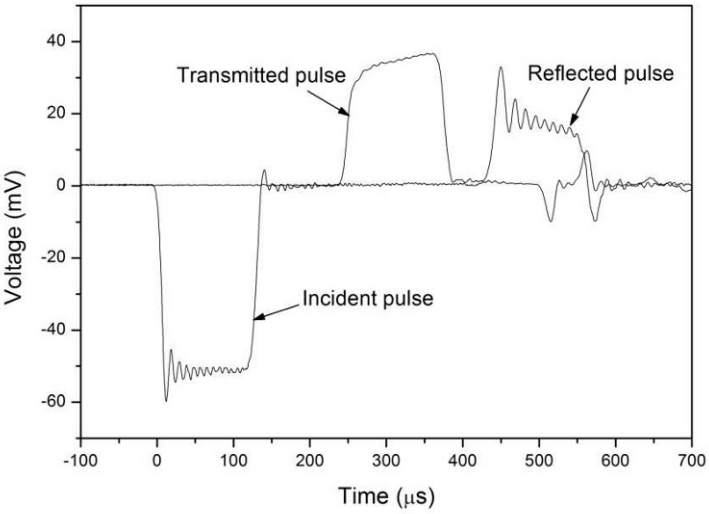

Figure 5.1 Typical oscilloscope records in a conventional Kolsky bar experiment on a work-hardening material *(Reproduced from Chen et al. (2003) with permission)*

5.2 Pulse Shaping

In order to achieve constant strain rates in Kolsky-bar experiments on ductile materials, the incident pulse should have a profile similar to the transmitted pulse which is usually a representative of stress response of the specimen material. Trial experiments are needed to provide approximate information of such a stress response, giving a starting point in regard to the profile of the incident pulse needed for facilitating constant strain rate. For the ductile materials with work hardening behavior, the incident pulse is typically of similar work hardening profile but with a higher amplitude. As mentioned in the previous section, the specimen is desired to be stress equilibrated as soon as possible to obtain valid elastic response of the specimen material. The initial rate of loading in the incident pulse should be low. Therefore, the incident pulse needs to have a

profile as the one illustrated in Fig. 5.2 for characterizing most work hardening ductile materials.

A single annealed copper disk is not sufficient to serve as the pulse shaper to produce a high-amplitude incident pulse as illustrated in Fig. 5.2 due to the low yield strength of copper. The dual pulse shaping technique as shown in Fig. 2.16 is needed for ductile material characterization. The dual pulse shaping generally consists of a soft pulse shaper, such as copper, stacked on a second pulse shaper made of a hard ductile material such as steel. The striker impacts on the copper disk first. Due to its low strength and high ductility, the copper disk is extensively compressed, producing a nearly linear but low-amplitude pulse. The rate of loading is relatively low at this stage. This produces the early portion in the incident pulse. When the copper disk is subjected to continuing compression, it eventually becomes extremely thin and nearly incompressible. The second ductile pulse shaper, e.g., steel, starts to play its role in shaping the incident pulse. Due to its typical elastic-plastic characteristic, the pulse transmitted through the second pulse shaper possesses a similar linear elasticity followed by a work hardening response. The amplitude depends on the flow strength and dimensions of the second pulse shaper, as well as the striking speed. In other words, the second pulse shaper dominates the incident pulse; whereas, the copper pulse shaper only lowers the rate of loading for the initial portion in the incident pulse. Combination of the material and dimensions of the first pulse shaper, as well as striking speed, is used to determine the initial loading rate of the incident pulse so that the specimen can be in stress equilibrium quickly. The material for the second pulse shaper is selected to have similar plastic flow behavior as the specimen material under investigation so that constant strain rate is achievable. When unloading stress-strain response of some ductile materials is investigated, reverse pulse shaping technique in association with momentum trap described in Fig. 2.22 should be employed to unload the specimen at the same constant strain rate as that in the loading portion. The reverse pulse shaping design depends on the unloading response of the specimen material, which is case by case.

It is noted that above strain rate refers to engineering strain rate. In some experiments, constant true strain rates, instead of constant engineering strain rates, are desired. Facilitating constant true strain rates is much more challenging in ductile material characterization. True strain (ε_T) can be calculated from engineering strain (ε_E) assuming the symbol takes positive in compression,

$$\varepsilon_T = -\ln(1-\varepsilon_E) \tag{5.1}$$

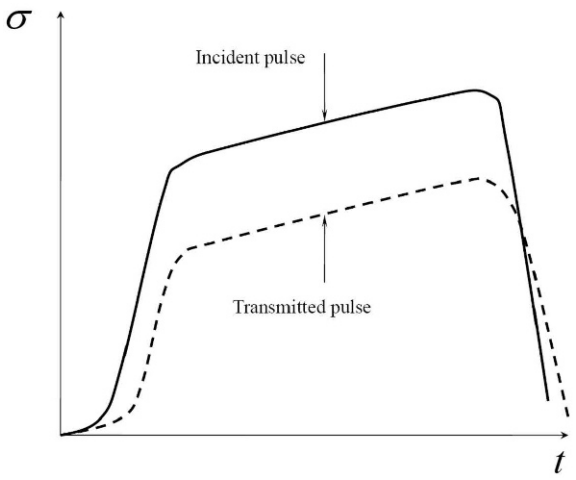

Figure 5.2 Illustration of pulse shaping design for ductile materials

Differentiating (5.1) with respect to time yields true strain rate

$$\varepsilon_T = \frac{\varepsilon_E}{1-\varepsilon_E} \tag{5.2}$$

Equation (5.2) can be rewritten as the following differential equation in terms of engineering strain,

$$\varepsilon_E + C\varepsilon_E = C \tag{5.3}$$

where $C = \varepsilon_T$ is a constant. Considering the initial condition,

$$\varepsilon_E\big|_{t=0} = 0 \tag{5.4}$$

Equation (5.3) has the solution,

$$\varepsilon = 1 - e^{-Ct} \tag{5.5}$$

or

$$\varepsilon_E = C \cdot e^{-Ct} \tag{5.6}$$

Since the reflected pulse represents engineering strain rate under stress equilibrium in a Kolsky-bar experiment, Equation (5.6) indicates that the reflected pulse should be in the form of exponential attenuation, as illustrated in Fig. 5.3, to facilitate constant true strain rate in specimen. Therefore, the pulse shaper should be carefully design to properly modify the incident pulse so that the reflected pulse schematically illustrated in Fig. 5.3 is produced. One approach is to use a tapered striker (Casem 2010).

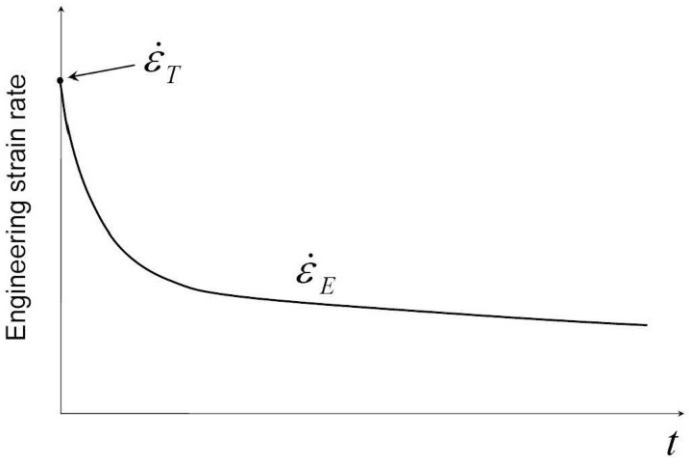

Figure 5.3 Engineering strain-rate history for constant true strain rate

5.3 Experiment Design for Ductile Materials

The experiment design for characterizing ductile materials depends on the specimen response, the desired testing conditions, and the strain range of interest. If the specimen material does not work-harden significantly and the main interest is to determine the dynamic flow stress as a function of plastic strain rate, conventional Kolsky bar experiments are very close to achieve the desired testing conditions on the specimen (constant plastic strain rate under dynamic equilibrated stress). The only undesired characteristic in the wave form is wave dispersion. With the knowledge of pulse shaping, a thin and small disk of a soft ductile material placed on the impact end of the incident bar can effectively minimize the wave dispersion. The specimen is then subjected to a well defined loading history. Changing the striking velocity will vary the strain rate in the specimen; whereas, changing the striker length varies the maximum strain in the specimen with a given thickness. It should be reminded that, in such experiments, the specimen is still in stress equilibrium process when the strains are small, the data at small strains may not be reliable. However, if the pulse shaper is properly designed so that stress equilibrium is achieved in the specimen at very early stages of loading, the elastic and early yielding response for the ductile specimen can be obtained accurately.

If the interest is on elastic and early plastic deformations, the response of the specimen is similar to that of a brittle material. Consequently, the pulse shaper design should be similar to the design for brittle materials. For those materials possessing strain-rate sensitivity in elasticity, the strain during initial strain acceleration should be small such that the most portion in elastic response and the following early plastic behavior are determined under valid conditions. As pointed out in Chapter 2.7, there exists a limit for achievable strain rate to determine the valid elastic response of the specimen material. It is noted that, if the elastic response of the specimen material is not sensitive to strain rate, such as most alloys, the initial strain acceleration does not affect the measurement of elastic response as long as the stress equilibrium is achieved. However, it is desirable that the strain rate reaches a constant before the specimen yields.

If the material has significant work hardening, dual pulse shaping is needed to facilitate constant strain rate and stress equilibrium. In the following section, we will present examples illustrating this case.

Most ductile materials can yield locally and are thus not very sensitive to stress concentrations. The hard platens and universal joints used in the experiments on brittle materials are typically not needed in the experiments, particularly when the ductile materials under investigation are more compliant than the bar material. However, when characterizing the ductile materials with high stiffness and strength, the platens are needed to obtain high-quality results and to protect the bar ends from indentation.

By contrast, some ductile materials, e.g., lead, may yield at low stress. The design of experiments for characterizing such materials is similar to that for soft materials. We will give an example of solder characterization in the last section of this Chapter.

5.3.1 Metals

We now take an example of characterizing the compressive response of 4340 steel alloy hardened to R_c45. The striker, incident, and transmission bars were 19.05-mm diameter C350 maraging steel. The incident and transmission bars had lengths of 3050 and 1525 mm, respectively, and the bar strain gages were located at 1670 mm from the impact end of the incident bar and at 245 mm from the specimen/bar interface on the transmission bar. The 4340 R_c45 specimen had a diameter of 6.35 mm and, to achieve a higher strain rate, a length of 3.11 mm.

A dual pulse shaping presented in Chapter 2.5 was employed. The dual pulse shaper consists of an annealed C11000 copper stacked on a 4340 R_c30 steel. Figure 5.4 shows the incident, reflected, and transmitted signals from such a dual-pulse-shaped experiment (Song et al. 2007a). The copper disk is 2.5 mm in diameter and 1.8 mm in thickness while the steel disk is 10.4 mm in diameter and 11.4 mm in thickness. The striker velocity was 29.95 m/s.

As seen in Fig. 5.4, the dual pulse shaping technique produced an incident pulse which has similar work hardening profile to the transmitted pulse. This is mainly contributed by the hard steel pulse shaper for the purpose of facilitating constant strain rate. A long toe region at the early stage of the incident pulse is also observed, which is the result of employing the soft anneal copper shaper. The initial slow rise in the incident pulse helps the specimen to achieve stress equilibrium quickly. In order to facilitate different strain rates, the striking velocity should vary, together with the dimensions of the copper and steel pulse shapers.

Figure 5.5 shows the incident pulses for different strain-rate characterization. The three incident pulses have similar profiles but different amplitudes, facilitating three different constant strain rates. Figure 5.6 shows the corresponding strain-rate histories. The strain rates obtained in the three experiments are nearly constants with different values, as observed in Fig. 5.6. The oscillations on the reflected pulses likely come from the high hardness of the specimen material. The strain rates can be calculated from averaging the oscillations in the strain-rate histories or the slope of its time integration (strain history).

Take an example of 1700 s^{-1} shown in Fig. 5.4, an average strain rate during the plastic flow strain rate of 1700 s^{-1} was measured from the slope of the strain-time curve over a time interval of 80 μs to 180 μs, as shown in Fig. 5.7 (Song et al. 2007a). At about 180 μs, the incident signal decays and the specimen begins to unload elastically. The stress comparison at both ends of the specimen is shown in Fig. 5.8 (Song et al. 2007a). The stress at the front end of the specimen is calculated using the difference in the incident and reflected strains (1.8), and the stress at the back end is calculated using the measured transmitted strain (1.9). The interface stresses are in reasonably good agreement, which implies that the specimen is nearly in dynamic stress equilibrium.

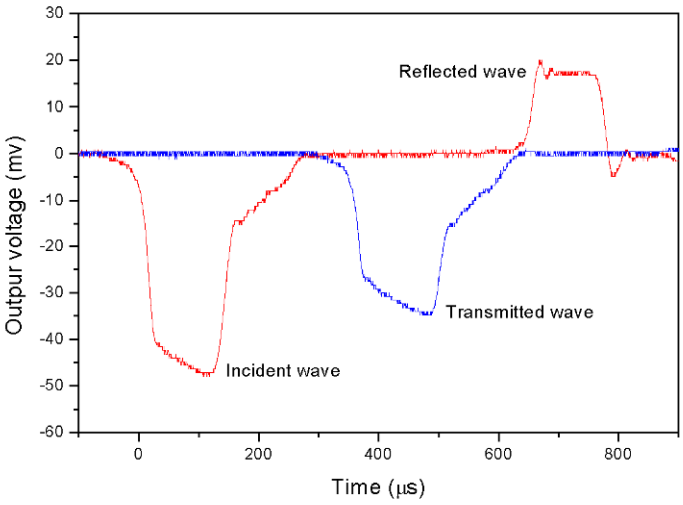

Figure 5.4 Experimental records of an experiment on 4340 steel
(Reproduced from Song et al. (2007a) with permission)

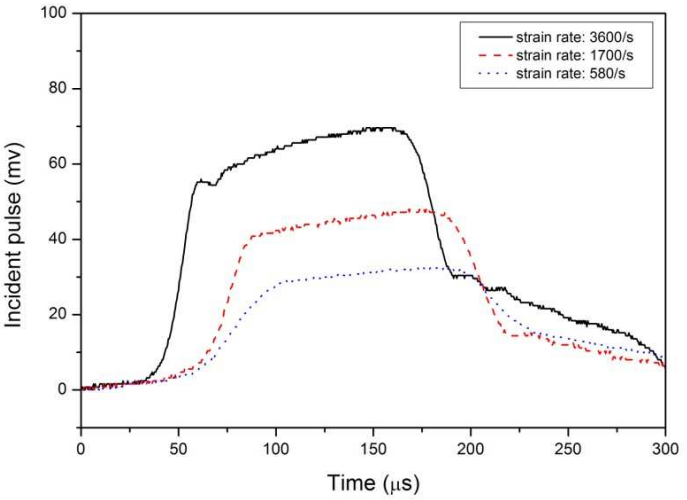

Figure 5.5 Pulse shaped incident pulses at various strain rates

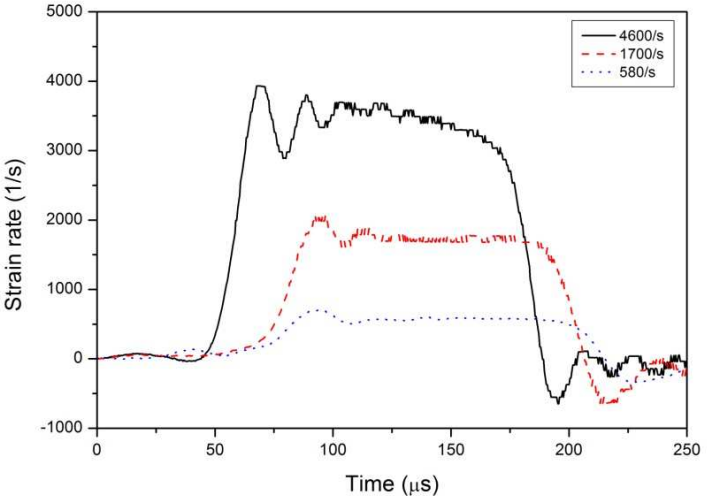

Figure 5.6 Strain rate histories

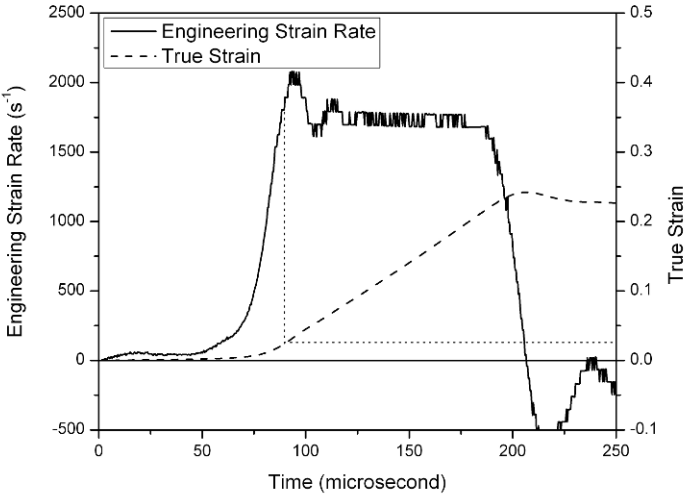

Figure 5.7 Time histories of strain rate and strain in the specimen
(Reproduced from Song et al. (2007a) with permission)

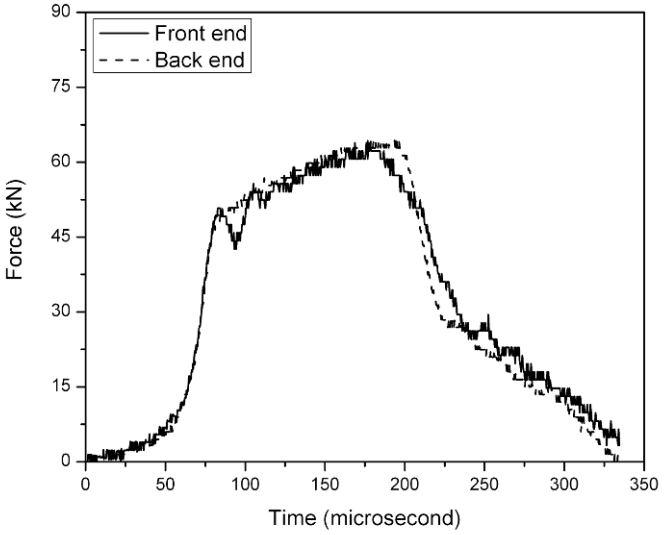

Figure 5.8 Comparison of stress histories at both ends of the specimen
(Reproduced from Song et al. (2007a) with permission)

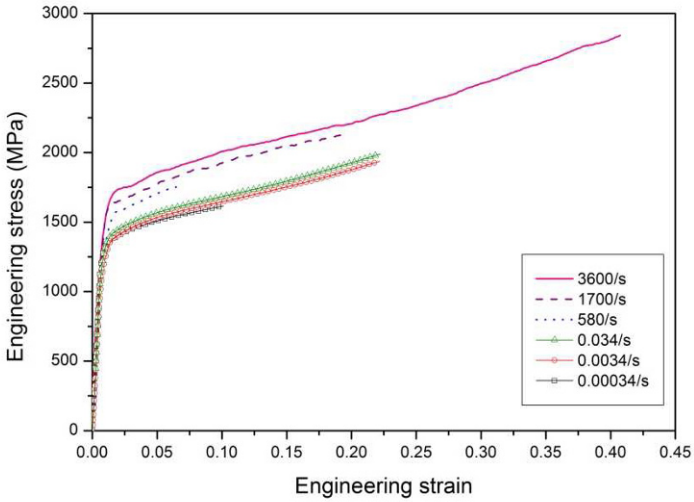

Figure 5.9 Engineering stress-strain curves of 4340 R_c45 steel
(Reproduced from Song et al. (2007a) with permission)

Figure 5.9 shows engineering compressive stress-strain curves of 4340 R_c43 steel at quasi-static and dynamic strain rates (Song et al. 2007a). The material exhibits linear elasticity followed by work hardening behavior with significant strain-rate effect. However, when the specimen is subjected to large deformation, engineering measurement may lack of interpretation of actual material response. Assuming the material is incompressible, the corresponding true stress-strain curves are shown in Fig. 5.10 (Song et al. 2007a). The true stress-strain curves show nearly perfect flow behavior. Strain-rate effect is still significant. At high strain rates, the strain accumulated within the strain acceleration stage may be over the yield strain. This results in relatively lower flow stress before the strain rate achieves the constant, as circled in Fig. 5.10. In order to determine the actual flow stress at the early stage, an analytical model was used to indirectly approach the early flow stress including the yield strength (Song et al. 2007a).

As shown in Fig. 5.10, the true stress-strain curves do not exhibit significant work hardening behavior. Instead, the stress softening is observed at high strain rates. This is due to the adiabatic temperature rise in the specimen during dynamic loading. A miniature thermocouple was

employed to measure the temperature rise in the specimen subjected to high-rate loading. The temperature rise histories in the specimens subjected to two different strain-rate loadings (1700 and 3600 s^{-1}) are shown in Fig. 5.11. The temperature rise softened the specimen, off-setting the work hardening. As an example, the true stress even becomes decreasing at high strain rates due to the significant temperature rise at large strains, as shown in Fig. 5.10.

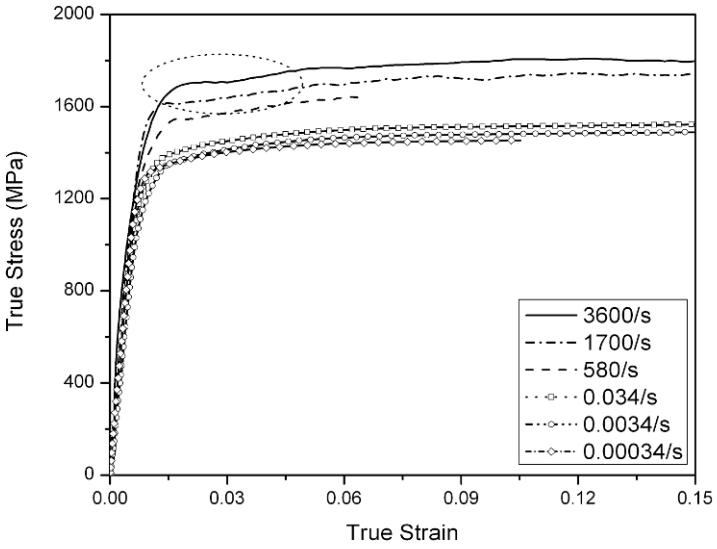

Figure 5.10 True stress-strain curves of 4340 R_c45 steel
(Reproduced from Song et al. (2007a) with permission)

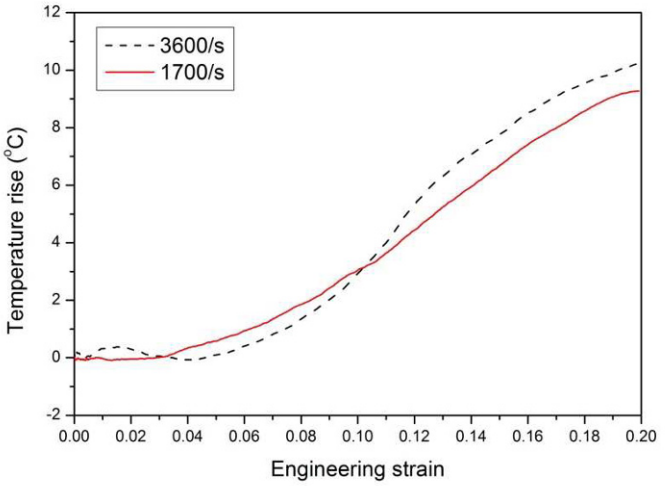

Figure 5.11 Temperature rise in the specimens at two different strain rates

When the specimen is subjected to high-rate loading, part of the produced plastic work at large deformation converts into heat in the specimen, resulting in temperature rise within the short loading duration. The fraction of the plastic work converted into heat can be estimated with the following equation (Hodowany et al. 2000),

$$\beta = \frac{\rho_s c_s \theta}{\sigma_T \varepsilon_{T,p}} \tag{5.7}$$

where β is the fraction of plastic work converted into heat; c_s is the specific heat of specimen material; θ is temperature-rise rate; and $\varepsilon_{T,p}$ refers to true plastic strain rate that can be calculated from engineering strain rate and strain with (5.2). Considering the specimen material is incompressible, the true stress (σ_T) in (5.7) can be calculated from engineering stress,

$$\sigma_T = (1 - \varepsilon_E)\sigma_E \tag{5.8}$$

The symbol for both stress and strain takes positive in compression here. Take an example, the values of parameters in (5.7) are listed in Table 5.1. The value of β is calculated as 0.76 with (5.7), indicating 76% of plastic work was converted into heat during the loading at the average true plastic strain rate of 1840 s^{-1}.

Table 5.1 Values taken for the parameters in (5.7)

Parameter	Value
ρ_s	7850 kg/m^3
c_s	477 J/kgK
θ	6.18×105 K/s
σ_T	1660 MPa
$\varepsilon_{T,p}$	1840 s^{-1}

With the use of dual pulse shaping technique, valid measurements of elastic and early plastic behavior can be obtained. We will give more examples showing the dual pulse shaping technique for ductile material characterization.

We now present the experiments on 1046 hot-rolled steel and 6061-T6 aluminum. Both steel and aluminum specimens had a common geometry with a length of 4.41 mm and a diameter of 8.88 mm. The dual pulse shaper consists of a half-hardened 1046 mild steel disk and an annealed *C*-11000 copper disk. The steel end of the dual pulse shaper is attached to the incident bar and the striker impacts the copper end.

Figure 5.12 shows the incident, reflected, and transmitted signals recorded from a typical experiment on the 1046 steel (Chen et al. 2003). With pulse shaping, the incident pulse was modified to produce a re-

flected signal with a nearly flat top that indicates a constant strain-rate history in the specimen. Furthermore, there is a small amplitude precursor ahead of the main reflected signal. Detailed data reduction reveals that this corresponds to the elastic deformation; whereas, the main reflected signal corresponds to the dynamic plastic flow in the specimen. During the elastic deformation, the specimen is stiff and deforms at a much lower strain rate. The details of this initial plateau in the reflected signal corresponding to the elastic deformation in the specimen are shown in Fig. 5.13 (Chen et al. 2003).

When the stress exceeds the dynamic yield strength, the stiffness of the specimen decreases significantly due to plastic flow, and this causes a much higher strain rate in the specimen. We note that the dynamic yield point is located at the transition between elastic and plastic strain response regions and the exact strain rate at dynamic yielding is actually not well defined. Figure 5.14 shows the dynamic compressive stress-strain curves from the experiments with and without pulse shaping at a close strain rate. The comparison shows that the difference in the elastic response is significant. The two curves start to merge after about 4% of strain.

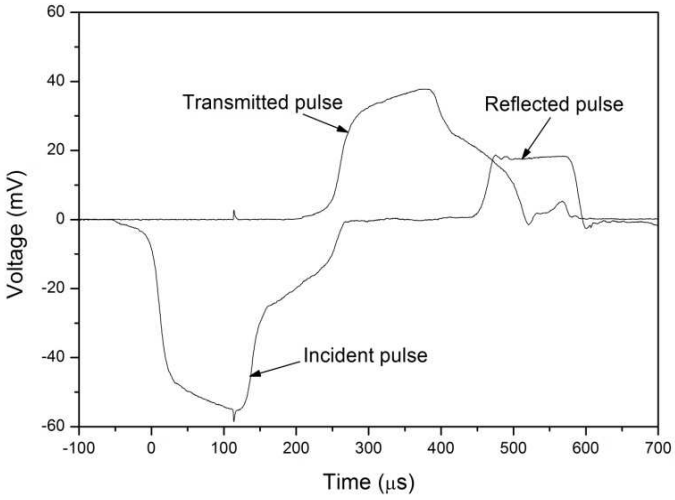

Figure 5.12 Oscilloscope records in a Kolsky bar experiment on 1046 steel
(Reproduced from Chen et al. (2003) with permission)

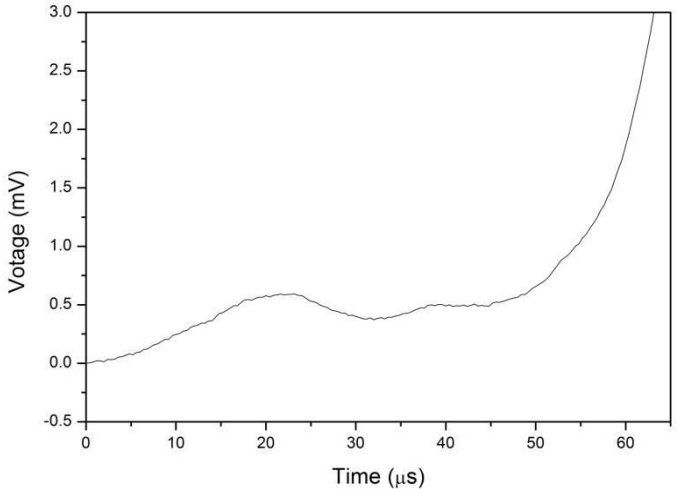

Figure 5.13 Reflected signal corresponding to elastic deformation
(Reproduced from Chen et al. (2003) with permission)

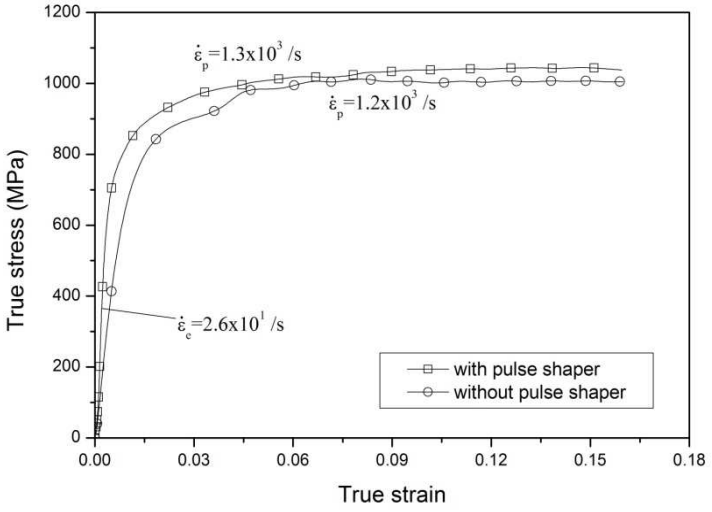

Figure 5.14 Dynamic stress-strain curves of 1046 steel from experiments with and without pulse shaping
(Reproduced from Chen et al. (2003) with permission)

Figure 5.15 shows oscilloscope records for 6061-T6 aluminum (Song et al. 2002), the characteristic of which is similar to the 1046 steel shown in Fig. 5.12. The initial portion with small amplitude in the reflected pulse is also observed, indicating the aluminum specimen deforms at a much lower strain rate in elasticity than that in plasticity. Figure 5.16 shows axial force versus time at the front end and the back of the specimen (Song et al. 2002). The nearly overlapping force histories in Fig. 5.16 indicate that the stress in the specimen is equilibrated very early in the experiment. The dynamic stress-strain curve reduced from this experiment is shown in Fig. 5.17 (Song et al. 2002). The Young's modulus from the stress-strain curve is approximately 70 GPa as determined from the early portion of the reflected and the transmitted signals shown in Fig. 5.15.

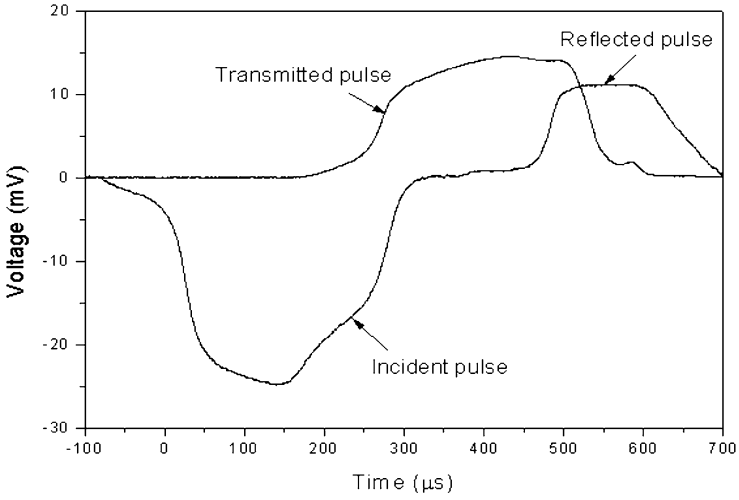

Figure 5.15 Oscilloscope records for 6061-T6 aluminum
(Reproduced from Song et al. (2002) with permission)

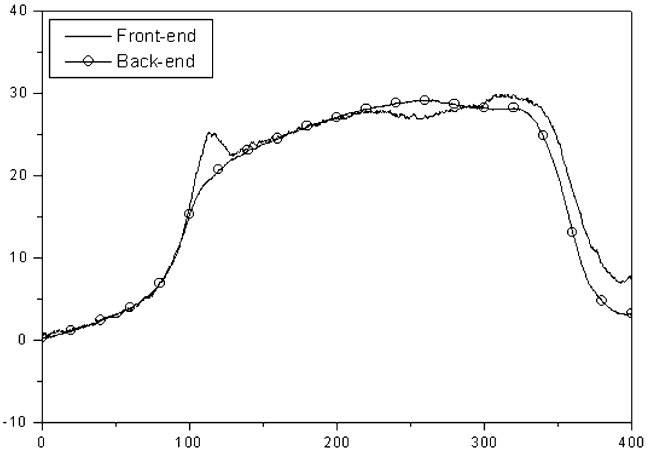

Figure 5.16 Comparison of force histories at both ends of the specimen
(Reproduced from Song et al. (2002) with permission)

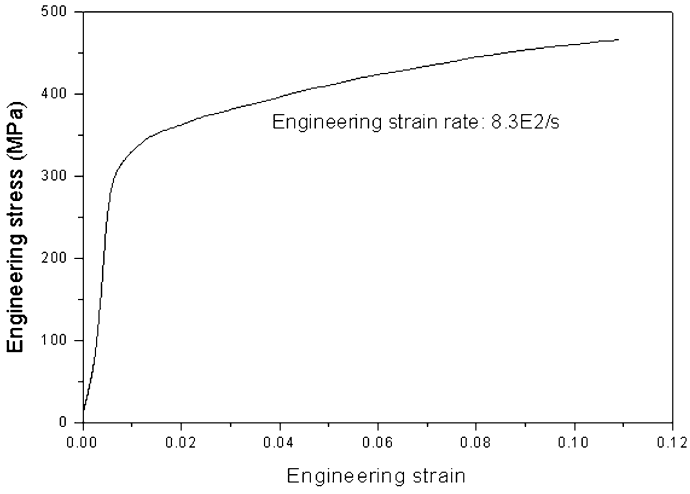

Figure 5.17 Dynamic stress-strain curve of 6061-T6 aluminum
(Reproduced from Song et al. (2002) with permission)

While conducting the experiments, it was noticed that the bar alignment and the specimen geometry, in particular the parallelism of the end faces, are very important in order to obtain accurate elastic behavior of the specimen material. The amplitude of the elastic precursor, from which the specimen elastic strain is integrated, is sensitive to the misalignment of the bars, the non-parallelism of the specimen ends, the flatness of the bar and the specimen end faces, and the initial contacting conditions between the specimen and the bars. These experiments demonstrate that, with proper pulse shaping, the data at small strains are not necessary invalid. In fact, the modulus of elasticity can be recovered. It is also noticed that, even with pulse shaping, not the entire elastic portion of the stress-strain curve was obtained under well-defined testing conditions. The specimen deformation accelerates from zero to a desired level. Strain is accumulated during this acceleration process. Therefore, the initial portion of the stress-strain curve is obtained during this acceleration process. However, this will not affect the elastic response for most metallic materials which are not rate dependent in elastic response.

5.3.2 Shape Memory Alloy

The stress-strain behavior of a shape memory alloy has distinct loading and unloading responses. Instead of a conventional stress-strain curve for most metals, a stress-strain loop that includes both loading and unloading portions must be characterized at a common constant strain rate. In this example, we present the design of a set of such experiments where both the loading and unloading portions of the pulses are controlled by pulse shaping, which is similar to the characterization of PMMA in Chapter 4.5.1. A reverse pulse-shaping technique described in Chapter 2.6 was used to generate an unloading profile to ensure the same constant strain rate as the loading strain rate under dynamic stress equilibrium. A C11000 half-hardened copper disk with a diameter of 6.35 mm and a thickness of 1.57 mm was selected as the front pulse-shaper while two C11000 annealed copper disks employed as the rear pulse-shapers were 2.39 mm in diameter and 0.51 mm in thickness. Using this technique, the dynamic stress-strain loop at a strain rate of 420 s^{-1} for a NiTi shape memory alloy was determined (Song and Chen 2004c). The steel Kolsky bar used for the experiments had a 12.70-mm diameter. The striker, incident, and transmission bars had a mass density of 8100 kg/m^3, a Young's

modulus of 200 GPa, an elastic wave speed of 4970 m/s, and lengths of 305 mm, 1829 mm, and 762 mm, respectively.

The shape memory alloy studied in these experiments is composed of nominal 55.8% nickel by weight and the balance is titanium. The NiTi shape memory alloy has a specified density of 6.5×10^3 kg/m^3, an austenite finish transition temperature A_f of 5-18˚C, and a melting point of 1310˚C. The cylindrical specimens had a dimension of 4.76-mm in diameter by 4.76-mm in length.

Figure 5.18 shows the incident, reflected, and transmitted pulses at the strain rate of 420 s^{-1} obtained with the modified Kolsky bar during both loading and unloading phases (Song and Chen 2004c). The fact that the difference between the incident and reflected pulses nearly overlap the transmitted pulse, as shown in Fig. 5.18, indicates that the specimen was in dynamic equilibrium over nearly the entire duration of the experiment. In addition, the strain-rate history, which is proportional to the reflected pulse in Fig. 5.18, indicates that not only the loading strain rate but also the unloading strain rate was maintained at the same constant value (420 s^{-1}) for most of the experiment duration. The strain-rate signal flipped its sign from compression (loading) to tension (unloading) at the peak of the loading.

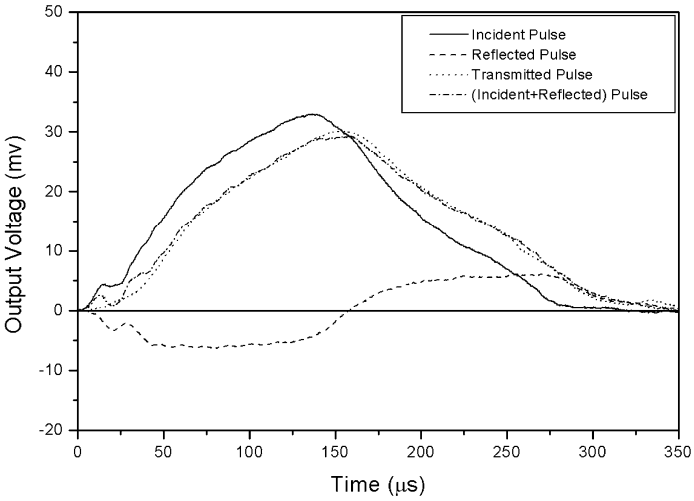

Figure 5.18 Experimental records of the bar signals on the shape memory alloy
(Reproduced from Song and Chen (2004c) with permission)

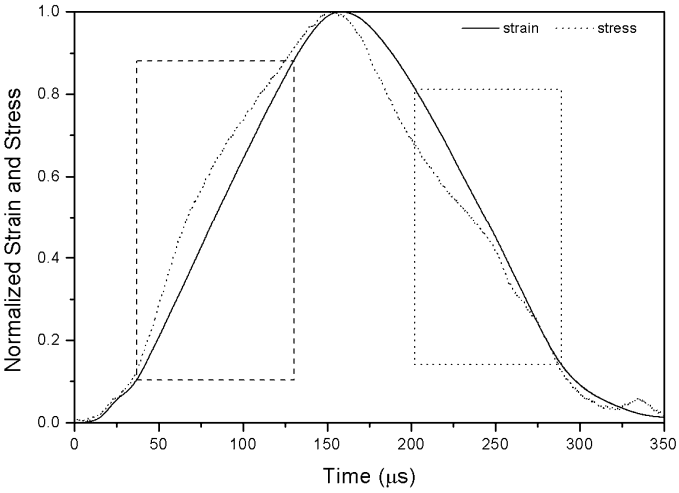

Figure 5.19 Stress and strain histories in the shape memory alloy specimen
(Reproduced from Song and Chen (2004c) with permission)

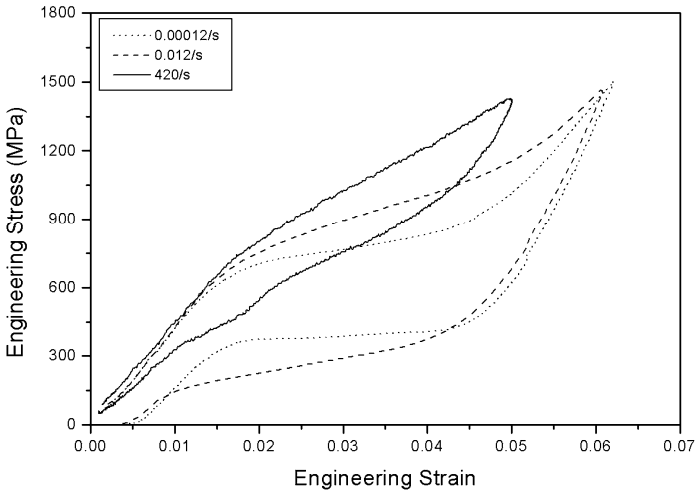

Figure 5.20 Compressive stress-strain loops of the shape memory alloy
(Reproduced from Song and Chen (2004c) with permission)

Figure 5.19 shows the detailed normalized strain and stress histories during the dynamic experiment (Song and Chen 2004c). The strain history is found to slightly lag behind the corresponding stress history. The dashed frames in Fig. 5.19 indicate the time ranges when the strain rate was maintained at the same value during loading and unloading.

Since the stress equilibrium in the specimen was also achieved within these time ranges (as shown in Fig. 5.18), the dynamic stress-strain loop at the strain rate of 420 s^{-1}, shown in Fig. 5.20, is an accurate measurement of the specimen response within the engineering strain ranges of 0.5% to 4.6% during loading and 0.7% to 4.3% during unloading (Song and Chen 2004c).

Due to the precise control of both loading and unloading histories, the stress-strain loops obtained from such dynamic experiments are directly comparable to those obtained under feed-back controlled quasi-static experiments. For the purpose of comparison, two quasi-static stress-strain loops of the NiTi shape memory alloy at the strain rates of 1.2×10^{-4} s^{-1} and 1.2×10^{-2} s^{-1} obtained with a hydraulically driven materials test system are also presented in Fig. 5.20. Both dynamic and quasi-static stress-strain curves exhibit some of fundamental characteristics of shape memory alloy behavior: an initial elastic behavior followed by a nonlinear superelastic behavior in the loading portion, and a nonlinear unloading behavior that had lower stresses at certain strains but a profile similar to that of the loading behavior. The loops show that the stress-strain behavior of the material is rate sensitive.

5.3.3 Alumina Filled Epoxy

Alumina filled epoxy is a composite material with alumina as fillers and epoxy as resin. Unlike most composite materials, the shape of the compressive stress-strain curve resembles that of a ductile metal. The composite has 43% by volume of alumina particles. The specimens were machined into cylinders with 12.7 mm in diameter and 6.35 mm in thickness from a large cylindrical billet of the alumina-filled epoxy composite. The Kolsky-bar setup is made of 7075-T651 aluminum alloy, with a common diameter of 19.05 mm, associated with a small annealed copper C11000 disk as the pulse shaper.

Figure 5.21 shows typical incident, reflected, and transmitted signals obtained from dynamic experiments at two different strain rates, 3.3×10^{2} s^{-1} and 7.3×10^{2} s^{-1} (Song et al. 2009c). The use of the pulse

shaper produces an extended rise time in the incident pulse, giving the specimen sufficient time to achieve dynamic stress equilibrium, which can be evaluated with (3.4). The equilibrium was examined in each experiment conducted. Figure 5.22 shows that the specimen reaches stress equilibration ~50 microseconds after initial loading (Song et al. 2009c). In addition, the shaped incident pulse minimized wave dispersion. Varying the dimensions of the copper pulse shaper and striking speed generates incident pulses with similar profiles but different amplitudes to achieve different constant strain rates in the specimen.

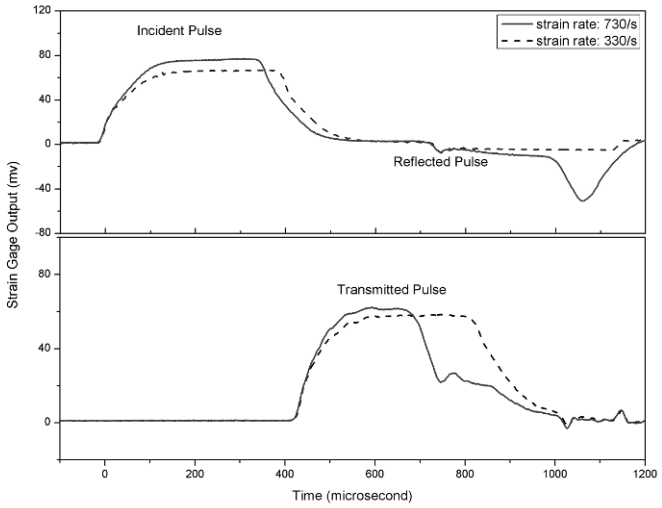

Figure 5.21 Experimental records from Kolsky-bar experiments on alumina-filled epoxy composite
(Reproduced from Song et al. (2009c) with permission)

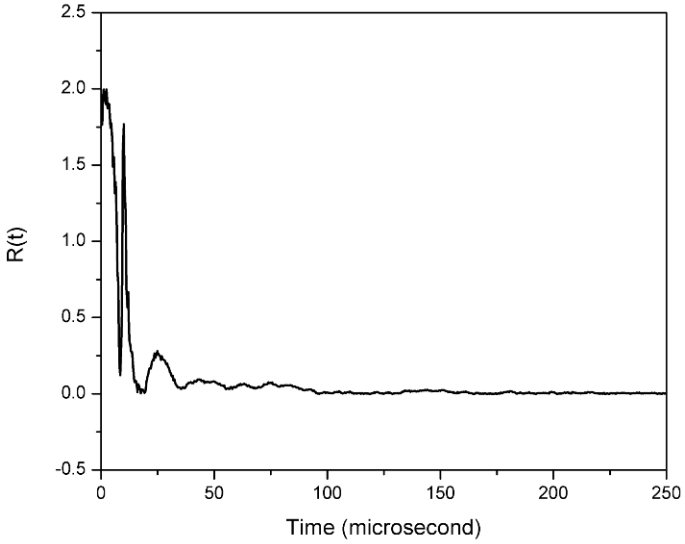

Figure 5.22 Dynamic equilibrium process in the specimen
(Reproduced from Song et al. (2009c) with permission)

The reflected pulse for the experiment at 330 s^{-1} in Fig. 5.21 has a long plateau, indicating the specimen is at a constant strain rate without catastrophic failure. By contrast, for the experiment at the strain rate of 730 s^{-1}, the reflected pulse has a higher plateau as expected but is followed by a sharp spike. This sharp spike corresponds to a sudden increase of strain rate due to material failure and loss of load-bearing capacity of the specimen. We have seen this type of signals in Chapter 3 dealing with brittle materials. The profiles of the transmitted pulses shown in Fig. 5.21, which are proportional to the stress histories in the specimens, indicate that the alumina-filled epoxy behaves similarly as an elastic-plastic material. The amplitude of the transmitted pulse is observed from Fig. 5.21 to increase with increasing strain rate, which indicates the strain-rate sensitivity of the material. Another detail worth being noticed is that the stress in the experiment at 330 s^{-1} drops because of unloading. Contrarily, the stress for the experiment at 730 s^{-1} decreases due to the failure of specimen.

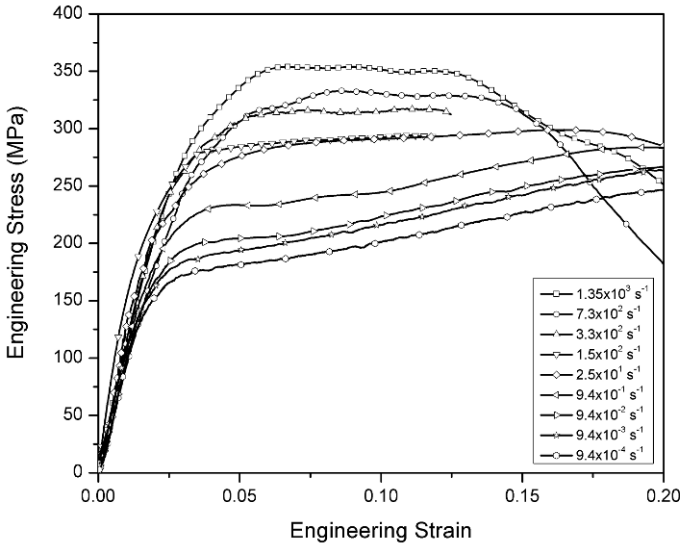

Figure 5.23 Compressive stress-strain curves of the alumina-filled epoxy composite
(Reproduced from Song et al. (2009c) with permission)

The stress-strain curves at various strain rates are shown in Fig. 5.23 (Song et al. 2009c). All stress-strain curves are very similar in their elastic behavior. The modulus of elasticity was measured approximately 12 GPa, which is not sensitive to strain rate within the range covered here. However, both yield strain and flow stress increase with increasing strain rate. In the quasi-static stress-strain curves obtained at the strain rates below 9.4×10^{-1} s^{-1}, an apparent work-hardening behavior is observed. However, when the strain rates are above 9.4×10^{-1} s^{-1}, the work-hardening behavior disappeared. The eventual failure strain decreases from approximately 20% at 9.4×10^{-4} s^{-1} to 12% at 1.35×10^{3} s^{-1}, although the macroscopic failure mode of the specimen was observed to be similar under both quasi-static and dynamic loading conditions.

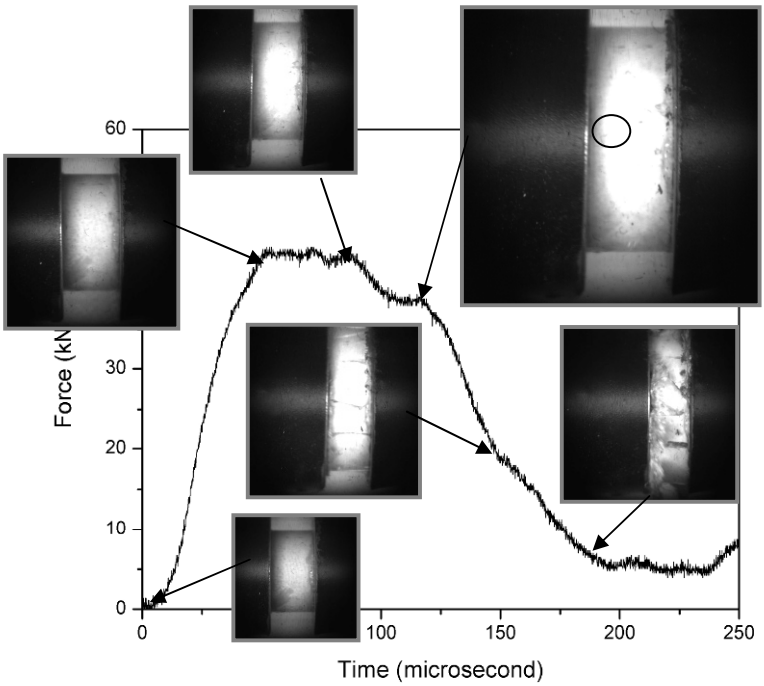

Figure 5.24 Dynamic damage and failure process in the specimen
(Reproduced from Song et al. (2009c) with permission)

Figure 5.24 shows a typical failure process and the corresponding force history in the specimen during a dynamic experiment at 1.35×10^3 s^{-1} (Song et al. 2009c). The images were taken with a Cordin 550 high-speed digital camera at a rate of 100,629 frames per second. As shown in Fig. 5.24, when the deformation of the specimen is clearly beyond the elastic range, say, near 100 μs on the time scale, no macroscopic cracks are visible on the specimen surface. When the loading is applied for 120 microseconds, the first surface crack is barely visible near the center of the specimen from the left end face. At this time, the force in the specimen has decreased from the peak. It is very likely that cracks have initiated earlier either inside or on the back surface of the specimen which could not be imaged. As the visible crack density increases on the imaged surface, the load-bearing capacity of the specimen

continues to decrease. Eventually, the specimen cylinder was split into several columns parallel to the loading direction.

5.3.4 Lead-free Solder

Solder joints in microelectronics devices are subjected to high-rate loading conditions in impact-related applications. For example, mobile electronics applications and automotive electronics devices subject the solder joints to impact and vibration, where the strain rates can be up to the order of 10^3 s^{-1}. Efficient design of the solder joints requires accurate material models that describe the high-rate behavior of the solder materials, which must be experimentally determined. In this group of Kolsky-bar experiments, the dynamic compressive behavior of a lead-free solder, Sn3.8Ag0.7Cu, was measured at various strain rates (Chan et al. 2009). The solder is relatively soft among the metallic materials family. Aluminum bars were used to facilitate enhanced transmitted wave signals. Copper tubes and disks were used as pulse shapers at strain rates of $220s^{-1}$ and $700s^{-1}$, respectively, to achieve constant strain rates under dynamic equilibrium.

Figure 5.25 shows a typical set of Kolsky-bar experimental records of the incident, reflected, and transmitted pulses. As shown in Fig. 5.25, the shaped incident pulse produces a reflected pulse with a flat plateau. This indicates a constant strain rate in the specimen if dynamic equilibrium is achieved, which is verified by the comparison of the force histories in front and on the back of the specimen, as shown in Fig. 5.26. The nearly overlapped force histories prove that the specimen is indeed loaded by equilibrated axial forces.

The validity of all Kolsky-bar experiments is checked. The data are then reduced to a group of compressive stress-strain curves as shown in Fig. 5.27. To investigate the strain-rate effects, quasi-static stress-strain curves are also shown in the figure. The results clearly demonstrate that the constitutive behavior of this lead-free solder is rate dependent, which must be accounted for in material model development.

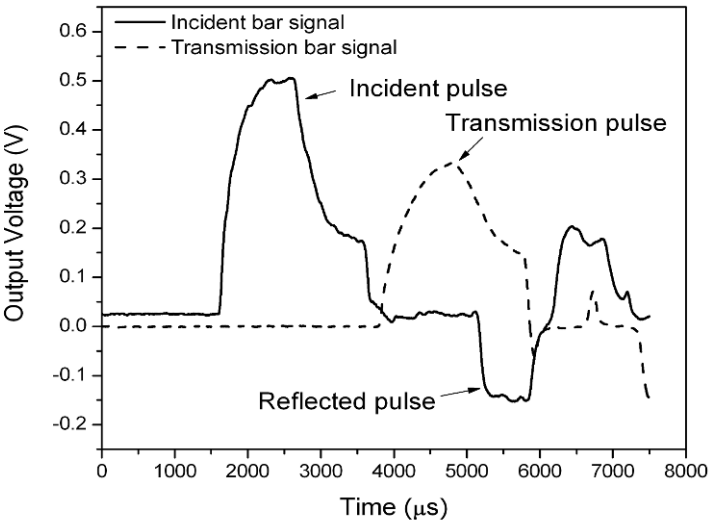

Figure 5.25 Experimental records from solder tests

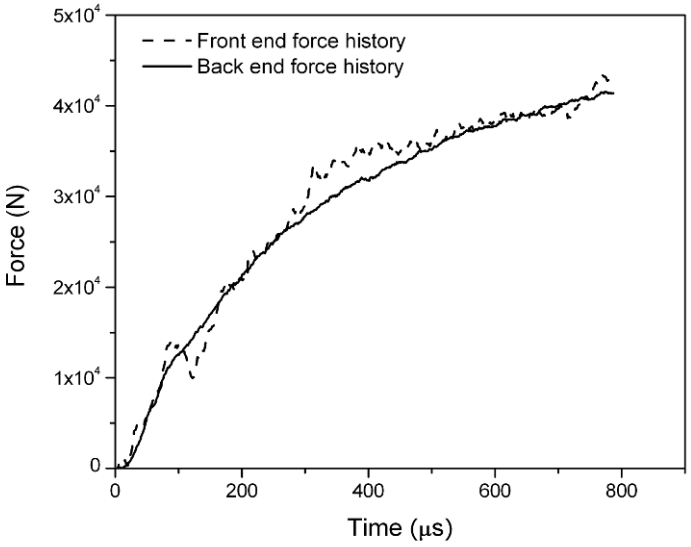

Figure 5.26 Dynamic equilibrium process in the solder specimen

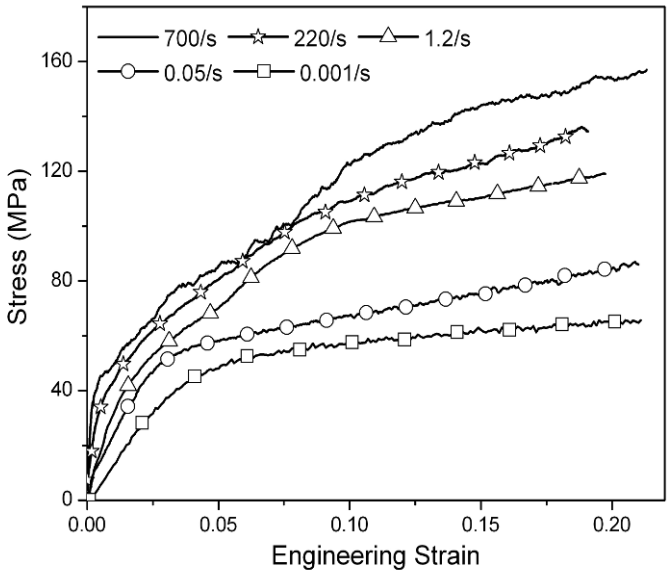

Figure 5.27 Compressive stress-strain curves of Sn3.8Ag0.7Cu solder

Chapter 6. Kolsky Compression Bar for Dynamic Triaxial Experiments

Triaxial experiments are commonly performed under quasi-static loading conditions on pressure-sensitive materials. In such an experiment, a cylindrical specimen is placed inside a pressure chamber where hydrostatic pressure is applied. Further axial pressure is then applied to measure the material response in terms of principal stress difference verses pressure or axial strain. A compression Kolsky bar can be modified through integration of pressure chambers such that further axial load is applied dynamically after hydrostatic pressure on the specimen. This chapter describes the design principle of a dynamic triaxial test system consisting of a Kolsky bar and two pressure vessels, the instrumentation for pressure and specimen deformation measurement inside a pressure chamber, and an example of using such a system to characterize the dynamic compressive response of sand under various hydrostatic pressures. In addition to the pressure boundary conditions on the lateral surface of the specimen, snug-fit sleeve can be used to supply dynamic triaxial load through displacement boundary conditions during a Kolsky compression bar experiment. Examples are given to determine the mechanical responses of an EPDM rubber and an epoxy syntactic foam under such dynamic lateral confinement.

6.1 Modified Kolsky Bar for Dynamic Triaxial Tests

The loading conditions in a Kolsky-bar experiment are mostly uniaxial stress, leading to a family of uniaxial stress-strain curves as a function of strain rates. The material responses under multiaxial stress conditions are related to uniaxial-stress responses through theories in constitutive modeling, such as von Mises theory (Meyers and Chawla 1999). This approach has been proven effective in modeling the dynamic plastic deformation of ductile metals. However, for materials the constitutive behavior of which is not well understood and modeled, experiments under both quasi-static and dynamic multiaxial loading conditions are necessary. The deformation physics and quantitative data revealed from such experiments form the basis for rate-dependent material model development.

There are two main types of methods to subject the specimen to multiaxial loading through either pressure or displacement boundary conditions. Displacement boundary conditions are typically achieved

W.W. Chen and B. Song, *Split Hopkinson (Kolsky) Bar: Design, Testing and Applications*, Mechanical Engineering Series, DOI 10.1007/978-1-4419-7982-7_6,

through jacketing the cylindrical surface of the specimen. For example, metal jackets have been used to radially confine cylindrical brittle specimens which are loaded in the axial direction (Chen and Ravichandran 1997). To explore the damage and failure processes of a transparent AlON, the specimens were compressed from two perpendicular directions (Paliwal et al. 2008). These types of lateral constrains are relatively straight forward to apply. However, the boundary conditions on the specimen lateral surface include both stress and displacement. When the specimen is soft, the boundary can be treated as nearly rigid. We will present examples for EPDM rubber and epoxy syntactic foam later in this chapter. On the other hand, when jackets are weak and plastically deformable, their effects are closer to pressure boundary conditions (Chen and Ravichandran 1997).

Pressure boundary conditions are achieved through hydrostatic pressure in a triaxial test. In such a test, a specimen is placed inside a pressure chamber and isotropically loaded by hydrostatic pressure. While maintaining the hydrostatic pressure constant, an additional axial load is then applied to generate shear stresses in the specimen under pressure. A typical specimen in a triaxial test is cylindrical in shape. The specimen is isolated from the confining fluid through a soft seal membrane that is placed over the specimen. Under isotropic pressure loading, the specimen strains are equal in all principal directions (axial and radial) if the specimen material is homogeneous and isotropic. Under further axial loading, the axial strain is different from the transverse strains. In such an experiment, the boundary condition on the lateral surface of the specimen is pressure only, making the stress state in the specimen clearly defined. Triaxial tests are conducted mostly under quasi-static loading conditions. With the increasing demand for high-rate mechanical response of materials under pressure, the dynamic version of triaxial tests is desired. Experimentally, a logical extension of the strain-rate range is to employ a Kolsky compression bar to supply the additional axial load in the shear phase of a triaxial test.

Christensen et al. (1972) and Lindholm et al. (1974) performed some of the most pioneering work in this area in the early 1970s. A pressure vessel was added to the test section of a Kolsky bar to subject the specimen to hydrostatic pressure before axial impact load. Christensen's and Lindholm's devices were capable of reaching confining pressures of 207- and 690-MPa, respectively. An improved version was developed recently (Frew et al. 2010). In this design, two pressure chambers are introduced. One chamber covers the testing section around the specimen to apply hydrostatic pressure on the specimen. This pressure will push the incident and transmission bars away from the specimen. Therefore, a second pressure chamber is introduced at the far end of the transmission

bar. The pressure in this second vessel is the same as the one surrounding the specimen, which pushes the transmission bar, specimen, and incident bar towards the striker. This potential motion is restricted by a symmetric tie-rod assembly that holds together an end plate on the impact end of the incident bar and the pressure vessel at the far end of the transmission bar. Since the tie-rods are placed symmetrically around the Kolsky bars and the test specimen, no bending moments are applied to the system. This feature is important to ensure the stability of the testing system under high pressure, which is an improvement to previous systems. The axial pressure supplied by the second pressure vessel and the lateral pressure supplied by the first vessel on the specimen surface, which have the same amplitude, create a hydrostatic pressure in the specimen. Soft seals are used between the chamber and the bars to keep the fluid from leaking while allowing the bars to move relatively freely in the axial direction.

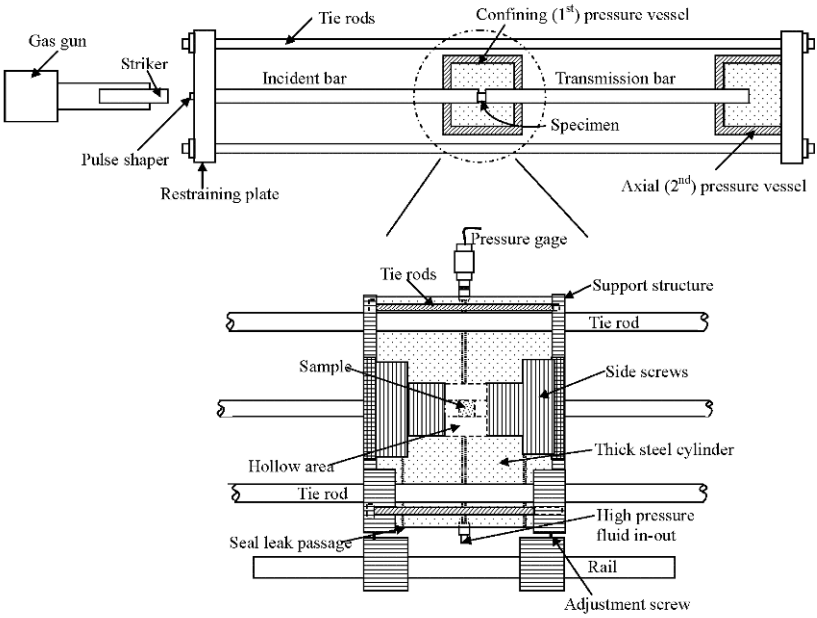

Figure 6.1 A schematic illustration of a dynamic triaxial test system

Figure 6.2 A photograph of a dynamic triaxial test system

After the hydrostatic pressure is applied and maintained, dynamic axial load is then applied by the impact of the striker to the incident bar, which subjects the specimen to dynamic triaxial loading conditions. A pulse shaper at the impact end of the incident bar controls the loading profile such that the specimen deforms uniformly at a nearly constant strain rate under a nearly equilibrated stress state. A schematic of this design of dynamic triaxial test is shown in Fig. 6.1, with a photograph of an actual setup shown in Fig. 6.2.

6.2 Specimen Design and Installation

The specimen design for the dynamic triaxial experiments is similar to that in a uniaxial compression experiment. For brittle materials such as glass and ceramics under multiaxial compression, the axial strengths may be significantly higher than the values under uniaxial stress loading such that the specimen cross-section area needs to be reduced. For high-strength ceramics, the axial compressive strength under triaxial loading may be too high to be failed before the yielding of the bars. For materials with low flow stresses, the initial specimen diameter should be carefully

chosen such that the specimen cross-sectional area does not exceed the bar ends when the maximum desired axial strain is reached during an experiment. Under sufficiently high pressure, some materials, commonly recognized as brittle materials, may go through brittle-ductile transitions, as illustrated by an example of lime stone later in this chapter.

The specimen installation is much more complicated in a dynamic triaxial test than that in a conventional Kolsky-bar experiment. Under high pressure, the pressure fluid may infiltrate into the specimen material and alter the mechanical response. Therefore, the specimen needs to be properly insulated from the fluid. A common practice to achieve this is to cover the specimen by a thin and flexible layer, such as rubber, that can be sealed to the bars. To install the specimen, the hydraulic fluid in the confining vessel around the test section is purged. One end cap on the pressure vessel around the testing section (Fig. 6.1) is then removed from the vessel. The vessel is translated to expose the specimen ends of the incident and transmission bars. A specimen is placed between the bars with a thin layer of membrane that covers the specimen and over the bar ends. Liquid rubber or gage coating may be painted onto the membrane to ensure that the specimen is isolated. The chamber is then reassembled and hydraulic fluid refilled. The pressure chambers are then connected to a high-pressure hydraulic system for applying hydrostatic pressure.

It should be noted that, although this Kolsky bar with triaxial testing capacity appears to be similar to a regular compression bar, there exists a large amount of elastic energy in the bar/tie-rod system when the hydrostatic pressure is applied. This bar is much less tolerant to misalignment and improper support spacings. The tie-rods must be adjusted carefully such that the load is evenly distributed to each rod. The compression bar in the middle bears axial compression load continuously during the entire duration of an experiment starting from the hydrostatic pressure. Therefore, the requirement on support spacings is stricter to prevent the bar from buckling under axial compression. It should be emphasized that extreme caution is necessary to perform the dynamic triaxial experiments due to the potential danger of the bar buckling.

6.3 Local Pressure and Deformation Measurements

During a quasi-static triaxial experiment, the histories of hydrostatic pressure, axial load, and dimensional variations of the specimen are monitored. Pressure transducers are installed on the hydrostatic pressure

feed lines to monitor and record the pressure in the chamber. The specimen length change may be measured either inside the chamber by a local Linear Variable Differential Transformer (LVDT) or outside the chamber with the LVDT attached to the loading shafts. The radial deformation of the cylindrical specimen may be measured by either LVDT based deformeters around the specimen (Bishop and Henkel 1962) or strain-gage based deformeters (Boyce and Brown 1976, Akers et al. 1986). The frequency response of such devices is typically up to 20 Hz, which is insufficient to record the experimental quantities in the order of 100 kHz under a Kolsky-bar loading.

To monitor the specimen size and local pressure variations inside the pressure chamber during a dynamic triaxial test, a dynamic local measurement system inside the specimen chamber has been developed (Kabir et al. 2010). Since the hydrostatic pressure phase of the experiment is quasi-static in nature, an external LVDT and a pressure gage on a feeding line are still applicable in the measurement of the axial deformation and hydrostatic pressure, respectively. However, the line pressure gage is not capable of measuring the rapid pressure changes during the impact phase of the experiment. A manganin pressure gage is installed inside the pressure chamber to record the dynamic pressure variations locally around the specimen. The manganin gages, together with compatible data-acquisition systems, are capable of measuring high-speed events, such as shock response of ceramics (Feng et al. 1998). The manganin gages are calibrated against the line pressure gage.

Under further axial loading at high rates with the total duration of around 200 μs, axial load and deformation of the specimen are measured by the stress waves in the Kolsky bars through the strain gages mounted on the bar surfaces, as discussed in Chapter 1. This method is used to compute the dynamic axial stress and strain in the dynamic triaxial experiments.

To measure the rapid diameter change of the specimen inside a small cavity of the pressure chamber, a capacitive transducer was developed. The working principle of the capacitive diameter transducer is to correlate the specimen diameter change to the distance change between two ring-shaped conductors. One conductor with a fixed diameter slightly larger than the specimen diameter at the end of deformation process is installed around the specimen. The symmetric axis of the ring aligns with that of the specimen. The other ring-shaped conductor is attached to the specimen lateral surface. The ring is flexible and moves with the specimen surface. The distance between the pair of ring-shaped conductors forms a capacitor. When the diameter of the specimen changes, the distance between the two conductors is altered, producing a measurable capacitance change. Figure 6.3 shows images of this design.

The moving conductor is a very light and soft spring around the specimen. The fixed conductor is a copper tube placed outside the spring. The copper tube is electrically isolated from the metal bars and chamber. The electrical signals are transmitted outside the chamber through sealed electrical connectors. This capacitance system measures the specimen diameter change at both quasi-static and high rates. In a typical experiment, the specimen diameter decreases quasi-statically under hydrostatic pressure, and then increases dynamically under the axial compression by stress-wave loading from the Kolsky bar.

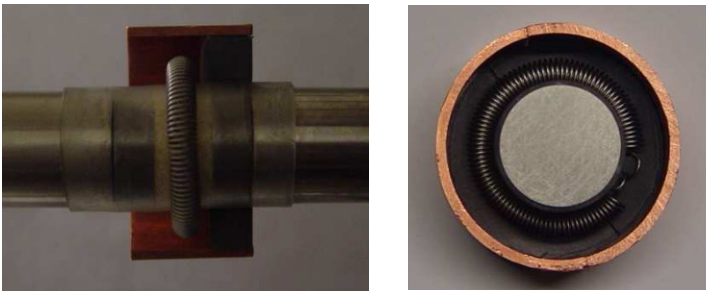

Figure 6.3 Capacitance system for specimen diameter measurement

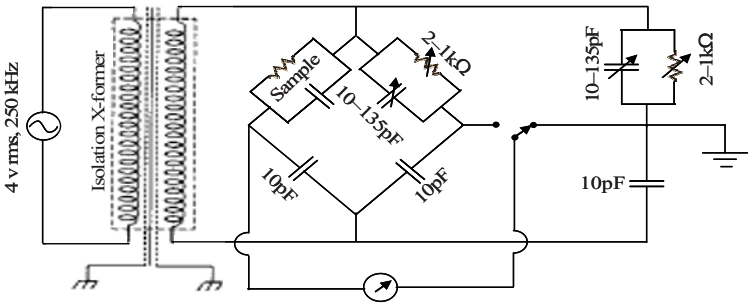

Figure 6.4 Circuit for the Schering Bridge for diameter measurement
(Reproduced from Kabir and Chen (2010) with permission)

The change of capacitance may be in the same order as the stray capacitance between the transducer probe and the ground. The data acquisition system needs to be selected carefully to capture the small capacitance change during the experiments without being affected by noise. In the design used by Kabir and Chen (2010) a Wagner-Earth voltage divider is employed to minimize stray capacitance in the system. A Schering bridge, which is considered to be one of the most sensitive, is employed for detecting the capacitance change. A lock-in amplifier is used as the detector for the bridge circuit balancing point. This circuit design used in this study is shown in Fig. 6.4 (Kabir and Chen 2010). The voltage output from the Schering bridge is calibrated to the specimen diameter change through the application of a known diameter to the capacitive transducer. Figure 6.5 shows a calibration curve which covers both the shrinking and expanding of the specimen diameter.

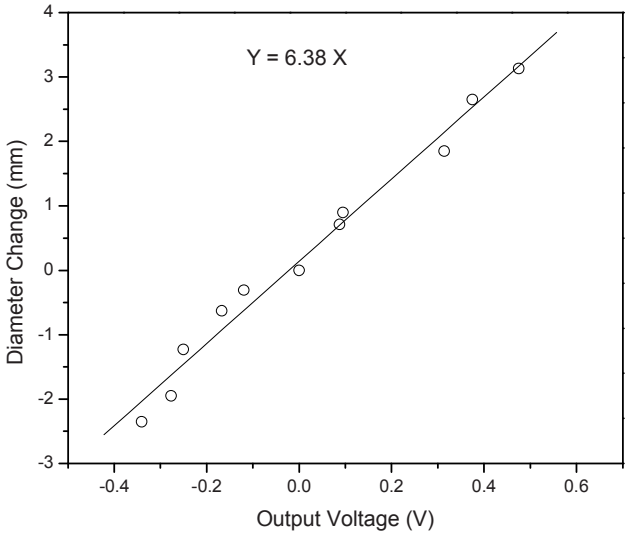

Figure 6.5 A calibration curve for diameter measurement

6.4 Pulse Shaping

Generally, the pulse shaping design for triaxial Kolsky-bar experiments may refer to the design for either brittle or ductile materials. Trial experiments are needed to approach the necessary pulse shapers to subject the specimen to desired testing conditions. Due to the additional stopper plate between the incident bar and the striker in the triaxial Kolsky bar, the incident pulses generated by the designed pulse shaper is slightly different from those predicted by the numerical solutions presented in Chapter 2.5. Extra iterations may be necessary in this case.

One unique issue associated with the dynamic triaxial experiment is the unloading of static compression in the incident bar when it is impacted by the striker. As described earlier, during hydrostatic compression on the specimen, both the incident and transmission bars are under axial compression. The amplitude of the compressive stress is the same as the pressure on the specimen. This compressive load is balanced by the tensile loads in the tie rods evenly distributed around the compression bars. At the impact end of the incident bar, the incident bar and the tie rods are connected by an end plate. A sink in the end plate houses a stopper disk that stops the incident bar from moving towards the striker. At the beginning of the high-rate phase, the striker impact through the sink hole onto the stopper plate through a pulse shaper. This impact generates the incident pulse in the incident bar. When with sufficient amplitude, this impact also pushes the stopper plate (together with the incident bar) away from the end plate. When the stopper plate is physically out of contact with the end plate, the static compressive load in the incident bar vanishes. So do the tensile loads in the tie rods. Since the hydrostatic pressure in the pressure chambers remain nearly unchanged, once the momentum transfer from the striker to the incident bar is completed, the incident bar is pushed back to against the stopper plate and is under static compression again. The tensile loads in the tie rods also resume.

Although the period for non-contact between the stopper plate and the end plate is very short, the duration is sufficient to cause very different incident bar signals recorded from a dynamic triaxial experiment as compared to a typical Kolsky-bar experiment under uniaxial compression. If the bar strain gage readings are set to zero (reference) at the beginning of the experiment, the readings will have a negative offset (corresponding to the amplitude of the static compressive stress) after the hydrostatic pressure is applied. Upon impact by the striker on the incident bar through the stopper plate and pulse shaper, the incident signal

reads further negative. The difference between the current negative value and the static negative offset is the dynamic incident pulse. Upon unloading of the incident pulse, the readings from the strain gages on the incident bar go back to zero, instead of the negative offset at the beginning of dynamic loading. This is because the incident bar is pushed away from the end plate, losing the static compressive stress inside. When the reflected pulse is recorded by the incident bar strain gages, the static compression in the incident bar may not have been restored yet. This causes the amplitude of the reflected stress reduced by the amount of the initial negative offset, causing serious error in the strain rate calculation. This must be compensated in data reduction in order to obtain the specimen strain rate and strain accurately.

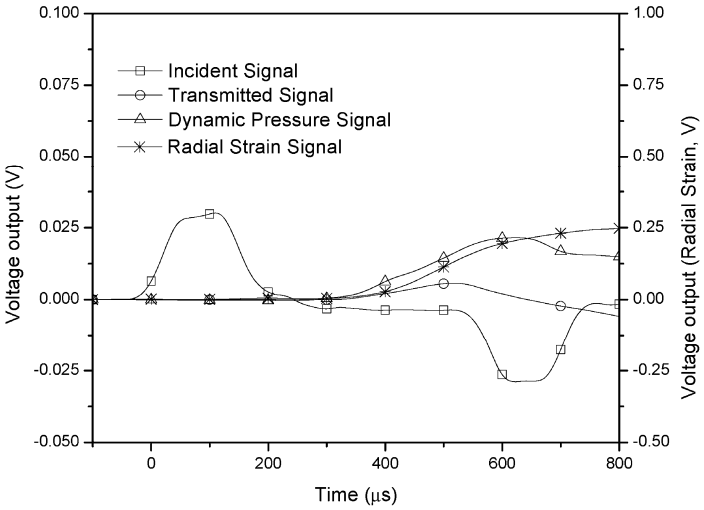

Figure 6.6 Laboratory records from a dynamic triaxial experiment

Figure 6.6 shows the experimental record from such an experiment on a sand specimen. The incident-bar strain gages were set to zero after the hydrostatic pressure phase, i.e., the negative offset, had been removed before the dynamic phase of the experiment. Therefore, the incident pulse in Fig. 6.6 starts from zero. After the unloading of the incident signal which is taken compression as positive, the incident pulse is seen to approach a negative value, corresponding to a “tensile” load in the in-

cident bar. Of course, there was no tensile load at this time (say, 400 μs) yet. The apparent tensile load is the result of losing static compressive load in the incident bar. Now, the reflected pulse, starting at about 550 μs, is built on top of this shifted reference line. This shift is not related to the dynamic strain rate in the specimen and must be corrected in data reduction. The duration of this shift in the incident bar reference line depends on the duration of the time when the incident bar being pushed away from the stopper plate, which in turn depends on a number of factors including the momentum in the striker impact and the amplitude of the static pressure. If the static pressure resumes during the recording time of the reflected pulse, a constant-strain-rate event will not appear so in the apparent reflected pulse, which should be corrected in data reduction.

6.5 Dynamic Multiaxial Response of Sand

Using the dynamic triaxial experimental setup described here, dynamic triaxial experiments have been conducted on Quikrete #1961® sand. The sand is silica based fine grain and is kiln dried and poorly graded. Most sand particles are in the diameter range from 150 to 450 μm. In the experiments presented in this example, dry sand specimens with an initial density of 1.5×10^3 kg/m^3 were used. The specimen diameter is selected to be the same as that of the bars (19 mm), with a length of 9.3 mm. The specimen length was determined after trial experiments to ensure uniform deformation in the specimen under dynamic stress equilibrium (Martin et al. 2009, Song et al. 2009a). The specimens are initially contained in polyolefin heat shrink tubes with a wall thickness of 0.3 mm and a length of 35 mm.

Upon axial dynamic loading, the specimen length reduces. This allows the incident bar to advance into the pressure chamber more than the transmission bar moving out, which results in a net increase in the bar volume inside the chamber. If the specimen volume changes, a net volume change inside the chamber should be computed accounting for volume changes from both the bars and the specimen. If the specimen does not shrink more than the bar volume increase, the fluid inside the vessel is further compressed, thereby raising the pressure inside the chamber. This dynamic pressure change, p, is proportional to the relative volume change of the fluid, $\frac{\delta V}{V_o}$, and the bulk modulus of the fluid, K,

$$p = -K\frac{\delta V}{V_o} \tag{6.1}$$

where V_o is the initial volume of the fluid in the chamber, δV is the net change in volume, and p is taken positive when in compression. This pressure variation needs to be quantitatively determined in order to accurately describe the pressure boundary conditions in the experiments.

To detect this dynamic pressure change in the chamber, manganin gages are placed inside the chamber. Figure 6.7 shows the dynamic pressure histories at two locations inside the chamber under initial hydrostatic pressure of 150 MPa when a sand specimen was deformed at the strain rate of 1000 s^{-1}. One gage was located at one end of the chamber, and the other was in the middle. The results show that the dynamic pressure is evenly distributed along the axial direction of the chamber; with a peak pressure around 3 MPa. This pressure change does not depend on the initial hydrostatic pressure in the chamber. Therefore, the effects of this dynamic pressure variation on the testing conditions relatively decrease as the initial pressure increases.

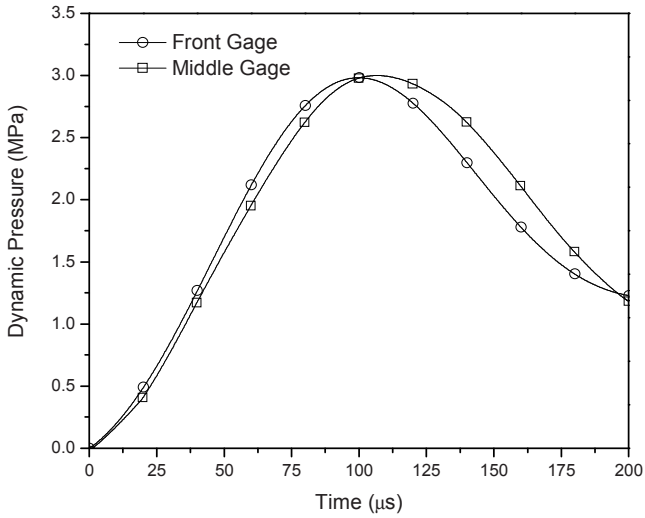

Fig. 6.7 Dynamic pressure variation inside the pressure chamber

During hydrostatic pressure phase, length and diameter changes of the specimen are measured by LVDT and the capacitive transducer, respectively. As an example, the strain history of an undrained sand sample in this phase is shown in Fig. 6.8. The specimen is pressurized to 100 MPa. Since the specimen is under hydrostatic pressure and the material is homogeneous and isotropic from a global point of view (sand is not such a material when examined more closely), the resultant strains along both the axial and radial directions are expected to be the same. The strain histories shown in Fig. 6.8, which take contraction as positive, verified this trend.

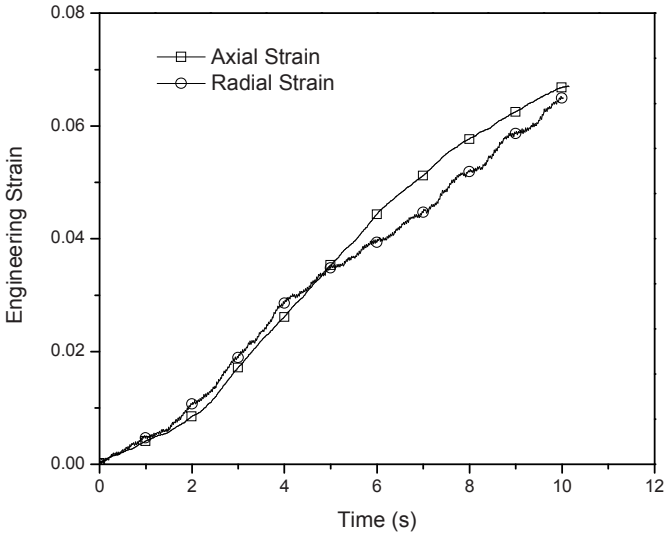

Figure 6.8 Specimen dimension change under hydrostatic pressure

While maintaining the hydrostatic pressure, the specimen is dynamically compressed along the axial direction at a strain rate of 1000/s. Figure 6.9 shows the dynamic axial strain history calculated using Kolsky-bar data reduction method after the offset in the reflected signal is

corrected. During this dynamic shear phase of the experiment, the specimen expands in the radial directions while contracting in the axial direction under the dynamic axial compression. The results in Fig. 6.9 take contraction as positive and expansion as negative.

With the methods to measure the stress and strain histories in the specimen during both hydrostatic pressure and dynamic axial impact stages, the mechanical response of the specimen material under triaxial loading conditions can be determined at various strain rates under various hydrostatic pressure levels. Under axial compression at the hydrostatic pressure of 100 MPa and the strain rate of 1000 s^{-1}, the principal stress difference as a function of axial strain is shown in Fig. 6.10 (Kabir et al. 2010).

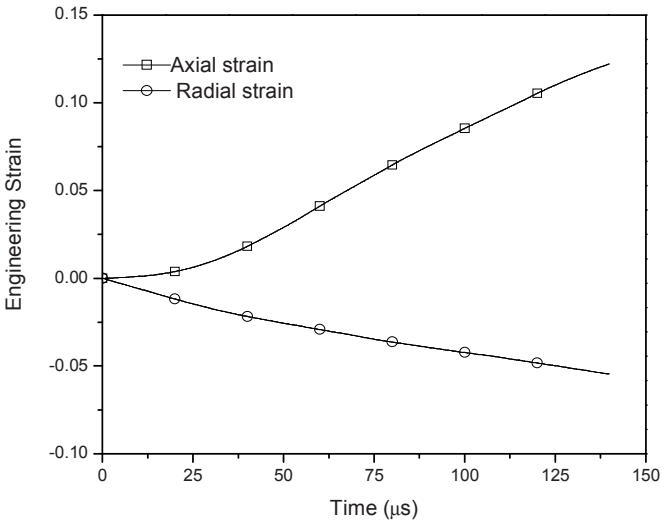

Figure 6.9 Dynamic strain histories in the sand specimen

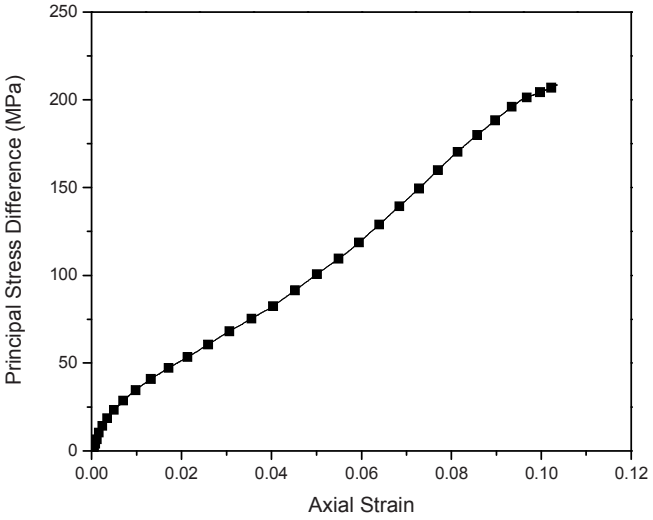

Figure 6.10 An example of dynamic triaxial experimental results on a sand *(Reproduced from Kabir et al. (2010) with permission)*

6.6 Response of Indiana Lime Stone under Pressure

An Indiana limestone tested in this example is a porous, medium-strength rock that contains over 90 percent calcite and less than 10 percent quartz, having a porosity of about 15 percent, and a grain-size ranging between 0.15 and 1.0 mm (ASTM D 4543 1991). The actual limestone samples had a Young's modulus of 24 GPa, density ρ_s = 2320 kg/m^3, calculated wave speed of 3200 m/s, and measured grain density ρ_g = 2700 kg/m^3 which gave an average porosity of 14.5%.

The Indiana limestone specimens were cored, perpendicular to the bedding plane, cut to near final length, and precision ground flat and parallel to within ±0.025 mm. Unlike sand samples, the limestone is a brittle material that requires high level of parallelism between the two loading surfaces. After an L/D study that showed minimum effects on the stress-strain response as the specimen L/D ratio was changed from 2:1 to 1:1, 12.7-mm-diameter by 12.7-mm-long specimens were used in the dy-

namic triaxial experiments to facilitate faster equilibrium. The dimensions for the test specimens are chosen to minimize the grain-size effects and time to stress equilibrium in the specimen, and to maximize the achievable strain rates of an experiment. This set of experiments was conducted by Dr. D.J. Frew.

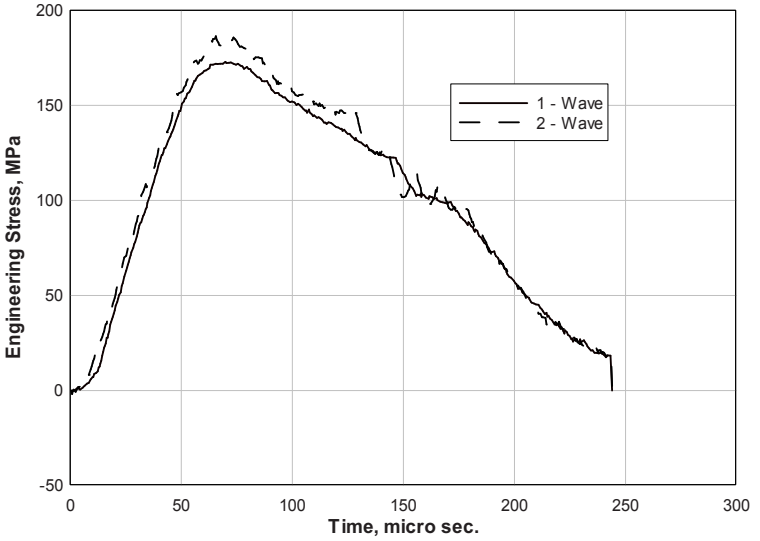

Figure 6.11 Equilibrium check on a dynamic triaxial experiment on a limestone.

The triaxial Kolsky-bar experiments were all conducted using 12.7-mm-diameter striker, incident, and transmission bars made of high-strength C-350 maraging steel with density ρ_B = 8100 kg/m^3, Young's modulus E_B = 200 GPa and bar wave velocity C_B = 4970 m/s. The incident and transmission bars were 3050- and 1825-mm in length, respectively, and the striker bar length was varied to achieve the desired pulse length for specific experiments.

Figure 6.11 shows the comparison of dynamic stress profiles in front and on the back of the limestone specimen. The specimen was under a 20 MPa initial hydrostatic pressure and dynamically loaded by a

Kolsky bar with a 152.4-mm-long striker impacting two annealed C11000 copper pulse shapers with diameters of 9.60 mm and thicknesses of 1.02 and 4.80 mm at a striking velocity of 28.4 m/s. The rise-time from the pulse shaped experiment in Fig. 6.11 is approximately 4 times longer than that from the non-pulse-shaped experiment. Equilibrium was achieved within the first 10 μs of the experiment and remained in equilibrium during the rest of the experiment. When the hydrostatic pressure goes to higher, the dimensions and materials of the two pulse shapers need to be varied accordingly, especially when the limestone specimen goes through a brittle-ductile transition.

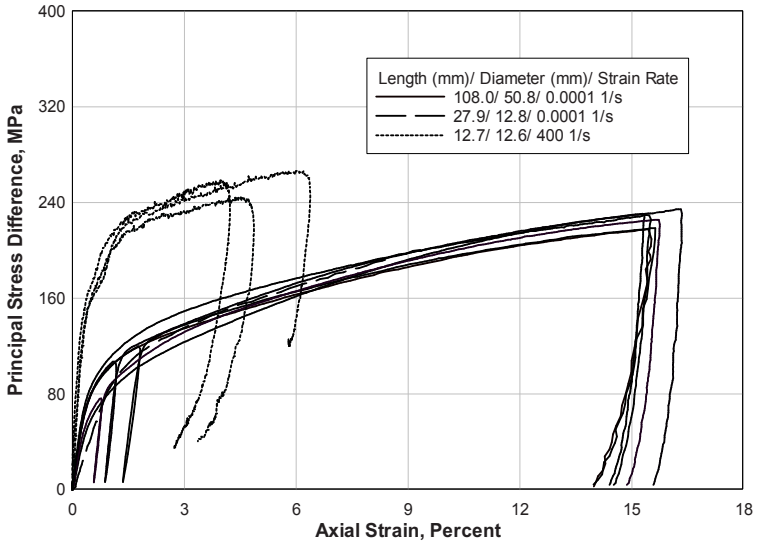

Figure 6.12 Principal stress difference as a function of axial strain under 100-MPa hydrostatic pressure

Figure 6.12 shows the variation of axial principal stress difference with the axial strain in the limestone specimen pressed under initial hydrostatic pressure of 100 MPa. The stress-strain curves are obtained both quasi-statically and dynamically at two specimen aspect ratios: L/D =

2:1 and 1:1. The specimen diameters under quasi-static loading were also varied from 12.8 mm to 50.8 mm. The results show that both the specimen diameter and aspect ratio do not affect the stress-strain response of the rock material in a noticeable way. Strain rate, on the other hand, produced significant difference in the material strength. At 100-MPa hydrostatic pressure, the stress-strain curves clearly indicate that the material went through brittle-ductile transitions under both quasi-static and dynamic loading conditions. The dynamic "flow" stress at 400 s^{-1} strain rate and ~2% of axial strain nearly doubles the value at a quasi-static strain rate (0.0001 s^{-1}). Because of similar stress states in the specimens, the dynamic triaxial testing technique facilitates the direct data comparison between quasi-static rates and dynamic rates, such as those shown in Fig. 6.12.

6.7 Dynamic Confinement Experiments on Soft Materials

The dynamic multiaxial experiments described in the previous sections provide well-defined pressure boundary conditions in the radial directions. To achieve such clear boundary conditions, the experimental procedure and the involved equipment are shown to be sophisticated. Alternatively, snug-fit sleeves have been used to facilitate radial confinement on the specimen. This method is much simpler. The complication is in the determination of the radial boundary conditions due to their mixed nature between stresses and displacements on the interface between the specimen and the sleeve. However, when the snug-fit sleeves of stiff materials are applied on soft specimens, the radial deformation of the stiff sleeves is negligible, providing a fixed displacement boundary on the specimen. In this case, the soft specimens can be considered in uniaxial strain but three-dimensional stress states (Bhushan and Jahsman 1976). This boundary condition is easily specified in numerical simulations. In this section, we present examples of such dynamic confinement experiments on an EPDM rubber and an epoxy syntactic foam, the mechanical responses of which under uniaxial stress loading are presented in Chapters 4.5.2.3 and 4.5.3.1, respectively.

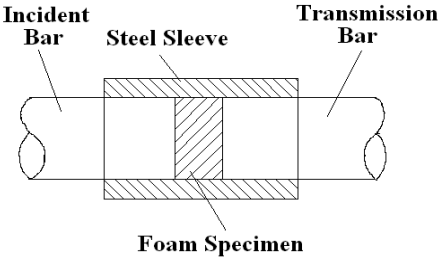

Figure 6.13 Testing section configuration for confinement experiments on epoxy syntactic foam
(Reproduced from Song et al. (2005c) with permission)

Dynamic confinement experiments are nearly the same as the conventional Kolsky-bar experiments except for the testing section where a metal sleeve surrounds the specimen. The specimen has the same diameter as the bars and the inside diameter of the metal sleeve, providing a snug-fit confinement to the soft specimen. Figure 6.13 shows an example schematic of the configuration of such a testing section for an epoxy syntactic foam (Song et al. 2005c). Since the stress state in the specimen changes in such a dynamic confinement experiment, the specimen material behaves differently from uniaxial stress experiments. The pulse shaping must be designed to facilitate constant strain rate deformation and stress equilibrium. Comparing to uniaxial stress experiments, the specimen is easier to achieve stress equilibrium under radial confinement because the stress wave in the specimen propagates at a nearly uniaxial strain wave speed which is faster than uniaxial stress wave speed. Facilitating constant strain-rate deformation may be very different from uniaxial stress experiments since the specimen response may change drastically under confinement. Below we present the changes in compressive stress-strain responses in an EPDM rubber and an epoxy syntactic foam under confinement, respectively.

Figure 6.14 shows a typical set of incident, reflected, and transmitted wave signals for dynamic confinement experiments on an EPDM rubber, the same material as presented in Chapter 4.5.2.3. Under confinement, the amplitude in the specimen stress that is represented by the transmitted wave in Fig. 6.14 significantly increases. As seen in Fig. 6.14, the amplitude of the transmitted wave signal actually approaches

that of the incident wave, resulting in a low-amplitude reflected pulse. This indicates that the soft rubber specimen becomes much stronger when it is radially confined. With a proper pulse shaping design, the rubber specimen deformed at a constant strain rate of 1.2×10^3 s^{-1}. Figure 6.15 shows axial dynamic compressive stress-strain curves of the EPDM rubber at various strain rates under nearly axial strain conditions (Song and Chen 2004a). For the purpose of comparison, the stress-strain curve under unaxial stress loading at the strain rate of 3.2×10^3 s^{-1} shown in Fig. 4.23(b) is also plotted in Fig. 6.15. Figure 6.15 clearly shows significantly increased stress amplitudes at the same strains when the specimen is confined, even though the shapes of stress-strain curves still have similar non-linear characteristics.

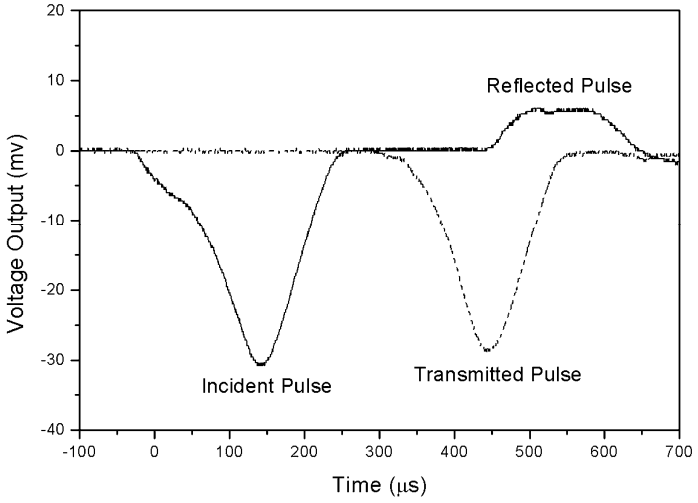

Figure 6.14 Typical incident, reflected, and transmitted signals
(Reproduced from Song and Chen (2004a) with permission)

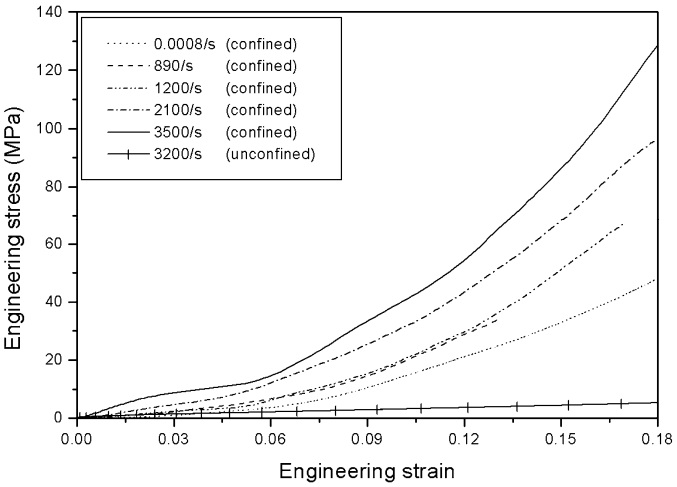

Figure 6.15 Dynamic stress-strain response of the EPDM rubber under confinement
(Reproduced from Song and Chen (2004a) with permission)

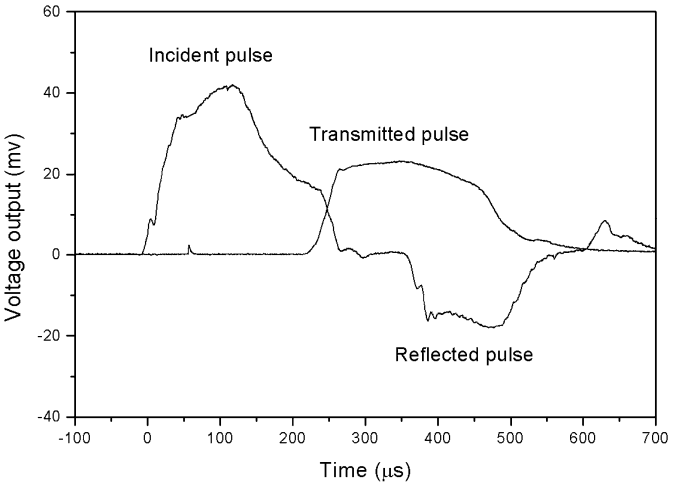

Figure 6.16 Oscilloscope records of incident, reflected, and transmitted signals
(Reproduced from Song et al. (2005c) with permission)

Figure 6.16 shows the oscilloscope records of incident, reflected, and transmitted pulses in a dynamic confinement experiment on an epoxy syntactic foam (Song et al. 2005c). The foam material is the same as that presented in Chapter 4.5.3.1. However, the transmitted signal under confinement shown in Fig. 6.16 is quite different from that shown in Fig. 4.24. The elastic-brittle response under unaxial stress conditions turns into elastic-plastic-like response under nearly uniaxial strain conditions. Due to the restriction in the radial deformation of the specimen, the material, even though the cell structures are crushed, cannot move away from the loading path, making it being continuously compressed. Consequently, the specimen behaves in a manner of slowly increased stress amplitude over time instead of a suddenly-dropped stress beyond yielding or failure. The specimen density also increases during the process of unaixial strain compression due to compressed volume of the specimen. In order to maintain constant strain-rate deformation in the confined specimen, the incident pulse needs to be properly modified with redesigned pulse shaping, as illustrated in Fig. 6.16. It is noted that, in this experiment, the momentum trap system presented in Chapter 2.6 was applied to load the specimen only once for the purpose of microscopic investigation of the specimen after dynamic loading.

Figure 6.17 shows the dynamic compressive stress-strain curves of the confined epoxy syntactic foam (Song et al. 2005c). The stress-strain curves of unconfined specimens shown in Fig. 4.27 are also shown in Fig. 6.17. Under radial confinement, not only the amplitudes in elastic modulus and yield (or failure) strength increase, but also the shape of the stress-strain curves changes, indicating a change in failure mechanism. A desire to look into the mechanism change prompted the use of single-loading system.

The radial confinement restricts the damage evolution in the specimen. The specimens after dynamic loading were not macroscopically failed. Thus, the load-bearing capacity of the foam material is improved under such multiaxial stress loading. Only small and short localized cracks were observed in the confined specimens after dynamic compression. These cracks compromise material strength. On the other hand, the increased material density during uniaxial-strain compression strengthens the material (Song et al. 2005c). An increasing stress amplitude indicates that the density-increasing effects are stronger than the damage-weakening effects in this foam.

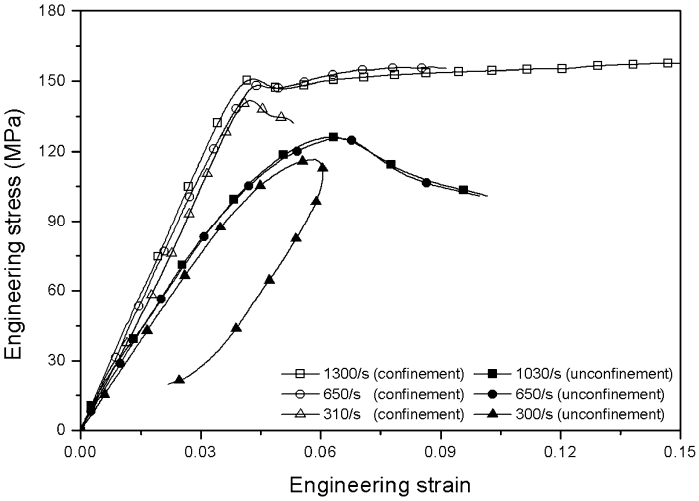

Figure 6.17 Dynamic stress-strain curves of the confined and unconfined specimens
(Reproduced from Song et al. (2005c) with permission)

Chapter 7. Kolsky Compression Bar Experiments at High/Low Temperatures

When the specimen temperature differs from the room temperature, timing of mechanical load becomes a variable due to heat conduction. There are two approaches to conduct experiments with the specimens heated or cooled. One is to heat/cool the specimen with the bars attached. The other is to bring the bars in contact with the specimen after it reaches a desired temperature. The latter is preferred particularly at very high temperatures since temperature gradient in the bars affects wave propagation, which must be corrected. This chapter describes methods for high/low temperature Kolsky-bar experiments. The design of a computer-controlled automated system for high temperature experiments is presented. Examples are given with specimen materials including a stainless steel, a shape memory alloy, a syntactic epoxy foam, and PMDI foams with different densities.

7.1 Heating/Cooling the Specimen

The selection of heating and cooling devices depends on the specimen materials under investigation and the desired testing conditions. For example, to simulate the conditions of rapid heating together with high strain rates encountered in high-speed machining situations, fast heating of the metallic specimen can be achieved by passing high-intensity electrical current through the specimen. In a Kolsky compression bar developed at National Institute of Standard and Technology (NIST) (Mates et al. 2008), the heating rate in the specimen by the electrical current can be as high as 6,000 K/s. Mechanical loading is applied immediately after the heating to plastically deform the specimen at strain rates up to 10^4 s^{-1}. By contrast, many brittle materials, such as most glasses and ceramics, thermal shocks generated by rapid heating may cause damage and failure in the specimen before mechanical load is applied. In the experiments where the microstructure needs to be preserved for further microscopic analysis, a specimen at high temperature after high-rate deformation must be quenched at a specific time (Song et al. 2010). In most experiments at high or low environmental temperatures, the specimens are heated or cooled in such a way that the temperature in the specimen is nearly in equilibrium.

W.W. Chen and B. Song, *Split Hopkinson (Kolsky) Bar: Design, Testing and Applications*, Mechanical Engineering Series, DOI 10.1007/978-1-4419-7982-7_7,

The heating of the specimens may be supplied by electrical current (Basak et al. 2004; Mates et al. 2008) or focused infrared radiation (Lennon and Ramesh 1998) at high heating rates, furnace (Frantz et al. 1984) or environmental chambers at lower heating rates. Inductive heating (Rosenberg et al. 1986) and other in-house built heaters have also been used. When heating to high temperatures, a heating environment with an inert gas, such as argon or nitrogen, is desired to reduce the surface oxidation of the specimen. High-rate cooling may be achieved by immersing the specimen in a liquid already at desired temperature. Cooling at lower rates can be achieved in various environmental chambers. If possible, a thermal couple attached on the specimen is desired to record the actual temperature history in the specimen. Figure 7.1 shows a commercial furnace with an opening for the specimen to enter and exit. Many such furnaces are available with precise temperature control systems. Figure 7.2 shows a sketch of an in-house built environmental system (Song et al. 2005d). The system has an open hole for the test section of the Kolsky bar. The heating elements in the system are used for high-temperature experiments; whereas, flow rate of liquid nitrogen through the coil pipe creates a low-temperature environment in the opening at a desired low temperature.

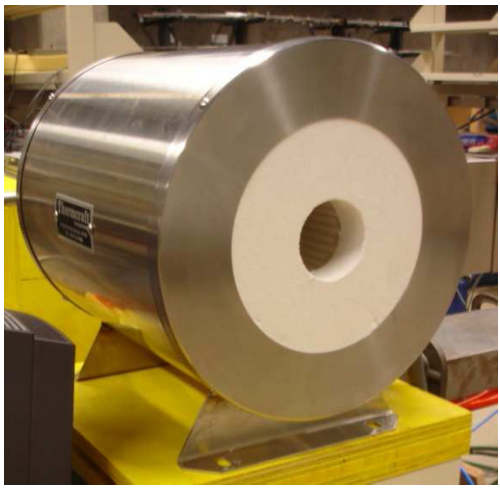

Figure 7.1 A commercial furnace to heating specimens

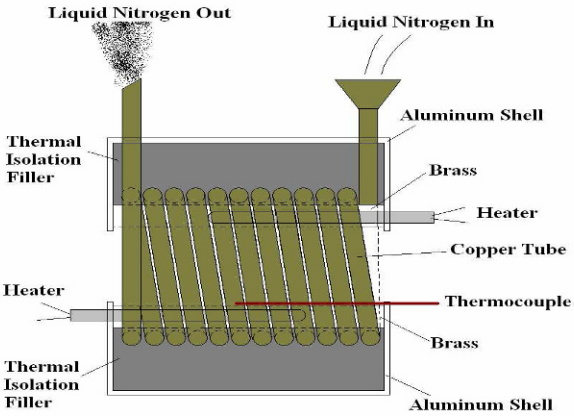

Figure 7.2 An example of in-house built environmental chamber
(Reproduced from Song et al. (2005d) with permission)

In the experiments with specimen temperatures differing from room temperature, timing of mechanical loading becomes a parameter that needs to be controlled in the experiments since heat can diffuse over time and alter the temperature and its distribution in the specimen. The main heat conduction path is through the metallic pressure bars. There are two approaches for the bars to be in contact with the specimens. One is to maintain constant contact between the bars and the specimen while the specimen is being heated up. This approach heats up the specimen and the bar ends together. Since the far ends of the bars are nearly at room temperature, there are temperature gradients along the bar axes. Depending on the desired temperature in the specimen, this temperature gradient may affect the wave propagation along the bar in a significant way. Chiddister and Malvern (1963) might have been the first to discuss the wave reflection and transmission in the bars with thermal gradients. The temperature gradients must be measured and the effects of the thermal gradients must be numerically corrected, particularly when the temperature is 600˚C or higher in steel bars. Figure 7.3 shows the effect of temperature on the modulus of elasticity for Inconel 718 steel (Seo et al. 2005). When the temperature is 600˚C or higher, the modulus of elasticity drastically decreases. Hence, the temperature gradient in the steel bar results in the gradient of modulus of elasticity. Changes in wave imped-

ance in terms of modulus of elasticity in the steel bar leads to disturbance to stress wave propagation. In addition, the exposure of the bar ends to high temperatures may anneal the bar material, which needs to remain elastic during the experiments. Due to these limitations, the direct-contact approach is not commonly used in compression experiments unless the temperature is not very high, such as those encountered in the characterization of polymers.

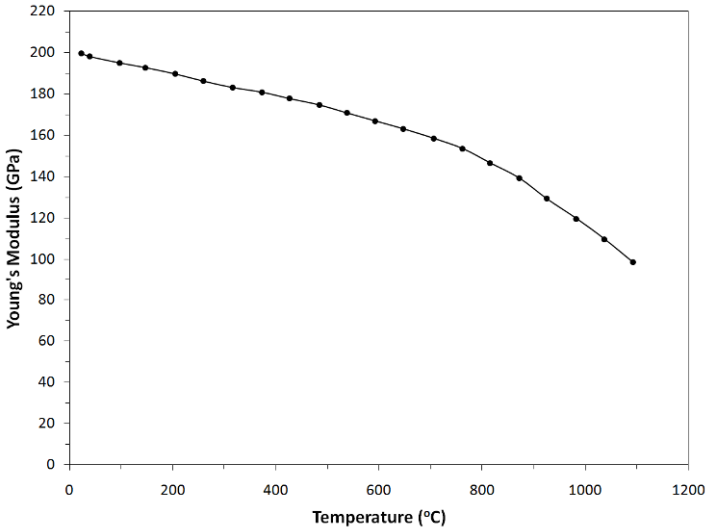

Figure 7.3 Effect of temperature on modulus of elasticity
(Reproduced from Seo et al. (2005) with permission)

The other approach is to expose the specimen to the temperature environment only. The bar ends are moved into contact with the specimen only shortly before the stress-wave loading. In this approach, when the room-temperature bar ends touch the hot/cold specimen, heat exchanges start immediately between the specimen and the bars. This leads to non-uniform temperature distribution on the specimen. The specimen temperature also changes instantly. One solution to keep the specimen at the desired and evenly distributed temperature is to add platens on both sides of the specimen. The platens can be the same material and diameter

as the bars or a temperature resistant material with impedance matching with that of the bars to minimize their disturbance to the wave propagation. The platens are in contact with the specimen and in the same environment chamber or furnace such that they have the same temperature as the specimen during the heating/cooling process. When the room-temperature bars are moved into contact with the platens, there are severe temperature gradients inside the platens. If the stress-wave loading is applied sufficiently quickly, the changes in the temperature and its distribution in the specimen are minimal. Due to the severe temperature gradients in the platens, the wave propagation through the platens may be affected, which is difficult to model and correct. However, the platens are typically thin enough that the entire specimen/platen test section assembly may be subjected to dynamic stress equilibrium through proper pulse shaping. Attempts to find the temperature distribution inside the platens through numerical simulations have been documented (Shazly et al. 2004).

The above challenges are usually encountered in high temperature Kolsky-bar experiments. Cold contact time (CCT) has been defined as the time during which the hot specimen stays in contact with the cold bars until being dynamically loaded. A short CCT is certainly desired in high-temperature Kolsky bar experiments. Experimental methods have been developed to facilitate relatively short CCT in high-temperature Kolsky-bar experiments. Frantz et al. (1984) developed an electric screw driven system to bring the bars into contact with the specimen pre-heated in a furnace. This design facilitates CCT as short as 400 ms with less than 5ºC decrease in specimen temperature. The design by Lennon and Ramesh (1998) can control the CCT to be as short as 1-2 ms. In their design, both the incident and transmission bars are initially separated from the hot specimen. An electropneumatic actuation system pushed the bars in contact with the specimen. In the following section, we will introduce an automated system that can adjust short CCT through precise timing control.

7.2 An Automated System for Precise Timing Control

From the descriptions in Chapter 7.1, it is obvious that, even with platens as temperature buffers, the specimen temperature will inevitably change when platens are in contact with the cold bars for an extended period of time waiting for the stress wave to arrive at the specimen. Ideally, the

stress waves should arrive immediately upon the contact between the bars and the specimen such that the temperature field in the specimen is nearly undisturbed. Alternatively, the stress wave should arrive at a fixed delay time after the contact such that heat exchange between the specimen and the bars is consistent. Both requirements (immediate loading or at a fixed delay) need precise control of the timing of the stress-wave arrival, which is difficult to achieve by manual operations. This section introduces an automated system to realize the required loading consistency in the Kolsky-bar experiments involving high/low temperatures, which was originally developed by Kuokkola and his students (Apostol et al. 2003).

The set-up is fully automated through controls over a series of pneumatic valves by a computer program. The mechanism of the automated control system is illustrated in Fig. 7.4 (Apostol et al. 2003). An environmental chamber or a furnace is used to set or change the specimen temperature. A pneumatically operated specimen manipulator is placed directly aiming at the opening of the environmental chamber or furnace. The specimen holder that is attached to the front of the manipulator places the specimen into the environmental chamber or furnace and then brings the specimen back to the test section with its centerline aligned with that of the bars after being retrieved from the temperature device. The transmission bar manipulator then moves the transmission bar towards the incident bar after the specimen is placed in the test section. A pneumatic circuit controls all the manipulators and valves, a pressurized air supply through software programming. To protect the temperature environment inside the chamber, the opening can also be covered by a door that is controlled by another pneumatic valve through the computer program.

In an experiment with this system, the specimen, together with its platens, is placed on the specimen holder. The specimen assembly is then fed into the environmental chamber or furnace through the opening for specimen. Temperature control is turned to a desired value prescribed in the computer program. A thermal couple attached on the specimen holder monitors the temperature variation on the specimen. While the temperature is on its way to the desired level, the striker is pushed into the gun barrel and the pulse shaper installed on the impact end of the incident bar. The gas gun chamber is filled with gas to necessary pressure. When the temperature reaches at a desired level in equilibrium, the thermal couple signal triggers the computer program to activate a valve to pull the specimen assembly out of the chamber/furnace and place the assembly in the test section of the Kolsky bar. Another valve is then turned on to activate the transmission bar manipulator to move the transmission bar towards the specimen and then push the specimen assembly in con-

tact with the incident bar, sandwiching the specimen assembly in the test section. The transmission-bar manipulator allows the transmission bar to move under stress-wave loading. The holding force is just sufficient to overcome the friction to move the transmission bar forward when activated by the computer program. While the pressure bars are being pushed together, the third valve launches the striker from the gas gun towards the pulse shaper on the impact end of the incident bar. Since the timing between all the operations is controlled by the computer program, the repeatability of the experiment is significantly improved, which is important in Kolsky-bar experiments when the specimen temperature is different from the ambient temperature. Figure 7.5 shows the main features of this system installed around the test section of a compression Kolsky bar. A close-up look at the specimen holder is shown in Fig. 7.6.

Figure 7.7 shows an experimental record of a dynamic high-temperature test using the system. In this figure, trace #1 indicates that, after heated to a desired temperature, the specimen assembly has returned to the test section. A position detector sends this signal signifying the proper positioning of the specimen. Trace #2 indicates that the transmission bar is in contact with the hot specimen assembly. Trace #3 signifies that the transmission bar has pushed the specimen assembly to be in contact with the incident bar. At this moment, the test section is ready to be loaded by the incident pulse of the Kolsky bar. Trace #4 is the strain gage signal from the incident bar surface. The time between Traces #3 and #4 can be adjusted in the computer program. In the specific example shown in Fig. 7.7, it takes about 42 ms for the stress wave to arrive at the specimen after it is sandwiched by the bars. The unique advantage of this automated system is that this time interval can be adjusted. Once the desired interval is determined, the system can repeat this interval from experiment to experiment, providing the necessary control over timing of loading in Kolsky-bar experiments at high/low temperatures.

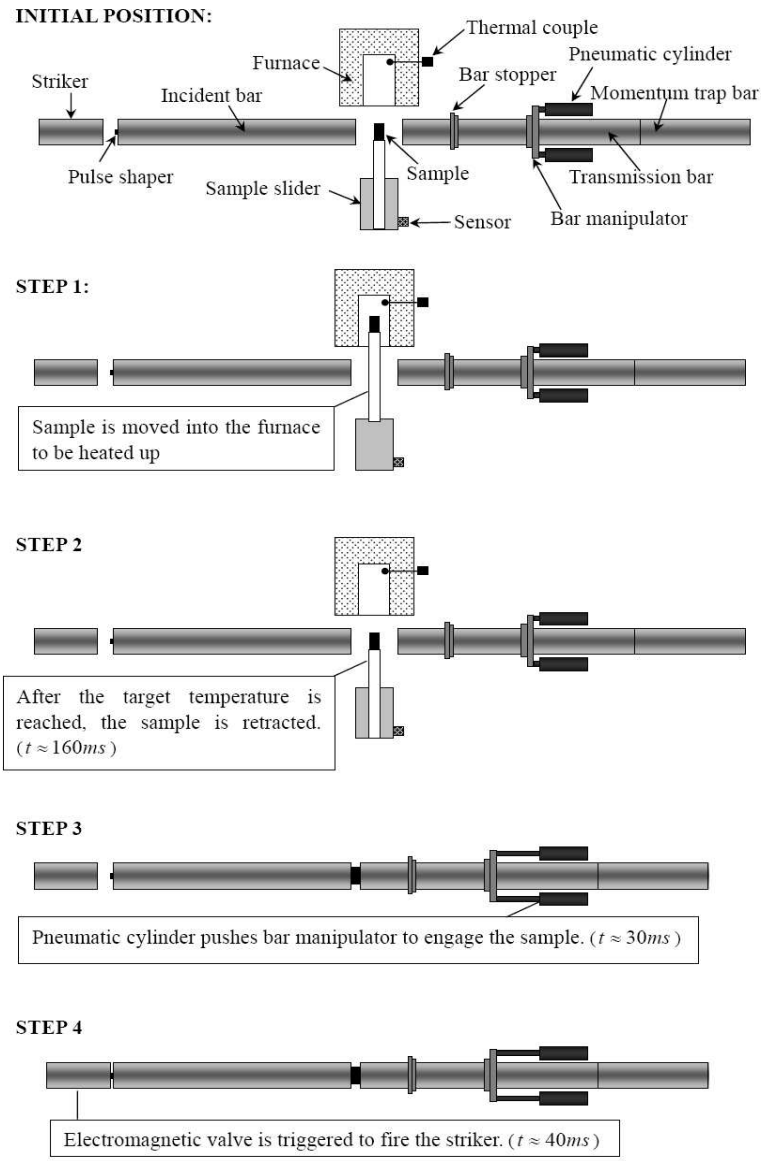

Figure 7.4 The automated control system

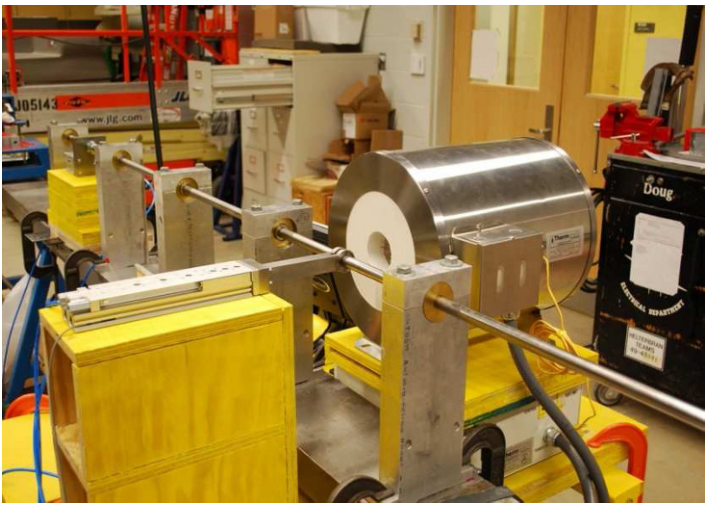

Figure 7.5 An automated system for high-temperature Kolsky bar experiments

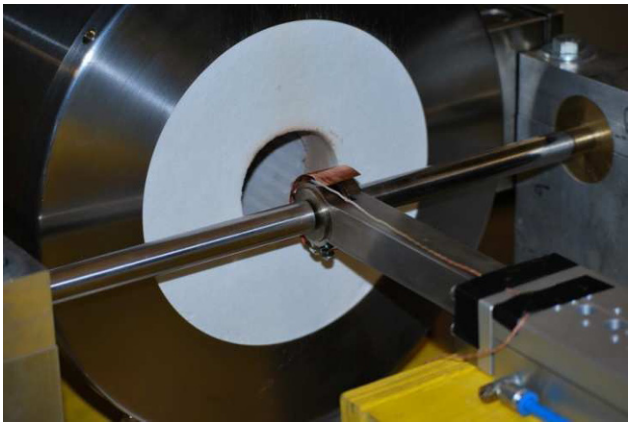

Figure 7.6 Details of the specimen holder

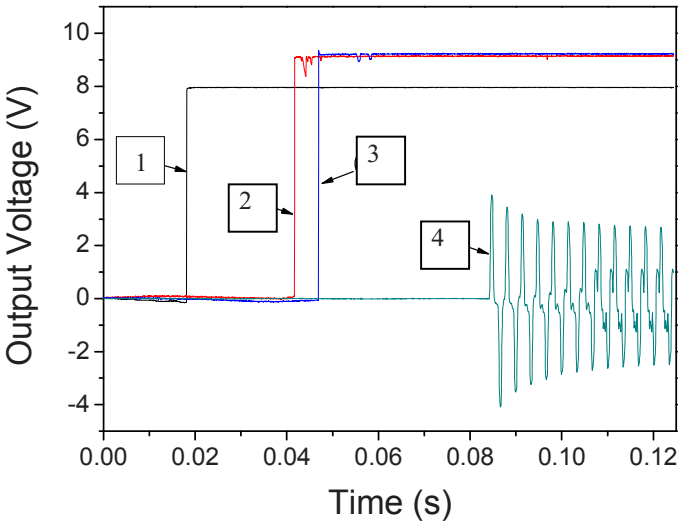

Figure 7.7 An experimental record illustrating the action sequence of a high-temperature compression Kolsky bar experiment

7.3 High Temperature Experiments on a Stainless Steel

The automated control system in Chapter 7.2 is one of the efficient approaches for high temperature Kolsky-bar experiments. However, other methods are also feasible as long as the specimen temperature is consistent during dynamic loading. In the following example of high temperature experiments on a 304L stainless steel, a Kolsky compression bar without the automated control system was used. The temperature history of each specimen was individually monitored.

The high-rate compressive response of 304L stainless steel was characterized at two elevated temperatures, 819˚C and 929˚C at a common strain rate of ~2500 s^{-1} (Song et al. 2010). The specimen assembly consists of two platens with the specimen in between. The assembly was heated before stress-wave loading while the bars remain at room temperature to avoid the temperature-gradient effect on the wave propaga-

tion in the bars. Upon contacting the cold bars, temperature gradients formed in the platens, leaving the temperature in specimen constant and uniform. Incident pulses are controlled with pulse shaping technique to produce constant strain-rate deformation and dynamic stress equilibrium in the specimen. In addition, a single loading feature was enabled such that recrystallization in the specimen can be related to the recorded histories of high-rate loading and high temperature. The mechanically loaded specimen was quenched into water at room temperature at 7 seconds or 30 seconds after loading to freeze the microstructures inside the specimen at different stages for further microscopic analysis. Dynamic recrystallization is one of the most important mechanisms for the microstructure evolution in materials with low to medium stacking fault energy to affect their macroscopic mechanical behavior. To ensure that recrystallization occurs in the specimen, the stainless steel specimens were compressed to large engineering strains over 0.5 at high rates and high temperatures.

A 19.05-mm-diameter C350 maraging steel Kolsky compression bar was used to conduct the high-rate characterization of the 304L stainless steel at elevated temperatures. The incident and transmission bars were 2388- and 1791-mm long, respectively. A 610-mm-long striker was used to generate an approximately 245-μs-long incident pulse, which can compress the specimen to the engineering strains over 0.5 at the strain rate of ~2500 s^{-1}. The cylindrical 304L stainless steel specimens had an initial diameter of 6.35 mm and length of 3.20 mm. The steel platens on both sides of the specimen were each 19.05 mm in diameter and 6.35-mm thick. The incident pulse was shaped using a 3.2-mm-diameter, 0.4-mm-thick annealed C11000 copper disk stacked on a 6.4-mm-diameter, 3.2-mm-thick M-2 tool steel disk to generate a nearly non-dispersive incident pulse that had an extended rise time for early stress equilibrium in the specimen and a flat plateau for constant engineering strain rate in the specimen. A liquid water-based glass suspension Deltaglaze 152 material was used as the high temperature lubricant to minimize the interfacial friction.

To monitor the temperature history of the specimen during the entire experiment duration, an OMEGA® K-type thermocouple was attached on the specimen surface. This thermocouple measured specimen temperature during pre-heating, dynamic loading, and post-load quenching stages of the experiment. The thermocouple had a 30-gage diameter. The thermal mass is small enough to have a sufficient response time for the Kolsky-bar experiments.

The momentum trapping system presented in Chapter 2.6 was employed to ensure a single loading on the specimen. Figure 7.8 shows a schematic of the experimental set up with the momentum trapping sys-

tem (Song et al. 2010). Figures 7.9 shows detailed configuration of the testing section. The 304L stainless steel cylindrical specimen was held with a thin disk made of light-weight ceramic wool. The specimen assembly that consists of the 304L steel specimen supported by the ceramic wool and a pair of steel platens sandwiching the specimen is placed and aligned to the pressure bars with a semi-circular steel channel. Figure 7.10 shows the configuration of the specimen assembly. The thickness of the ceramic wool disk is less than half of the specimen thickness so that the ceramic wool disk will not be loaded in axial direction during the experiment. Moreover, the ceramic wool disk has a bigger hole than the steel specimen to avoid providing additional lateral confinement to the specimen during compression.

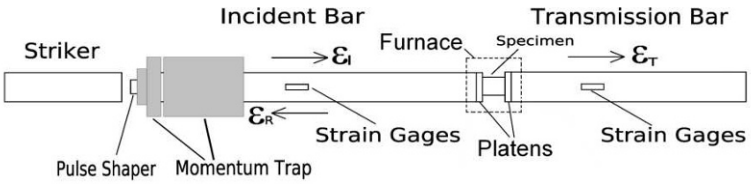

Figure 7.8 A schematic of the experimental setup for high-rate, high-temperature experiments
(Reproduced from Song et al. (2010) with permission)

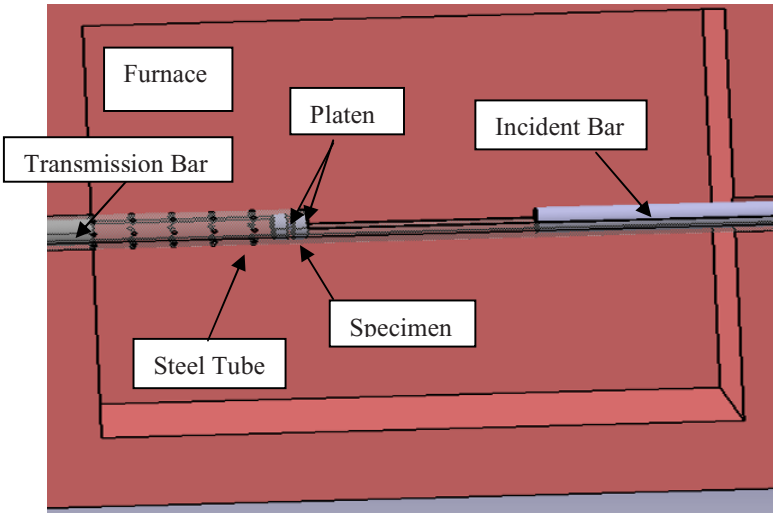

Figure 7.9 Configuration of the testing section
(Reproduced from Song et al. (2010) with permission)

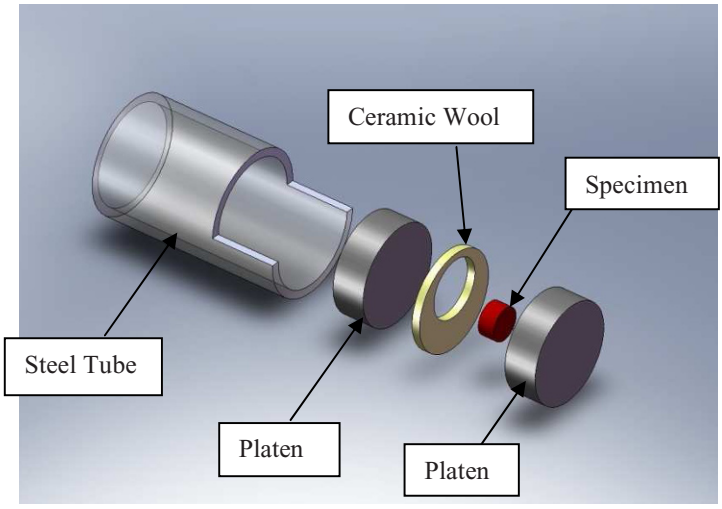

Figure 7.10 Configuration of specimen assembly
(Reproduced from Song et al. (2010) with permission)

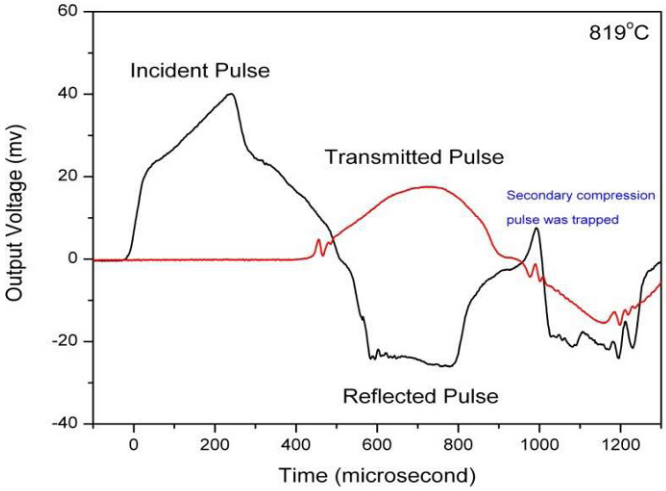

Figure 7.11 Experimental records of a high-rate, high-temperature experiment on 304L stainless steel
(Reproduced from Song et al. (2010) with permission)

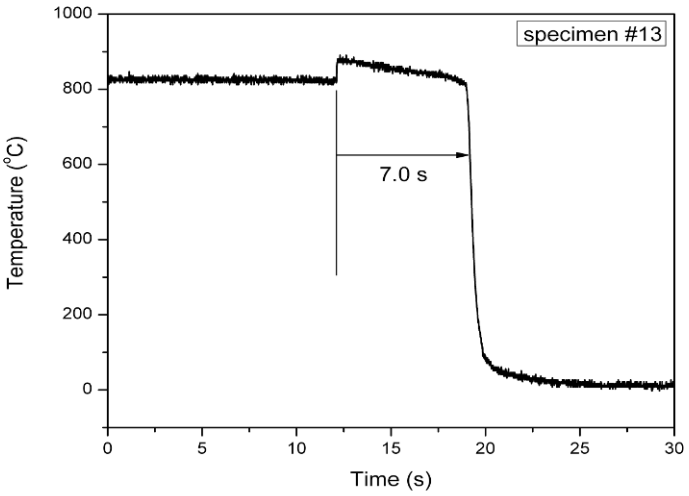

Figure 7.12 Temperature history in the specimen
(Reproduced from Song et al. (2010) with permission)

Figure 7.11 shows the incident, reflected, and transmitted pulses obtained from an experiment on the 304L stainless steel at an elevated temperature of 819ºC (Song et al. 2010). The figure shows that the profile-controlled incident pulse ensures the specimen in dynamic equilibrium during dynamic loading. Under stress equilibrium, the plateau in the reflected pulse shown in Fig. 7.11 represents the constant strain-rate history in the specimen. Furthermore, the secondary compressive wave was trapped and in turn changed to a tensile wave by using the momentum trap (Fig. 7.11). The specimen was thus loaded in compression only once.

Figure 7.12 shows the temperature history in the specimen measured with the thermocouple attached on the specimen surface over the entire experiment duration (Song et al. 2010). The temperature in the specimen was stabilized at 819ºC in the furnace. Then the specimen was dynamically compressed at the instant of 12th second. During dynamic compression, the temperature in the specimen rose from 819 ºC to 846ºC due to adiabatic heating from the plastic deformation in the specimen. Seven seconds after dynamic compression, the specimen was dipped into water for quenching, resulting in a sudden temperature drop at the instant of 19th second. Such complete thermal histories, together with the well-defined single loading history, are necessary to relate the microscopic recrystallization in the specimen to its thermal and mechanical loading histories.

Figure 7.13 shows a detailed temperature history in the specimen before and during dynamic compression, which is zoomed in for more details from Fig. 7.12. In this figure, the dynamic compression is set to start at time zero ($t = 0$). During dynamic compression, the specimen temperature increased with the increasing strain, or plastic work. The strain history is also shown in Fig. 7.13. Due to the short time duration of the dynamic loading, the energy available from plastic work adiabatically heated up the specimen, as discussed in Chapter 5.3.1. This adiabatic deformation produced an approximate temperature rise of 27 ºC in the specimen. The nearly linear history of strain in Fig. 7.13 also indicates that the specimen deformed at a constant strain rate of ~2450 s^{-1} to an engineering strain of 0.5.

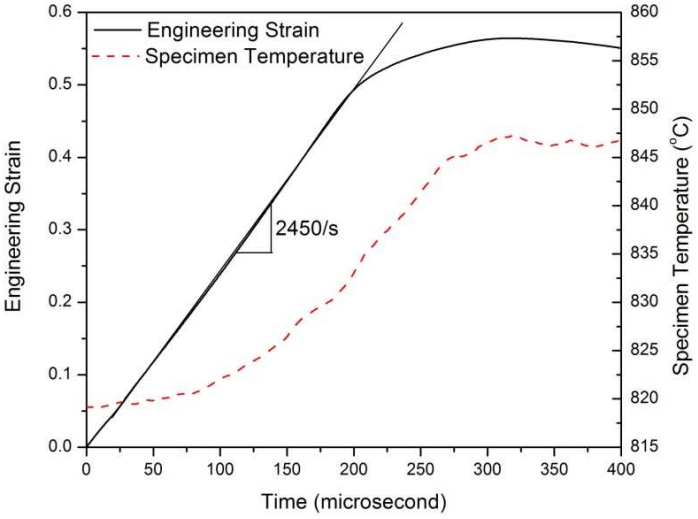

Figure 7.13 Strain and temperature histories in the specimen during dynamic compression
(Reproduced from Song et al. (2010) with permission)

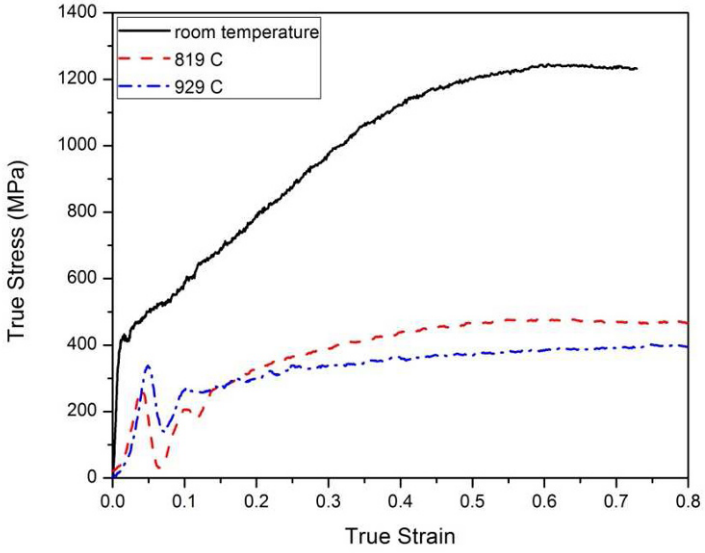

Figure 7.14 Dynamic compressive stress-strain curves of 304L stainless steel at various temperatures
(Reproduced from Song et al. (2010) with permission)

Following the same procedure, dynamic experiments on the 304L stainless steel were conducted at the same high strain rate but at another elevated temperature, 929 ºC. At this temperature, 7- and 30-second quenching times were carried out, respectively. Figure 7.14 summarizes the dynamic compressive stress-strain curves at the strain rate of 2450 s^{-1} at room temperature (23ºC), 819ºC, and 929ºC, respectively (Song et al. 2010). Due to employment of the long striker, the specimen was compressed to large deformation over 50% engineering strain. As shown in Fig. 7.14, temperature significantly affects the stress-strain response of the stainless steel. The flow stress at room temperature is nearly twice of that at elevated temperatures. It is noted that the stress-strain curves at both elevated temperatures exhibit oscillations at small strains, which is different from that obtained at room temperature. This may be due to the microstructure changes in the specimen at elevated temperatures. Furthermore, the microstructure changes are complex, resulting in mixed effects of temperature. The flow stress at large strains (>15%) at 819ºC is higher than that at 929ºC. However, when the strain is less than 15%, the flow stress at 819ºC is lower than that at 929ºC as shown in Fig. 7.14.

7.4 Temperature Effects on a Shape Memory Alloy

Phase transformation is a typical characteristic of shape memory alloys (SMAs). An SMA possesses an austenite phase at high temperatures and a martensitic phase at low temperatures, with a transition temperature in between. An SMA object appears to be permanently deformed at a low temperature in its martensitic phase. When it is heated to above the transition temperature of phase transformation, the alloy returns to its original shape in austenite phase. In addition to the temperature-induced phase transformations, martensitic transformation can also be induced by mechanical stress in a certain temperature range. In this temperature range, the austenite crystal structure in the stress-free alloy will transform into martensitic phase when an external stress exceeding the on-set stress for stress-induced martensite (SIM) is applied.

The temperature around the transition temperature of phase transformation for SMAs is of most interest. As an example of the same material introduced in Chapter 5.3.2, the SMA is NDC (Nitinol Devices & Components, Fremont, CA) SE508 which consists of 55.8% nickel by weight and the balance titanium. The austenite finish transition temperature is between 5 and 18ºC. The temperature range under investigation

here is set from 0 to 50ºC, covering the phase transformation transition temperature. Since the temperature is only 25 ºC above or below room temperature, the effect of temperature gradient on stress-wave propagation is negligible. The heating/cooling chamber shown in Fig. 7.2 was placed between the incident bar and the transmission bar (around the specimen) to control environmental temperatures.

The VascoMax maraging steel bars used for the experiments had a common diameter of 12.3 mm and lengths of 1830, 762, and 305 mm for the incident, transmission, and striker bars, respectively. In order to investigate the temperature effect on both loading and unloading stress-strain response of the SMA, the reverse pulse shaping technique presented in Chapter 2.6 was also implemented to the Kolsky-bar experiments. The front pulse shaping ensures the specimen deforms at constant strain rates under stress equilibrium while the rear pulse shaping unloads the specimen at the same constant strain rate. Except for the environmental temperature, the experimental procedure is the same as that presented in Chapter 5.3.2.

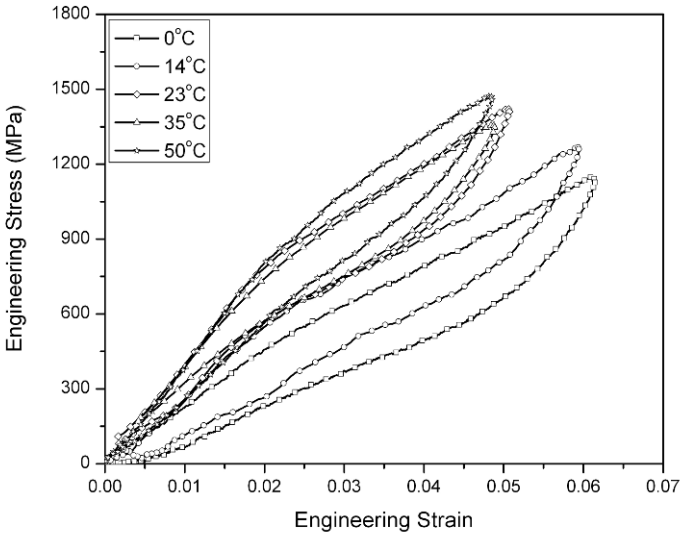

Figure 7.15 Dynamic stress-strain curves of the Nitinol SE508 at various temperatures
(Reproduced from Chen and Song (2006) with permission)

Figure 7.15 summarizes the dynamic compressive stress-strain curves at the strain rate of 430 s^{-1} for the Nitinol SE508 SMA at environmental temperatures of 0, 14, 23, 35, and 50ºC (Chen and Song 2006). Although the environmental temperature varied within a small range of 50 ºC, significant temperature effect was observed in the resultant stress-strain responses. As the environmental temperature decreases from 50 to 0ºC, the slopes of both the loading and unloading stress-strain curves decreased. When the environmental temperature is below room temperature, i.e., 14ºC and 0ºC, the strain does not return to zero, as indicated by the residual strain in the unloading stress-strain curves at these temperatures, even though the specimen has been completely unloaded. The specimen eventually recoverd all strains at room temperature. This phenomenon indicates that, under high-rate deformation, the reverse phase transformation needing thermal energy input may not be as fast as the forward SIM. When the environmental temperature is close to the phase transformation temperature, the heat is drawn from the specimen to assist the reverse transformation. The temperature in the specimen may drop below the phase transformation temperature during the unloading. The reverse transformation is consequently terminated unless more heat is drawn from the environment to drive the specimen temperature back above the transition temperature. It is also observed that, although 0ºC is below the transition temperature of phase transformation of the SMA, superelasticity is still reached. This indicates that the forward SIM driven by stress actually released heat into the specimen, resulting in the actual specimen temperature above the transition temperature of phase transformation during the superelastic deformation in the specimen.

7.5 Temperature Effects on an Epoxy Syntactic Foam

This set of experiments explores the effects of temperature on the dynamic compressive properties of a syntactic epoxy foam. The epoxy syntactic foam is the same material as described in Chapter 4.5.3.1, which had a glass transition temperature of 70ºC. The cylindrical specimens had a diameter of ~12.60 mm and a thickness of ~4.10 mm.

The Kolsky bar used was made of 7075-T6 aluminum alloy and had a common diameter of 19.05 mm. The incident, transmission, and striker bars were 2134-, 803-, and 305-mm long, respectively. Annealed C-11000 copper disks were used to shape the incident pulse to ensure nearly constant strain-rate deformation of specimens under dynamic

equilibrated stresses. The single-loading feature employed in the stainless steel experiments (Fig. 7.8) was also used on the aluminum bar to facilitate microscopic examinations on damage mode in the syntactic foam after loading.

Specimen temperature consists of adiabatic temperature rise during dynamic compression and environmental temperature. The environmental temperature is controlled by the environmental chamber. Unlike the stainless steel specimens that went through large strains at high rates, the adiabatic temperature rise in the epoxy syntactic foam specimens during dynamic compression is expected to be negligible. To verify this, a miniaturized thermocouple was embedded into the specimen to record the temperature history during dynamic loading. The T-type thermocouple with a low thermal mass and a small diameter of 75 μm was placed inside the specimen through a small hole. Since the specimen was damaged by the small hole for thermocouple before mechanical loading, the measurements of temperature rise therefore provided only an estimation of the adiabatic heating.

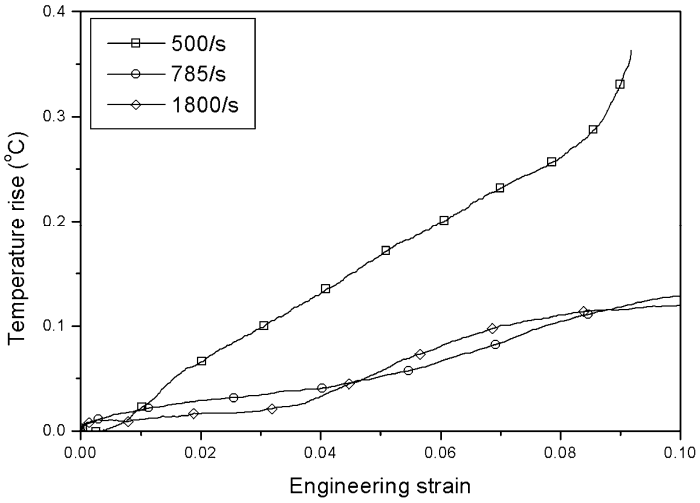

Figure 7.16 Adiabatic temperature rise in syntactic epoxy foam specimens deforming at different high rates
(Reproduced from Song et al. (2005d) with permission)

Figure 7.16 shows the temperature rise in the syntactic epoxy foam specimens as a function of engineering strain during dynamic compression at strain rates of 500, 785, and 1800 s^{-1}, respectively (Song et al. 2005d). The adiabatic temperature rise in the specimen is verified to be small in all three cases. Little heat was generated during dynamic compression because of the small failure strain and low failure strength of the epoxy syntactic foam. Although it is clear that the effects of adiabatic temperature rise in the syntactic foam specimen are negligible, it is interesting to note that the temperature rise at the strain rate of 500 s^{-1} is higher than that at the strain rates of 785 and 1800 s^{-1}. This phenomenon may be the result of a change in the failure/damage mechanism in specimen. The mechanical energy in the specimen during dynamic deformation is dissipated either through the formation and propagation of small cracks or through the generation of heat, or both. In a related study (Song et al. 2004b), it was observed that more microcracks formed in the foam specimen under higher-rate dynamic loading than under lower-rate dynamic loading. The mechanical energy in the specimen at higher dynamic strain-rate deformation was mostly dissipated through the formation and propagation of small cracks

To control the environmental temperature, a heating/cooling system schematically shown in Fig. 7.2 was placed between the incident bar and the transmission bar over the test section of the Kolsky bar. Since the temperature range of the syntactic foam in the most proposed engineering applications is expected to be approximately -55˚C to 75˚C, the temperatures at which the Kolsky-bar experiments were conducted at -54ºC, -25ºC, 0ºC, 23ºC(room temperature), 50ºC, and 74ºC, which spanned over the glass transition temperature of 70˚C for the epoxy syntactic foam.

The experimental procedure is the same as that described in Chapter 4.5.3.1. Figure 7.17 shows the resultant dynamic uniaxial compressive stress-strain curves at the temperatures of -54ºC, -25ºC, 0ºC, 23ºC, 50ºC, and 74ºC at the strain rate of 550 ±10% s^{-1} (Song et al. 2005d). In Fig. 7.17, unloading portions in the low temperature stress-strain curves (-54˚C and -25˚C) were recorded since the maximum strains achieved in both experiments were slightly below the failure strain. However, no unloading part was meaningful in the other stress-strain curves due to specimen failure. The stress-strain curves of the syntactic foam show that the material is strongly sensitive to environmental temperature at the same strain rate: the initial modulus of elasticity, maximum failure stress and the strain at maximum stress are all dependent on environmental temperature.

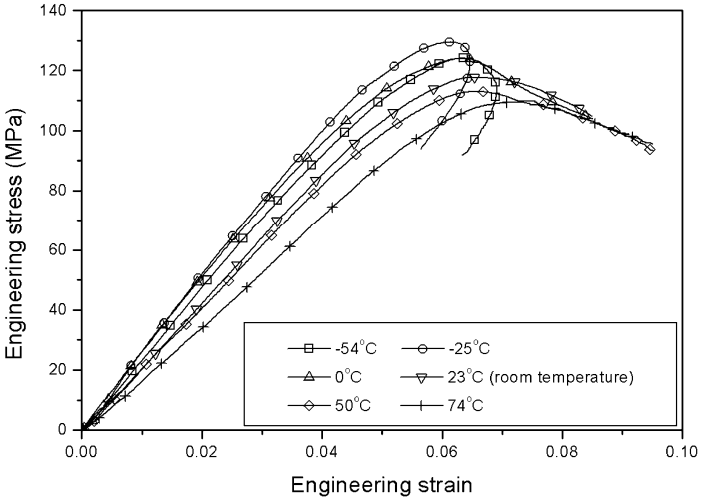

Figure 7.17 Dynamic compressive stress-strain curves at various temperatures *(Reproduced from Song et al. (2005d) with permission)*

Within the range of environmental temperature in this research, an approximate threshold temperature value of -25ºC separated the trends of temperature dependencies into two regions. When environmental temperature is above the threshold value (-25ºC), the stress-strain curves exhibit increasing initial modulus of elasticity and maximum failure strength, but decreasing maximum failure strain with decreasing environmental temperature at the same strain rate. However, when environmental temperature is below the threshold value, both the modulus of elasticity and maximum failure strength decreased with decreasing temperature. The maximum failure strain increased at the temperature of -54ºC in comparison to that at the temperature of -25ºC. The stress-strain curve at the temperature of -25ºC had the highest values of initial modulus of elasticity (2.60 GPa) and maximum failure strength (130 MPa), and the lowest value of maximum failure strain (6.1%) within the temperature range from -54ºC to 74ºC.

At a fixed strain rate, e.g., 550 s^{-1}, when environmental temperature was above the threshold temperature of -25ºC, thermal-softening may dominate the stress-strain behavior. However, when a specimen was in an environment with a temperature below -25ºC, damage-softening due to the formation and propagation of cracks in specimen dominates over the lower-temperature-induced hardening. It is also noted that, when the environmental temperature exceeded the glass transition temperature (70ºC) of the foam material, the initial modulus of elasticity did not exhibit significant decrease.

The specimens after mechanical tests were mounted into epoxy resin to examine the failure modes with optical microscopy. Due to the utilization of pulse shaping and single loading, specimens were loaded only once during dynamic compression. The failure modes preserved in the specimens after mechanical loading thus correspond to the well-defined loading history. Figures 7.18(a), (b), and (c) show the micrographs of the recovered specimens after mechanical tests at the same strain rate of 550 s^{-1} at various temperatures (0ºC, 23ºC, and 74ºC) (Song et al. 2005d). At a low temperature, e.g., 0ºC, a significant crack, which connected glass-microspheresites, was observed in the specimen, as shown in Fig. 7.18(a). This crack oriented ~45º to the loading axis. When the temperature rose to 23ºC, instead of significant cracks, some microcracks were formed through connecting a few glass microspheresites (Fig. 7.18(b)). As the temperature further close to 74ºC, less glass microspheresites were found to connect together (Fig. 7.18(c)). Most of glass microspheresites distributed in specimen separately (Fig. 7.18(d)), implying less microcracks in specimen at high temperatures. The results of micrographs in Fig. 7.18 indicate that the specimen exhibits brittle behavior at low temperatures, as indicated by the connecting microspheresites that leads to the formation of small cracks (Fig. 7.18(a)), but the failure mode changes at high temperatures where no connected microspheresites were observed (Figs. 7.18(c) and (d)).

To further investigate the effects of environmental temperature on dynamic compressive response of the foam, dynamic compressive experiments at the temperatures of 50ºC, 23ºC, 0ºC, and -54ºC at a higher strain rate of 1100/s were then conducted. The resultant dynamic compressive stress-strain curves are shown in Fig. 7.19 (Song et al. 2005d). The experimental results at this higher strain rate exhibited similar dependencies of the stress-strain behavior on environmental temperature as those at the strain rate of 550 s^{-1}.

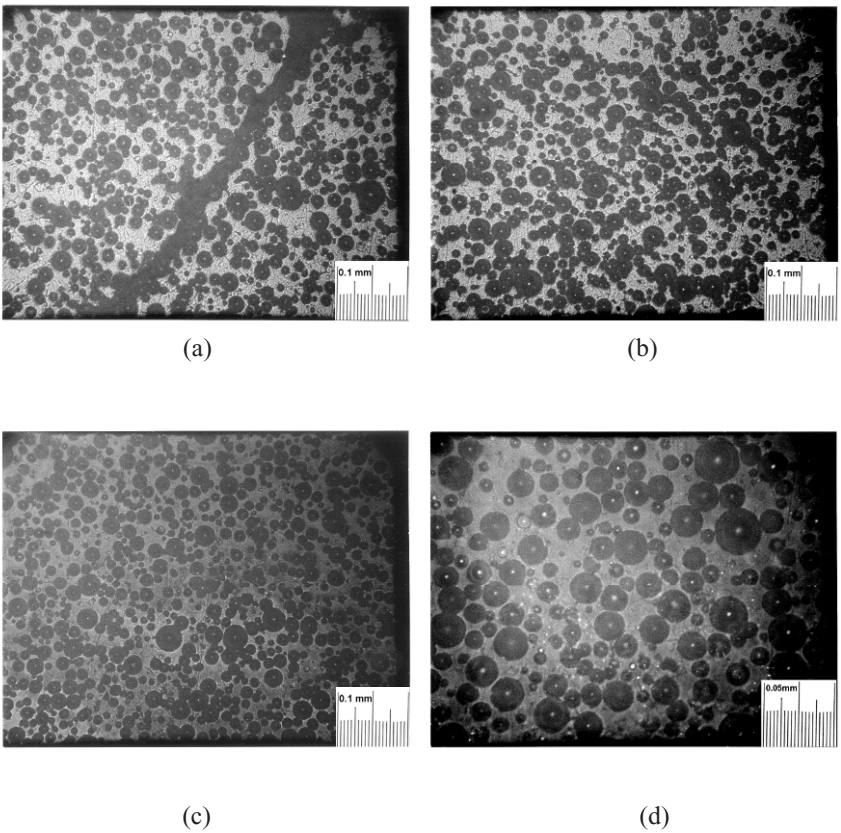

(a) (b)

(c) (d)

Figure 7.18 Failure modes in specimens
(a) 0ºC; (b) 23ºC; (c) 74ºC, 100X; (d) 74ºC 200X
(Reproduced from Song et al. (2005d) with permission)

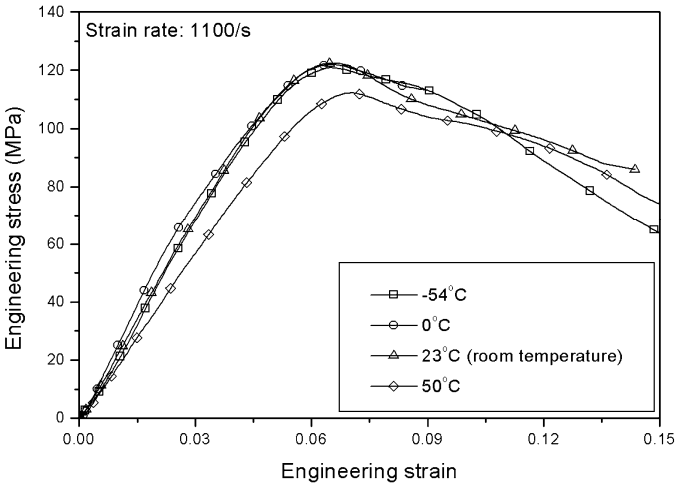

Figure 7.19 Dynamic compressive stress-strain curves at various temperatures (1100 s^{-1})
(Reproduced from Song et al. (2005d) with permission)

7.6 Temperature Effects on PMDI Foams

The compressive stress-strain response of the PMDI foam materials with different densities at room temperature has been described in Chapter 4.5.3.2. Here, we present the effects of temperature on the compressive response of the PMDI foam materials with three different densities (0.31×10^3, 0.41×10^3, and 0.55×10^3 kg/m^3). Dynamic compression experiments were conducted at various temperatures (-54ºC, -12ºC, 50ºC, 74ºC), in addition to room temperature (22 ºC). These experiments had a fixed dynamic strain rate of 3×10^3 s^{-1} (Song et al. 2009d).

The heating/cooling chamber shown in Fig. 7.2 was used to control temperature in the experiments. The temperature was the only variable in this set of experiments. Strain rate was maintained to be nearly identical for each density foam material. Figures 7.20, 7.21, and 7.22 show the compressive stress–strain curves of the foam materials with three differ-

ent densities at various temperatures (Song et al. 2009d). For foam materials with a certain density, temperature influences the plateau stress of the foam materials. For the materials with densities of 0.31×10^3 and 0.41×10^3 kg/m^3, the stress-strain curves do not significantly change in shape when the temperature varies (Figs. 7.20 and 7.21). However, the shape of the stress–strain curve for the 0.55×10^3 kg/m^3 foam material changes from low to high temperatures. As shown in Fig. 7.22, all of the stress–strain curves exhibited an ''N'' shape except for that obtained at the temperature of 347 K (74ºC). Instead, the stress–strain curve at 347 K exhibits a long plateau, which was similar to the curves obtained at low strain rates (Fig. 4.35(c)). The variation in the shapes of stress–strain curves was due to different deformation and collapse mechanisms at different temperatures. The material appears more brittle at lower temperatures, causing sudden collapse of the cell structures. At high temperatures, the foam material is more ductile, resulting in plastic buckling as the major deformation. Even under impact loading, the 0.55×10^3 kg/m^3 foam specimen still exhibited load-bearing capability at high temperatures.

We take the yield strength of the foam materials at various temperatures to determine the temperature effect more quantitatively. The results are shown in Fig. 7.23 (Song et al. 2009d). The yield strength increases with decreasing temperature for all three foam materials. However, the sensitivity of the yield strength to the temperature depends on the density of the foam material, as indicated by the different slopes in the temperature sensitivity curves in Fig. 7.23.

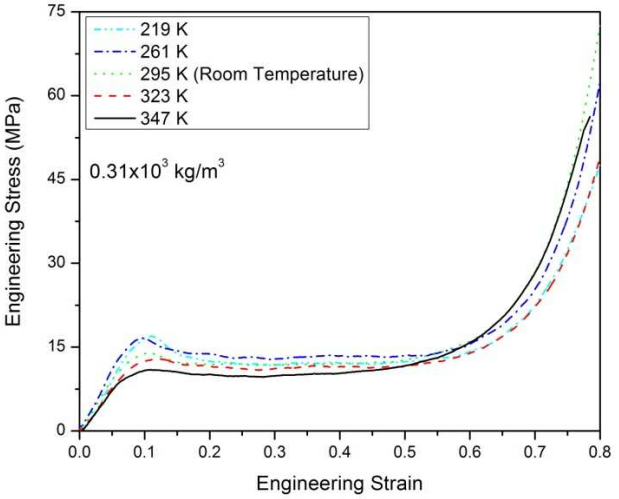

Figure 7.20 Stress-strain curves of 0.31×10^3 kg/m^3 foam at various temperatures
(Reproduced from Song et al. (2009d) with permission)

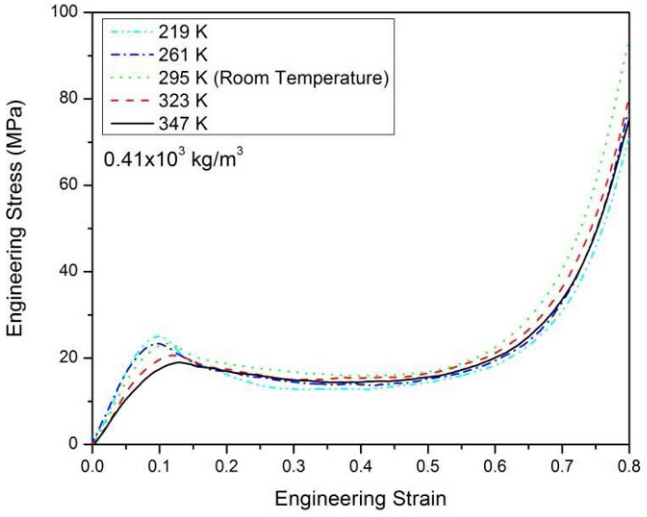

Figure 7.21 Stress-strain curves of 0.41×10^3 kg/m^3 foam at various temperatures
(Reproduced from Song et al. (2009d) with permission)

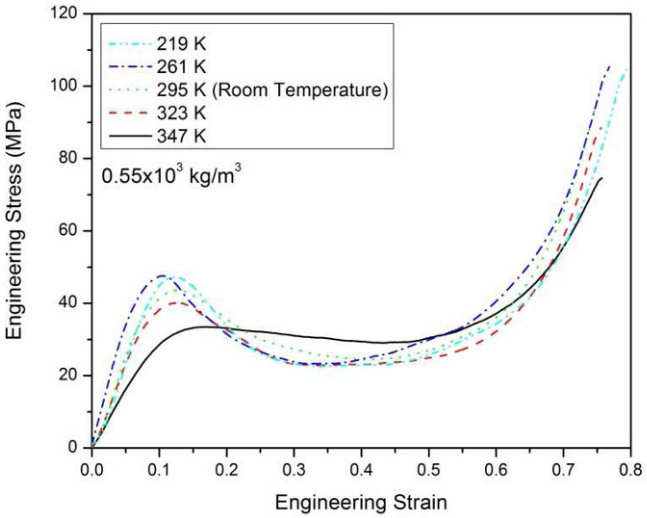

Figure 7.22 Stress-strain curves of 0.55×10^3 kg/m^3 foam at various temperatures
(Reproduced from Song et al. (2009d) with permission)

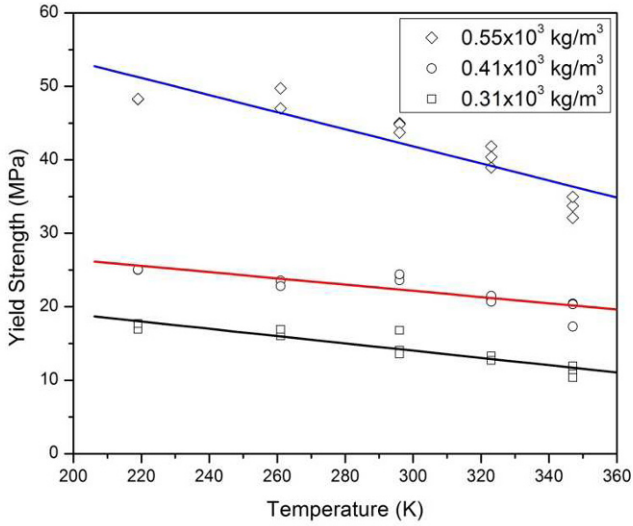

Figure 7.23 Temperature sensitivities of the foam materials with different densities
(Reproduced from Song et al. (2009d) with permission)

Chapter 8. Kolsky Bar for Dynamic Tensile/Torsion Experiments

In addition to the compression version of the Kolsky bar, there are bars that subject the specimen under tension, torsion, and combined torsion/axial loading conditions to explore the high-rate response of materials under more diversified stress states. The work principles of these bars are similar to that of Kolsky compression bar. However, the loading mechanisms are more complicated than the simple bar-to-bar impact seen in compression experiments. The specimens in both tension and torsion experiments must be attached to the bar ends, which brings in the complication of gage-section identification in strain-rate calculations. This chapter describes various designs of Kolsky bars to conduct dynamic experiments for the specimen stress-strain response under uniaxial tension, pure torsion, combined tension/torsion, or compression/torsion. The designs of specimens will also be described. Examples of high-rate uniaxial tension experiments on polymers, bones, and high-performance fibers are provided.

8.1 Methods to Apply Dynamic Tension on Specimens

Tensile versions of the Kolsky bar started to emerge in 1960's. Harding et al. (1960) developed a method that is schematically shown in Fig. 8.1 to conduct dynamic tension experiments. In their design, the input bar is made of a hollow tube. An elastic bar is attached inside the hollow tube with a yoke connected to the tube end to determine the input loading condition (Fig. 8.1(a)). The specimen assembly shown in Fig. 8.1(b) then replaces the elastic bar for dynamic tension test under the same loading condition. This two-step method was later modified by placing incident and transmission bars with a specimen in between inside the tube for dynamic tensile testing of composites, as shown in Fig. 8.2 (Harding and Welsh 1983). This modified design is nearly the same as the earlier design by Hauser in 1966 as shown in Fig. 8.3. The principle behind these designs is to transfer the external impact into axial tension through an external tube which is connected to the Kolsky-bar system. This approach allows the launching device from a compression bar, i.e. a gas gun, be directly used for the tension bar. However, the entire tension setup is inside a solid tube, which is not efficient in terms of instrumentation (e.g., strain gages on the incident and transmission bar surfaces or temperature sen-

W.W. Chen and B. Song, *Split Hopkinson (Kolsky) Bar: Design, Testing and Applications*, Mechanical Engineering Series, DOI 10.1007/978-1-4419-7982-7_8,

sors on the specimen) and visual observation (e.g., high-speed imaging of the specimen deformation process or optical strain measurements). Other forms of generating tensile loading continue to emerge.

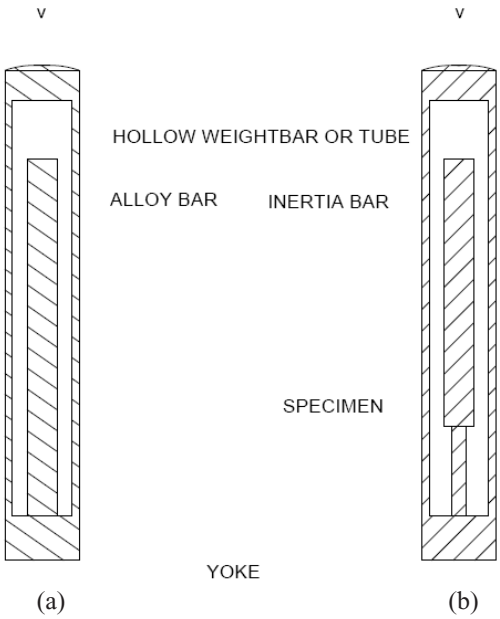

Figure 8.1 An earlier version of tension bar developed by Harding et al. (1960)

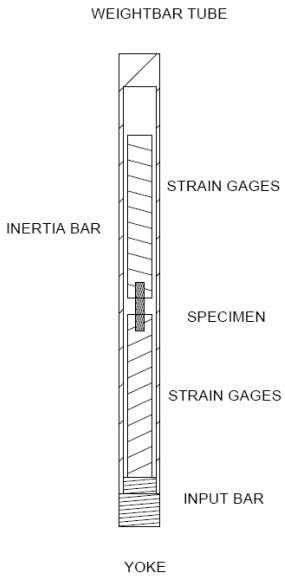

Figure 8.2 A modification of the system by Harding and Welsh (1983)

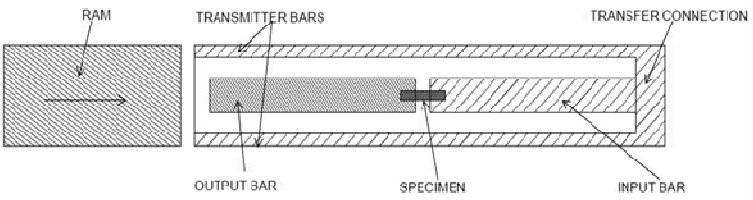

Figure 8.3 Hauser's design of Kolsky tension bar

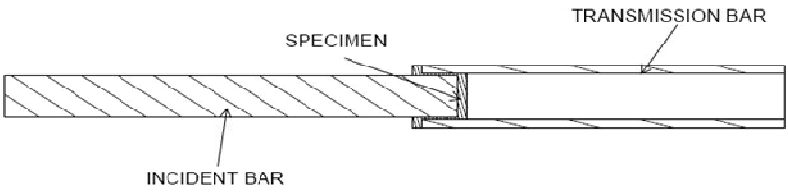

Figure 8.4 A "top-hat" specimen for dynamic tension tests

The simplest modification is a "top-hat" specimen geometry proposed by Lindholm and Yeakley (1968). In this design, a "top hat" specimen is sandwiched between the incident bar and a hollow transmission tube. Figure 8.4 shows a configuration of this design. The compression stress waves in the incident bar strike the inside of the specimen hat, which causes a tensile load on the specimen gage section. The stress wave then propagates into the transmission tube in compression. To increase the stress amplitude in the specimen, the specimen gage section was not entirely solid. Lindholm and Yeakley (1968) split their tube portion of the hat specimen into four arms with a length to width ratio of 2. Using a specimen hat has minimal modifications to the Kolsky compression bar and does not require attaching the specimen to the bar ends which typically involves threading both the specimen and bar ends. By placing different specimens on the side of hat-shaped specimen section, Lindholm and Yeakley's design also accommodates the testing of multiple specimens in one experiment. Mohr and Gary (2007) recently proposed an M-shaped specimen that uses a compression bar to apply dynamic tensile load on small specimens.

Nicholas (1981) proposed a very clever way of utilizing a compression bar to perform tensile experiments. His design is schematically shown in Fig. 8.5. A specimen is threaded onto the ends of the incident and transmission bar in the test section. A rigid collar is placed over the specimen to allow the compression wave to pass through the collar and leave the specimen virtually untouched by the initial compression wave. The cross-sectional area of the collar is much larger than that of the specimen. Most of the compression energy in the incident bar due to the impact of striker is transferred into the transmission bar. When the com-

pression stress wave travels to the free end of the transmission bar, it is reflected back as a tensile wave propagating back towards the specimen. When this tensile wave arrives at the specimen, the rigid collar cannot support the tensile wave and the specimen is subjected to a dynamic tensile pulse. Nicholas' setup uses a conventional Kolsky compression bar setup of 4130 steel with the ends being heat treated to about Rc47 to ensure that the ends would not deform during loading. This method involves minimum modifications to the existing Kolsky compression bar. The only modifications are to thread the bar ends and to make a rigid collar. However, the specimen in this design is inevitably subjected to compression before tension even though the collar is used.

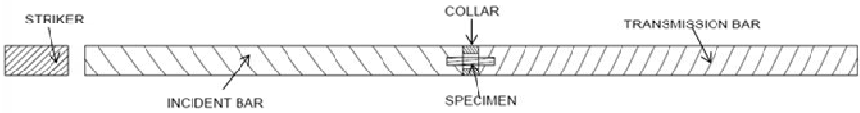

Figure 8.5 Generation of tensile load using compression wave reflection

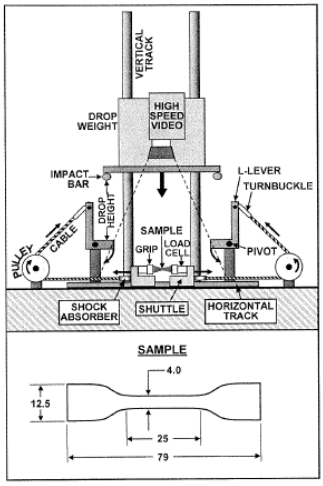

Figure 8.6 A drop-weight driven tensile tester
(Reproduced from Mott et al. (2007) with permission)

At lower rates, Mott et al. (2007) modified a drop tower with a pulley system to test elastomers at strain rates of 10 to 1600 s^{-1}. The setup drops a 100 kg weight onto an L-lever. A set of impact bars are attached to the drop weight plate in order to allow the lever to rotate and to attain line contact with the L-lever system (Fig. 8.6). The L-lever is allowed to pivot using low friction bearings; it is also connected to a pulley system that in turn connects to a shuttle piece. The shuttle piece grips onto the sample and subjects the sample to tensile loading. It is critical that the L-lever system is aligned meticulously in order to accommodate even loading.

The most commonly used loading method in a Kolsky tension bar is direct tension. Similar to the compression case, there are two main types of direct tension methods. One is to store elastic energy by stretching a section of the incident bar in tension (Staab and Gilat 1991; Cadoni et al. 2009). The section begins at the far end (from the specimen) of the incident bar. A clamp divides the pre-stressed and stress-free sections. The sudden release of the clamp allows the release of stored energy in the form of tensile stress waves, which propagate towards the specimen and load it dynamically in tension. Figure 8.7 shows a system using stored energy (Cadoni et al. 2009). In this setup, a pre-stressed bar is used to store the tensile elastic energy. The sudden breaking of a brittle intermediate piece results in a tensile wave in the incident bar. The brittle blocking piece may be a clamp with a sudden-release feature. In such a system, the way the brittle piece breaks or the clamp releases is difficult to control. Therefore, pulse shaping in these systems is not feasible.

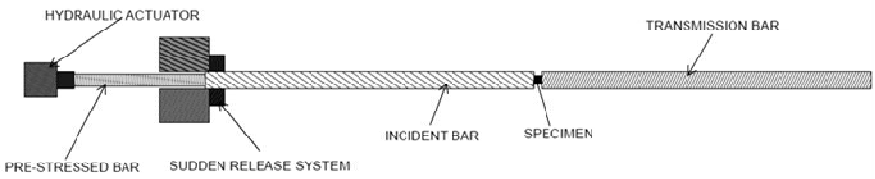

Figure 8.7 Generating a tensile pulse using stored energy

The other approach to generate direct tension in the incident bar is to strike a flange at the end of the incident bar with a form of kinetic energy. One approach to generate the kinetic energy is to use a rotating disk loading system with impact hammers (Kawata et al. 1979). Figure 8.8 show a schematic of such a loading system in a Kolsky tension bar.

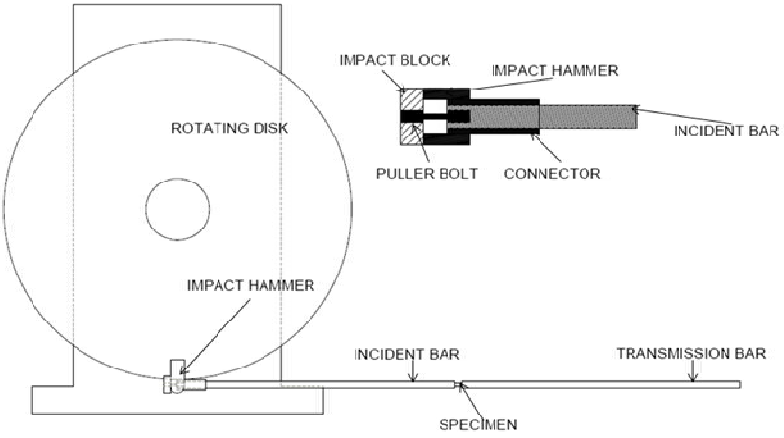

Figure 8.8 A rotating-disk loading system on a tension bar
(Reproduced from Kawata et al. (1979) with permission)

Before the disk is accelerated, the hammers are retracted into the disk through a caging device. An electromagnetic controller releases the hammers when the disk is rotating at the desired speed, subjecting the hammers to impact on the block which is connected to the incident bar with a prefixed metal bar, as shown in Fig. 8.8. The prefixed metal bar is thus stretched to fracture, generating a tensile pulse in the incident bar. The prefixed metal bar provides a means for pulse shaping. With the proper use of the material and geometry of the bar, the shape of the incident pulse can be controlled to some extent. Figure 8.9 shows a similar system with a more elaborate design for waves traveling in the incident bar after the hammer impact (Li et al., 1993). This tensile setup can actu-

ally conduct dynamic experiments under single and multiple tension loads.

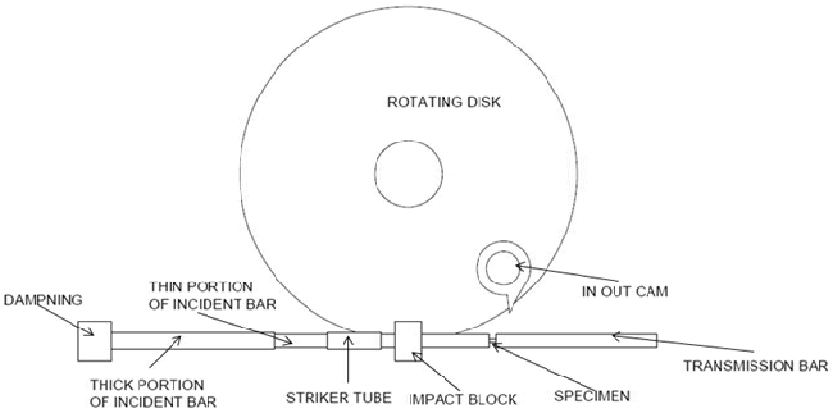

Figure 8.9 A rotating-disk bar for tension and tension-tension loads
(Reproduced from Li et al. (1993) with permission)

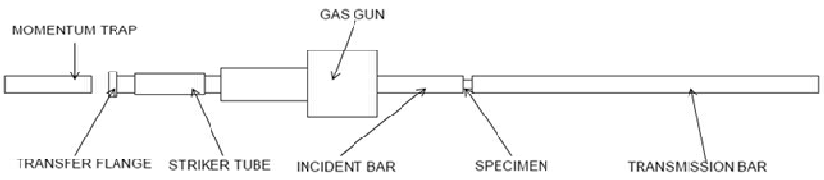

Figure 8.10 A direct impact tension bar

Another direct loading method is to drive a tubular striker by either a gas gun or a spring system. The tube slides on the incident bar. When the tube impacts on a flange at the end of the incident bar, a tensile pulse is generated in the incident bar and propagates to the specimen. Except for the tubular striker and the tensile test section, this method is similar to the Kolsky compression bar. Figure 8.10 shows a schematic of such a system. The gas gun chamber can be designed to envelope the bar, as shown in Fig. 8.10, or on the side of the bar as shown in Fig. 8.11 (Owens and Tippur 2009). The momentum trapper on the left side provides the possibility for single-loading capability on the specimen when the gap between the trapper and the flange on the incident bar is properly set. The gap should close after the generation of the first incident pulse, as illustrated in Fig. 2.25 (Nemat-Nasser et al. 1991). The impact surfaces between the striker and the flange provide a platform for placing pulse shapers that control the profiles of the incident pulses.

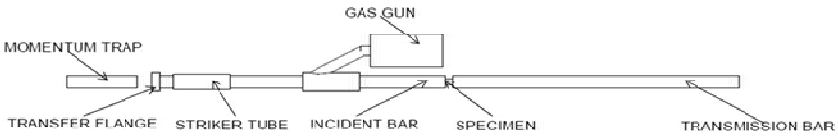

Figure 8.11 A different design of the direct-impact tension bar
(Reproduced from Owens and Tippur (2009) with permission)

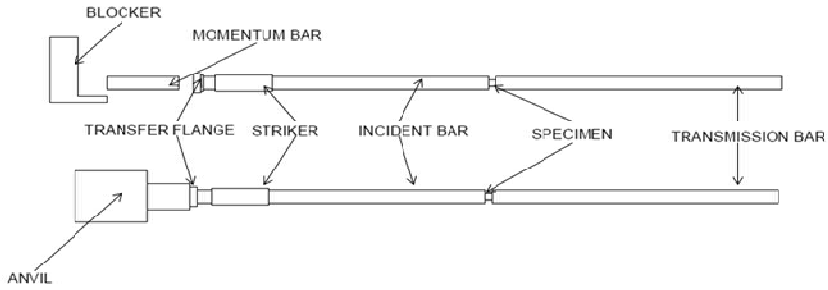

Figure 8.12 A direct impact tension bar for multiple loading
(Reproduced from Ogawa (1984) with permission)

The interface between the flange and the momentum trapper provides another platform for controlling loading pulses. Figure 8.12 shows a design for the momentum-trapping system that, when properly arranged, can load the specimen with multiple loads such as tension-tension and tension-compression-tension (Ogawa 1984). The desired loading conditions were achieved by the employment of a momentum bar or an anvil that controlled the impedance mismatch between the incident bar and the momentum-control devices. The second loading pulse arriving at the specimen was either tension or compression.

In the design shown in Fig. 8.13, the momentum-control device is a massive bar to divert most of the impact force to the trapper (Nie et al. 2009). The purpose is to strike the flange at velocities sufficiently high for consistency while generating a low-amplitude incident pulse for loading a soft specimen. The design in Fig. 8.13 also uses a compound incident bar where an aluminum bar with a smaller diameter (smaller impedance) connects to the initial steel portion of the incident bar. This connection reflects part of the low-amplitude incident pulse back into the steel portion of the incident bar, further reducing the amplitude of the incident pulse that propagates along the aluminum bar to the soft specimen.

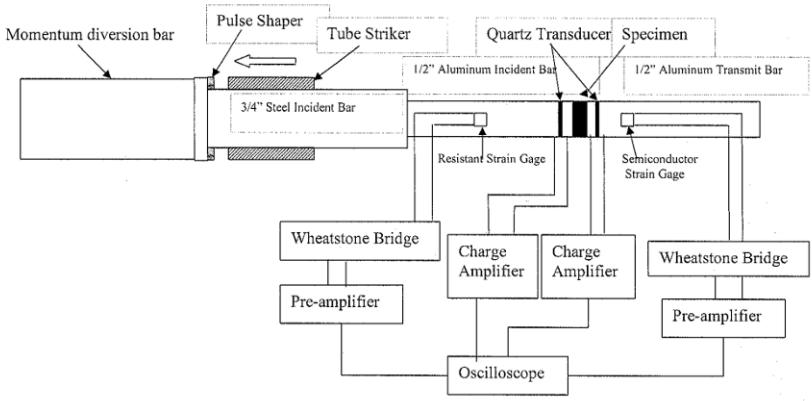

Figure 8.13 A tension bar for soft specimens
(Reproduced from Nie et al. (2009) with permission)

8.2 Tension Specimen Design

The design considerations for tension specimens are similar to compression specimen in terms of dynamic equilibrium and the strength limit of the Kolsky bars. In tension experiment design, there are more factors that need to be taken into account. The largest variation from compression experiments is that the specimen must be firmly connected to the bar ends in tensile experiments. The joint between the specimen and the bars may be clamped, threaded, bonded, or specially gripped. The clamped joint is used mostly for materials that are difficult to thread or bond, for example, soft tissues or polymers. Figure 8.14 shows the clamping system to attach a rubber specimen to the tension bar ends. The specimen is a sheet that is wrapped around the bar ends and then clamped to the bars. The inner surface of the clamp is artificially made rough to improve the clamping and to prevent uneven shear deformation over the specimen thickness in the clamped area (Nie et al. 2009).

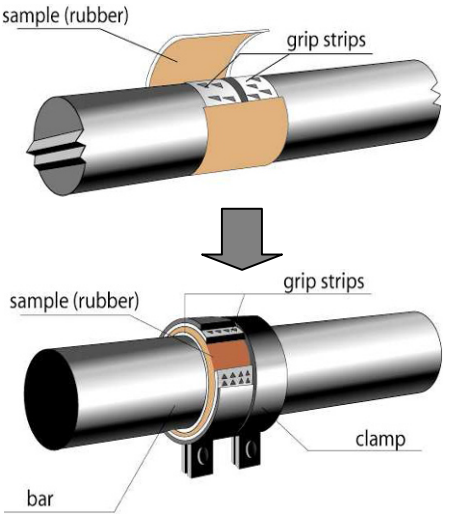

Figure 8.14 A clamped tension specimen
(Reproduced from Nie et al. (2009) with permission)

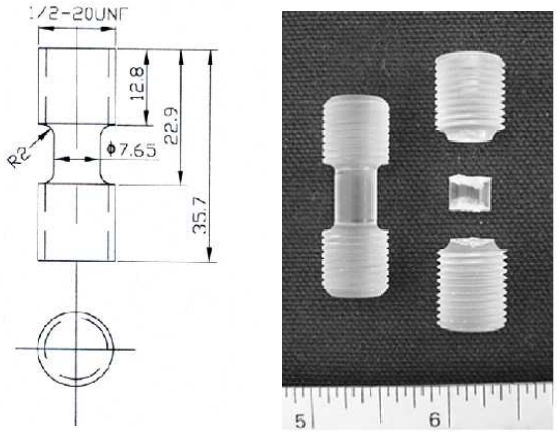

Figure 8.15 A threaded tension specimen
(Reproduced from Chen et al. (2002a) with permission)

Figure 8.15 shows the geometry of a glassy polymer tension specimen before and after dynamic failure. The specimen was tested using a 19-mm diameter Kolsky tension bar with female ½-20 threads on the bar ends (Chen et al. 2002a). The fillet design between the threaded section and the gage section of the specimen is critical to minimize stress concentrations in the specimen. For specimens that are not suitable to be wrapped or threaded, for example flat composite coupons, bonded joint becomes a popular choice. The flat specimen is fit into slots at the bar ends and glued. If the specimen has specific mounting requirements, adaptors can be made to connect the specimen to the bar ends. Figure 8.16 shows an example of a cement tension specimen, which is glued to adaptors at the bar ends. The glued joint ensures that there is no slippage during the dynamic tensile loading. However, it is experimentally not efficient to remove the specimen from the bonded joints after mechanical loading.

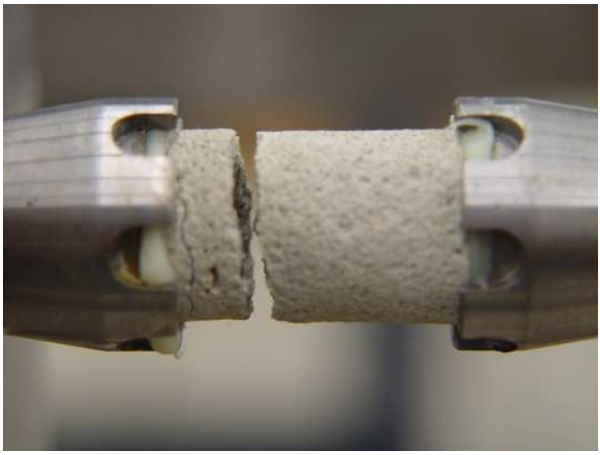

Figure 8.16 A cement tension specimen glued to adaptors

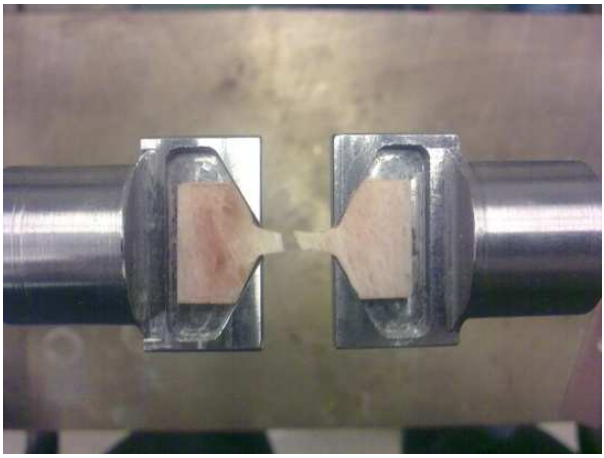

Figure 8.17 A pair of special grips for bone specimen in tension

Some of the tensile specimens have additional gripping requirements where grips with specific purposes are designed. As an example, Fig. 8.17 shows a pair of tension grips that hold a bone specimen. Like most biological tissue specimens, the mechanical response of bone specimens depends on the time duration from the termination of animal to specimen preparation and then to mechanical testing. The properties also depend on the way the samples are preserved before mechanical loading. Due to the time to cure, glued joint is typically not acceptable in the experiments on these materials. The special grips shown in Fig. 8.17 facilitate fast specimen installation and replacement.

Due to the dynamic equilibrium requirements, the specimen length is limited. Therefore, the end effects are more severe in these specimens. Furthermore, the strain rate in the specimen is calculated by the difference between the bar-end velocities divided by the specimen length. In the case of the dumbbell-shaped tension specimens, the gage length is not well determined. The deformation of transition regions of the specimen may be counted as the gage-section deformation, which leads to an over-estimated specimen strain. In the elastic deformation range, Albertini and Montagnani (1977) suggested a way to correct the strain in the specimen,

$$\varepsilon = \varepsilon_m - \sigma \frac{E - E_m}{E E_m} \tag{8.1}$$

where ε_m and σ are calculated from raw data using (1.13) and (1.14), respectively. The specimen length is taken as the length of the gage section. E_m is the measured Young's modulus, which is typically lower than the actual value E. For most metallic and ceramic materials, the value of E does not vary from quasi-static to Kolsky bar strain rates.

Despite such artificial correction measures, the unknown end-effect zone and the vague gage length form a major concern for uncertainties in the data reduction for strain-rate and strain histories in the tension specimen. For this reason, strain measurements directly from specimen surface are preferred. For example in a brittle specimen, a strain gage is mounted on the surface of the specimen gage section as an effective method. For specimen materials that deform to larger strains, optical methods provide more accurate measurements.

One optical method is digital image correlation (DIC) which proves to be very effective (Gilat et al. 2009). Both 2-D and 3-D full field specimen surface deformation histories can be recorded and analyzed using this method. The 2-D strain fields can be imaged by one camera with its optical axis perpendicular to the plane of deformation. By contrast,

the 3-D strain fields need images taken from two different angles and can be imaged either by two synchronized high-speed digital cameras or by projecting images from two directions to different portions of one camera aperture. The experiment is performed the same way as a regular Kolsky tension bar test with the gage section accessible for optical camera access. The specimen surface is prepared with a random pattern for automatic position tracking. A high-speed camera is triggered when the specimen starts to deform and records the deformation process. For typical Kolsky bar experiments, the camera speed needs to be around 80,000 to 300,000 frames per second. A DIC analysis then tracks the motion of the random dots on the pattern and calculates the progressive full-field displacement and strain fields. With the known imaging frame rate, the strain rate can be determined. This method provides direct strain measurement over the entire specimen surface. In addition, the end-effect zone may be visible from the images.

8.3 Pulse Shaping in Tension Experiments

Similar to compression experiments, the desired profiles of the incident pulses are determined by the specimen response and intended loading conditions on the specimen such as strain rate and ultimate strain. Unlike compression experiments where the impact surface of the incident bar is available to attach well-designed pulse shapers to tailor the incident pulses, the impact surface is not available (in the cases of pre-stressed bars) or very limited (in the cases of rotating wheel and tubular impact). Only limited pulse-shaping efforts have been reported based on trial-and-error approaches (Chen et al. 2002, Nie et al. 2009). A new design that can fully utilize the compression pulse-shaper techniques is emerging (Guzman et al. 2010, Song et al. 2010).

8.4 Methods to Generate Dynamic Torque

Compared to the Kolsky compression and tension bars, the torsion version of the Kolsky bar eliminates the radial inertia effects in the bars. Therefore a torsion test is most closely described by one-dimensional stress wave theory since the wave propagation in the elastic bars is non-

dispersive. Baker and Yew (1966) developed the original torsion bar on top of a lathe. Figure 8.18 is a schematic of this design.

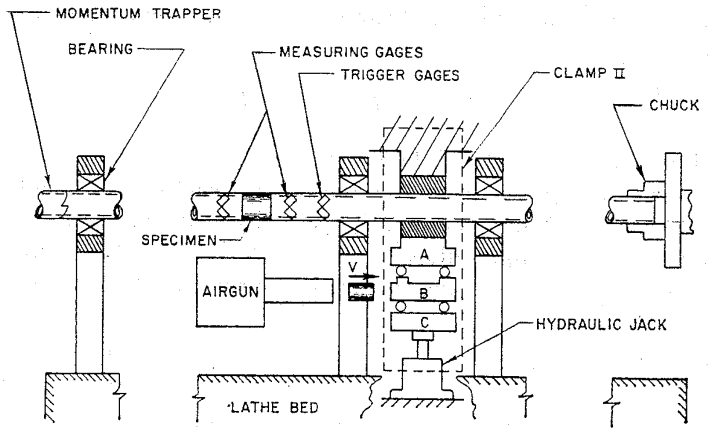

Figure 8.18 Baker and Yew's design of Kolsky torsion bar
(Reproduced from Baker and Yew (1966) with permission)

This design has similarities to the pre-stressed versions of the tension bars. As shown in Fig. 8.18, the lathe chuck clamps on the loading end of the incident bar on the right side of the figure. A hydraulic clamp holds the incident bar at a selected location. The section of the incident bar between the clamp and the chuck will be pre-stressed in torsion. The length of this section depends on the needed duration of the loading pulse. The specimen is a thin tube which was brazed to the incident and transmission bars. The far end of the transmission bar is connected to a momentum trapper through a one-direction jaw. During an experiment, the pre-stressed section is twisted by the chuck within the elastic range of the incident bar. The clamp is then suddenly released by shooting a projectile against a movable link in the clamp system (Fig. 8.18). This lets the torsional strain energy to propagate towards the specimen in the form of one-dimensional shear wave. When the shear wave arrives at the specimen, part of the wave is reflected back due to impedance mismatch between the bar and the specimen and the rest propagates through the

specimen into the transmission bar. The surface strains associated with the waves are recorded using the surface strain gages mounted 45° from the axial direction. The data analysis is the same as in the compression or tension bars.

Duffy et al. later (1971) used explosive loading to initiate the one-dimensional torsion waves in the incident bar. They used copper pulse smoother to filter out the high-frequency components in the initial torsion wave generated by the detonation of the explosive, which is the first documented effort for pulse shaping. Most torsion bars use mechanical methods to store torsional strain energy in a pre-stressed section of the incident bar similar to Baker and Yew (1966). The torque generator may be a simple pulley or a hydraulic rotation actuator. Figure 8.19 shows a schematic of a typical torsion bar setup where the clamp is also shown in detail.

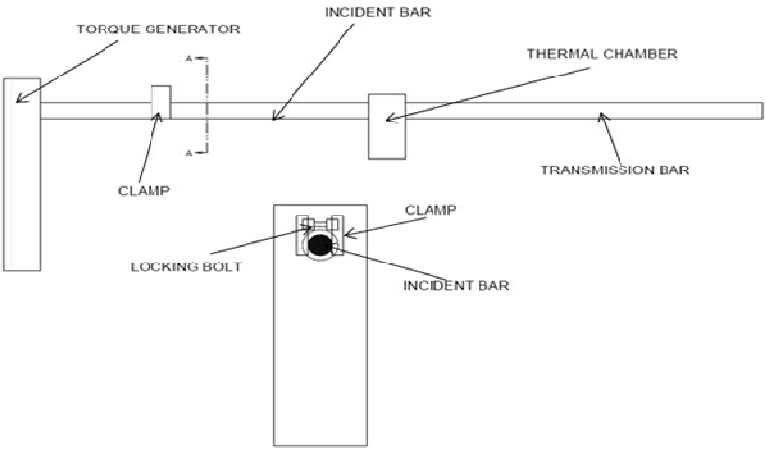

Figure 8.19 A typical torsion bar

In the setup shown in Fig. 8.19, a torque generator (mechanically driven pully) is used to twist the incident bar between the pulley and the clamp position (marked A-A). The clamp consists of two side columns with the incident bar in between. The tops of the columns are connected by a locking bolt (pin) that has a very sharp notch in the middle (see A-A View). The incident bar is clamped in the middle. The clamping force is provided by a hydraulic actuator near the bottom. When the actuator is in action, the bar is compressed across its diameter, and the locking pin is in tension. The initial clamping force should be sufficiently high such that the incident bar is firmly clamped without any slip when the torque is applied. However, the initial clamping force should not break the locking pin. When the torque is at a desired level (determined by the intended strain rate and specimen response), further clamping force is applied by the hydraulic actuator. The increasing clamping force produces increasing tensile load in the locking pin until the pin fails suddenly at the sharp notch. The torque then transmits into the incident bar in the form of torsion wave. To generate a clean incident pulse, the material for the locking pin should have a brittle fracture, such as cast iron or strong aluminum alloys.

8.5 Torsion Specimen Design

Since there exists strain gradient along the radius of a cylinder under twist, the specimen in a torsion bar experiment is typically a thin tube to approach uniform strain in the gage section. The typical specimen designs for torsion experiments are shown in Fig. 8.20 (Hartley et al. 1987). Both have short and thin-walled central gage sections. The specimen on the left side has circular flanges that can be bonded to the bar ends. The large area of the flanges provides sufficient bond area to support the torsion load necessary to deform the much-smaller gage section plastically. The advantage of the circular flanges is that the impedance of the specimen in this portion can be matched with that of the bars, which minimizes disturbances to the one-dimensional wave propagation through the bars. If the specimen material has a high strength that overcomes the bond interface strength, this specimen design will not be applicable any longer. Instead, hexagonal (as seen on the right side of Fig. 8.20), or square flanges should be used as they can be firmly clamped by the recesses in the bar ends with matching shapes. In addition to dynamic shear stress-strain curves, the outside of the specimen gage sections can

be marked and high-speed imaged to study shear localization under high-rate loading conditions.

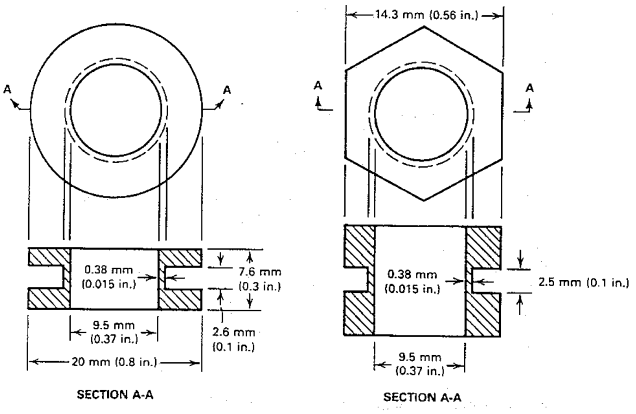

Figure 8.20 Shear specimen geometry
(Reproduced from Hartley et al. (1987) with permission)

8.6 Combined Axial/Torsion Loading

The Kolsky torsion bars with a pre-stressed section are readily modified to conduct dynamic experiments on specimens with combined axial and torsion loading. The pre-stress section is not limited in one type of stored strain energy. For example, when the bar is clamped at its claming location, a pulley may be used to twist the bar to store torsional strain energy in the pre-stressed section. Meanwhile, a hydraulic actuator may also be introduced to induce tensile or compressive strain energy in the same pre-stressed section. The sudden release of the clamp thus generates two types of elastic waves in the incident bar simultaneously, which is tension or compression, in addition to shear. However, the shear wave will arrive at the specimen behind the axial wave due the differences in wave speeds.

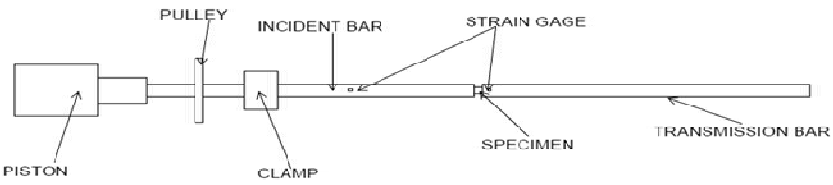

Figure 8.21 A compression/torsion bar for dynamic friction study
(Reproduced from Huang and Feng (2004) with permission)

Figure 8.21 schematically shows a compression/torsion bar for dynamic friction studies (Huang and Feng 2004). To investigate the friction behavior on an interface, normal pressure with a controllable amplitude is required across the interface before a shear load is applied to determine the friction coefficient. This loading pattern is exactly what the device shown in Fig. 8.21 can provide. Similar designs have been used to study dynamic friction (Rajagopalan and Prakash 1999, Espinosa et al. 2000).

8.7 Examples of Dynamic Tensile Experiments

8.7.1 Epoxy and PMMA

In this section, the dynamic stress-strain responses and failure behavior of an epoxy, Epon 828/T-403, and a PMMA are tested under high strain-rate uniaxial tension conditions. The Kolsky-bar setup for high-rate tension experiments is schematically shown in Fig. 8.22. The striker is a tube sliding outside the incident bar. In order to increase the magnitude of the weak transmitted signal, an aluminum alloy tube was used as the transmission bar. At the specimen-transmission bar interface, an aluminum alloy end cap was press-fit and then welded onto the hollow tube to provide a threaded grip for the specimen. This end cap could disturb the one-dimensional wave propagation in the aluminum tube. However a pulse-shaper is used to control the profile of the incident pulse with a substantially increased rise-time and to filter out high-frequency components in the waveform, so that the cap is in dynamic equilibrium together

with the specimen. The pulse shaper is necessary anyway to facilitate dynamic stress equilibrium and constant strain rate in the polymer specimen with low wave speeds.

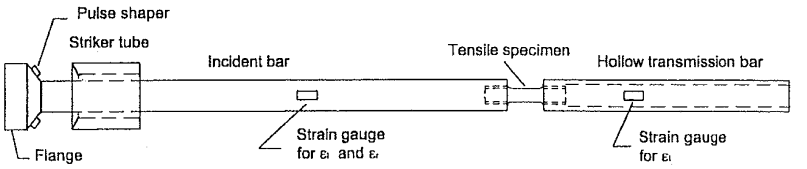

Figure 8.22 The experimental setup for dynamic polymer tension tests
(Reproduced from Chen et al. (2002) with permission)

With the solid steel incident bar and hollow aluminum transmission bar, the strain calculation needs to account for the change in the relationship between the bar-end velocity and the measured strain signal on the tube. The tensile strain history in the specimen is

$$\varepsilon(t)=\left(\frac{C_{BI}}{L_S}-\frac{E_I A_I}{E_T A_T}\frac{C_{BT}}{L_S}\right)\int_0^t \varepsilon_i(\tau)d\tau-\left(\frac{C_{BI}}{L_S}+\frac{E_I A_I}{E_T A_T}\frac{C_{BT}}{L_S}\right)\int_0^t \varepsilon_r(\tau)d\tau \tag{8.2}$$

where subscripts I and T represent the incident bar and the hollow transmission tube, respectively. For the modified tension bar used for the experiments presented, the lengths of the maraging steel striker tube and incident bar were 152 and 2130 mm, respectively, and the length of the 6061-T6 aluminum hollow transmission tube was 762 mm. They all had a common outer diameter of 19 mm. The inner diameter of the transmission tube was 16 mm.

The specimen materials are two amorphous polymers, an amine-cured DGEBA epoxy (Shell Epon 828 epoxy resin with a Texaco T-403 hardener using a 100/36 weight ratio) and a PMMA. The epoxy with a mass density of 1.14×10^3 kg/m^3 and a glass transition temperature of 55°C was cured at room temperature for over seven days. The PMMA

was purchased from a commercial vender. The specimens were then machined to a dumbbell shape with the dimensions specified in Fig. 8.15. The specimen length was determined by trial tests to check dynamic stress equilibrium in the specimens. Before dynamic loading, all the Epon epoxy specimens were heated in a sealed container in a furnace to 60°C, kept at that temperature for four hours, and cooled down to room temperature overnight. The same procedure was repeated on PMMA specimens except that the annealing temperature was 110°C. This procedure was designed to relieve any residual stress in the specimens from material handling and machining.

Uniaxial tension experiments on the epoxy were performed using the modified Kolsky tension bar. To explore the rate effects over a wider range, quasi-static tension experiments were also performed. The tensile response was obtained at four strain rates: $2.46\times10^{-3}\,s^{-1}$, $2.26\times10^{-1}\,s^{-1}$, $8.0\times10^{2}\,s^{-1}$, and $1.2\times10^{3}\,s^{-1}$ (Chen et al. 2002a). The tensile stress-strain curves are shown in Fig. 8.23.

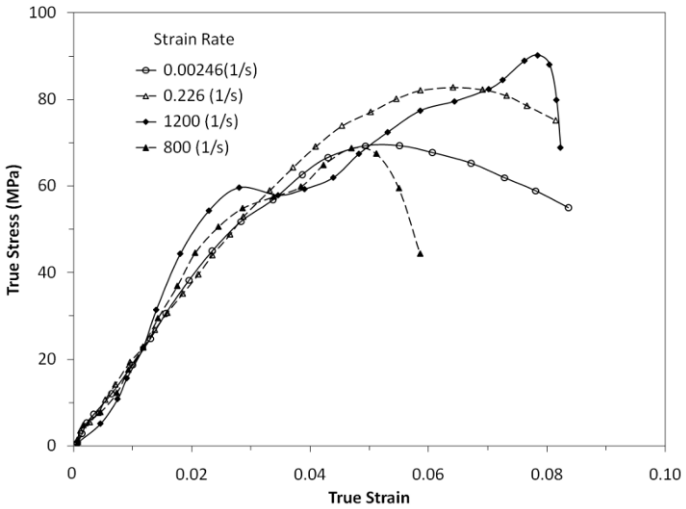

Figure 8.23 Tensile stress-strain curves of Epon 828/T-403 epoxy
(Reproduced from Chen et al. (2002a) with permission)

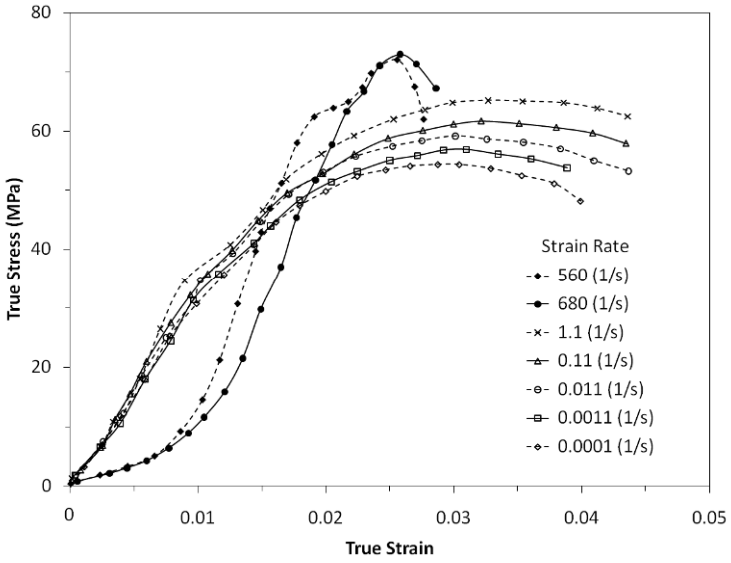

Figure 8.24 Tensile stress-strain curves of PMMA
(Reproduced from Chen et al. (2002a) with permission)

The results shown in Fig. 8.23 indicate that the peak strength was reached during a dynamic test at a smaller strain as compared to quasi-static tests. The results in Fig. 8.23 do not show clear strain-rate dependence of the material's peak tensile strength, which is in contrast to the rate sensitivity in compression of this material (Chen and Zhou 1998). The specimens fractured in a brittle manner during dynamic tensile loading, which is consistent with the smaller failure strains. By contrast, during quasi-static tension tests, these specimens failed in a ductile manner with a necking process. The brittle-ductile transition is considered to be the strain-rate effect. The fact that more than one fracture-surface exist, as shown in Fig. 8.15, indicates that dynamic stress equilibrium had been reached before fracture occurred. However, the fracture was near the fillets, which indicts that stress concentration near the fillets played a role. Ideally, the fracture should occur near the middle of the gage section.

Figure 8.24 summarizes the tensile stress-strain curves of the PMMA over a strain-rate range of 1.0×10^{-4} to 6.8×10^{2} s^{-1}. Similar to the behavior of Epon 828/T-403, the results Fig. 8.24 indicate that the strain

corresponding to the peak strength in dynamic experiments is smaller than that from quasi-static experiments. The peak tensile strength under dynamic loading is slightly higher than its quasi-static counterpart of the material. Similar to the behavior of Epon epoxy, the specimens failed in a ductile manner with a necking process during quasi-static tests. However, under dynamic tensile loading, the failure changed to a brittle fracture manner. The initial toe region of the dynamic tensile stress-strain curves may come from the engagement process of the threaded joints between the specimen and the bar ends.

8.7.2 Bovine Tendon

In this example, a Kolsky tension bar was used to determine the tensile stress-stretch behavior of the bovine tendon under dynamic loading (Cheng et al. 2009). Dynamic Mullins effects on the tendon stress-strain response were also explored. The tendon specimens can deform to large strains. To properly hold the tendon specimen without slipping during tensile loading, grips similar to the 'cryo-jaw' device (Cheng and Chen 2003) were used. This gripping method introduced minimum disturbances to the stress wave propagations in the Kolsky tension bar. To translate the testing machine crosshead displacement into the actual strains in the gage section of the specimen, Miller's (2001) equation was employed for the specific specimen configuration of rectangular cross section used in this research (Cheng and Chen 2003). A laser displacement measurement device was used to measure the actual strain history in the specimen. The device includes a laser diode, a line head, and a photo detector. The details and working principles of the laser device are given by Ramesh and Narasimhan (1996). The only difference is that the device was turned by 90° from Ramesh and Narasimhan's design to measure the width changing of an opening gap. Since the tendons are of relatively weak strength, a hollow transmission bar was again used to accurately measure the transmitted force signal. To achieve early stress equilibrium and a constant strain rate in the specimen, pulse-shaping was employed. Furthermore, to evaluate the Mullins effects under dynamic loading conditions, it is important for the specimen to be loaded only once during one loading cycle. A momentum trapping bar was used to prevent undesired repeated pulses. A schematic illustration of the dynamic experimental setup is shown in Fig. 8.25.

The tendon specimens used in this set of experiments had rectangular cross-sections. Four specimens were excised from one tendon segment, as shown in Fig. 8.26. The specimens were then kept hydrated for tests. The gauge section of the specimens was 3×2 mm^2 in cross-sectional area and 8 mm in length.

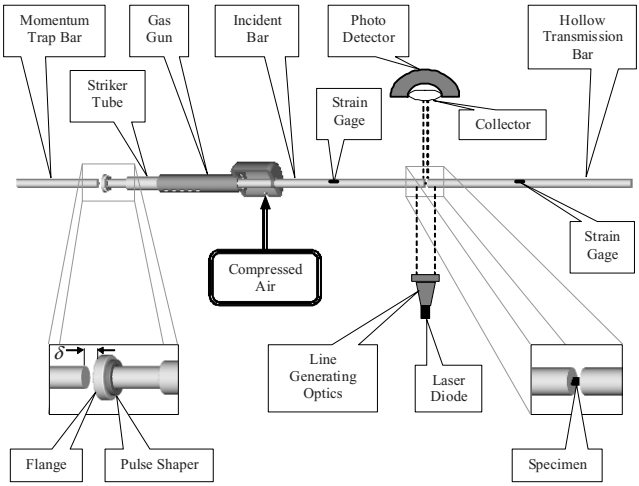

Figure 8.25 A Kolsky tension bar for tendon tension experiments
(Reproduced from Cheng et al. (2009) with permission)

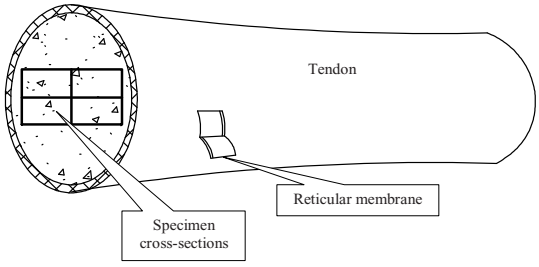

Figure 8.26 Tendon tension specimen preparation
(Reproduced from Cheng et al. (2009) with permission)

Figure 8.27 shows the dynamic stress-strain behavior of the tendon specimen over three loading cycles. Since it is difficult to completely eliminate the repeated loading from the tension bar setup used in this study, the actual maximum strain of the first impact experiment is about 0.20. The subsequent loading paths are well below the first one and gradually approach a stable path. The differences between the stress-stretch curves from different loading cycles are similar to the Mullins effects observed in rubbers under quasi-static cyclic loading conditions. Similar phenomena were also observed when the tendon was loaded repeatedly under quasi-static rates, although the dynamic stress-stretch curves have higher slopes than their quasi-static counterparts. These results show that the mechanical responses of tendons depend on the loading history and strain rate. The stress-strain response of a fresh tendon (such as the one marked by "1st loading" in Fig. 8.27) is quite different from an exercised tendon (such as the other two curves in Fig. 8.27), under both quasi-static and dynamic loading conditions. The peak stresses of the curves in Fig. 8.27 correspond to the start of unloading in each experiment.

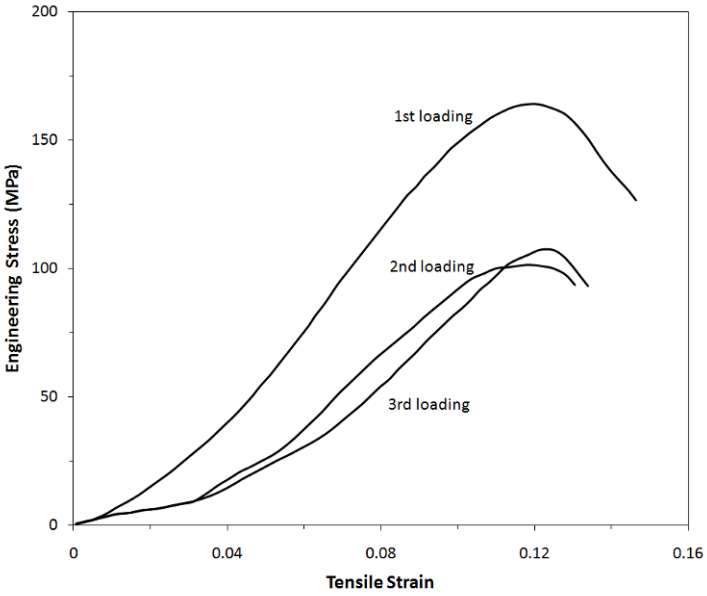

Figure 8.27 Dynamic tensile stress-strain curves of bovine tendon at a strain rate of 2500 s^{-1}

(Reproduced from Cheng et al. (2009) with permission)

8.7.3 Rubber

Dynamic tensile response of the EPDM rubber presented in Chapter 4.5.2.3 was determined using a modified Kolsky tension bar. The soft sheet specimen was wrapped around the ends of the aluminum bars to form a tubular geometry, as shown in Fig. 8.14. The inner surface of the tube was glued to the cylindrical surfaces of the bar ends. The outer surface of the specimen was clamped. Trial experiments were performed to select clamps that introduced minimum disturbances to the wave propagations in the bars. Thin metal liners with rough surfaces were attached to both the bar surface and the inner surface of the clamp such that shear deformation in the specimen during tension is minimized. This specimen geometry minimizes not only 3-D stress state but also radial inertia effects. Similar to Kolsky compression bar experiments, the quartz-crystals required for equilibrium checking in soft material testing are located near the bar ends.

The tension bar used in this study is schematically shown in Fig. 8.13. It consists of a momentum diversion bar, a compound incident bar, a tubular striker, and a transmission bar. The 25.4 mm diameter steel momentum diversion bar has a length of 2692 mm. The 2286-mm long steel section of the incident bar has a diameter of 19.0 mm and the 1830-mm long aluminum section has a diameter of 12.7 mm. The 12.7 mm aluminum transmission bar is 1830-mm long. The steel tubular striker, which rides on the steel portion of the incident bar, has the same cross-sectional area as the steel incident bar and is 533-mm long. During an experiment, the momentum diversion bar is in contact with the flange at the end of the incident bar. The tubular striker is driven by a gas gun towards the flange-end of the incident bar and impacts against the flange. Upon impact, the momentum diversion bar absorbs most of the impact energy because of its larger cross-sectional area. The stress in the steel portion of the incident bar, σ_I, induced by the impact of the striker traveling at an initial velocity V_0, is

$$\sigma_I = \frac{\rho_B C_B V_0 A_I}{2A_I + A_M} \tag{8.3}$$

where V_0 is the striking velocity of the tubular striker; and A_I and A_M are the cross-sectional area of the striker, which is the same as that of the steel section of the incident bar, and the momentum diversion bar, respectively. With the dimension described above, the incident bar stress

amplitude reduces by nearly 47% after the momentum diversion bar is used. As the incident tensile pulse further propagates to the steel/aluminum joint of the incident bar, the stress in the aluminum section of the incident bar, σ_a, is

$$\sigma_a = 2\frac{A_I}{A_a}\frac{1}{1+R}\sigma_I \tag{8.4}$$

where A_a is the cross-section area of the aluminum section, $R = \frac{\rho C A_I}{\rho_a C_a A_a}$ is impedance ratio between the steel and the aluminum sections of the incident bar. With the experimental setup used in this study, σ_a is about 60% of σ_I. Thus, with the momentum diversion bar and the steel/aluminum joint, the amplitude of the incident stress is only about 1/3 of that produced in a conventional tension bar. This allows much higher striking velocities to generate relatively low but repeatable incident stress pulses needed for soft material testing.

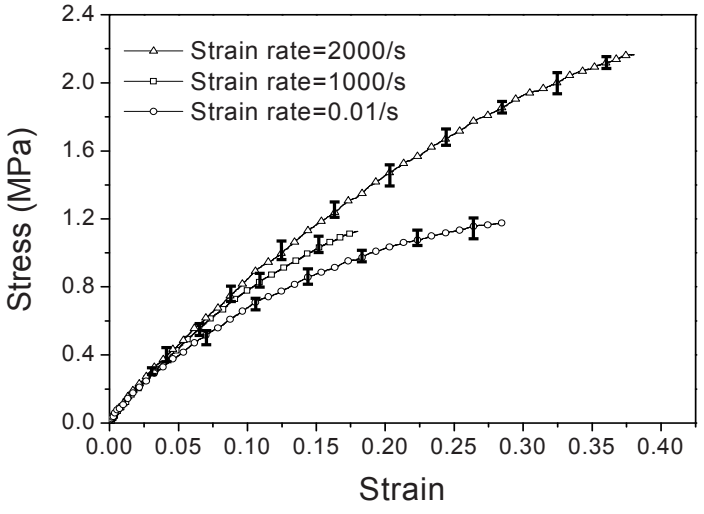

Figure 8.28 Tensile stress-strain curves of EPDM rubber at various strain rates

(Reproduced from Nie et al. (2009) with permission)

Figure 8.28 shows the dynamic tensile stress-strain curves of the EPDM rubber at two different high strain rates and a reference quasi-static strain rate (Nie et al. 2009). Each stress-strain curve presented in the figure is the mean curve of five experiments conducted under identical loading conditions. Error bars are also shown on each curve to indicate the scattering range of the stress-strain curves obtained under each identical loading condition. The tensile stress-strain curves of the EPDM exhibit non-linear behavior with significant strain-rate dependency, which is a characteristic of typical viscoelastic materials. In comparison to its compressive response presented in Chapter 4.5.2.3, the EPDM is softer in tension.

Chapter 9. Kolsky Compression Bar Experiments at Intermediate Strain Rates

Most Kolsky bars characterize dynamic material properties at strain rates between 5×10^2 and 1×10^4 s^{-1}. On the other hand, quasi-static material testing machines operate under closed-loop control at strain rates below 1 s^{-1}. However, many applications require stress-strain data around the intermediate strain-rate range of 5×10^1 - 5×10^2 s^{-1}, where data is scarce for any material. This chapter describes designs of Kolsky bars to conduct dynamic experiments at strain rates below 10^2 s^{-1}, which is the upper limit of modified quasi-static methods. The overlap in strain rates achieved by the modified Kolsky bar and quasi-static techniques bridges the gap in the intermediate strain-rate range, which also facilitates the system-error examination between the quasi-static and dynamic testing methods.

9.1 Lack of Data at Intermediate Strain Rates

The amplitude of strain rate in many applications such as automobile collision locates in the range of intermediate rates, which is usually defined between 10^0 and 10^2 s^{-1}. These strain rates are not achievable with either conventional Kolsky bars or quasi-static testing frames. Experimental data within this intermediate rate range have always been desirable to be filled, so that full-range rate-dependent material models can be developed with applications spanning over the entire strain-rate range.

The intermediate strain-rate range has also been of interest from a mechanics point of view. At high strain rates, inertia effects must be considered in both experiment design and the resultant data interpretation; whereas, they are negligible at low strain rates. The role of inertia effects in the design of experiments at intermediate strain rates is yet to be examined. Many materials have been found to have different strain-rate sensitivities at high and low strain rates in their stress-strain responses. For instance, the strain-rate sensitivity may be more significant at high rates than at low rates for some materials. Transitions in the strain-rate sensitivities occur, in general, in this intermediate strain-rate range. In terms of experimental techniques, the strain rates achieved in drop-weight experiments fall into this intermediate range. However, the drop-weight experiments do not directly provide stress-strain responses of materials.

W.W. Chen and B. Song, *Split Hopkinson (Kolsky) Bar: Design, Testing and Applications*, Mechanical Engineering Series, DOI 10.1007/978-1-4419-7982-7_9,

Quasi-static testing frames have been modified to approach the intermediate strain rates. The upper limit obtained in such experiments can reach 1×10^{2} s^{-1} depending on the stiffness and gage length of the specimen. At these high rates, the testing frames usually have to be operated in an open-loop manner, which brings uncertainties similar to uncontrolled Kolsky-bar tests and drop-weight experiments.

With better controls over the loading conditions through pulse shaping, the Kolsky bar may be modified for intermediate-rate experiments. However, there are a number of demanding challenges in the expansion to the lower strain rates with this technique. First, the striking speed should be low in Kolsky-bar experiments to deform the specimens at intermediate rates. The experiments are more difficult when the specimens are soft requiring slow impact velocities. For instance, in order to deform a 3-mm-thick specimen at a strain rate of 5×10^{1} s^{-1}, the velocity difference at the specimen ends (or the ends of incident and transmission bar) is required to be 1.5 m/s. This is the same as the striking speed if the specimen impedance is negligible compared to the bar impedance. Recall that thin specimens are one of the requirements in the high-rate characterization of soft materials. This situation is unavoidable in the design of dynamic experiments on soft materials. The commonly used gas gun in a Kolsky bar may not be able to generate such a low impact velocity in a stable and consistent way. The second challenge for Kolsky bar in intermediate-rate testing is the duration of loading. The loading duration needs to be sufficiently long to deform the specimen to large strains when the strain rate is low. If the specimen is to be deformed to a strain of 0.5 (50%) at the strain rate of 5×10^{1} s^{-1}, a loading pulse duration of 1 ms is required, which needs an aluminum or a steel striker to be approximately 2.5-m long. Besides a long striker, such a long incident pulse also requires long incident and transmission bars to avoid overlapping of the stress waves. The Kolsky-bar experiments thus need to be designed to overcome these challenges to conduct intermediate strain-rate experiments.

9.2 Material Testing Methods at Intermediate Rates

In order to produce a long but relatively low speed impact, a “slow bar” technique was developed, as illustrated in Fig. 9.1 (Zhao and Gary 1997). A hydraulic jack and a reservoir of compressed air to maintain the pressure are used to offer a sufficiently long push to the Kolsky bar at a sta-

ble and relatively constant velocity. This slow-bar loading device can generate a loading pulse with a duration over 100 ms, or even unlimited as viewed from time scales commonly seen in Kolsky-bar experiments. Measurements of bar strains are becoming much more challenging due to possibly overlapped pulses. For example, a 10-ms-long pulse requires aluminum or steel bars of at least 50-m long in order to avoid overlapping of the pulses, which is not spatially realistic in most laboratories. The overlapped pulses in experimental records are commonly seen in such intermediate-rate experiments and need to be numerically separated.

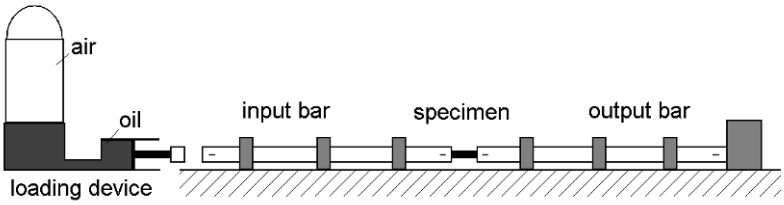

Figure 9.1 "Slow bar" setup
(Reproduced from Zhao and Gary (1997) with permission)

The method of "2-point" strain measurement has been developed to separate the waves (Zhao and Gary 1997). The principle of the "2-point" strain-measurement technique is to use two sets of strain gages at two different locations, usually close to each end, of the bar, as shown in Fig. 9.2. The recorded signal by each set of strain gages is the mixture of an "ascending" wave, ε_{asc}, and a "descending" wave, ε_{des}, that propagate in opposite directions (Fig. 9.2),

$$\varepsilon(t)=\varepsilon_{asc}(t)+\varepsilon_{des}(t) \tag{9.1}$$

The following conditions are satisfied at the locations A and B,

$$\varepsilon_{ascA}(t)=\varepsilon_{A}(t) \quad \text{when } t<R_A \tag{9.2}$$

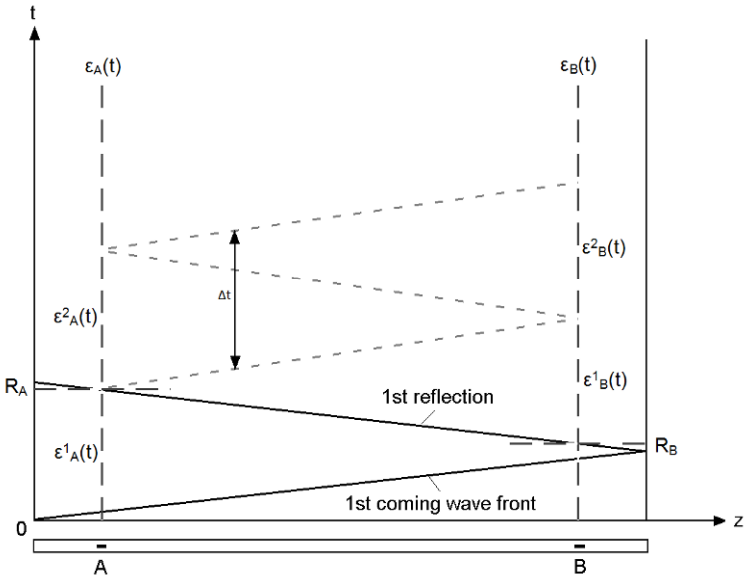

Figure 9.2 Scheme for wave separation
(Reproduced from Zhao and Gary (1997) with permission)

$$\varepsilon_{ascB}(t) = 0 \qquad \text{when } t < R_B \tag{9.3}$$

The measured strain signals at the locations A and B are divided into small pieces ε_A^i and ε_B^i with an equal time interval Δt which is the round trip time for the stress wave propagating between the two locations,

$$\varepsilon_A^i(t) = \begin{cases} \varepsilon_A(t) & R_A + (i-2)\Delta t \le t \le R_A + (i-1)\Delta t \\ 0 & otherwise \end{cases} \tag{9.4}$$

$$\varepsilon_B^i(t) = \begin{cases} \varepsilon_B(t) & R_B + (i-1)\Delta t \le t \le R_B + i\Delta t \\ 0 & otherwise \end{cases} \tag{9.5}$$

When $i=1$ ($R_A-\Delta t \le t \le R_A$), the strain signal at the location A is not overlapped, which means the measured strain signal is the same as the actual signal. Such information obtained at the location A can be deduced to the other strain gage location, B, after wave dispersion is corrected. Alternatively, the information at the location A can be directly used for the location B when the wave dispersion is minimized with the pulse shaping technique presented in Chapter 2.5. The "ascending" wave at the location B is thus known. Consequently, the corresponding "descending" wave at the location B for $i=1$ ($R_B \le t \le R_B+\Delta t$) can be calculated,

$$\varepsilon_{desB}^{1}(t)=\varepsilon_{B}^{1}(t)-\varepsilon_{ascB}^{1}(t) \tag{9.6}$$

After the "descending" wave at the location B, ε_{desB}^{1} , is known, the "ascending" wave at the location A for the next interval can be calculated with the same process. Following the same procedure, the separated strain signals at both locations A and B are calculated for all the time intervals. After the waves are separated, the standard data reduction scheme for Kolsky bar experiments can be applied for stress-strain calculations.

The "2-point" strain measurement has been found to be efficient to separate the waves that are a mixture of single "ascending" and "descending" waves. For the cases that the loading duration is much longer than that the bar length can accommodate, the waves are much more difficult to be separated. To use the wave signals, the bars must be made longer such that multiple overlapping of stress waves does not occur for the time period when the stress-strain data are taken. Figure 9.3 shows an example of a long Kolsky-bar system (Song et al. 2008). The actual photograph of the long Kolsky bar is shown in Fig. 9.4. The 19.05-mm-diameter pressure bars are made of 7075-T6 aluminum alloy. The overall length of the long Kolsky-bar system is 27.4 m including a 4.6-m-long pneumatic gun barrel (Fig. 9.3(a)). To avoid transporting excessively long bars after machining, both the incident and transmission bars are assembled with three individual segments. Each segment is 3.66-m long, making the incident and transmission bars each 11.0 m in full length. The individual segments were connected with precision joints as shown in Fig. 9.3(b). The joints were manufactured with a sliding fit maintaining a tolerance of ±0.0125 mm to minimize the possible wave disturbance. In addition, anti-seize grease was used to prevent galling inside the aluminum joints when the bars were assembled together.

Figure 9.5 shows the signals measured with three sets of strain gages at different locations on the incident bar (Song et al. 2008). Each

set of strain gages locates nearly in the middle of each individual sector. The strain-gage signals are plotted individually with offsets in Fig. 9.5 for clear illustration. Reflections are observed in Fig. 9.5, which are caused by imperfect joints, but the amplitudes are sufficiently small that they can be neglected.

Due to the extended length of the long bars, wave dispersion becomes more severe. As illustrated in Chapter 2.5, pulse shaping technique is efficient to physically eliminate the high-frequency components in the incident pulse and thus to minimize wave dispersion. The pulse shaping technique becomes particularly important for minimizing wave dispersion in the long Kolsky-bar system. Figure 9.6 shows typical strain gage output signals measured at different locations (Strain gages 1 and 2 in Fig. 9.3(a)) in the long Kolsky bar when a shaped incident pulse propagated through the bar. The two traces are overlapped each other while the oscillations riding on the pulses due to wave dispersion were physically eliminated.

The long gun barrel shown in Fig. 9.3(a) makes it possible to launch an aluminum or a steel striker as long as 4.6 m, which can produces an approximately 1.8-ms-long pulse according to (1.1). Equation (1.1) also indicates that using a striker with lower wave speed makes it more efficient to generate a long pulse. For instance, nylon has a wave speed of ~1400 m/s. A nylon striker can produce a pulse nearly 3 times longer than that generated by an aluminum striker with the same length. In other words, in order to produce the same duration of loading pulse, the length of a nylon striker needs to be only a third of the length of a conventional aluminum striker.

Due to the low-amplitude incident pulses required in intermediate strain rate experiments, these experiments also demand very low striking velocities in comparison to the higher-rate experiments. The commonly used gas gun may not launch the striker stably and consistently at such low speeds. Using a polymer striker is a simple solution to compensate this deficiency without extensive modification of the gas gun system. The characteristic of relatively low wave impedance of the polymers can generate a loading pulse with lower amplitude even though the impact velocity is relatively high. The low wave speeds in the polymer strikers also produce longer wave durations that are necessary for the experiments where large strains in the specimens are required.

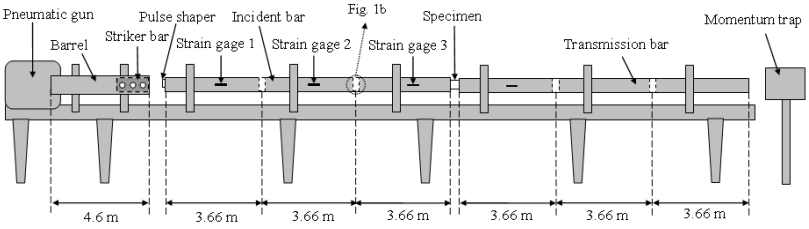

(a)

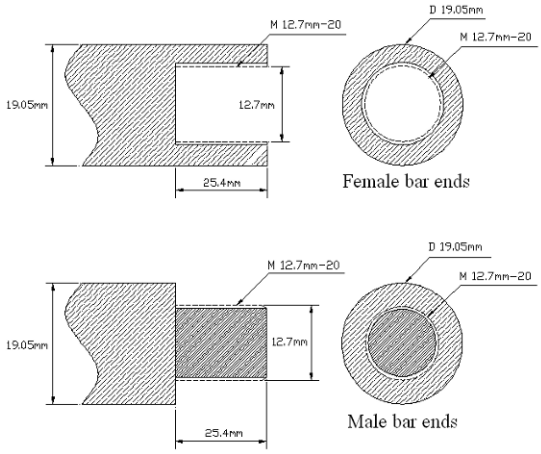

(b)

Figure 9.3 Long Kolsky bar system.
(a) overall setup;
(b) details of bar connections
(Reproduced from Song et al. (2008) with permission)

Figure 9.4 A photograph of a long Kolsky bar

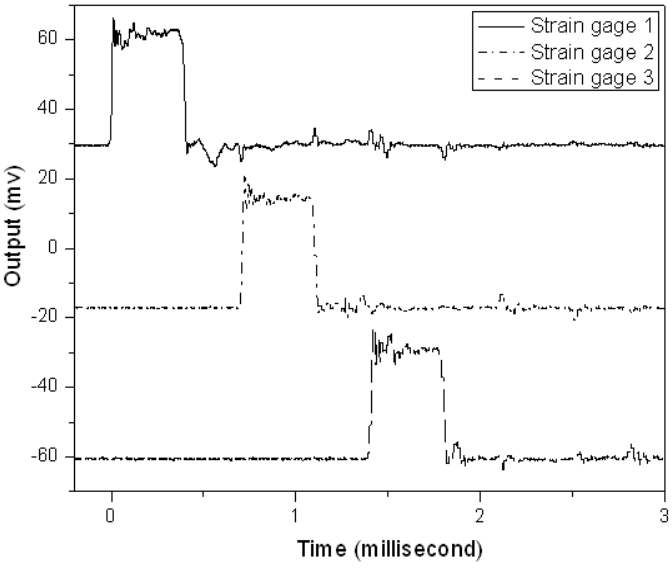

Figure 9.5 Strain gage signals at different locations
(Reproduced from Song et al. (2008) with permission)

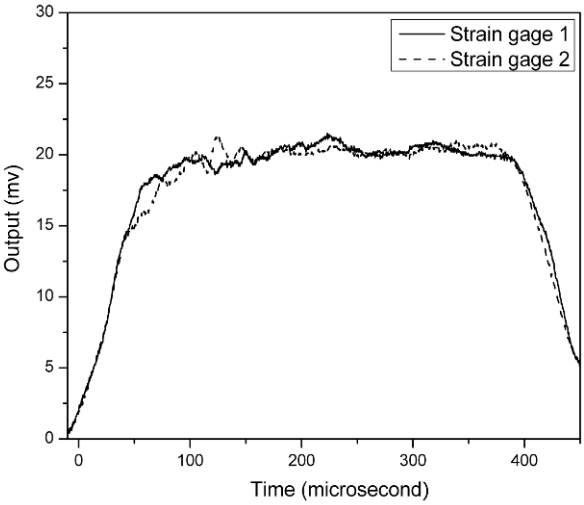

Figure 9.6 Strain gage outputs in the long Kolsky bar showing a nearly non-dispersive pulse generated by pulse shaping *(Reproduced from Song et al. (2008) with permission)*

Figure 9.7 shows the schemes of stress wave propagation (X-t) and corresponding relationship between stress and particle velocity (σ-v) when aluminum or polymer strikers impact on an aluminum incident bar. The wave propagation is illustrated with different fonts for both strikers, as indicated in Fig. 9.7. When the aluminum incident bar is impacted by a low-impedance (polymer) striker, the loading duration becomes longer than that impacted by the same material (aluminum) striker, $T < T'$. If the striking velocity is the same, v_1, both stress and particle velocity generated in the aluminum incident bar are lower when using a polymer striker. The stress and particle velocity in a linear elastic material are related by the following equations,

$$\begin{cases} \sigma_2 = \rho_{st} C_{st} \left(v_2 - v_1 \right) \\ \sigma_2 = -\rho_b C_b v_2 \end{cases} \tag{9.7}$$

Equation (9.7) has the solutions,

$$\sigma_2 = -\frac{\rho_{st}C_{st} \cdot \rho_b C_b}{\rho_{st}C_{st} + \rho_b C_b} v_1 \tag{9.8}$$

$$v_2 = \frac{\rho_{st}C_{st}}{\rho_{st}C_{st} + \rho_b C_b} v_1 \tag{9.9}$$

In these relations, the stress takes negative in compression. Equations (9.8) and (9.9) demonstrate that, at the same impact velocity, a striker with lower wave impedance produces lower stress amplitude and particle velocity in the incident bar. Or, in order to produce a pulse with a certain amplitude, the impact velocity of the low-impedance striker is required to be higher, which may fall into the stable working range of conventional gas guns.

Figure 9.7 also shows that, when the striker is made of the same material (aluminum) as the incident bar, the striker will stay in contact with the incident bar after dynamic loading. However, if the wave impedance of the striker is lower than that of the incident bar, such as the polymer striker in Fig. 9.7, the unloading wave will reflect at the interface between the striker and the incident bar due to mismatched wave impedance. It further produces a tensile stress at this interface, as indicated "3" in Fig. 9.7. This tensile stress separates the striker from the incident bar after dynamic loading, leaving the impact end of the incident bar in stress–free condition, which simplifies the boundary conditions in the wave separation operation.

When the strain gages are attached close to the impact end of the incident bar, it is obvious that the recording length of the strain gages is nearly doubled without being overlapped in the recorded incident pulse. The same applies to the transmission bar so that the transmitted pulse is not overlapped. However, the reflected pulse in the incident bar is overlapped by its secondary reflection from the free impact end. Since the impact end is in free boundary condition, the reflected pulse can be exactly retrieved (Chen and Song 2005, Song et al. 2007d). The recorded reflected pulse, ε_{record}, is the result of the reflected pulse, ε_{ref}, overlapped by its secondary reflection, $\varepsilon_{ref\,2}$,

$$\varepsilon_{record}(t) = \varepsilon_{ref}(t) + \varepsilon_{ref\,2}(t) \tag{9.10}$$

At the free impact end, we have

$$\varepsilon_{ref\,2}=\begin{cases}0 & t\le\Delta t \quad (a)\\ -\varepsilon_{ref}\left(t-\Delta t\right) & t>\Delta t \quad (b)\end{cases} \tag{9.11}$$

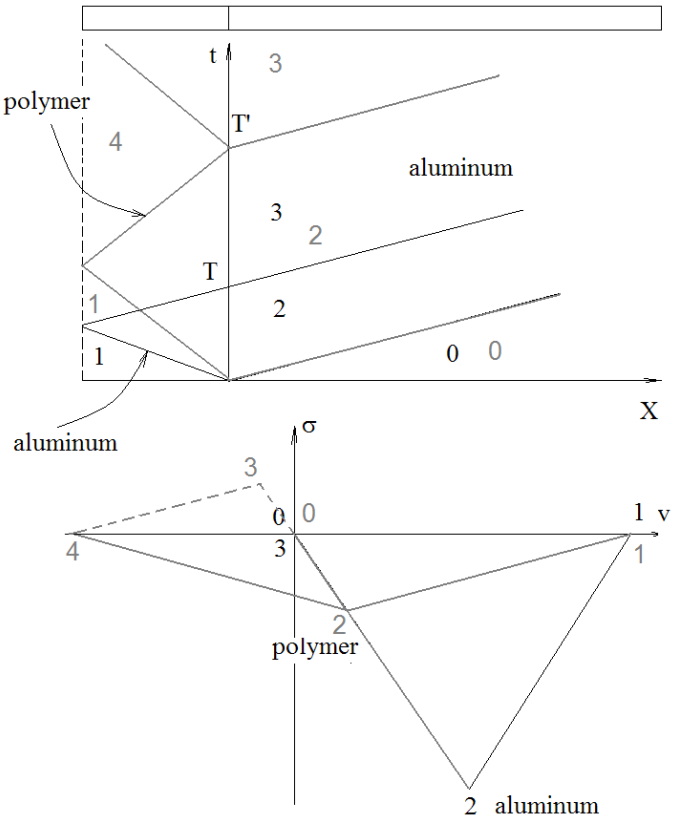

Figure 9.7 Wave propagation when impacted by different strikers

where

$$\Delta t = \frac{2l_0}{C_b} \tag{9.12}$$

is the round-trip time of the pulse from the strain-gage location to the free impact end. Therefore, the actual reflected pulse is expressed as

$$\varepsilon_{ref} = \begin{cases} \varepsilon_{record} & t \le \Delta t \quad (a) \\ \varepsilon_{record} + \varepsilon_{ref}\left(t - \Delta t\right) & t > \Delta t \quad (b) \end{cases} \tag{9.13}$$

Equation (9.13) indicates that, the recorded reflected pulse is not overlapped until $t = \Delta t$. When $t \le \Delta t$, the actual reflected pulse is the same as the recorded pulse. After $\varepsilon_{ref}\left(t \le \Delta t\right)$ is known, the actual reflected pulse at $\Delta t < t \le 2\Delta t$ can be calculated with (9.13(b)) and the rest is deduced following the same procedure till the actual reflected pulse is fully retrieved.

Comparing to the experiments at higher rates, the specimen deforming at an intermediate rate is much easier to achieve stress equilibrium due to much lower rate of loading. This means (1.11) is satisfied, so that the reflected pulse can also be calculated from the difference between the incident and transmitted pulses, both of which are not overlapped when attaching the strain gages closer to the bar ends,

$$\varepsilon_{ref} = -\left(\varepsilon_{inci} - \varepsilon_{tran}\right) \tag{9.14}$$

Other methods to calculate the specimen strain include direct optical measurement of the specimen deformation. The optical measurements may be high-speed optical extensometer, laser displacement measurement, digital image correlation, and high speed photography.

In intermediate-rate Kolsky-bar experiments, the duration of loading is still somewhat limited. For example, the loading duration should be shorter than the round-trip time for stress wave in a full length of the transmission bar plus the attached momentum trap bar. Otherwise, the transmission bar may fly off from the specimen due to reflection at the free far end so that the specimen is unloaded before the actual unloading wave arrives. A rigid wall may be attached to the far end of the transmission bar to avoid this. However, the reflected compression pulse from the rigid wall will load the specimen from the transmission bar side and then reflect back and transmit into the incident bar. This results in a very

complicated analysis of stress wave propagation in the whole Kolsky-bar system.

9.3 Intermediate Strain-rate Characterization of Polymeric Foams

The long-bar option described in the previous section may not be feasible in many laboratories due to the space limitations. For materials with small failure strains, intermediate-rate experiments may be performed using Kolsky bars for higher-rate experiments. Here we give an example of a Kolsky bar that was modified for intermediate strain rate testing by moving the bar strain gages closer to the bar ends and was used for characterizing the syntactic epoxy foam discussed in Chapter 4.5.3.1. The bar system is illustrated in Fig. 9.8. It is nearly the same as the standard Kolsky bar for soft material characterization (Fig. 4.13) except for the new strain gage locations on the bars.

In this group of experiments, the striker, which is made of the same material (7075-T651 aluminum alloy) as the bars, is 1524-mm long, producing an incident loading pulse as long as 600 μs. However, using small piece of copper disk as the pulse shaper significantly extends the unloading duration. The total duration of the incident pulse is over 1 ms, as shown in Fig. 9.9 (Song et al. 2007d). This 1-ms-long pulse requires an incident bar with a minimum length of 5 m to avoid overlapping of the pulses. The 3685-mm-long incident bar in this experiment does not satisfy this requirement, motivating the modification of attaching strain gages close to the impact end of the incident bar (Fig. 9.8). In this case, the incident pulse is separated from the reflected pulse. However, the reflected pulse is inevitably overlapped by its reflection at the impact end, as show in Fig. 9.9. By contrast, the transmission bar and the additional momentum trap bar are sufficiently long so that the transmitted pulse is not overlapped in the transmission bar gage location.

The reflected pulse can be recovered with (9.13) or (9.14) when the stress equilibrium is achieved. Figure 9.10 shows the stress equilibrium process in the specimen, which are directly measured with the quartz crystal transducers. The specimen is observed in stress equilibrium over the entire duration of loading because of the low rate of loading during the intermediate-rate experiment. After the reflected pulse is recovered, the strain-rate history can be calculated with (1.12). Figure 9.10 shows

the comparison of the strain-rate histories recovered with (9.13) and (9.14). Even though different methods are used, the recovered reflected pulses are consistent. According to the recovered reflected pulses, the specimen was deformed at a nearly constant strain rate of 160 s^{-1} until it failed at approximately 450 μs.

Characterization of the material at lower strain rates requires longer pulses. As mentioned in Chapter 9.2, a lower impedance striker can produce long pulses of loading. As an example, a 1220-mm-long nylon striker was used to produce a pulse with a duration over 1.4 ms, which is shown in Fig. 9.11. A 12.50-mm thick soft rubber was used as the pulse shaper to produce a pulse with a similar shape to that shown in Fig. 9.9 for achieving constant strain rate deformation in the specimen. For such a long pulse of loading, the reflected pulse is overlapped with not only its secondary reflection but also the unloading portion of the incident pulse. Equation (9.13) is not applicable any more for the reflected pulse recovery. When the amplitude of the strain rate (or the reflected pulse) is small, the amplitudes of both incident and transmitted pulses are very close, making it erroneous to recover the reflected pulse with (9.14). Methods other than the reflected signal are needed to determine the strain histories in the specimen. In the experiments reported here, to obtain credible deformation history in the specimen in this case, a high-speed digital camera (Cordin 550) was employed to take sequential images of the specimen deformation over the 1.4 ms duration of loading. The high-speed digital camera was set at the speed of 15,407 frames per second (FPS), corresponding to frame interval of 64.9 μs.

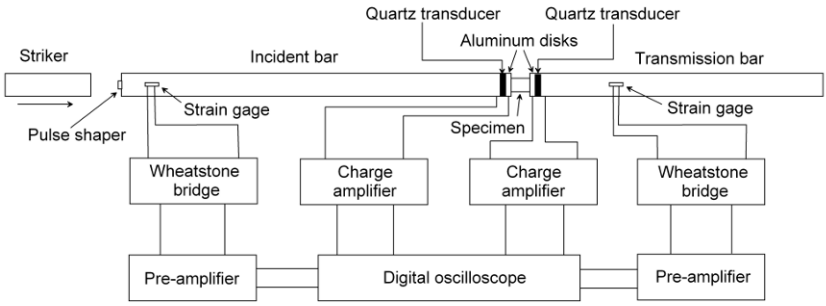

Figure 9.8 Kolsky bar for intermediate rate characterization
(Reproduced from Song et al. (2007d) with permission)

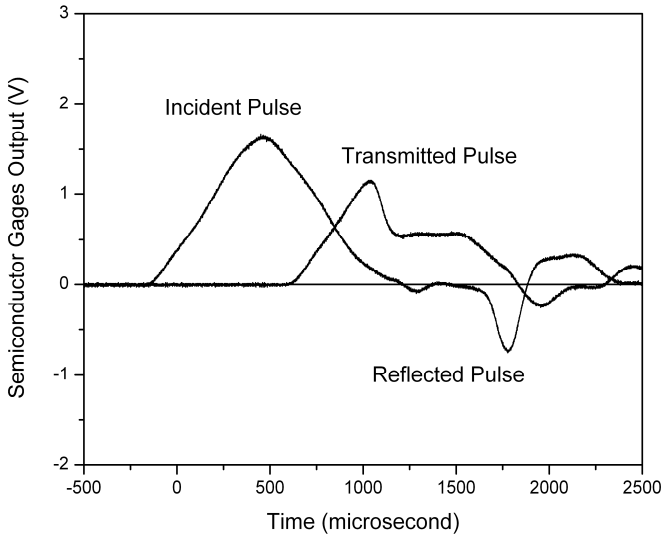

Figure 9.9 Typical pulses in an intermediate-rate Kolsky bar experiment on the syntactic epoxy foam
(Reproduced from Song et al. (2007d) with permission)

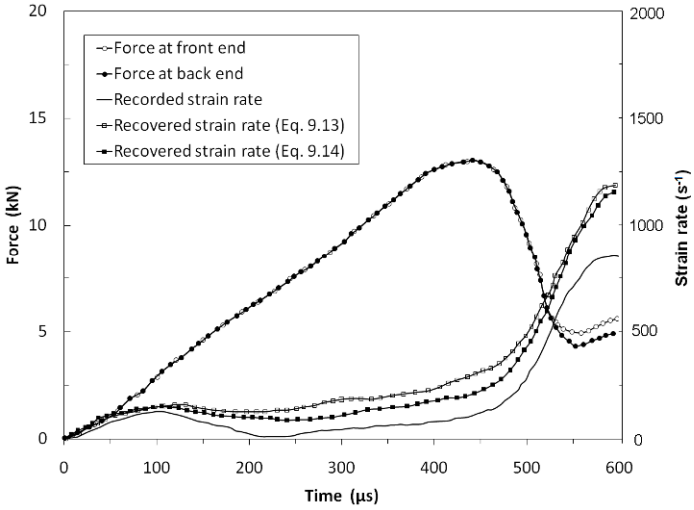

Figure 9.10 Recorded and recovered strain-rate histories and force equilibrium in the specimen.
(Reproduced from Song et al. (2007d) with permission)

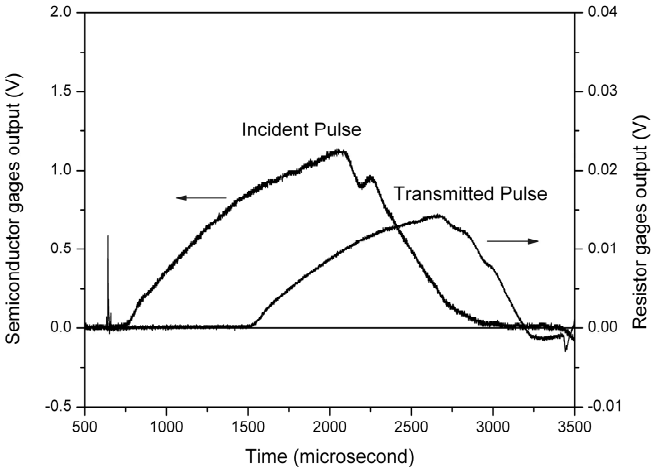

Figure 9.11 Pulses obtained from a Kolsky bar experiment with a nylon striker and a rubber pulse shaper
(Reproduced from Song et al. (2007d) with permission)

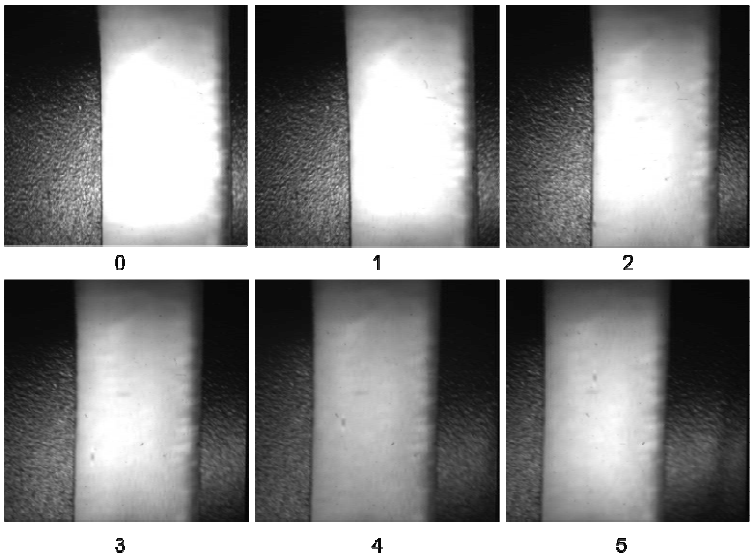

Figure 9.12 High-speed images for intermediate-rate deformation of the syntactic epoxy foam
(Reproduced from Song et al. (2007d) with permission)

Figure 9.12 shows some representative high speed images. The dark portions in the images are the bar ends and the bright center portion is the specimen. The incident bar end moves into the images from the right side while the transmission bar end moves out of the images towards left. The distance between the dark/bright boundaries in each image yields the specimen deformation with respect to time. Figure 9.13 shows the engineering strain history of the specimen obtained from the high-speed images. The specimen is found to deform at a nearly constant strain rate of 45 s^{-1}. This strain rate is possibly the lower limit for the Kolsky-bar experiment on this foam material. It is noted that this strain rate achieved in the experiment is in the same range as the upper limit (over 10 s^{-1}) that is achievable in quasi-static experiments.

Figure 9.14 shows the stress-strain curves of the syntactic foam obtained from low to high strain rates with intermediate rates (45 and 160 s^{-1}) included. The data at and below 10 s^{-1} were obtained from quasi-static experiments using a servo-hydraulic test machine while the data at and above 700 s^{-1} were obtained from high-rate (regular) Kolsky-bar experiments. The effect of strain rate on the failure stress of the material is shown in Fig. 9.15. It is illustrated that the data in the strain rate range from 0.1 to 500 s^{-1} were not obtained in previous studies, but obtained with the intermediate-rate Kolsky-bar experiments introduced in this Chapter. The intermediate rate data fill the gap between the low and high strain rates. Such experimental results obtained at intermediate strain rates are still limited for any material.

Because of the small failure strains in the foam specimens, the bars used above are not necessarily very long. A long Kolsky bar, such as the one shown in Fig. 9.3, is needed for material characterization at large deformation. Here we present another example that uses the long Kolsky bar (Figs. 9.3 and 9.4) to characterize a PMDI foam at intermediate strain rates (Song et al. 2008).

A polyurethane foam pulse shaper was used to generate a long loading pulse even though impacted by an aluminum striker. The cell-collapse stress of the foam limits the amplitude of the incident pulse. Due to the low wave impedance and low strength of the pulse-shaping foam, the momentum in the aluminum striker can only be transferred through the foam to the incident bar progressively, making an incident pulse of a long-duration. As shown in Fig. 9.16, an incident pulse longer than 3 ms was generated by a 2500-mm-long aluminum striker impacting on a 14.5 (length)×13.5 (width)×9 (height) mm^3 polyurethane foam block with a density of 0.32×10^3 kg/m^3. The incident pulse shown in Fig. 9.16 was recorded with the strain gages attached close to the impact end of the incident bar, providing a non-overlapped incident pulse for the first 3.2 ms. Equation (9.14) was used to recover the overlapped reflected pulse and

then to calculate the strain history, as shown in Fig. 9.17. The stress history in the specimen is also shown in Fig. 9.17. The specimen was compressed at a nearly constant strain rate of 70 s^{-1} while the stress response corresponds plastic yielding followed by a cell-collapse plateau, as indicated in Fig. 9.17. This strain rate is again comparable to the upper rates that conventional quasi-static testing frames may achieve.

Figure 9.18 summarizes the compressive stress-strain curves obtained from the long Kolsky bar and MTS experiments at the strain rate of ~50 s^{-1} (Song et al. 2008). The stress-strain curves are observed to be overall consistent even though different experimental methods were used. The scatter of stress-strain curves was found to come from the variation in cell structures and foam density (Song et al. 2008). Figure 9.19 presents the strain-rate effects on the yield strength of the foam material from low to high strain rates obtained by MTS, long Kolsky bar, and conventional pulse-shaped Kolsky-bar methods (Song et al. 2008). The results show that the intermediate-rate data cover the range that could not be experimentally achieved in the past, making the observed linear strain-rate sensitivity more substantiated.

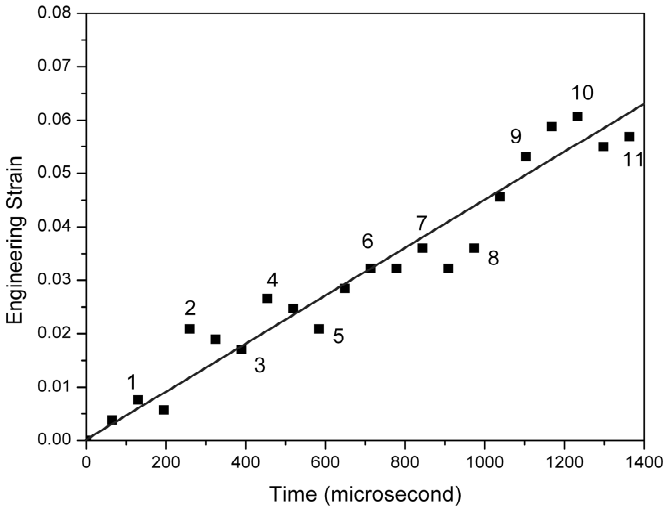

Figure 9.13 Strain history obtained from high-speed images
(Reproduced from Song et al. (2007d) with permission)

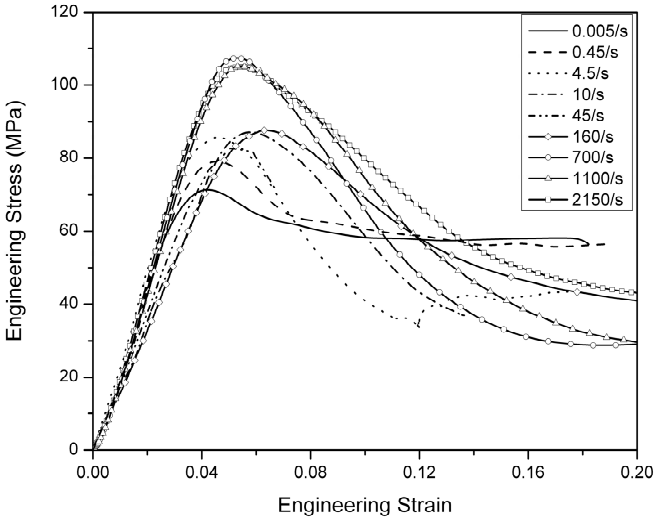

Figure 9.14 Compressive stress-strain curves at various strain rates
(Reproduced from Song et al. (2007d) with permission)

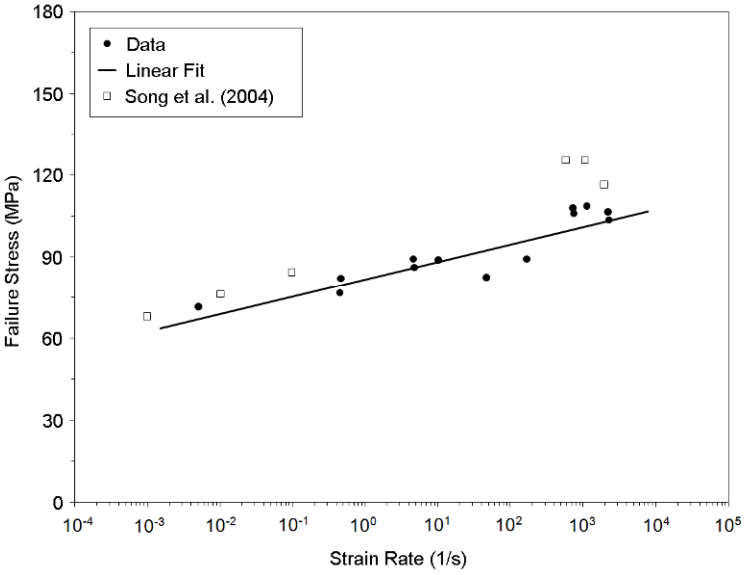

Figure 9.15 Strain rate effect on failure stress.
(Reproduced from Song et al. (2007d) with permission)

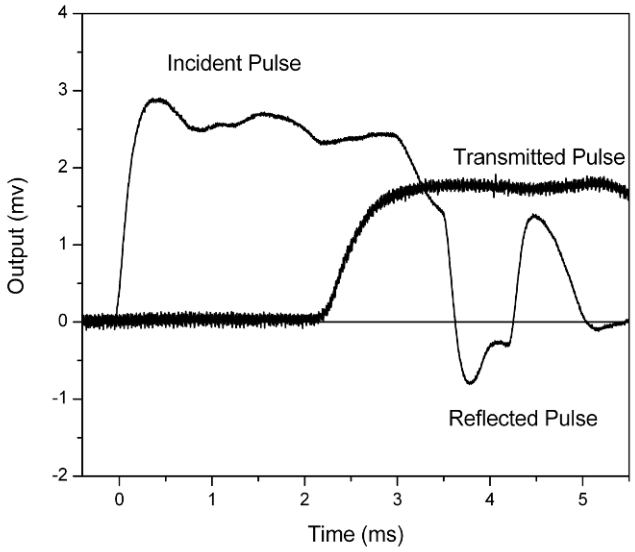

Figure 9.16 Pulses obtained from a long Kolsky bar experiment on a PMDI foam material
(Reproduced from Song et al. (2008) with permission)

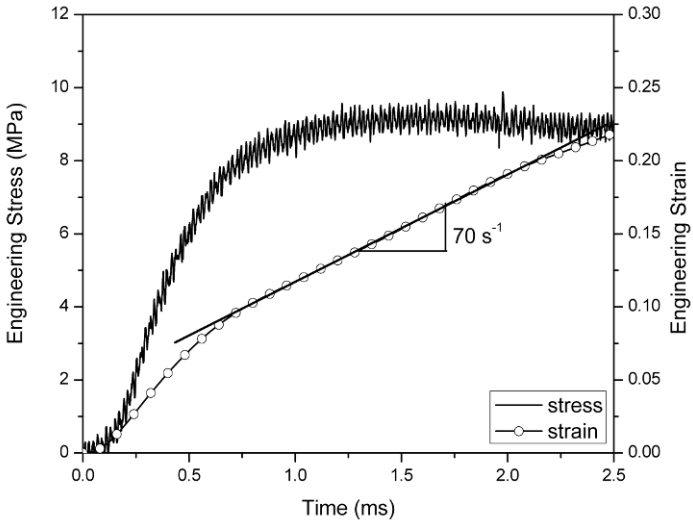

Figure 9.17 Stress and strain histories in the foam specimen
(Reproduced from Song et al. (2008) with permission)

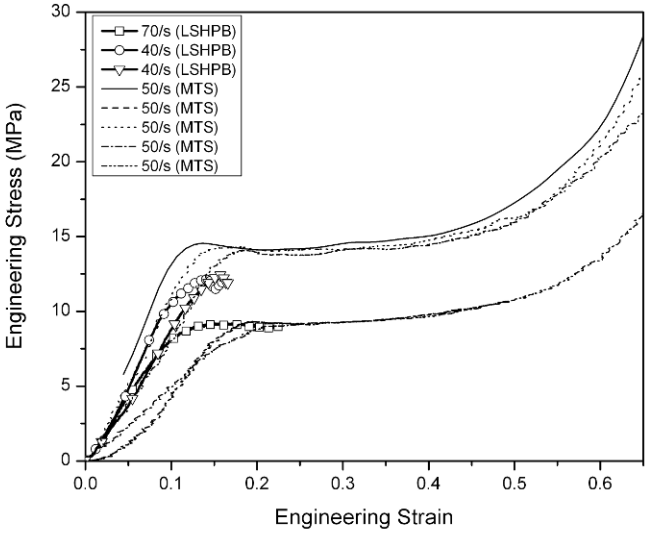

Figure 9.18 Compressive stress-strain curves obtain from MTS and long Kolsky bar at ~50 s^{-1}
(Reproduced from Song et al. (2008) with permission)

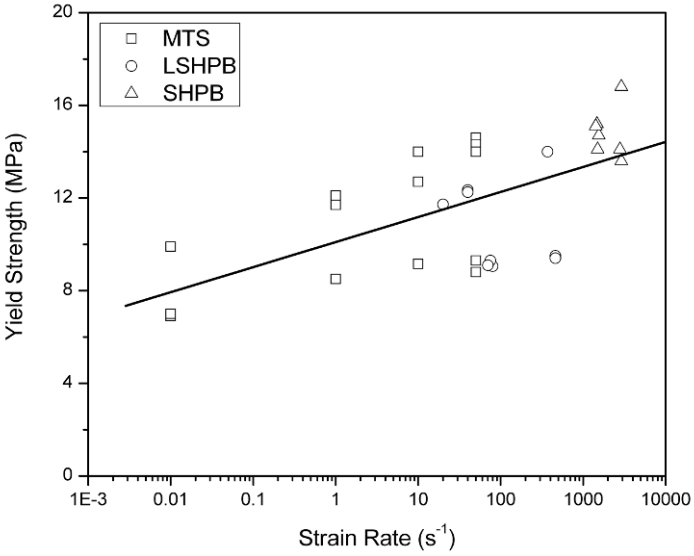

Figure 9.19 Strain-rate effects on the yield strength of the PMDI foam material
(Reproduced from Song et al. (2008) with permission)

Chapter 10. Kolsky Bar for Dynamic Structural Experiments

Kolsky bars rely on stress wave propagation in elastic bars to apply dynamic load on a specimen and to measure the loading and deformation histories in the specimen. This principle of using stress waves to supply dynamic loading and to remotely detect mechanical events can be equally employed to characterize the dynamic response of various structures. In this chapter, we review some of the recent applications of different versions of the Kolsky bars including (1) determination of dynamic fracture behaviors of notched specimens, (2) determination of the biaxial flexural strength of thin brittle sheets, (3) examination of the dynamic response of micro-machined structures, and (4) low-speed penetration.

10.1 Dynamic Fracture

A crack in a material begins to propagate when the stress intensity factor at the crack tip reaches a critical value under either quasi-static or dynamic loading. Standardized procedures are available to determine the fracture toughness of materials under quasi-static loading conditions. For example, in an ASTM procedure to determine the fracture toughness of ceramics (ASTM Standard C1421-01b 2001), precracked beam specimens are loaded in three- or four-point bending configurations. The loading rates during these quasi-static tests are controlled through the actuator displacement rates between 0.0005 to 0.005 mm/s on the testing machine. The employment of such low rates is necessary to ensure that stable crack propagation is achieved before peak load and that the peak load measured at the load cell approximately corresponds to the fracture toughness value locally at the crack tip.

Under impact loading, the critical stress intensity value corresponding to crack initiation for propagation is the dynamic initiation fracture toughness. Due to the wave-propagation nature in these experiments, accurate determination of the initiation toughness has been a challenge in dynamic testing methods. There have been no standard methods yet although many techniques have been proposed. Elastic stress wave propagation in bars become widely used methods for both loading and sensing. Most experimental configurations for dynamic fracture toughness determination are extensions of the corresponding quasi-static versions. How-

W.W. Chen and B. Song, *Split Hopkinson (Kolsky) Bar: Design, Testing and Applications*, Mechanical Engineering Series, DOI 10.1007/978-1-4419-7982-7_10,

ever, the involvement of elastic stress waves requires more attention in experiment design to obtain accurate results.

The methods for dynamic fracture toughness determination using stress waves can be categorized into three groups: high rate bending, high rate tension, and dynamic wedging. The high rate bending methods are direct extension of the quasi-static standard techniques. In the methods in this group, specimen designs are either one-, three-, or four-point bending of pre-cracked beams. The dynamic loading methods employed are mainly modified Kolsky bars. For data reduction, most methods used quasi-static equations to correlate far-field peak load measured by the transmitted signal with the local fracture toughness at crack tip. To explore the effects of stress wave propagation in the specimen under dynamic loading, Böhme and Kalthoff (1982) performed a series of well instrumented experiments on three-point bending specimens with a drop weight tower. A typical configuration of such experiments is shown in Fig. 10.1.

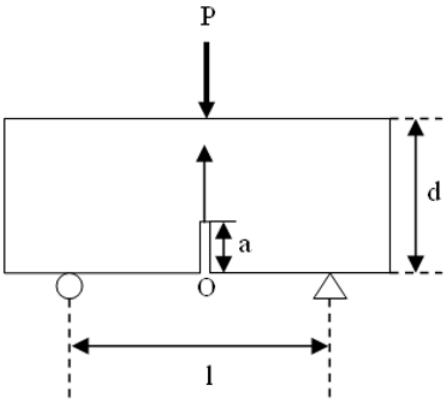

Figure 10.1 Three-point bending configuration for dynamic fracture experiments
(Reproduced from Böhme and Kalthoff (1982) with permission)

In their experiments, Böhme and Kalthoff (1982) measured the load histories at the loading point and the two supporting points, the displacement histories between the supports and the specimen, and the crack tip stress-intensity factor history. The results showed that the load history recorded from the loading point synchronizes neither with the histories at the supports, nor with the crack tip stress-intensity factor history. Furthermore, when the loading point was impacted, the specimen jumped off the support at the supporting points and then regained contact 400 μs later. During the initial stages of the loading process, the specimen was under one-point bending rather than three-point. Their results also showed that the loading rate at the crack tip fluctuated severely, instead of remaining at the desired constant level. Therefore, the crack tip stress intensity factor in such dynamic bending experiments does not synchronize with far-field load measurements, which are typically the loads at the supporting points. Due to the sudden impact at the loading point, the bending motion of the specimen may also be coupled with the vibrations at its resonance frequency. The measured load from the supporting points is thus mixed with material strength and specimen inertia. With the complicated relationship between the loading history measured at the supports and that experienced by the crack-tip, if there is any, quasi-static equations relating the far-field peak loading to fracture toughness are hardly valid under dynamic loading.

The issue of "loss of contact" during dynamic fracture testing was experimentally investigated more recently by Jiang and Vecchio (2007). They used a voltage measurement circuit across the specimen/loading pin interfaces, together with high speed photography. They concluded that the three-point bend specimen remains in contact with the front impactor and back loading pins throughout the first loading duration.

To obtain valid dynamic fracture toughness as a function of loading rate from dynamic bending experiments, Weerasooriya et al. (2006) incorporated the pulse-shaping technique in their four-point-bending experiments using a Kolsky bar to determine the dynamic initiation fracture toughness of ceramics at high rates. Instead of suddenly loading the precracked beam specimen in the testing section of the Kolsky bar, the incident pulse was controlled to have a much lower increasing rate in loading, allowing the beam specimen to achieve dynamic force equilibrium. In this way, the loading history at the supporting points is synchronized with that in the entire specimen, allowing the interpretation of the crack tip loading state by the far-field loading measurements. Furthermore, the loading pulse is shaped such that the loading rate at the crack tip is nearly constant during an experiment, enabling the determination of loading-rate effects. The migration of the pulse shaping technique for Kolsky-bar experiments facilitates the determination of the dynamic initiation frac-

ture toughness as a function of loading rate for a silicon carbide (SiC-N) and Plexiglas (PMMA). Figure 10.2 shows the gage section in four-point bending configuration of the experimental setup used by Weerasooriya et al. (2006). Quartz crystal force transducers are employed on both sides of the test section. The bars are made of an aluminum alloy.

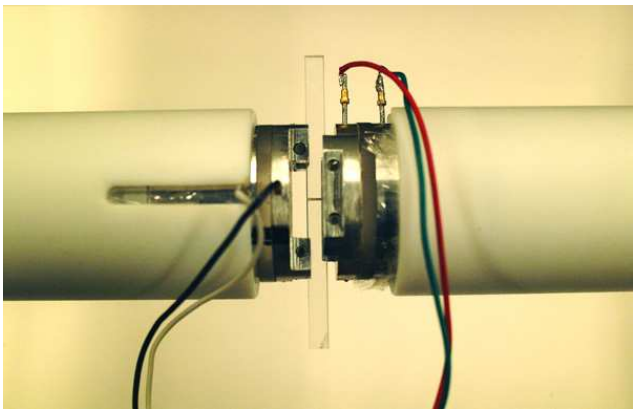

Figure 10.2 The gage section of a Kolsky bar for fracture experiments
(Reproduced from Weerasooriya et al. (2006) with permission)

Figure 10.3 shows the oscilloscope records of an experiment using an aluminum Kolsky bar modified for the dynamic fracture experiments (Weerasooriya et al. 2006). The 7075-T6 aluminum incident and transmission bars are 31.75-mm in diameter and 3658-mm in length. The X-cut quartz crystals have the same diameter as the aluminum bars. The transmitted pulse as measured by the resistor strain gages mounted on the transmission bar did not show any recognizable signal. The measurements from the quartz crystal force transducers are used instead. The nearly identical oscilloscope traces recorded from the two piezoelectric force transducers mounted in front and behind the specimen indicate that the pre-cracked specimen is nearly under dynamic equilibrium over the entire duration of the experiment. The quasi-static equation can thus be applied to relate the peak far-field load to the dynamic fracture tough-

ness. These traces also show that the loading rate over the entire specimen is nearly constant as indicated by the nearly constant slope of the force histories recorded by the quartz crystals.

The overlapped quartz crystal traces indicate that no resonance was excited in the specimen during the dynamic loading. Unlike Kolsky tension or compression bar experiments where the specimen is stiff and thus has very high resonance frequencies, the beam specimen is a structure and has much lower natural frequencies. The loading pulse should be designed such that the loading pulse frequency is far below the fundamental natural frequency of the specimen. We now analyze the frequency response of the specimen system schematically shown in Fig. 10.4 (Cheng et al. 2002).

The equation of motion expressed in terms of particle displacement for a straight and constant cross-section rod is

$$\frac{\partial^2 u}{\partial x^2} - \frac{1}{c_0^2}\frac{\partial^2 u}{\partial t^2} = 0 \tag{10.1}$$

which is the well-known one-dimensional wave equation, with a general solution

$$u(x,t) = f(x - C_0 t) + g(x + C_0 t) \tag{10.2}$$

The first term on the right-hand side represents a forward-moving wave along the positive x-direction (i.e., the bar loading axis) and the second is a backward-moving wave. In an idealized half infinite-length longitudinal rod such as the transmission bar before any wave reflection, only a forward-moving wave exists. However, in the incident bar, both the forward incident waves and the backward reflected waves exist within the window of solution period. In addition, these waves overlap near the specimen end.

To facilitate a computer simulation of the transmitted signal as a function of the incident signal frequencies, spectral analysis method based on a discrete Fourier transform (DFT) is applied (Cheng et al. 2002). Equation (10.2) is thus transformed into

$$u(x,t) = \sum_{n=0}^{N-1} U(x;n)\, e^{i\omega_n t} \tag{10.3}$$

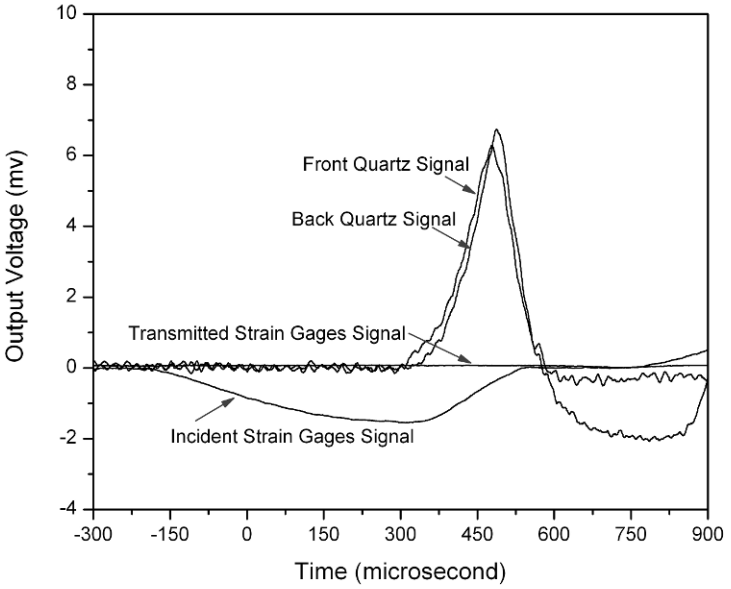

Figure 10.3 Experimental record of a dynamic fracture experiment on a SiC-N
(Reproduced from Weerasooriya et al. (2006) with permission)

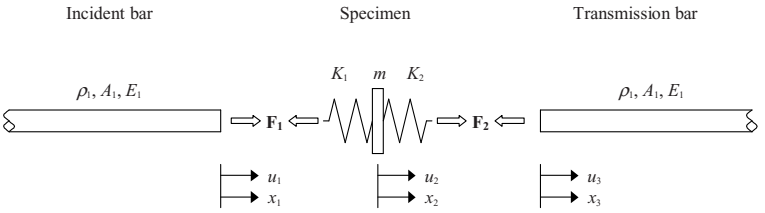

Figure 10.4 A model for specimen resonance analysis
(Reproduced from Chen et al. (2002) with permission)

where N is the length of the DFT, $U(x;n)$ are the DFT components of the displacement $u(x,t)$, ω_n is the angular frequency, and n is an index. Substitution of (10.3) into (10.1) yields an ordinary differential equation, which has a solution

$$U(x,n) = ae^{-ikx} + be^{ikx} \tag{10.4}$$

where $k = \omega_n / C_0 = \omega_n \sqrt{\rho / E}$.

The coefficients a and b are undetermined amplitudes that depend on each frequency. Substitution of (10.4) into (10.3) yields the particle displacement as functions of position (x) and time (t) which has both forward and backward terms

$$u(x,t) = \sum_{n=0}^{N-1} ae^{-i(kx-\omega_n t)} + \sum_{n=0}^{N-1} be^{i(kx+\omega_n t)} \tag{10.5}$$

The particle displacements in the incident and transmission bars can thus be expressed as

$$u_1(x,t) = \sum_{n=0}^{N-1} a_1 e^{-i(k_1 x_1-\omega_n t)} + \sum_{n=0}^{N-1} b_1 e^{i(k_1 x_1+\omega_n t)} \tag{10.6}$$

and

$$u_2(x,t) = \sum_{n=0}^{N-1} a_2 e^{-i(k_2 x_2-\omega_n t)} \tag{10.7}$$

The coefficients a_1, b_1, and a_2 are determined by boundary conditions.

When the bar material is linearly elastic, the loads at the bar ends can be related to the displacement gradients,

$$E_1 A_1 \left.\frac{\partial u_1(x_1,t)}{\partial x_1}\right|_{x_1=0} = \mathrm{F}_1(t) = \sum_{n=0}^{N-1} F_1(n) e^{i\omega_n t} \tag{10.8}$$

and

$$E_2 A_2 \left.\frac{\partial u_2(x_2,t)}{\partial x_2}\right|_{x_2=0} = \mathrm{F}_2(t) = \sum_{n=0}^{N-1} F_2(n)\, e^{i\omega_n t} \tag{10.9}$$

The lumped mass of the specimen moves according to Newton's second law,

$$\mathrm{F}_2 - \mathrm{F}_1 = m\frac{d^2\,\mathrm{u}_3}{dt^2} \tag{10.10}$$

which should vanish for the specimen under dynamic force equilibrium ($F_2 = F_1$) in an ideal dynamic experiment. In addition, the linear elasticity of the specimen stiffness is divided into the two springs connected to the incident and transmission bar ends and is described with

$$\mathrm{F}_1 = K_1(\mathrm{u}_2 - \mathrm{u}_1) \tag{10.11}$$

and

$$\mathrm{F}_2 = K_2(\mathrm{u}_2 - \mathrm{u}_3) \tag{10.12}$$

The boundary conditions expressed by (10.8)-(10.12) can be written in terms of the corresponding Fourier components respectively as follows

$$-ik_1 E_1 A_1 a_1 + ik_1 E_1 A_1 b_1 = F_1 \tag{10.13}$$

$$-ik_2 E_2 A_2 a_2 = F_2 \tag{10.14}$$

$$F_2 - F_1 = -m\omega_n^2 u_3 \tag{10.15}$$

$$F_1 = K_1 u_3 - K_1 a_1 - K_1 b_1 \tag{10.16}$$

$$F_2 = K_2 a_2 - K_2 u_3 \tag{10.17}$$

With the pulse-shaping technique, we know the incident pulse precisely. Therefore, a_1, is known among the variables. There are five unknowns (F_1, F_2, b_1, a_2, and u_3) and five equations of boundary conditions (10-13) – (10.17), which can be written in a matrix form

$$\begin{bmatrix} 1 & 0 & -ik_1E_1A_1 & 0 & 0 \\ 0 & 1 & 0 & ik_2E_2A_2 & 0 \\ 1 & -1 & 0 & 0 & -m\omega_n^2 \\ 1 & 0 & K_1 & 0 & -K_1 \\ 0 & 1 & 0 & -K_2 & K_2 \end{bmatrix} \begin{Bmatrix} F_1 \\ F_2 \\ b_1 \\ a_2 \\ u_3 \end{Bmatrix} = \begin{Bmatrix} -ik_1E_1A_1a_1 \\ 0 \\ 0 \\ -K_1a_1 \\ 0 \end{Bmatrix} \tag{10.18}$$

A transfer function, $H_1(\omega_n)$, between two of the solvable variables, F_1 and F_2, can explicitly express the status of dynamic equilibrium. The transfer function, which should be unity in an ideal experiment, is found to be

$$H(\omega_n) = \frac{F_2}{F_1} = \frac{1}{1 - \dfrac{m\omega_n^2}{k_2} + i\dfrac{m\omega_n^2}{k_2E_2A_2}} \tag{10.19}$$

A typical variation of H as a function of frequency is shown in Fig. 10.5, with the parameters taken from the experimental setup for SiC-N fracture experiments, where the specimen mass m is 3.314×10^{-3} kg, the specimen elastic stiffness K_2 is 0.3569×10^5 N/m, the transmission bar cross-sectional area A_2 is 7.9173×10^{-4} m^2, the transmission bar material density ρ_2 is 2800 kg/m^3, and the transmission bar material Young's modulus E_2 is 72 GPa. As shown in Fig. 10.5, the first resonant frequency is 1651.7 Hz. The base frequency of the loading pulse is around 700 Hz, which is far below the resonant frequency. The transfer function H thus has a value close to unity (dynamic equilibrium) as can be observed in Fig. 10.5.

The first resonant frequency is a restriction for the highest frequency component in the incident pulse to pass through the specimen without significant dispersion. The specimen can only be in a dynamic equilibrium state when the incident pulse is band-limited within this first resonant frequency. If the loading frequency is higher than the first resonant frequency, the phase angle of the force signal on the transmission bar side is 180° (π) from the applied loading. This is consistent with the phenomenon observed by Böhme and Kalthoff (1982) in their experiments where the specimen jumped off supports when impacted at the loading point.

To determine the dynamic initiation fracture toughness of SiC-N ceramic material and its rate effects, four-point bending experiments on Chevron-notched specimens under both quasi-static and dynamic loading conditions were conducted at US Army Research Laboratory (Weerasooriya et al. 2006). The dynamic experiments were conducted using a modified Kolsky bar. The fracture toughness was calculated with the following equation,

$$K_{Ivb} = Y^*_{\min}\left[\frac{P_{\max}\left(S_0 - S_i\right)\times 10^{-6}}{BW^{3/2}}\right] \tag{10.20}$$

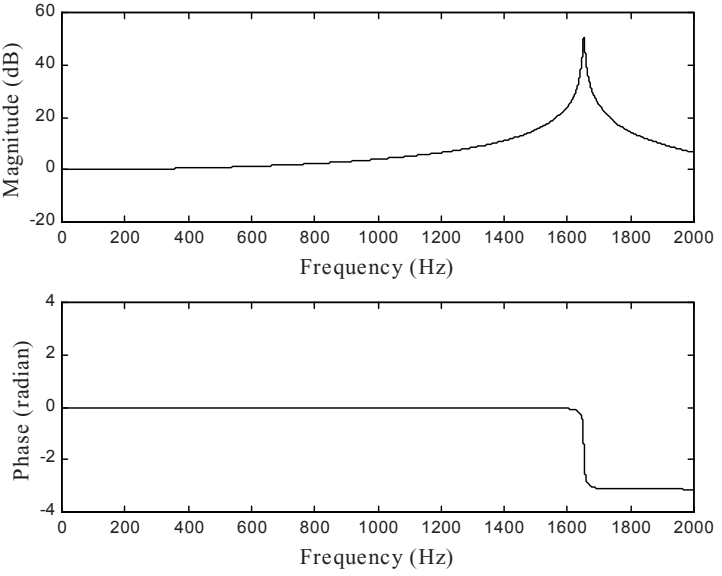

Figure 10.5 Variation of force ratio on specimen ends as a function of frequency
(Reproduced from Chen et al. (2002) with permission)

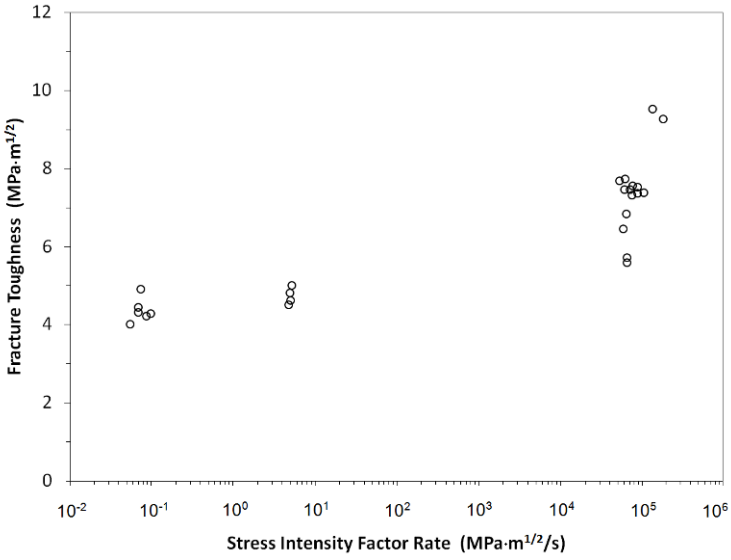

Figure 10.6 Variation in SiC-N initiation fracture toughness with loading rate *(Reproduced from Weerasooriya et al. (2006) with permission)*

where K_{Ivb} is the fracture toughness of a brittle four-point bending beam specimen with a Chevron notch, P_{max} is the measured peak axial force by the quartz crystals, B is the width of the specimen with a height W, S_0 is the distance between the two supporting points on the notch side of the specimen, and S_i is the distance between the two loading points on the other side of the specimen. The parameter Y^*_{min} is calculated based on the shape of the Chevron notch (Weerasooriya et al. 2006). The dependence of fracture toughness on the loading rate is shown in Fig. 10.6, which indicates that the average fracture toughness varied from 4.5 to 5.0 MPa·m$^{1/2}$ in the quasi-static range to 5.5 – 9.5 MPa·m$^{1/2}$ in the dynamic range.

Similar experiments were conducted on notched PMMA beams, also at the US Army Research Laboratory. The results are shown in Fig. 10.7, which indicates that the average fracture toughness varied from around 1.5 MPa·m$^{1/2}$ in the quasi-static range to about 3.3 MPa·m$^{1/2}$ in the dynamic range.

The use of Kolsky bar to determine the dynamic fracture toughness has been extensively reviewed (Jiang and Vecchio 2009). However, experimental data have been scarce nowadays. There has been no standard method or even a well-agreed common approach for such experiments.

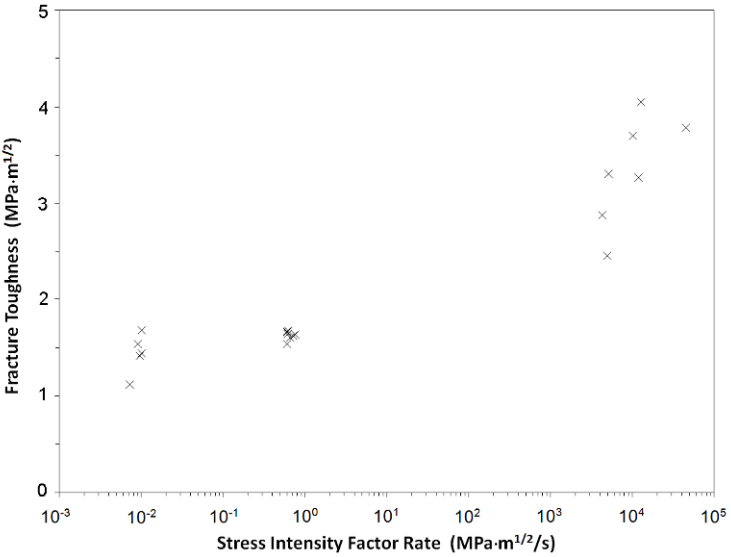

Figure 10.7 Variation in PMMA initiation fracture toughness with loading rate

Besides bending configuration, dynamic fracture has also been realized by direct tension on notched rods, compact tension (CT) specimens, and pre-cracked beams (Suresh et al. 1990, Deobald and Kobayashi 1992, Owen et al. 1998). Suresh et al. (1990) used explosive loading on a Kolsky tension bar to dynamically load circumferentially notched and cyclically fatigue-precracked ceramic rods, as schematically shown in Fig. 10.8. The dynamic stress intensity factor at the circumferential crack tip was calculated using the specific specimen geometry and the load history as measured by a strain gage mounted on the transmission bar. The length of the specimens was 33.6 mm with the pre-crack located at 25.4 mm for room temperature tests and 458 mm with the pre-crack in the middle for elevated temperature experiments. A long specimen is neces-

sary for high-temperature experiments to allow furnace space. Owen et al. (1998) used a conventional Kolsky tension bar to obtain the dynamic initiation fracture toughness of 2024-T3 aluminum from samples of thin (1.5-2.5 mm) sheets (Fig. 10.9). The pre-cracked specimen has a width of w = 12.7 mm and a length of l = 57 mm. During an experiment, the transmitted pulse is recorded as the dynamic tensile loading history and the initial crack length is measured on the fracture surface. A quasi-static equation is used to relate the recorded tensile stress history and initial crack length to the dynamic stress intensity factor, from which the dynamic initiation toughness is calculated. The use of such an equation indicates the assumption of dynamic equilibrium in the specimen.

Deobald and Kobayashi (1992) used reflected tensile wave to load the crack tip (Fig. 10.10), which is similar to the Nicholas' design of Kolsky tension bar using a compression bar facility. A precrack is made in the middle of a 50.8-mm long ceramic specimen. A 25.4-mm long striker of the same cross-section and the same material is driven to impact one end the precracked bar. The crack opening displacement (COD) is measured using a laser-interferometric displacement gage (LIDG) commonly used in fatigue experiment (Sharpe 1989). The measured stress and COD histories are then interpreted into the dynamic initiation fracture toughness, dynamic branching fracture toughness, and crack propagation velocity. In this type of experiments, due to the fact that high-rate dynamic tensile load is applied from one side of the specimen, the crack tip may not under Mode-I fracture due to unsymmetric loading as demonstrated in Fig. 10.11 (Maekawa and Shibata 1995). Furthermore, unless the crack initiates during the first pass of the stress pulse, which requires local measurement near the crack tip, the stress waves sweep through the crack tip back and forth. The stress state at the crack tip does not synchronize with the far-field load measurements. In addition, the loading rate at the crack tip is not constant.

Another approach to dynamically load the pre-cracked specimen is dynamic wedging proposed by Klepaczko (1982), which is illustrated in Fig. 10.12. In these experiments, the specimens are wedge loaded compact tension (WLCT) configuration, which is modified from the standard compact tension design to accommodate the loading wedge. Dynamic loading is facilitated by a Kolsky bar. Although this method avoids the uneven loading that occurred in the dynamic tension experiments, the friction between the wedge and the specimen is a concern in accurate data reduction.

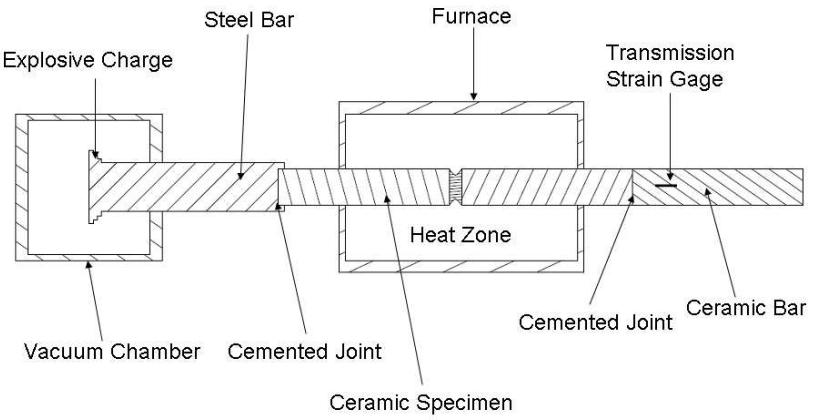

Figure 10.8 Direct tension experiments by Suresh et al. (1990)

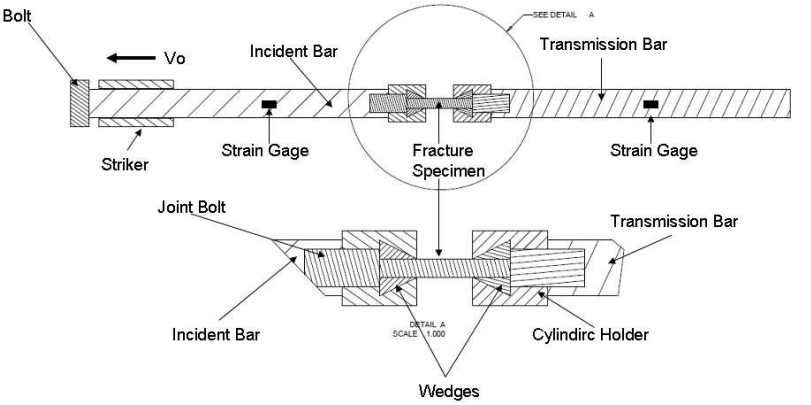

Figure 10.9 Direct tension experiments by Owen et al. (1998)

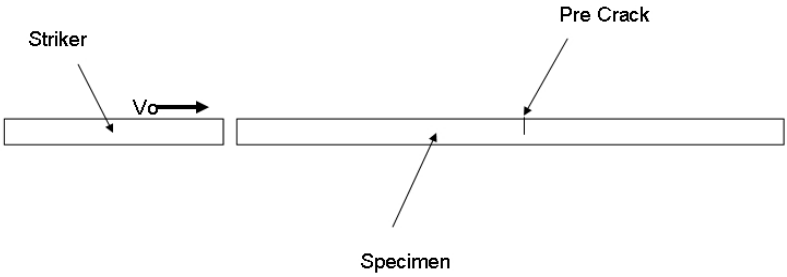

Figure 10.10 Reflected tension experiments by Deobald and Kobayashi (1992)
(Reproduced from Deobald and Kobayashi (1992) with permission)

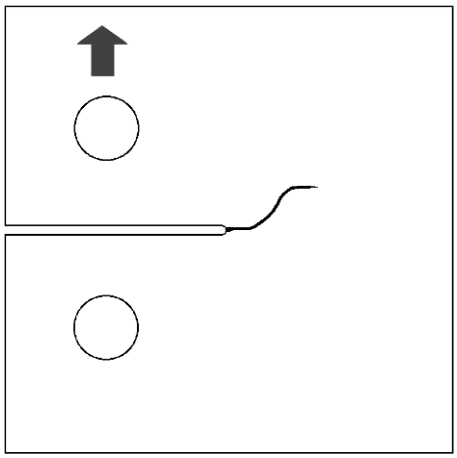

Figure 10.11 Asymmetric crack under direct tension

Sun and Han (2004) used a smaller wedging specimen and studied the static and dynamic Mode I delamination fracture in uni-directional composite materials. Figure 10.13 shows a schematic illustration of such a dynamic experimental setup. The same gage section was used in both quasi-static and dynamic experiments. The value of the dynamic fracture toughness was found to approximately equal the static fracture toughness. However, the dynamic energy release rate was found to increase significantly with the crack speed. Besides Mode I delamination experiments, the setup shown in Fig. 10.13 can also be used to conduct dynamic experiments to measure Mode II fracture toughness. This is achieved by modifying the test section in a three-point bending configuration and using an end notched flexure (ENF) specimen ("K II mode" in Fig. 10.13).

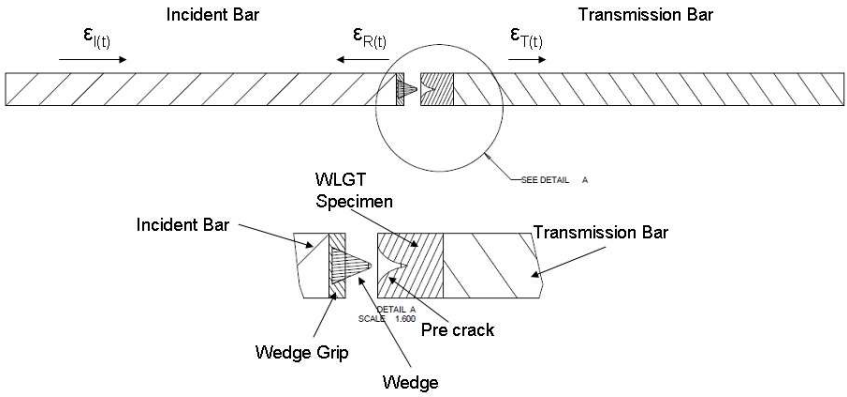

Figure 10.12 Dynamic wedging setup and specimen

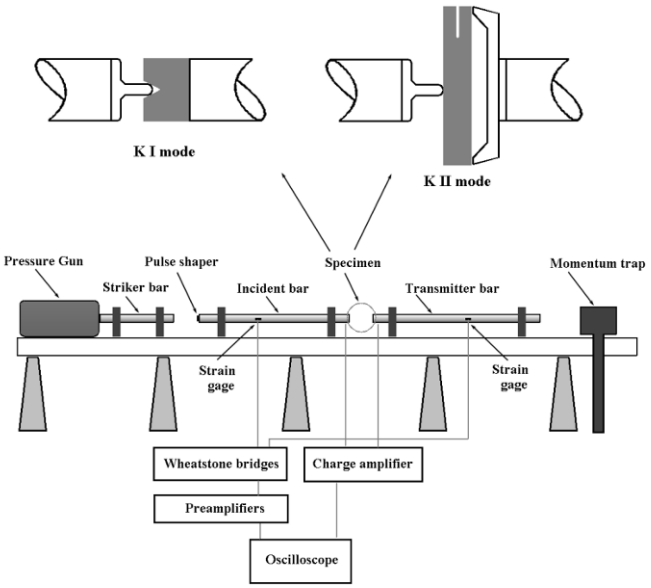

Figure 10.13 Dynamic wedging experiments

10.2 Dynamic Equi-biaxial Bending Experiments

Thin ceramic sheets are widely used in engineering applications. Electrically insulating thin sheets are used for electronic substrate applications in nearly all semiconductor products. Ceramic membranes are used as molecular filters in fuel cells and solid oxide electrolyzers for oxygen generation. Ceramic armors and transparent armors are often built with a layered structural design. Effective utilization of materials in such struc-

tures requires the accurate characterization of the mechanical properties of those materials in the form of thin sheets. The American Society of Testing and Materials (ASTM) has a standard using piston-on-3-ball tests to obtain the equi-biaxial flexural strength of ceramic sheets (ASTM F 394-78 1995). In such a test, a thin ceramic sheet is placed on three balls sitting 120° apart on a circular pattern. A piston pushes at the center of the circle from the other side of the ceramic sheet, thus producing an equi-biaxial flexural loading condition. For the loads to be more evenly distributed on the ceramic sheet, the three supporting balls may be replaced by a ring. The piston could also be replaced by a smaller ring, a ball, or simply pressure. The resultant configurations are called ring-on-ring, ball-on-ring, and pressure-on-ring tests, respectively.

The piston-on-three-ball and ring-on-ring testing configurations have been extended into dynamic loading range. Cheng et al. (2002) presented an experimental method that integrated the piston-on-three-ball configuration on to the testing section of a modified Kolsky compression bar. In the experiments conducted using this method, the desired dynamic loading rates are precisely controlled. The range of loading rates is analytically determined by a similar procedure leading to equation (10.19) by using parameters for the piston-on-three-ball setup. This analysis limits the loading rates such that no resonance frequencies in the specimen are excited. Using this technique, the loading rate effects on the flexural strength of yttria-stabilized zirconia thin sheets were determined. The configuration of the dynamic piston-on-3-ball method is shown schematically in Fig. 10.14 (Cheng et al. 2002).

The dynamic version of the equibiaxial ring-on-ring testing method has also been developed with a modified Kolsky bar. The ring-on-ring configuration according to ASTM C1499 (2003) is adapted to the test section of a Kolsky bar (Nie et al. 2010). A pair of concentric steel rings hardened to HRC 60 and polished was attached to concentric aluminum substrates on the Kolsky bar so that the system alignment is secured. The diameters of those concentric rings are 12.5 mm and 25 mm, respectively, with a ring tip radius of 2.5 mm. The incident and transmission bars of the Kolsky bar setup are made of 6061-T6 aluminum alloy with a common diameter of 31.75 mm. In addition to the ring fixture, a pair of universal joints (introduced in Chapter 3.3) which are of the same diameter of the bars was also placed between the gage section and the transmission bar. During specimen-installation, this pair of surfaces is the last to engage, eliminating misalignment and ensuring an even contact between the loading rings and the specimen surface.

To preserve the failure modes on the brittle disk specimens, the feature of single-pulse loading as described in Chapter 2.6 is employed in the modified Kolsky-bar setup. A schematic of the experimental setup is

shown in Fig. 10.15, with an image of the test section shown in Fig. 10.16 (Nie et al. 2010).

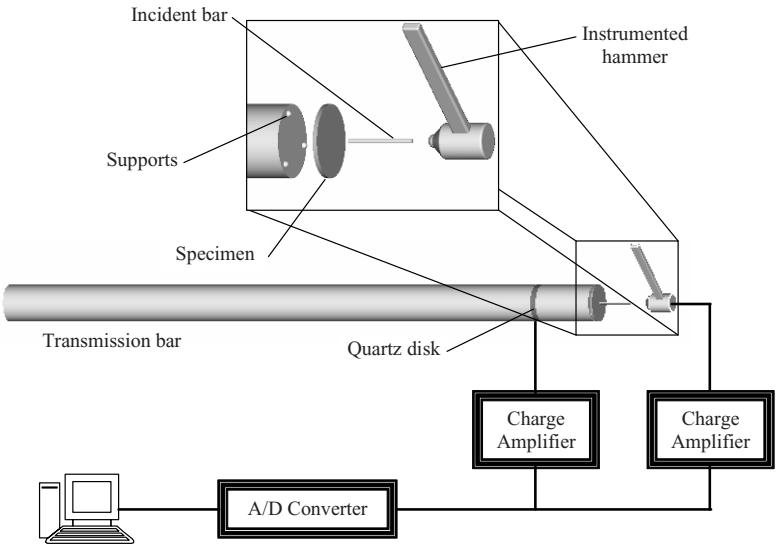

Figure 10.14 Dynamic piston-on-three-ball setup
(Reproduced from Cheng et al. (2002) with permission)

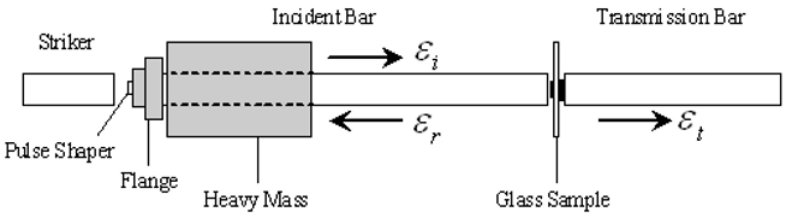

Figure 10.15 A modified Kolsky bar dynamic ring-on-ring experiments
(Reproduced from Nie et al. (2010) with permission)

The material studied by this set of experiments is a borosilicate glass. The chemical composition of the glass is 80.5% SiO_2, 12.7% B_2O_3, 3.5% Na_2O, and 2.5% Al_2O_3. The glass has a density $\rho = 2.21\, g/cm^3$, Poisson's ratio $\nu = 0.19$, longitudinal wave speed $C_L = 5508\, m/s$, and shear wave speed $C_s = 3417\, m/s$. Disk specimens of 2 mm in thickness and 45 mm in diameter were cut and ground from 3.3-mm thick flat plates. The top and bottom surfaces of these glass disks were mechanically polished to 40/20 scratch/dig and the overall surface roughness to be less than 20 angstroms. In order to reduce the possibility of edge failures, the circumferences of the disks were fire polished to eliminate sharp surface cracks induced by grinding. The as-polished samples were then divided into 3 groups. The first group has the as-polished surfaces. The tensile surfaces of the second group of samples were ground by 180-grit sandpapers. The last group was etched by 5 wt.% of HF acid aqueous solution for 15 minutes, which resulted in a 20-μm reduction in thickness at each surface. The etched specimens were subjected to mechanical loading within several minutes after etching.

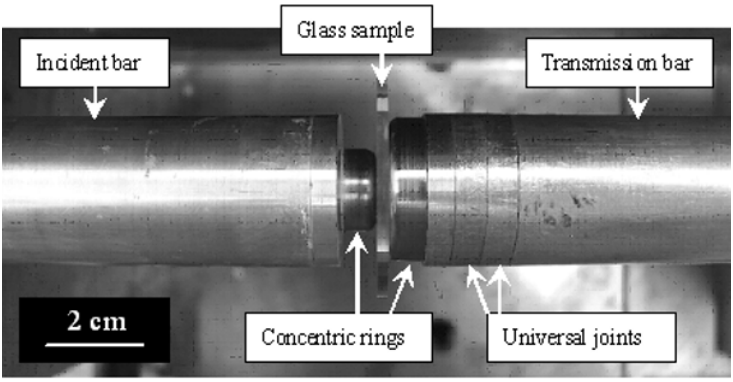

Figure 10.16 A side view of the test section of the actual experimental setup

Dynamic experiments were carried out using the modified Kolsky bar setup shown in Fig. 10.15. Figure 10.16 shows a photograph of the testing section of the actual experimental setup. To load the disk specimen at a nearly constant loading rate without exciting resonance, the loading pulse was carefully designed and controlled. In a ring-on-ring flexural experiment, the specimen loading rate is proportional to the deflection rate (Nie et al. 2010). So the profile of loading pulse needs to be determined in such a way that the reflected wave (deflection rate history of the specimen) has a plateau after initial rise. In this study, an annealed copper disk pulse shaper of 1 mm in thickness and 3.3 mm in diameter was used to generate the desired incident pulse at a resultant specimen loading rate of approximately 5×10^6 MPa/s. Equi-biaxial flexural tests were also conducted on all 3 groups of glass samples at three other loading rates (0.52 MPa/s, 42 MPa/s, 3500 MPa/s) on a servohydraulic machine to study the rate effects on the equi-biaxial strength.

The equi-biaxial strength values for borosilicate glass specimens at different loading rates and surface conditions are shown in Fig. 10.17. The results indicate that the surface modifications significantly affect the flexural strength of the glass material. The sandpaper grinding degrades the strength by 60-70% from the as-polished surface condition. However, HF acid etching on polished specimens enhances the surface tensile strength by 200-400%, depending on the applied loading rates. The experimental results also indicate that the flexural strength is loading-rate sensitive. Under all surface conditions, the strength increases with loading rates. But the rate of strength increase levels out after the loading rate exceeds ~3500 MPa/s.

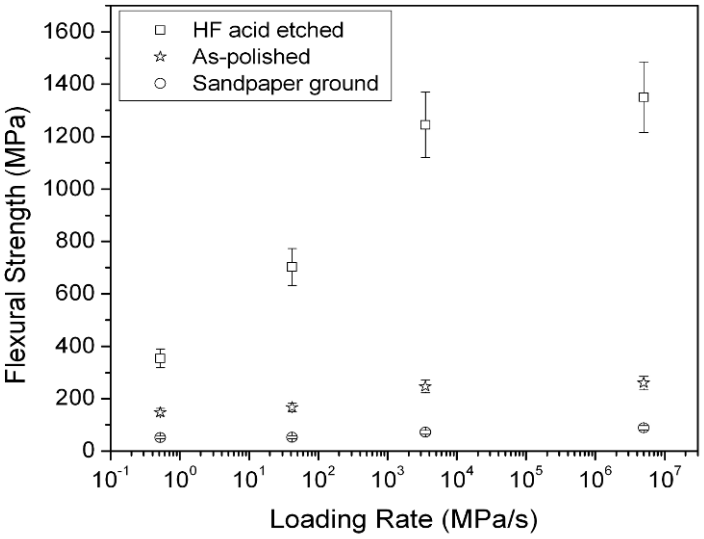

Figure 10.17 Equi-biaxial flexural strength of a borosilicate glass
(Reproduced from Nie et al. (2010) with permission)

10.3 Dynamic Response of Micro-machined Structures

Micro-machined structures have potential to be used under extreme loading conditions. For example, to gain a fundamental understanding of projectile penetration process for concrete and geological targets, micro-machined accelerometers are used to measure the rigid-body deceleration of the projectile, which can reach 20,000 G (1 G = 9.81m/s^2), to provide a measure of net force on the projectile nose. These accelerometers, together with onboard recording packages, are structurally mounted inside the projectiles. Due to the critical function of the accelerometers in the penetration events, the performance of the accelerometers must be evaluated and calibrated. Previous studies have documented performance evaluation techniques used to validate high amplitude accelerations. Kolsky-bar pulse shaping techniques have become available to create con-

trollable and repeatable acceleration pulses (Frew et al., 2002) to evaluate acceleromaters used for penetration applications (Forrestal et al. 2003).

In the tests presented here, a series of modified Kolsky-bar experiments were conducted to evaluate a new, damped, high-shock accelerometer (Frew et al. 2009). Pulse shapers were used to create a long duration, non-dispersive stress pulse in an aluminum bar that interacted with a tungsten disk at the end of the incident bar. The stress at the aluminum bar-disk interface was measured with a quartz gage. The actual acceleration at the free-end of the disk was measured by both the accelerometer under evaluation (PCB 3991) and a reference Endevco 7270A accelerometer (Fig. 10.18).

Figure 10.18 The tungsten disk assembly with accelerometers mounted

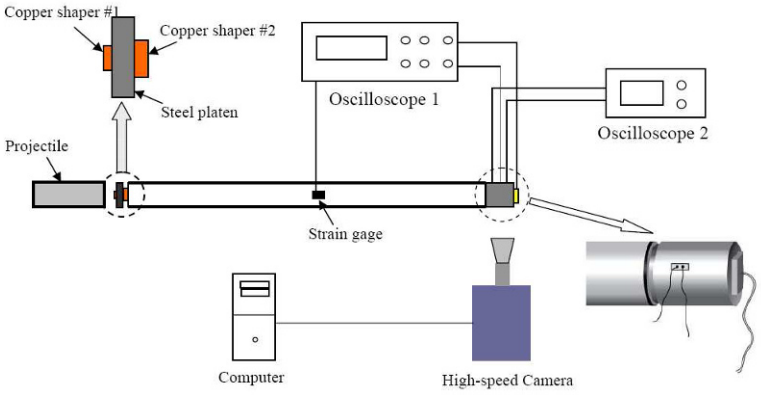

Figure 10.19 The accelerometer evaluation apparatus

Figure 10.19 shows a schematic of the Kolsky-bar apparatus, which does not have a transmission bar. The incident bar is a 3.05-m-long, 19.05-mm-diameter, 7075-T651 aluminum rod. Resistor strain gages are mounted diametrically opposed 0.76m from the impact end. A 17.78-mm-thick tungsten disk is bounded with a 0.25-mm-thick quartz crystal force transducer on one side with conductive epoxy. A 19.05-mm-diameter maraging steel striker with a length of either 152.4 or 609.6 mm was launched from a gas gun to the required velocities. One or two annealed C11000 cylindrical copper pulse shapers were used to create the required non-dispersive incident stress pulses that produced nearly constant-amplitude accelerations for the experiments.

When the incident pulse arrives at the tungsten disk assembly (quartz, tungsten, and accelerometers), due to the high impedance of the tungsten disk, a compression wave reflects back into the incident bar and the quartz gage measures the sum of the incident and reflected force pulses. When the incident stress wave stops increasing, the peak stress is reflected back as a tensile wave from the free end of the tungsten assembly that separates the tungsten assembly from the incident bar, which is caught in a soft catcher. The rise time of the stress pulse in the incident bar is long enough and the tungsten disk assembly is short enough that the response of the assembly with mass m can be considered as rigid-body motion. The acceleration, $a(t)$, can be calculated from the force measurement, F_q, by the quartz crystal with Newton's second law

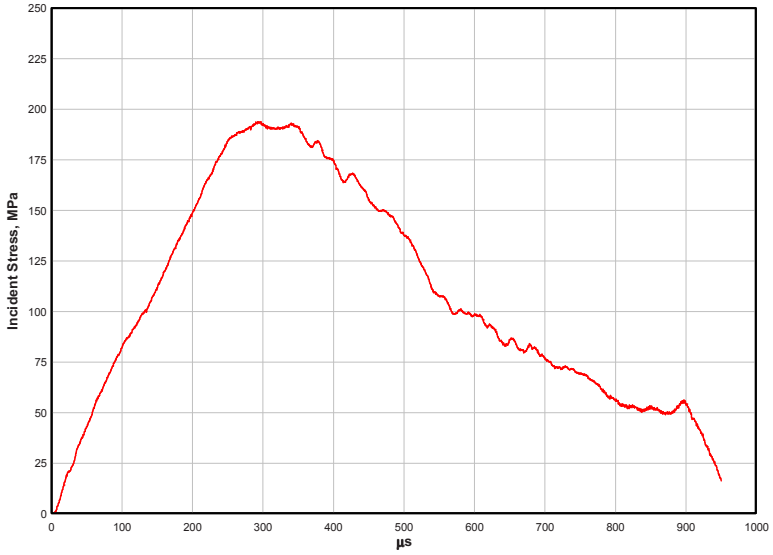

Figure 10.20 The incident pulse for constant acceleration

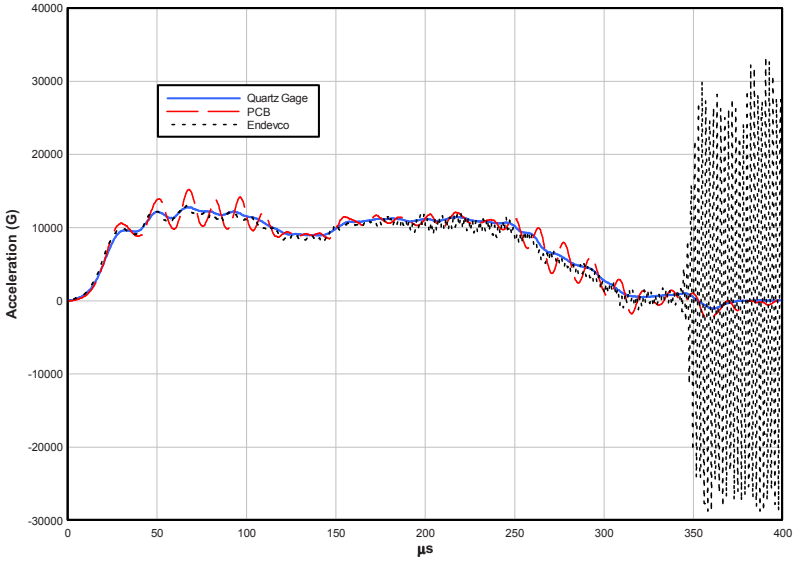

Figure 10.21 The acceleration measured by different devices

$$a(t) = \frac{F_q}{m} \tag{10.21}$$

Figure 10.20 shows the incident stress pulse from a mid-level acceleration experiment. This incident pulse generated a nearly constant acceleration of about 10,000 Gs for approximately 300 μs in the tungsten disk assembly, as shown in Figure 10.21. The output from the new PCB accelerometer oscillates around the reference Endevco accelerometer and the quartz crystal output. However, all three outputs show good correlation. At 350 μs, when the tungsten disk separated from the aluminum incident bar, the reference accelerometer experienced high amplitude oscillations.

A similar Kolsky-bar setup has been used to evaluate the performance of a recently developed micro-machined accelerometer. A novel high–G MEMS digital accelerometer is under development at Purdue University. Cantilever beams corresponding to different acceleration levels are fabricated on low resistivity silicon on insulator (SOI) wafers using micromachining techniques. Cantilevers created from SOI wafers have uniform single-crystal nature with negligible residual stresses. The cantilevers have spring constants in the order of 184 – 462 N/m for a deflection of 2 μm corresponding to different acceleration levels of 20 – 40 kGs. This in turn corresponds to beams of length of 533-630 μm and width of 70-100 μm as well as thickness of 20 μm. The beams are fabricated in a 0.3 cm by 0.3 cm die which is then packaged and wire bonded in a ceramic package, which is then placed in a tungsten package and potted with STYCAST 1090SI for shock testing and evaluation.

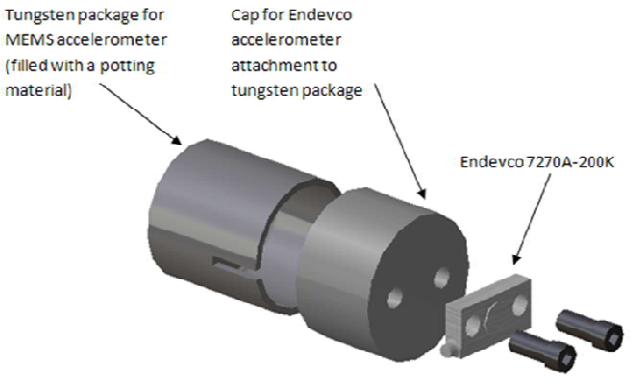

Figure 10.22 The test section for MEMS accelerometer evaluation

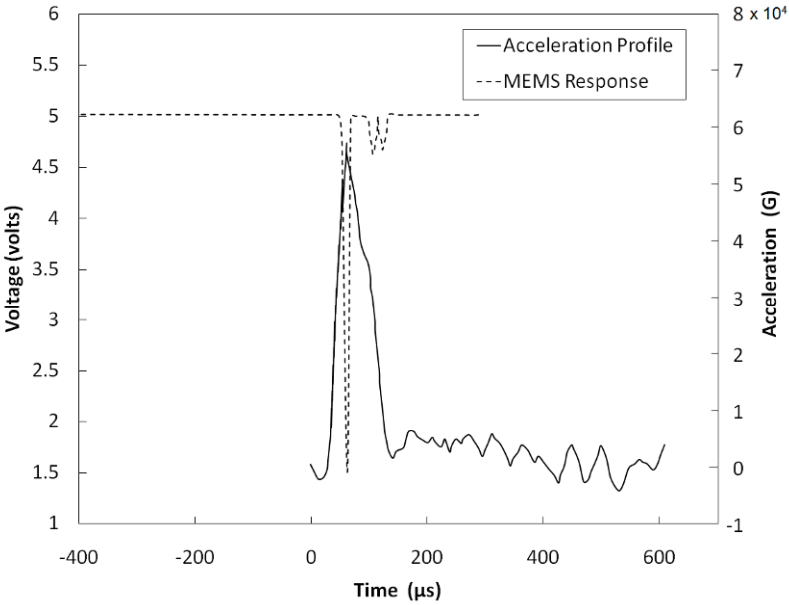

Figure 10.23 An experimental record for MEMS accelerometer evaluation

The controlled acceleration environment is provided by the pulse-shaping method and a Kolsky incident bar. The experimental setup is similar to that shown in Fig. 10.18. The tungsten "fly-way" package containing the new MEMS accelerometers and a reference Endevco accelerometer is shown in Fig. 10.22.

An experimental record is shown in Fig. 10.23 where the acceleration history and the accelerometer function are recorded. The target activation acceleration of this specific accelerometer is 40 kG. The results show that the accelerometer output is initially at 5 volts. As the acceleration level increases from zero to about 55 kG, the accelerometer output voltage drops to 1.5 volts. When the acceleration level drops down below 50 kG, the accelerometer output returns to 5 volts. After a brief fluctuation between 4.5 and 5 volts, the accelerometer output remains at 5 volts. The results show that the accelerometer turns on once the acceleration crossed the designed acceleration threshold and turns off once the acceleration falls below the threshold. However, the threshold acceleration missed the 40 kG design target. Furthermore, the brief fluctuations in ac-

celerometer voltage output after the main switching function may indicate that undesired vibration exists in the micromachined cantilever beam. Thus, the evaluation tests point to the directions of further design and fabrication improvements for the novel accelerometers, which is the purpose of the modified Kolsky-bar experiments.

Another type of small structures is LIGA structures made of metals. When the size of the metal structure is very small and the loading rate is high, the mechanical response of the materials is not known. A Kolsky-bar setup was utilized to provide the shock environment for these devices (Lu et al. 2006). By varying the striker length, the pulse shaper, and the striker velocity, desired loading profiles were generated at the free end of the input bar, where the fixture and specimen were attached. The experimental setup is the same as that shown in Fig. 10.18. The small metal specimens are attached to the bar end through a small fixture. A few types of the specimens are shown in Fig. 10.24.

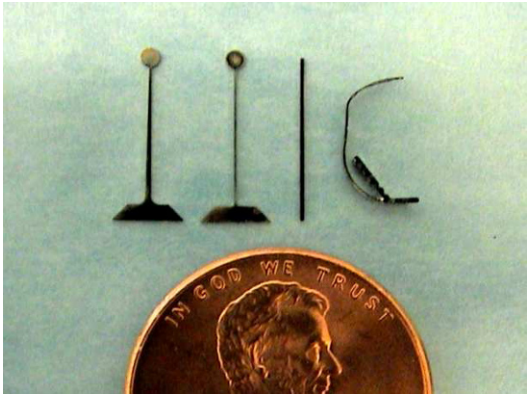

Figure 10.24 LIGA Ni specimens
(Reproduced from Lu et al. (2006) with permission)

The metal that was used to make the small structures is nickel. The mechanical properties of the Ni depend on the processing methods. The Watt bath Ni used for making the specimens has a yield strength of about 1.3 GPa under quasi-static loading conditions. The mounting condition of a tapered cantilever LIGA Ni beam on the Kolsky-bar end is shown in

Fig. 10.25. The beam has a concentrated mass on its tip. The fixture that connects the base of the cantilever beam and the Kolsky-bar end on the right side is an aluminum bridge that is bonded to the bar end.

When the incident pulse arrives at the bar end, the base of the cantilever is accelerated and the beam is bent dynamically. During the experiment, the deformation and displacement of the specimen are recorded by a high speed digital camera. Finite element simulations of the experiments by considering large elastic deformations are also conducted using the experimentally measured acceleration profile as the loading input. An example of the pulse-shaped incident pulse is shown in Fig. 10.26. A straight line drawn on the first slope of the incident pulse can be used to calculate the acceleration history on the bar end, which has a small specimen and a fixture attached. The mass of the attachments is negligible and so is its influence to the stress waves in the incident bar. The acceleration produced by this incident pulse was 20 kG and lasted 160 μs.

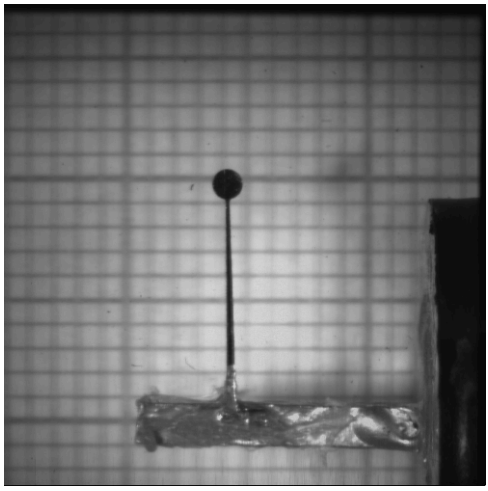

Figure 10.25 A LIGA Ni cantilever mounted on the bar end
(Reproduced from Lu et al. (2006) with permission)

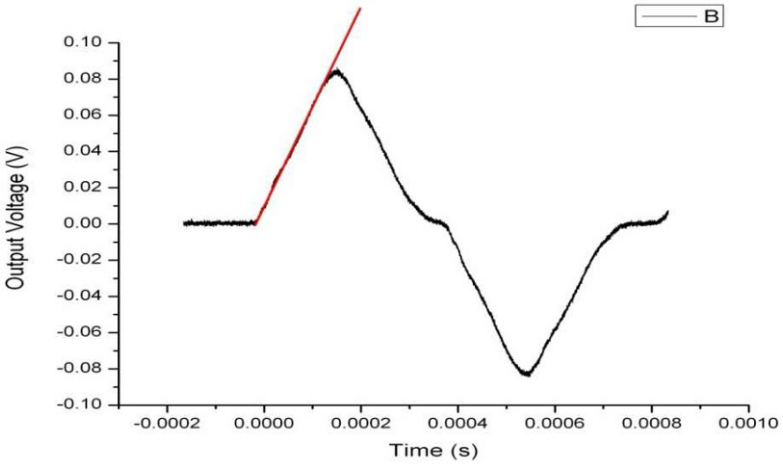

Figure 10.26 An incident pulse that generates constant acceleration on specimen
(Reproduced from Lu et al. (2006) with permission)

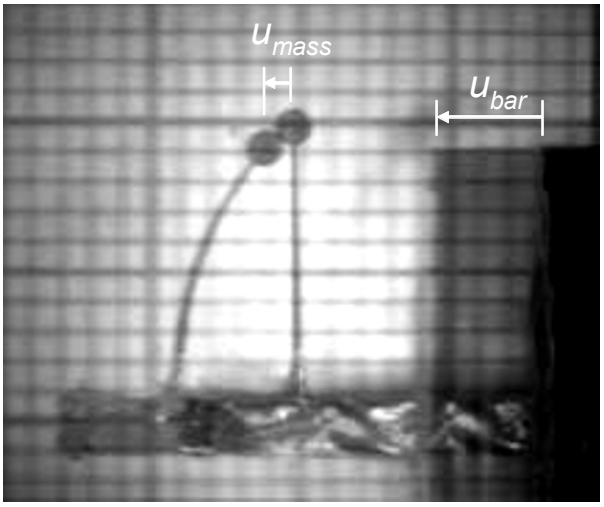

Figure 10.27 The deformed cantilever under 20 kG base acceleration
(Reproduced from Lu et al. (2006) with permission)

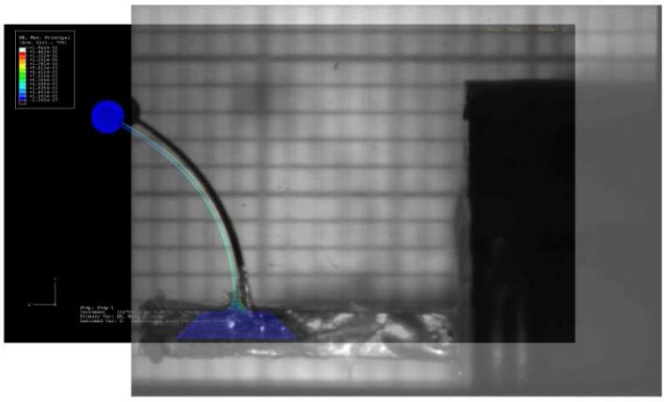

Figure 10.28 A comparison of an experimental image and simulation results
(Reproduced from Lu et al. (2006) with permission)

Figure 10.27 shows two overlapped high-speed images of the specimen deformation status. The image of the straight specimen was taken just before the arrival of the incident pulse at the specimen. The deformed beam was imaged 196 μs after the onset of a constant acceleration of 20,000 G. The base was undergoing a 20 kG deceleration at this time. During this loading period, the bar end moved a distance of 3.465 mm, whereas the concentrated mass on the beam top moved only 1.024 mm. The difference in the movements is the beam end deflection. Such deformation can be recorded at every instant the high-speed camera taking an image. Figure 10.28 shows a high-speed image taken at 470 μs after the onset of 20 kG acceleration, which looks like a shadow. The bar end is not moving at this time and the beam is in free vibration. The nearly overlapping image shown in Fig. 10.28 is the results of finite element simulation, which indicates reasonable agreement with the experimental image.

The images clearly show large deformation in the cantilever specimen. However, no permanent deformation was found on the specimen after the dynamic loading and deformation. The maximum strain in the numerical model of the specimen is found to be 1.6%, which corresponds to a 3.2 GPa stress when the Young's modulus is taken as 200 GPa, a typical value for Watt bath Ni. Compared to the 1.3 GPa quasi-static yield strength, the ability of the LIGA specimen to achieve much higher

stress level without yielding at high rates needs to be further explored. Such Kolsky-bar experiments have recently performed in the evaluation of MEMS structures (Sheehy et al. 2009, Kimberley et al. 2010).

10.4 Low-speed Penetration

Since the incident and reflected pulses can be related to the bar-end motion and loading histories, the incident bar of a Kolsky compression bar can be used to serve as an instrumented low-speed penetrator.

In this example, the instrumented penetrator is used to explore the penetration resistance of compacted alumina (Al_2O_3) powder targets (Rojas and Chen 2003). The results recorded by the instrumented penetrator show that, at a low packing density and with low striking velocities, the ceramic powder flows extensively in a local region around the tip of the projectile. The depth-of-penetration data agree well with the predictions of a cavity-expansion theory.

Pure alumina powder (grain size ~ 2.31 μm) was mechanically compacted in a cylindrical steel container. A hole opened up at the center of one flat end of the container allows the incident bar as a penetrator to enter the compacted powder. The gap between the opening and the penetrator is sealed and pressurized to resist the ceramic powder ejecta in a controlled manner during penetration process, although it turned out that the seal was not necessary as observed in experiments. There was little ejecta due to the low packing density of the powder target. Figure 10.29 shows the ceramic powder target at the end of the incident bar.

To compact the 2.31 μm grain size alumina powder to a density as high as possible, commercially purchased pure alumina powder was placed in a 141.28 mm outside diameter steel cylinder with an inside diameter of 129.62 mm and a length of 123.82 mm. A steel plate was welded to one end of the cylinder, serving as the base for the material container. Another steel plate with a 20.75-mm-diameter hole in the center for the incident bar to go through served as the front cover of the target. The plate was machined so it has a relatively loose pressure fit with the outside diameter of the cylinder. The striker was 19.1 mm in diameter and 304.8 mm long. Due to the wave-driven motion of the instrumented bar, the depth of penetration is proportional to the length of the striker. The end of the incident bar that enters the target has two types of end geometry: flat and semi-spherical. For each experiment, the depth of penetration was recorded with corresponding strain pulse passing through the

strain gages mounted on the incident bar. Each pass of the stress wave corresponds to the end motion of the bar into the target, which accumulates to the overall depth of penetration. The accumulation was found to agree with the overall depth of penetration well.

Several depth-of-penetration models were used to compare the model predictions with the experimental results. The results show that the penetration model that accounts for material strain hardening and rate sensitivity agrees well with the experimental results. The penetration equation for a strain hardening and strain rate sensitivity target with spherical-nosed rods (Warren and Forrestal 1997) is given by

$$\frac{P}{\left(L+\frac{2a}{3}\right)}=\frac{1}{C}\left(\frac{\rho_p}{\rho_t}\right)\left\{\begin{array}{l}\ln\left[1+\frac{2B}{3A}\left(\sqrt{\frac{\rho_t}{Y}}V_0\right)+\frac{C}{2A}\left(\sqrt{\frac{\rho_t}{Y}}V_0\right)^2\right] \\ +\frac{4B}{\sqrt{18AC-4B^2}}\left[\tan^{-1}\left[\frac{2B}{\sqrt{18AC-4B^2}}\right]-\tan^{-1}\left[\frac{3C\left(\sqrt{\frac{\rho_t}{Y}}V_0\right)+2B}{\sqrt{18AC-4B^2}}\right]\right]\end{array}\right\} \tag{10.22}$$

Table 10.1 summarizes the experimental results and the comparison with the predictions of three penetration models (a Tate model with no effects from strain hardening or rates, a model with hardening effects and the Warren-Forrestal model (10.22)) for the low-speed penetration of a 19.1-mm diameter penetrator with a flat head into the ceramic powder targets. The results clearly show that the Warren-Forrestal model accounting for both target material strain hardening and rate sensitivity agrees best with experimental results.

Table 10.2 summarizes the results from penetration experiment with a semi-spherical-nosed penetrating bar. The model is only the one with strain hardening and rate sensitivity. The results again show that the model predictions agree well with the depth of penetration measurements from the experiments.

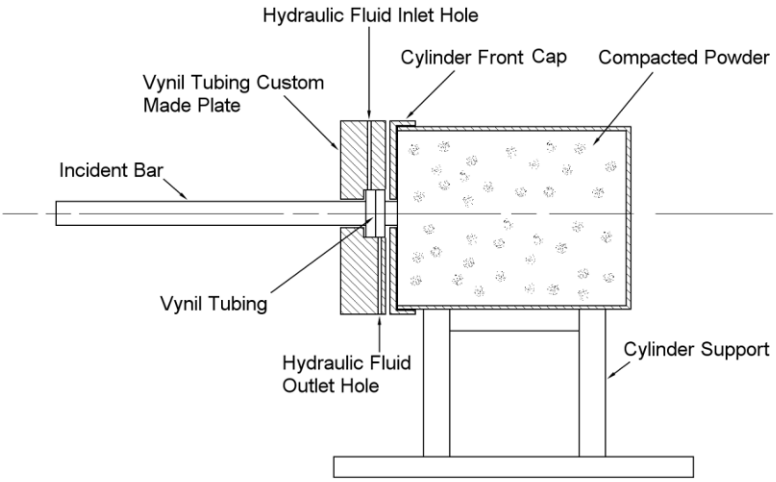

Figure 10.29 Instrumented low-speed penetration into ceramic powder

Table 10.1 Depth of penetration (m) from experiments and models

V_0 (m/s)	P (m)	P from Tate Model	Strain Hardening	P from (10.22).
2.69	0.1145	0.1653	0.1738	0.1147
2.39	0.1073	0.1302	0.1369	0.1033
2.27	0.1038	0.1176	0.1236	0.0987
2.17	0.1019	0.1081	0.1137	0.0951
1.90	0.0956	0.0827	0.0870	0.0842

Table 10.2 Depth of penetration by a semi-spherical nose penetrator

Penetration Velocity, V_0 (m/s)	Theoretical Penetration (m)	Actual Penetration (m)
2.69	0.1180	0.1208
2.39	0.1063	0.1099
2.27	0.1016	0.1025
2.17	0.0978	0.0986
1.90	0.0866	0.0903

APPENDIX A

PULSE SHAPING FORTRAN CODE

```
$DEBUG

C
C       HOPKINSON BAR PULSE SHAPING PROGRAM HOP9-1 (9/20/99)
C
C       THIS PROGRAM CALCULATES THE INCIDENT STRESS IN THE
C        SPLIT HOPKINSON BAR FOR A PULSE SHAPING MATERIAL
C       WITH KNOWN MATERIAL PROPERTIES.

        PARAMETER    (NPS=15000)
        DOUBLE PRECISION HM(NPS),HI(NPS),EC(NPS),T(NPS),
     +                  DELT(NPS)
        DOUBLE PRECISION STRAINI(NPS),STRESSI(NPS),TMS(NPS)
        DOUBLE PRECISION STRNRT(NPS),V1(NPS),V2(NPS),AM
        DOUBLE PRECISION DHM,DDELT,DT,DEC,SIGCSTR,ECSTR,
     +                  VALUE1,VALUE4

C       CA110 COPPER MODEL
C
C       SIGO=550000000.
C       AN=0.0875
C       AM=4.
C
C       CA110 'ANNEALED' COPPER MODEL REGULAR
C
C       SIGO=625000000.
C       AN=0.32
C       AM=4.25
C
C       CA110 'ANNEALED' COPPER MODEL THIN
C
        SIGO=750000000.
        AN=0.37
        AM=4.25
C
C       NEMAT-NASSER'S CONSTANTS (CA 101)
C
C       SIGO=570000000.
C       AN=0.2
C       AM=9.9e25
C
C       COPPER PARAMETERS
C
        YOUNGC=117.21E03
```

W.W. Chen and B. Song, *Split Hopkinson (Kolsky) Bar: Design, Testing and Applications*, Mechanical Engineering Series, DOI 10.1007/978-1-4419-7982-7,

```
      HOIN=0.0317
      HOM=HOIN*0.0254
      DIAO=0.402
      AO=DIAO**2*0.7854
      HSTEPI=0.00005*0.0254
      STEP=50
C
C     BAR PROPERTIES  (C-350)
C
      E=200E9
      RHO=8100
      C=4969
      A=0.7465**2*0.7854
C
C     BAR PROPERTIES (ALUMINUM)
C
C     E=72.0e9
C     RHO=2780
C     C=5089
C     A=0.750**2*0.7854
C
C     STRIKER PARAMETERS
C
      RHOST=RHO*1.0885
      CST=SQRT(E/RHOST)
      VO=12.28
      ALEN=6.
      ST=2*ALEN*0.0254/CST
C
C     INCREMENTS
C
      STAR1=HSTEPI/200
      STAR2=HSTEPI/10000
      STAR3=HSTEPI/52500
      STAR4=HSTEPI/25000
      AK1=(2*SIGO*AO)/(RHOST*CST*VO*A)
      AK=(SIGO*AO)/(VO*A)*(1/(C*RHO)+1/(CST*RHOST))
C
C     INITIAL VALUES
C
      HM(1)=HOM
      HI(1)=HOM/0.0254
      EC(1)=0
      T(1)=0
      DELT(1)=0
      STRAINI(1)=0
      STRESSI(1)=0
```

```
      V1(1)=VO
      V2(1)=0.0
      TMS(1)=0
      STRNRT(1)=(VO)/HOM
      SIGMAX=0.99*0.5*RHO*C*VO/1E6
      COUNT=1
C
C     OPEN OUTPUT FILES
C
      OPEN(UNIT=7,FILE='OUTPUT1.TXT',STATUS='UNKNOWN')
      WRITE(7,5) HM(1),HI(1),EC(1),T(1),DELT(1),STRAINI(1)
     +   ,STRESSI(1),TMS(1),STRNRT(1),V1(1), V2(1)
    5 FORMAT(11(F15.8,1X))
C
C     OPEN DEBUG FILE
C
      OPEN(UNIT=8,FILE='OUTPUT2.TXT',STATUS='UNKNOWN')
      OPEN(UNIT=9,FILE='OUTPUT3.TXT',STATUS='UNKNOWN')
      OPEN(UNIT=10,FILE='OUTPUT4.TXT',STATUS='UNKNOWN')
C
C     DO LOOP FOR FIRST TRAVEL OF WAVE (ST) IN STRIKER
C
      DO 1000 I=2,NPS
  100                 DHM=HM(I-1)-HSTEPI
  200                 DHI=DHM/0.0254
                      DEC=(HOM-DHM)/HOM
      DT=(HOM/VO)*(1.0/(1.0-AK*((DEC**AN)/((1.0-(DEC**AM))
     +   *(1.0-DEC)))))*(DEC-EC(I-1))+T(I-1)
                       DDELT=DT-T(I-1)
                       IF(I.EQ.2)THEN
                              DELTP=DDELT+1.5E-9
                              DELTM=DDELT-1.5E-9
                              GO TO 300
                      ENDIF

      IF(DDELT.LE.DELTP.AND.DDELT.GE.DELTM)THEN
                              HSTEPI=HM(I-1)-DHM
                              GO TO 300
                      ENDIF
                      IF(DDELT.GT.DELT(2))THEN
                              DHM=DHM+STAR2
                      GO TO 200
                      ENDIF
                      IF(DDELT.LT.DELT(2))THEN
                              DHM=DHM-STAR2
                      GO TO 200
                      ENDIF
```

```
 300                    HM(I)=DHM
                        HI(I)=DHI
                        EC(I)=DEC
                        T(I)=DT
                        DELT(I)=DDELT
                  STRAINI(I)=(SIGO*AO)/(E*A)*(EC(I)**AN)/((1.0-
     +                EC(I)**AM)*(1.0-EC(I)))
                        STRESSI(I)=STRAINI(I)*(E/1E6)
                        IF(STRESSI(I).GE.SIGMAX)THEN
                                STRESSI(I)=SIGMAX
                                STRAINI(I)=STRESSI(I)/(E/1E6)
                                HM(I)=HM(I-1)
                                HI(I)=HI(I-1)
                                EC(I)=EC(I-1)
                                SIGCSTR=(STRESSI(I)*(1-EC(I))*A)/AO
                                ECSTR=EC(I)
                        ENDIF
                        V1(I)=VO-(STRESSI(I)*1E6)/(RHOST*CST)
                        V2(I)=(STRESSI(I)*1E6)/(RHO*C)
                        TMS(I)=T(I)*1E6
                        STRNRT(I)=(V1(I)-V2(I))/HOM
        WRITE(7,400)HM(I),HI(I),EC(I),T(I),DELT(I),STRAINI(I),
     +          STRESSI(I),TMS(I),STRNRT(I),V1(I),V2(I)
 400    FORMAT(11(F15.8,1X))
                        IF(STRNRT(I).LE.0.0)THEN
                                STRNRT(I)=0.0
                                NUN=I
                                N=I
                                GO TO 10001
                        ENDIF
                        IF(T(I).GE.ST)THEN
                                N=I
                                COUNT=2
                                GO TO 1001
                        ENDIF
 1000   CONTINUE
C
C       DO LOOP FOR SECOND TRAVEL OF WAVE (2*ST) IN STRIKER
C
 1001   PRINT*, 'GOING TO SECOND'
        DO 2000 II=N+1,NPS
                        DHM=HM(II-1)-STAR1
 2100                   DHI=DHM/0.0254
                        DEC=(HOM-DHM)/HOM
        DT=(HOM/VO)*(1.0/(1.0-AK*(DEC**AN)/((1.0-DEC**AM)*(1.0-
     +          DEC))-AK1*(EC(II-N)**AN)/((1.0-EC(II-N)**AM)*(1-
     +          EC(II-N)))))*(DEC-EC(II-1))+T(II-1)
```

```
                    DDELT=DT-T(II-1)
                    IF(DDELT.LE.0.0)THEN
                        NN=II-1
                        NUN=NN
                        SIGCSTR=(STRESSI(II-1)*(1-EC(II-
     +                      1))*A)/AO
                        ECSTR=EC(II-1)
                        GO TO 10001
                    ENDIF

          IF(DDELT.LE.DELTP.AND.DDELT.GE.DELTM)THEN
                        HSTEPI=HM(II-1)-DHM
                        GO TO 2200
                    ENDIF
                    IF(DDELT.GT.DELT(2))THEN
                        DHM=DHM+STAR3
                    GO TO 2100

                    ENDIF
                    IF(DDELT.LT.DELT(2))THEN
                        DHM=DHM-STAR3
                    GO TO 2100
                    ENDIF
2200                HM(II)=DHM
                    HI(II)=DHI
                    EC(II)=DEC
                    T(II)=DT
                    DELT(II)=DDELT

          STRAINI(II)=(SIGO*AO)/(E*A)*(EC(II)**AN)/((1.0-
     +                EC(II)**AM)*(1.0-EC(II)))
                    STRESSI(II)=STRAINI(II)*(E/1E6)
                    IF(STRESSI(II).GT.((RHO*C*VO)/(2E6)))THEN
                        STRESSI(II)=(RHO*C*VO)/(2E6)
                        STRAINI(II)=STRESSI(II)/(E/1E6)
                    ENDIF
               V1(II)=(VO-(2*STRESSI(II-N)*1E6)/(RHOST*CST))-
     +                 (STRESSI(II)*1E6)/(RHOST*CST)
                    V2(II)=(STRESSI(II)*1E6)/(RHO*C)
                    TMS(II)=T(II)*1E6
                    STRNRT(II)=(V1(II)-V2(II))/HOM
          WRITE(7,2700)HM(II),HI(II),EC(II),T(II),DELT(II),STRAINI(II),
     +          STRESSI(II),TMS(II),STRNRT(II),V1(II),V2(II)
2700      FORMAT(11(F15.8,1X))
                    IF(STRNRT(II).LE.0.0)THEN
                        STRNRT(II)=0.0
                        NN=II
```

```
                                        NUN=II
                                        PRINT *,ST
                                        GO TO 10001
                                ENDIF
                                IF(II.EQ.(2*N))THEN
                                        NN=II
                                        COUNT=3
c                                       WRITE(8,*)NN,T(II)
                                        PRINT *,'GOING TO 3'
                                        GO TO 2001
                                ENDIF
 2000   CONTINUE
C
C       DO LOOP FOR THIRD TRAVEL OF WAVE (3*ST) IN STRIKER
C
 2001   DO 3000 III=NN+1,NPS
                DHM=HM(III-1)-STAR1
 3100           DHI=DHM/0.0254
                DEC=(HOM-DHM)/HOM
                DT1=AK*(DEC**AN)/((1.0-DEC**AM)*(1.0-DEC))
                DT2=AK1*(EC(III-N)**AN)/((1.0-EC(III-N)**AM)*(1-
    +            EC(III-N)))
                DT3=AK1*(EC(III-NN)**AN)/((1.0-EC(III-NN)**AM)*(1-
    +            EC(III-NN)))
        DT=(HOM/VO)*(1.0/(1.0-DT1-DT2-DT3))*(DEC-EC(III-1))+T(III-1)
                DDELT=DT-T(III-1)
                IF(DDELT.LE.0.0)THEN
                        NNN=III-1
                        NUN=NNN
                        SIGCSTR=(STRESSI(III-1)*(1-EC(III-1))*A)/AO
                        ECSTR=EC(III-1)
                        GO TO 10001
                ENDIF

        IF(DDELT.LE.DELTP.AND.DDELT.GE.DELTM)THEN
                        HSTEPI=HM(III-1)-DHM
                        GO TO 3200
                ENDIF
                IF(DDELT.GT.DELT(2))THEN
                        DHM=DHM+STAR3
                        GO TO 3100
                ENDIF
                IF(DDELT.LT.DELT(2))THEN
                        DHM=DHM-STAR3
                        GO TO 3100
                ENDIF
 3200           HM(III)=DHM
```

```
                HI(III)=DHI
                EC(III)=DEC
                T(III)=DT
                DELT(III)=DDELT
                STRAINI(III)=(SIGO*AO)/(E*A)*(EC(III)**AN)/
     +          ((1.0-EC(III)**AM)*(1.0-EC(III)))
                STRESSI(III)=STRAINI(III)*(E/1E6)
                IF(STRESSI(III).GT.((RHO*C*VO)/(2E6)))THEN
                        STRESSI(III)=(RHO*C*VO)/(2E6)
                        STRAINI(III)=STRESSI(III)/(E/1E6)
                ENDIF
                V1(III)=VO-(STRESSI(III)*1E6)/(RHOST*CST)-
     +           (2*STRESSI(III-N)*1000000)/(RHOST*CST)-
     +           (2*STRESSI(III-NN)*1E6)/(RHOST*C)
                V2(III)=(STRESSI(III)*1E6)/(RHO*C)
                TMS(III)=T(III)*1E6
                STRNRT(III)=(V1(III)-V2(III))/HOM
        WRITE(7,3700,ERR=999)HM(III),HI(III),EC(III),T(III),DELT(III),
     +  STRAINI(III),STRESSI(III),TMS(III),STRNRT(III),V1(III),V2(III)
 3700           FORMAT(11(F15.8,1X))
                IF(STRNRT(III).LE.0.0)THEN
                        STRNRT(III)=0.0
                        NNN=III
                        NUN=III
                        GO TO 10001
                ENDIF
                IF(III.EQ.(3*N))THEN
                        NNN=III
                        COUNT=4
                        PRINT*,'GOING TO 4'
                        GO TO 4001
                ENDIF
 3000 CONTINUE
C
C       DO LOOP FOR FORTH TRAVEL OF WAVE (4*ST) IN STRIKER
C
 4001   DO 4000 IIII=NNN+1,NPS
                DHM=HM(IIII-1)-STAR1
 4100           DHI=DHM/0.0254
                DEC=(HOM-DHM)/HOM
                DT1=(DEC**AN)/((1.0-DEC**AM)*(1.0-DEC))
                DT2=(EC(IIII-N)**AN)/((1.0-EC(IIII-N)**AM)*
     +           (1-EC(IIII-N)))
                DT3=(EC(IIII-NN)**AN)/((1.0-EC(IIII-NN)**AM)*
     +           (1-EC(IIII-NN)))
        DT4=(EC(IIII-NNN)**AN)/((1.0-EC(IIII-NNN)**AM)*
     +           (1-EC(IIII-NNN)))
```

```
      DT=(HOM/VO)*(1.0/(1.0-AK*DT1-AK1*(DT2+DT3+DT4)))*
     +          (DEC-EC(IIII-1))+T(IIII-1)
                DDELT=DT-T(IIII-1)
                IF(DDELT.LE.0.0)THEN
                        NNNN=IIII-1
                        NUN=NNNN
                        SIGCSTR=(STRESSI(IIII-1)*(1-EC(IIII-1))*A)/AO
                        ECSTR=EC(IIII-1)
                        GO TO 10001
                ENDIF
                IF(DDELT.LE.DELTP.AND.DDELT.GE.DELTM)THEN
                        HSTEPI=HM(IIII-1)-DHM
                        GO TO 4200
                ENDIF
                IF(DDELT.GT.DELT(2))THEN
                        DHM=DHM+STAR3
                        GO TO 4100
                ENDIF
                IF(DDELT.LT.DELT(2))THEN
                        DHM=DHM-STAR3
                        GO TO 4100
                ENDIF
 4200           HM(IIII)=DHM
                HI(IIII)=DHI
                EC(IIII)=DEC
                T(IIII)=DT
                DELT(IIII)=DDELT
      STRAINI(IIII)=(SIGO*AO)/(E*A)*(EC(IIII)**AN)/((1.0-
     +          EC(IIII)**AM)*(1.0-EC(IIII)))
                STRESSI(IIII)=STRAINI(IIII)*(E/1E6)
                IF(STRESSI(IIII).GT.((RHO*C*VO)/(2E6)))THEN
                        STRESSI(IIII)=(RHO*C*VO)/(2E6)
                        STRAINI(IIII)=STRESSI(IIII)/(E/1E6)
                ENDIF
                V1(IIII)=VO-(STRESSI(IIII)*1E6)/(RHOST*CST)-
     +            (2*STRESSI(IIII-N)*1E6)/(RHOST*CST)-(2*
     +            STRESSI(IIII-NN)*1E6)/          (RHOST*CST)-(2*
     +            STRESSI(IIII-NNN)*1E6)/(RHOST*CST)
                V2(IIII)=(STRESSI(IIII)*1E6)/(RHO*C)
                TMS(IIII)=T(IIII)*1E6
                STRNRT(IIII)=(V1(IIII)-V2(IIII))/HOM
                PRINT *, IIII, EC(IIII), TMS(IIII)
      WRITE(7,4700,ERR=999)HM(IIII),HI(IIII),EC(IIII),T(IIII),
     +  DELT(IIII),STRAINI(IIII),STRESSI(IIII),TMS(IIII),STRNRT(IIII),
     +  V1(IIII),V2(IIII)
 4700 FORMAT(11(F15.8,1X))
                STRNRT(IIII)=(V1(IIII)-V2(IIII))/HOM
```

```
                IF(STRNRT(IIII).LE.0.0)THEN
                                STRNRT(IIII)=0.0
                                NNNN=IIII
                                NUN=IIII
                                GO TO 10001
                ENDIF
                IF(IIII.EQ.(4*N))THEN
                        NNNN=IIII
                        NIV=IIII
                        COUNT=5
                        PRINT*,'GOING TO 5'
                        GO TO 5001
                ENDIF
        NNNN=IIII
 4000   CONTINUE
C
C       DO LOOP FOR FIFTH TRAVEL OF WAVE (5*ST) IN STRIKER
C
 5001   DO 5000 IIIII=NNNN+1,NPS
                DHM=HM(IIIII-1)-STAR3
 5100           DHI=DHM/0.0254
                DEC=(HOM-DHM)/HOM
                DT1=(DEC**AN)/((1.0-DEC**AM)*(1.0-DEC))
                DT2=(EC(IIIII-N)**AN)/((1.0-EC(IIIII-N)**AM)*
     +           (1-EC(IIIII-N)))
        DT3=(EC(IIIII-NN)**AN)/((1.0-EC(IIIII-NN)**AM)*
     +           (1-EC(IIIII-NN)))
                DT4=(EC(IIIII-NNN)**AN)/((1.0-EC(IIIII-NNN)**AM)*
     +          (1-EC(IIIII-NNN)))
                DT5=(EC(IIIII-NNNN)**AN)/((1.0-EC(IIIII-NNNN)**AM)*
     +          (1-EC(IIIII-NNNN)))
        DT=(HOM/VO)*(1.0/(1.0-AK*DT1-AK1*(DT2+DT3+DT4+DT5)))*
     +          (DEC-EC(IIIII-1))+T(IIIII-1)
                DDELT=DT-T(IIIII-1)
                IF(DDELT.LE.0.0)THEN
                        NNNN=IIIII-1
                        NUN=NNNN
                        SIGCSTR=(STRESSI(IIIII-1)*
     +                    (1-EC(IIIII-1))*A)/AO
                        ECSTR=EC(IIIII-1)
                        GO TO 10001
                ENDIF
                IF(DDELT.LE.DELTP.AND.DDELT.GE.DELTM)THEN
                        HSTEPI=HM(IIIII-1)-DHM
                        GO TO 5200
                ENDIF
                IF(DDELT.GT.DELT(2))THEN
```

```
                        DHM=DHM+STAR4
                        GO TO 5100
                ENDIF
                IF(DDELT.LT.DELT(2))THEN
                        DHM=DHM-STAR4
                        GO TO 5100
                ENDIF
 5200           HM(IIIII)=DHM
                HI(IIIII)=DHI
                EC(IIIII)=DEC
                T(IIIII)=DT
                DELT(IIIII)=DDELT
        STRAINI(IIIII)=(SIGO*AO)/(E*A)*(EC(IIIII)**AN)/
     +          ((1-EC(IIIII)**AM)*(1.0-EC(IIIII)))
                STRESSI(IIIII)=STRAINI(IIIII)*(E/1E6)
                IF(STRESSI(IIIII).GT.((RHO*C*VO)/(2E6)))THEN
                        STRESSI(IIIII)=(RHO*C*VO)/(2E6)
                        STRAINI(IIIII)=STRESSI(IIIII)/(E/1E6)
                ENDIF
        V1(IIIII)=VO-(STRESSI(IIIII)*1E6)/(RHOST*CST)-
     +          (2*STRESSI(IIIII-N)*1000000)/(RHOST*CST)-
     +          (2*STRESSI(IIIII-NN)*1000000)/(RHOST*CST)
     +          -(2*STRESSI(IIIII-NNN)*1E6)/(RHOST*CST)-
     +           (2*STRESSI(IIIII-NNNN)*1E6)/(RHOST*CST)
        V2(IIIII)=(STRESSI(IIIII)*1E6)/(RHO*C)
                TMS(IIIII)=T(IIIII)*1E6
                STRNRT(IIIII)=(V1(IIIII)-V2(IIIII))/HOM
                        PRINT *, IIIII, EC(IIIII), TMS(IIIII)
        WRITE(7,5700,ERR=999)HM(IIIII),HI(IIIII),EC(IIIII),T(IIIII),
     +          DELT(IIIII),STRAINI(IIIII),STRESSI(IIIII),TMS(IIIII),
     +          STRNRT(IIIII),V1(IIIII),V2(IIIII)
 5700   FORMAT(11(F15.8,1X))
                IF(STRNRT(IIIII).LE.0.0)THEN
                                STRNRT(IIIII)=0.0
                                NNNNN=IIIII
                                NUN=IIIII
                                PRINT *, 'STRNRT ZERO'
                                GO TO 10001
                ENDIF
                IF(IIIII.EQ.(5*N))THEN
                        NV=IIIII
                        NNNNN=IIIII
                        COUNT=6
                        PRINT*, 'GOING TO 6'
                        GO TO 6001
                ENDIF
        NNNNN=IIIII
```

```
 5000    CONTINUE
C
C        DO LOOP FOR SIXTH TRAVEL OF WAVE (6*ST) IN STRIKER
C
 6001    DO 6000 IV=NNNNN+1,NPS
                 DHM=HM(IV-1)-STAR3
 6100            DHI=DHM/0.0254
                 DEC=(HOM-DHM)/HOM
                 DT1=(DEC**AN)/((1.0-DEC**AM)*(1.0-DEC))
                 DT2=(EC(IV-N)**AN)/((1.0-EC(IV-N)**AM)*
     +                   (1-EC(IV-N)))
                 DT3=(EC(IV-NN)**AN)/((1.0-EC(IV-NN)**AM)*
     +                   (1-EC(IV-NN)))
                 DT4=(EC(IV-NNN)**AN)/((1.0-EC(IV-NNN)**AM)*
     +                   (1-EC(IV-NNN)))
                 DT5=(EC(IV-NNNN)**AN)/((1.0-EC(IV-NNNN)**AM)*
     +                   (1-EC(IV-NNNN)))
          DT6=(EC(IV-NNNNN)**AN)/((1.0-EC(IV-NNNNN)**AM)*
     +           (1-EC(IV-NNNNN)))
          DT=(HOM/VO)*(1.0/(1.0-AK*DT1-AK1*(DT2+DT3+DT4+DT5+
     +           DT6)))*(DEC-EC(IV-1))+T(IV-1)
                 DDELT=DT-T(IV-1)
                 IF(DDELT.LE.0.0)THEN
                          NNNN=IV-1
                          NUN=NNNN
                          SIGCSTR=(STRESSI(IV-1)*(1-EC(IV-1))*A)/AO
                          ECSTR=EC(IV-1)
                          PRINT*, 'DDELT.LE.0.0'
                          GO TO 10001
                 ENDIF
                 IF(DDELT.LE.DELTP.AND.DDELT.GE.DELTM)THEN
                          HSTEPI=HM(IV-1)-DHM
                          GO TO 6200
                 ENDIF
                 IF(DDELT.GT.DELT(2))THEN
                          DHM=DHM+STAR4
                          GO TO 6100
                 ENDIF
                 IF(DDELT.LT.DELT(2))THEN
                          DHM=DHM-STAR4
                          GO TO 6100
                 ENDIF
 6200            HM(IV)=DHM
                 HI(IV)=DHI
                 EC(IV)=DEC
                 T(IV)=DT
                 DELT(IV)=DDELT
```

```
      STRAINI(IV)=(SIGO*AO)/(E*A)*(EC(IV)**AN)/((1-EC(IV)**AM)*
     +            (1.0-EC(IV)))
                  STRESSI(IV)=STRAINI(IV)*(E/1E6)
                  IF(STRESSI(IV).GT.((RHO*C*VO)/(2E6)))THEN
                        STRESSI(IV)=(RHO*C*VO)/(2E6)
                        STRAINI(IV)=STRESSI(IV)/(E/1E6)
                  ENDIF
      V1(IV)=VO-(STRESSI(IV)*1E6)/(RHOST*CST)-(2*STRESSI(IV-N)
     +            *1000000)/(RHOST*CST)-(2*STRESSI(IV-
     +             NN)*1000000)/(RHOST*CST)
     +            -(2*STRESSI(IV-NNN)*1E6)/(RHOST*CST)-
     +             (2*STRESSI(IV-NNNN)*1E6)/(RHOST*CST)-
     +            (2*STRESSI(IV-NNNNN)*1E6)/(RHOST*CST)
                        V2(IV)=(STRESSI(IV)*1E6)/(RHO*C)
                  TMS(IV)=T(IV)*1E6
                  STRNRT(IV)=(V1(IV)-V2(IV))/HOM
                  PRINT *, IV, EC(IV), TMS(IV)
      WRITE(7,6700,ERR=999)HM(IV),HI(IV),EC(IV),T(IV),
     +
      DELT(IV),STRAINI(IV),STRESSI(IV),TMS(IV),STRNRT(IV),
     +            V1(IV),V2(IV)
 6700 FORMAT(11(F15.8,1X))
                  STRNRT(IV)=(V1(IV)-V2(IV))/HOM
                  IF(STRNRT(IV).LE.0.0)THEN
                              STRNRT(IV)=0.0
                              NSIX=IV
                              NUN=IV
                              PRINT *, 'STRNRT ZERO'
                              GO TO 10001
                  ENDIF
                  IF(IV.EQ.(6*N))THEN
                        NVI=IV
                        NSIX=IV
                        COUNT=7
                        PRINT *,'GOING TO 7'
                        GO TO 7001
                  ENDIF
      NSIX=IV
 6000 CONTINUE
C
C     DO LOOP FOR SEVENTH TRAVEL OF WAVE (7*ST) IN
C      STRIKER
C
 7001 DO 7000 IVI=NSIX+1,NPS
                  DHM=HM(IVI-1)-STAR1
 7100             DHI=DHM/0.0254
                  DEC=(HOM-DHM)/HOM
```

```
                DT1=(DEC**AN)/((1.0-DEC**AM)*(1.0-DEC))
                DT2=(EC(IVI-N)**AN)/((1.0-EC(IVI-N)**AM)*
     +           (1-EC(IVI-N)))
                DT3=(EC(IVI-NN)**AN)/((1.0-EC(IVI-NN)**AM)*
     +           (1-EC(IVI-NN)))
                DT4=(EC(IVI-NNN)**AN)/((1.0-EC(IVI-NNN)**AM)*
     +           (1-EC(IVI-NNN)))
           DT5=(EC(IVI-NNNN)**AN)/((1.0-EC(IVI-NNNN)**AM)*
     +           (1-EC(IVI-NNNN)))
           DT6=(EC(IVI-NNNNN)**AN)/((1.0-EC(IVI-NNNNN)**AM)*
     +           (1-EC(IVI-NNNNN)))
           DT7=(EC(IVI-NSIX)**AN)/((1.0-EC(IVI-NSIX)**AM)*
     +           (1-EC(IVI-NSIX)))
           DT=(HOM/VO)*(1.0/(1.0-AK*DT1-AK1*(DT2+DT3+DT4+DT5+
     +            DT6+DT7)))*(DEC-EC(IVI-1))+T(IVI-1)
                DDELT=DT-T(IVI-1)
                IF(DDELT.LE.0.0)THEN
                        NUN=IVI-1
                        SIGCSTR=(STRESSI(IVI-1)*(1-EC(IVI-1))*A)/AO
                        ECSTR=EC(IVI-1)
                        PRINT*, 'DDELT.LE.0.0'
                        GO TO 10001
                ENDIF
                IF(DDELT.LE.DELTP.AND.DDELT.GE.DELTM)THEN
                        HSTEPI=HM(IVI-1)-DHM
                        GO TO 7200
                ENDIF
                IF(DDELT.GT.DELT(2))THEN
                        DHM=DHM+STAR3
                        GO TO 7100
                ENDIF
                IF(DDELT.LT.DELT(2))THEN
                        DHM=DHM-STAR3
                        GO TO 7100
                ENDIF
7200            HM(IVI)=DHM
                HI(IVI)=DHI
                EC(IVI)=DEC
                T(IVI)=DT
                DELT(IVI)=DDELT
           STRAINI(IVI)=(SIGO*AO)/(E*A)*(EC(IVI)**AN)/
     +           ((1-EC(IVI)**AM)*(1.0-EC(IVI)))
                STRESSI(IVI)=STRAINI(IVI)*(E/1E6)
                IF(STRESSI(IVI).GT.((RHO*C*VO)/(2E6)))THEN
                        STRESSI(IVI)=(RHO*C*VO)/(2E6)
                        STRAINI(IVI)=STRESSI(IVI)/(E/1E6)
                ENDIF
```

```
      V1(IVI)=VO-(STRESSI(IVI)*1E6)/(RHOST*CST)-(2*STRESSI
     +        (IVI-N)*1000000)/(RHOST*CST)-(2*STRESSI(IVI-
     +        NN)*1000000)/(RHOST*CST)-(2*STRESSI(IVI-
     +        NNN)*1E6)/(RHOST*CST)-(2*STRESSI(IVI-NNNN)
     +        *1E6)/(RHOST*CST)-(2*STRESSI(IVI-
     +         NNNNN)*1E6)/(RHOST*CST)
     +        -(2*STRESSI(IVI-NSIX)*1E6)/(RHOST*CST)
      V2(IVI)=(STRESSI(IVI)*1E6)/(RHO*C)
              TMS(IVI)=T(IVI)*1E6
              STRNRT(IVI)=(V1(IVI)-V2(IVI))/HOM
              PRINT *, IVI, EC(IVI), TMS(IVI)
      WRITE(7,7700,ERR=999)HM(IVI),HI(IVI),EC(IVI),T(IVI),
     +DELT(IVI),STRAINI(IVI),STRESSI(IVI),TMS(IVI),STRNRT(IVI),
     +V1(IVI),V2(IVI)
 7700 FORMAT(11(F15.8,1X))
              IF(STRNRT(IVI).LE.0.0)THEN
                              STRNRT(IVI)=0.0
                              NSEV=IVI
                              PRINT *, 'STRNRT ZERO'
                              GO TO 10001
              ENDIF
              IF(IVI.EQ.(7*N))THEN
                      NVII=IVI
                      NSEV=IVI
                      COUNT=8
                      PRINT*,'GOING TO 8'
                      GO TO 8001
              ENDIF
      NSEV=IVI
 7000 CONTINUE
C
C     DO LOOP FOR EIGHTH TRAVEL OF WAVE (8*ST) IN STRIKER
C
 8001 DO 8000 IVII=NSEV+1,NPS
              DHM=HM(IVII-1)-STAR1
 8100         DHI=DHM/0.0254
              DEC=(HOM-DHM)/HOM
      DT1=(DEC**AN)/((1.0-DEC**AM)*(1.0-DEC))
      DT2=(EC(IVII-N)**AN)/((1.0-EC(IVII-N)**AM)*(1-EC(IVII-N)))
      DT3=(EC(IVII-NN)**AN)/((1.0-EC(IVII-NN)**AM)*
     +        (1-EC(IVII-NN)))
      DT4=(EC(IVII-NNN)**AN)/((1.0-EC(IVII-NNN)**AM)*
     +        (1-EC(IVII-NNN)))
      DT5=(EC(IVII-NNNN)**AN)/((1.0-EC(IVII-NNNN)**AM)*
     +        (1-EC(IVII-NNNN)))
      DT6=(EC(IVII-NNNNN)**AN)/((1.0-EC(IVII-NNNNN)**AM)*
     +        (1-EC(IVII-NNNNN)))
```

```
      DT7=(EC(IVII-NSIX)**AN)/((1.0-EC(IVII-NSIX)**AM)*
     +          (1-EC(IVII-NSIX)))
      DT8=(EC(IVII-NSEV)**AN)/((1.0-EC(IVII-NSEV)**AM)*
     +          (1-EC(IVII-NSEV)))
      DT=(HOM/VO)*(1.0/(1.0-AK*DT1*AK1*(DT2+DT3+DT4+
     +           DT5+DT6+DT7+DT8)))*          (DEC-EC(IVII-1))+T(IVII-
1)
                DDELT=DT-T(IVII-1)
                IF(DDELT.LE.0.0)THEN
                        PRINT*,'*'
                        NUN=IVII-1
                        SIGCSTR=(STRESSI(IVII-1)*(1-EC(IVII-1))*
     +                              A)/AO
                        ECSTR=EC(IVII-1)
                        PRINT*, 'DDELT.LE.0.0'
                        GO TO 10001
                ENDIF
                IF(DDELT.LE.DELTP.AND.DDELT.GE.DELTM)THEN
                        HSTEPI=HM(IVII-1)-DHM
                        GO TO 8200
                ENDIF
                IF(DDELT.GT.DELT(2))THEN
                        DHM=DHM+STAR3
                        GO TO 8100
                ENDIF
                IF(DDELT.LT.DELT(2))THEN
                        DHM=DHM-STAR3
                        GO TO 8100
                ENDIF
 8200           HM(IVII)=DHM
                HI(IVII)=DHI
                EC(IVII)=DEC
                T(IVII)=DT
                DELT(IVII)=DDELT
      STRAINI(IVII)=(SIGO*AO)/(E*A)*(EC(IVII)**AN)/(1.0-EC(IVII))
                STRESSI(IVII)=STRAINI(IVII)*(E/1E6)
                IF(STRESSI(IVII).GT.((RHO*C*VO)/(2E6)))THEN
                        STRESSI(IVII)=(RHO*C*VO)/(2E6)
                        STRAINI(IVII)=STRESSI(IVII)/(E/1E6)
                ENDIF
      V1(IVII)=VO-(STRESSI(IVII)*1E6)/(RHOST*CST)-
     +          (2*STRESSI(IVII-N)*1000000)/(RHOST*CST)-
     +          (2*STRESSI(IVII-NN)*1000000)/(RHOST*CST)
     +          -(2*STRESSI(IVII-NNN)*1E6)/(RHOST*CST)-
     +           (2*STRESSI(IVII-NNNN)*1E6)/(RHOST*CST)-
     +           (2*STRESSI(IVII-NNNNN)*1E6)/(RHOST*CST)
     +          -(2*STRESSI(IVII-NSIX)*1E6)/(RHOST*CST)-
```

```
     +              (2*STRESSI(IVII-NSEV)          *1E6)/(RHOST*CST)
          V2(IVII)=(STRESSI(IVII)*1E6)/(RHO*C)
                   TMS(IVII)=T(IVII)*1E6
                   STRNRT(IVII)=(V1(IVII)-V2(IVII))/HOM
                   PRINT *, IVII, EC(IVII), TMS(IVII)
          WRITE(7,8700,ERR=999)HM(IVII),HI(IVII),EC(IVII),T(IVII),
     +    DELT(IVII),STRAINI(IVII),STRESSI(IVII),TMS(IVII),
     +    STRNRT(IVII),V1(IVII),V2(IVII)
 8700     FORMAT(11(F15.8,1X))
                   IF(STRNRT(IVII).LE.0.0)THEN
                                  STRNRT(IVII)=0.0
                                  NUN=IVII
                                  PRINT *, 'STRNRT ZERO'
                                  GO TO 10001
                   ENDIF
                   IF(IVII.EQ.(8*N))THEN
                            NVIII=IVII
                            NUN=IVII
                            COUNT=9
                            GO TO 10001
                   ENDIF
          NEIG=IVII
 8000     CONTINUE
  999     PRINT *,'BAD'
C
C         UNLOADING
C
10001     PRINT *,'UNLOADING'
          PRINT *, N,NN,NNN,NIV,NV,NVI,NVII
          VALUE=DELT(2)
          DO 10000 J=NUN+1,NPS
                   DHM=HM(J-1)+STAR4
10100                      DHI=DHM/0.0254
                           DEC=(HOM-DHM)/HOM
                           IF(COUNT.EQ.11)THEN
                                    STRESSJJN=STRESSI(J-N)
                                    STRESSJJNN=STRESSI(J-NN)
                                    STRESSJJNNN=STRESSI(J-NNN)
                                    STRESSJJNIV=STRESSI(J-NIV)
                                    STRESSJJNV=STRESSI(J-NV)
                                    STRESSJJNVI=STRESSI(J-NVI)
                                    STRESSJJNVII=STRESSI(J-NVII)
                                    STRESSJJNVIII=STRESSI(J-NVIII)
                                    STRESSJJNIX=STRESSI(J-NIX)
                                    STRESSJJNX=STRESSI(J-NX)
                                    VALUE1=1-
     +                               (2*STRESSJJN*1E6)/(VO*RHOST*CST)
```

```
      VALUE2=(2*STRESSJJNN*1E6)/(VO*RHOST*CST)

      VALUE3=(2*STRESSJJNNN*1E6)/(VO*RHOST*CST)

      VALUE4=(2*STRESSJJNIV*1E6)/(VO*RHOST*CST)

      VALUE5=(2*STRESSJJNV*1E6)/(VO*RHOST*CST)

      VALUE6=(2*STRESSJJNVI*1E6)/(VO*RHOST*CST)

      VALUE7=(2*STRESSJJNVII*1E6)/(VO*RHOST*CST)

      VALUE8=(2*STRESSJJNVIII*1E6)/(VO*RHOST*CST)

      VALUE9=(2*STRESSJJNIX*1E6)/(VO*RHOST*CST)

      VALUE10=(2*STRESSJJNX*1E6)/(VO*RHOST*CST)
                              VALUE11=(AO)/(VO*A*(1-
     +                           DEC))*(1/(RHO*C)+1/(RHOST*CST))*
     +                          ((SIGCSTR*1E6)-YOUNGC*(ECSTR-
     +                           DEC))
            DT=(HOM/VO)*(1.0/(VALUE1-VALUE2-VALUE3-
     +                 VALUE4-VALUE5-VALUE6-VALUE7-VALUE8-
     +                 VALUE9-VALUE10-VALUE11))*
     +                 (DEC-EC(J-1))+T(J-1)
                       ENDIF
                       IF(COUNT.EQ.10)THEN
                              STRESSJJN=STRESSI(J-N)
                              STRESSJJNN=STRESSI(J-NN)
                              STRESSJJNNN=STRESSI(J-NNN)
                              STRESSJJNIV=STRESSI(J-NIV)
                              STRESSJJNV=STRESSI(J-NV)
                              STRESSJJNVI=STRESSI(J-NVI)
                              STRESSJJNVII=STRESSI(J-NVII)
                              STRESSJJNVIII=STRESSI(J-NVIII)
                              STRESSJJNIX=STRESSI(J-NIX)
                              VALUE1=1-
     +                          (2*STRESSJJN*1E6)/(VO*RHOST*CST)

      VALUE2=(2*STRESSJJNN*1E6)/(VO*RHOST*CST)

      VALUE3=(2*STRESSJJNNN*1E6)/(VO*RHOST*CST)

      VALUE4=(2*STRESSJJNIV*1E6)/(VO*RHOST*CST)

      VALUE5=(2*STRESSJJNV*1E6)/(VO*RHOST*CST)
```

```
      VALUE6=(2*STRESSJJNVI*1E6)/(VO*RHOST*CST)

      VALUE7=(2*STRESSJJNVII*1E6)/(VO*RHOST*CST)

      VALUE8=(2*STRESSJJNVIII*1E6)/(VO*RHOST*CST)

      VALUE9=(2*STRESSJJNIX*1E6)/(VO*RHOST*CST)
                              VALUE10=(AO)/(VO*A*(1-
     +                         DEC))*(1/(RHO*C)+1/(RHOST*CST))
     +                        *((SIGCSTR*1E6)-YOUNGC*(ECSTR-
     +                         DEC))
            DT=(HOM/VO)*(1.0/(VALUE1-VALUE2-VALUE3-
     +                 VALUE4-VALUE5-VALUE6-VALUE7-VALUE8-
     +                 VALUE9-VALUE10))*(DEC-EC(J-1))+T(J-1)
                       ENDIF
                       IF(COUNT.EQ.9)THEN
                              STRESSJJN=STRESSI(J-N)
                              STRESSJJNN=STRESSI(J-NN)
                              STRESSJJNNN=STRESSI(J-NNN)
                              STRESSJJNIV=STRESSI(J-NIV)
                              STRESSJJNV=STRESSI(J-NV)
                              STRESSJJNVI=STRESSI(J-NVI)
                              STRESSJJNVII=STRESSI(J-NVII)
                              STRESSJJNVIII=STRESSI(J-NVIII)
                              VALUE1=1-
     +                         (2*STRESSJJN*1E6)/(VO*RHOST*CST)

      VALUE2=(2*STRESSJJNN*1E6)/(VO*RHOST*CST)

      VALUE3=(2*STRESSJJNNN*1E6)/(VO*RHOST*CST)

      VALUE4=(2*STRESSJJNIV*1E6)/(VO*RHOST*CST)

      VALUE5=(2*STRESSJJNV*1E6)/(VO*RHOST*CST)

      VALUE6=(2*STRESSJJNVI*1E6)/(VO*RHOST*CST)

      VALUE7=(2*STRESSJJNVII*1E6)/(VO*RHOST*CST)

      VALUE8=(2*STRESSJJNVIII*1E6)/(VO*RHOST*CST)
                              VALUE9=(AO)/(VO*A*(1-
     +                         DEC))*(1/(RHO*C)+1/(RHOST*CST))
     +                        *((SIGCSTR*1E6)-YOUNGC*(ECSTR-
     +                         DEC))
                       DT=(HOM/VO)*(1.0/(VALUE1-VALUE2-
     +                         VALUE3-VALUE4
```

```
+            -VALUE5-VALUE6-VALUE7-VALUE8-VALUE9))*(DEC-
+           EC(J-1))+T(J-1)
                  ENDIF
                  IF(COUNT.EQ.8)THEN
                        STRESSJJN=STRESSI(J-N)
                        STRESSJJNN=STRESSI(J-NN)
                        STRESSJJNNN=STRESSI(J-NNN)
                        STRESSJJNIV=STRESSI(J-NIV)
                        STRESSJJNV=STRESSI(J-NV)
                        STRESSJJNVI=STRESSI(J-NVI)
                        STRESSJJNVII=STRESSI(J-NVII)
                        VALUE1=1-
+                        (2*STRESSJJN*1E6)/(VO*RHOST*CST)

    VALUE2=(2*STRESSJJNN*1E6)/(VO*RHOST*CST)

    VALUE3=(2*STRESSJJNNN*1E6)/(VO*RHOST*CST)

    VALUE4=(2*STRESSJJNIV*1E6)/(VO*RHOST*CST)

    VALUE5=(2*STRESSJJNV*1E6)/(VO*RHOST*CST)

    VALUE6=(2*STRESSJJNVI*1E6)/(VO*RHOST*CST)

    VALUE7=(2*STRESSJJNVII*1E6)/(VO*RHOST*CST)
                  VALUE8=(AO)/(VO*A*(1-
+                  DEC))*(1/(RHO*C)+1/(RHOST*CST))
+                 *((SIGCSTR*1E6)-YOUNGC*(ECSTR-DEC))
           DT=(HOM/VO)*(1.0/(VALUE1-VALUE2-VALUE3-
+           VALUE4-VALUE5-VALUE6-VALUE7-VALUE8))*(DEC-
+           EC(J-1))+T(J-1)
                  ENDIF
                  IF(COUNT.EQ.7)THEN
                        STRESSJJN=STRESSI(J-N)
                        STRESSJJNN=STRESSI(J-NN)
                        STRESSJJNNN=STRESSI(J-NNN)
                        STRESSJJNIV=STRESSI(J-NIV)
                        STRESSJJNV=STRESSI(J-NV)
                        STRESSJJNVI=STRESSI(J-NVI)
                        VALUE1=1-
+                        (2*STRESSJJN*1E6)/(VO*RHOST*CST)

    VALUE2=(2*STRESSJJNN*1E6)/(VO*RHOST*CST)

    VALUE3=(2*STRESSJJNNN*1E6)/(VO*RHOST*CST)

    VALUE4=(2*STRESSJJNIV*1E6)/(VO*RHOST*CST)
```

```
      VALUE5=(2*STRESSJJNV*1E6)/(VO*RHOST*CST)

      VALUE6=(2*STRESSJJNVI*1E6)/(VO*RHOST*CST)
                              VALUE7=(AO)/(VO*A*(1-
     +                         DEC))*(1/(RHO*C)+1/(RHOST*CST))
     +                        *((SIGCSTR*1E6)-YOUNGC*(ECSTR-
     +                        DEC))
                              DT=(HOM/VO)*(1.0/(VALUE1-VALUE2-
     +                         VALUE3-VALUE4-VALUE5-VALUE6-
     +                         VALUE7))*(DEC-EC(J-1))+T(J-1)
                    ENDIF
                    IF(COUNT.EQ.6)THEN
                              STRESSJJN=STRESSI(J-N)
                              STRESSJJNN=STRESSI(J-NN)
                              STRESSJJNNN=STRESSI(J-NNN)
                              STRESSJJNIV=STRESSI(J-NIV)
                              STRESSJJNV=STRESSI(J-NV)
                              VALUE1=1-
     +                        (2*STRESSJJN*1E6)/(VO*RHO*C)

      VALUE2=(2*STRESSJJNN*1E6)/(VO*RHO*C)

      VALUE3=(2*STRESSJJNNN*1E6)/(VO*RHO*C)

      VALUE4=(2*STRESSJJNIV*1E6)/(VO*RHO*C)

      VALUE5=(2*STRESSJJNV*1E6)/(VO*RHO*C)
                              VALUE6=(AO)/(VO*A*(1-
     +                         DEC))*(1/(RHO*C)+1/(RHOST*CST))
     +                        *((SIGCSTR*1E6)-YOUNGC*(ECSTR-
     +                        DEC))
                              DT=(HOM/VO)*(1.0/(VALUE1-VALUE2-
     +                         VALUE3-VALUE4-VALUE5-
     +                         VALUE6))*(DEC-EC(J-1))+T(J-1)
                    ENDIF
                    IF(COUNT.EQ.5)THEN
                              STRESSJJN=STRESSI(J-N)
                              STRESSJJNN=STRESSI(J-NN)
                              STRESSJJNNN=STRESSI(J-NNN)
                              STRESSJJNIV=STRESSI(J-NIV)
                              VALUE1=1-
     +                        (2*STRESSJJN*1E6)/(VO*RHOST*C)

      VALUE2=(2*STRESSJJNN*1E6)/(VO*RHOST*CST)

      VALUE3=(2*STRESSJJNNN*1E6)/(VO*RHOST*CST)
```

```
      VALUE4=(2*STRESSJJNIV*1E6)/(VO*RHOST*CST)
                              VALUE5=(AO)/(VO*A*(1-
     +                         DEC))*(1/(RHO*C)+1/(RHOST*CST))
     +                        *((SIGCSTR*1E6)-YOUNGC*(ECSTR-
     +                         DEC))
                                    DT=(HOM/VO)*(1.0/(VALUE1-
     +                               VALUE2-VALUE3-VALUE4-
     +                               VALUE5))*(DEC-EC(J-1))+T(J-1)
                        ENDIF
                        IF(COUNT.EQ.4)THEN
                              STRESSJJN=STRESSI(J-N)
                              STRESSJJNN=STRESSI(J-NN)
                              STRESSJJNNN=STRESSI(J-NNN)
                              VALUE1=1-
     +                        (2*STRESSJJN*1E6)/(VO*RHOST*CST)

      VALUE2=(2*STRESSJJNN*1E6)/(VO*RHOST*CST)

      VALUE3=(2*STRESSJJNNN*1E6)/(VO*RHOST*CST)
                              VALUE4=(AO)/(VO*A*(1-
     +                         DEC))*(1/(RHO*C)+1/(RHOST*CST))
     +                        *((SIGCSTR*1E6)-YOUNGC*(ECSTR-
     +                         DEC))
                              DT=(HOM/VO)*(1.0/(VALUE1-VALUE2-
     +                         VALUE3-VALUE4))*
     +                        (DEC-EC(J-1))+T(J-1)
                        ENDIF
                        IF(COUNT.EQ.3)THEN
                              STRESSJJN=STRESSI(J-N)
                              STRESSJJNN=STRESSI(J-NN)
                              VALUE1=1-
     +                        (2*STRESSJJN*1E6)/(VO*RHOST*CST)

      VALUE2=(2*STRESSJJNN*1E6)/(VO*RHOST*CST)
                              VALUE4=(AO)/(VO*A*(1-
     +                         DEC))*(1/(RHO*C)+1/(RHOST*CST))
     +                        *((SIGCSTR*1E6)-YOUNGC*(ECSTR-
     +                         DEC))
                              DT=(HOM/VO)*(1.0/(VALUE1-VALUE2-
     +                         VALUE4))*(DEC-EC(J-1))+T(J-1)
                        ENDIF
                        IF(COUNT.EQ.2)THEN
                              STRESSJJN=STRESSI(J-N)
                              VALUE1=1-
     +                        (2*STRESSJJN*1E6)/(VO*RHO*C)
                              VALUE4=(AO)/(VO*A*(1-
```

```
     +                                DEC))*(1/(RHO*C)+1/(RHOST*CST))
     +                               *((SIGCSTR*1E6)-YOUNGC*(ECSTR-
     +                                DEC))
                                     DT=(HOM/VO)*(1.0/(VALUE1-
     +                                VALUE4))*(DEC-EC(J-1))+T(J-1)
                           ENDIF
                           DDELT=DT-T(J-1)
C
C          FIRST DATA POINT WILL HAVE VERY LITTLE CHANGE IN
C          STRAIN.
C          THEREFORE, IT IS NECESSARY TO LET TIME ADVANCE AND
C          HOLD STRAINS CONSTANT.
C
                           IF(DDELT.LT.0.0)THEN
                                 DELT(J)=DELT(J-1)
                                 T(J)=T(J-1)+DELT(J)
                                 TMS(J)=T(J)*1E6
                                 STRESSI(J)=STRESSI(J-1)
                                 STRAINI(J)=STRAINI(J-1)
                                 HM(J)=HM(J-1)
                                 HI(J)=HI(J-1)
                                 EC(J)=EC(J-1)
          V1(J)=VO-(STRESSI(J)*1E6)/(RHOST*CST)-(2*STRESSJJN*1E6)/
     +          (RHOST*CST)-(2*STRESSJJNN*1E6)/(RHOST*CST)-
     +           (2*STRESSJJNNN*1E6)/
     +          (RHOST*CST)-(2*STRESSJJNNN*1E6)/(RHOST*CST)-
     +           (2*STRESSJJNIV*1E6)/
     +          (RHOST*CST)-(2*STRESSJJNV*1E6)/(RHOST*CST)-
     +           (2*STRESSJJNVI*1E6)/
     +          (RHOST*CST)-(2*STRESSJJNVII*1E6)/(RHOST*CST)-
     +           (2*STRESSJJNVIII*1E6)
     +          /(RHOST*CST)-(2*STRESSJJNIX*1E6)/(RHOST*CST)-
     +           (2*STRESSJJNX*1E6)/(RHOST*CST)
                                 V2(J)=(STRESSI(J)*1E6)/(RHO*C)
                                       STRNRT(J)=(V1(J)-V2(J))/HOM
                                       GOTO 10201
                           ENDIF

          IF(DDELT.LE.DELTP.AND.DDELT.GE.DELTM)THEN
                                 GO TO 10200
                           ENDIF
                           IF(DDELT.GT.VALUE)THEN
                                 IF(BETA.EQ.0)THEN
                                       DHM=DHM-STAR4/3
                                       BETA=1
                                       GOTO 10100
                                 ENDIF
```

```
                        BETA=1
                        DHM=DHM-STAR4
                        GOTO 10100
                    ENDIF
                    IF(DDELT.LT.VALUE)THEN
                        IF(BETA.EQ.1)THEN
                            DHM=DHM+STAR4/2
                            BETA=0
                            GOTO 10100
                        ENDIF
                        DHM=DHM+STAR4
                        BETA=0
                        GOTO 10100
                    ENDIF
10200               CONTINUE
                    HM(J)=DHM
                    HI(J)=DHI
                    EC(J)=DEC
                    T(J)=DT
                    DELT(J)=DDELT
      STRESSI(J)=AO/((1-EC(J))*A)*(SIGCSTR-YOUNGC*(ECSTR-
     +               EC(J)))
                    STRAINI(J)=STRESSI(J)/(E/1E6)
      V1(J)=VO-(STRESSI(J)*1E6)/(RHOST*CST)-(2*STRESSJJN*1E6)/
     +          (RHOST*CST)-(2*STRESSJJNN*1E6)/(RHOST*CST)-
     +          (2*STRESSJJNNN*1E6)/
     +          (RHOST*CST)-(2*STRESSJJNNN*1E6)/(RHOST*CST)-
     +          (2*STRESSJJNIV*1E6)/
     +          (RHOST*CST)-(2*STRESSJJNV*1E6)/(RHOST*CST)-
     +          (2*STRESSJJNVI*1E6)/
     +          (RHOST*CST)-(2*STRESSJJNVII*1E6)/(RHOST*CST)-
     +          (2*STRESSJJNVIII*1E6)
     +          /(RHOST*CST)-(2*STRESSJJNIX*1E6)/(RHOST*CST)-
     +          (2*STRESSJJNX*1E6)/(RHOST*CST)
                        V2(J)=(STRESSI(J)*1E6)/(RHO*C)
                        TMS(J)=T(J)*1E6
                        STRNRT(J)=(V1(J)-V2(J))/HOM
C
C       THE CALCULATED STRNRT(J) ABOVE ASSUMES
C       UNLOADING IS OCCURING. IF THE
C       STRAIN RATE IS POSITIVE, STRNRT(J) IS NOT VALID.
C       THEREFORE, THE PROGRAM
C       LETS TIME ADVANCE AND HOLDS THE STRESS AND STRAIN
C       CONSTANT.

                    IF(STRNRT(J).GT.0.0)THEN
                        STRESSI(J)=STRESSI(J-1)
```

```
                              STRAINI(J)=STRAINI(J-1)
                              HM(J)=HM(J-1)
                              HI(J)=HI(J-1)
                              EC(J)=EC(J-1)
      V1(J)=VO-(STRESSI(J)*1E6)/(RHOST*CST)-(2*STRESSJJN*1E6)/
     +        (RHOST*CST)-(2*STRESSJJNN*1E6)/(RHOST*CST)-
     +         (2*STRESSJJNNN*1E6)/
     +        (RHOST*CST)-(2*STRESSJJNNN*1E6)/(RHOST*CST)-
     +         (2*STRESSJJNIV*1E6)/
     +        (RHOST*CST)-(2*STRESSJJNV*1E6)/(RHOST*CST)-
     +         (2*STRESSJJNVI*1E6)/
     +        (RHOST*CST)-(2*STRESSJJNVII*1E6)/(RHOST*CST)-
     +         (2*STRESSJJNVIII*1E6)
     +        /(RHOST*CST)-(2*STRESSJJNIX*1E6)/(RHOST*CST)-
     +        (2*STRESSJJNX*1E6)/(RHOST*CST)
                              V2(J)=(STRESSI(J)*1E6)/(RHO*C)
                              STRNRT(J)=(V1(J)-V2(J))/HOM
C
C     DOES NOT WRITE THE ADVANCE, JUST KEEPS TRACK OF IT
C
                              GO TO 10800
                         ENDIF
10201                    PRINT *, J,EC(J),TMS(J)
                         IF(STRESSI(J).LT.0.0)THEN
                                   STRESSI(J)=0.0
      WRITE(7,10700,ERR=999)HM(J),HI(J),EC(J),T(J),DELT(J),
     +        STRAINI(J),STRESSI(J),TMS(J),STRNRT(J),V1(J),
     +        V2(J)
                                   GO TO 20000
                         ENDIF
      WRITE(7,10700,ERR=999)HM(J),HI(J),EC(J),T(J),DELT(J),
     +        STRAINI(J),STRESSI(J),TMS(J),STRNRT(J),V1(J),
     +        V2(J)
10700 FORMAT(11(F15.8,1X))
10800                    IF(J.EQ.(COUNT*N))THEN
                              PRINT*, J,STRNRT(J),TMS(J)
                              IF(COUNT.EQ.2)NN=J
                              IF(COUNT.EQ.3)NNN=J
                              IF(COUNT.EQ.4)NIV=J
                              IF(COUNT.EQ.5)NV=J
                              IF(COUNT.EQ.6)NVI=J
                              IF(COUNT.EQ.7)NVII=J
                              IF(COUNT.EQ.8)NVIII=J
                              IF(COUNT.EQ.9)NIX=J
                              IF(COUNT.EQ.10)NX=J
                              COUNT=COUNT+1
                         ENDIF
```

```
10050              CONTINUE
10000 CONTINUE
20000 CLOSE(UNIT=7)
          CLOSE(UNIT=8)
          CLOSE(UNIT=9)
          CLOSE(UNIT=10)
          STOP
          END
```

References

Akers, S.A., Reed, P.A., Ehrgott, J.Q.: WES high-pressure uniaxial strain and triaxial shear test equipment. Miscellaneous Paper SL-86-11, U.S. Army Engineers, Waterways Experiment Station, Vicksburg, MS (1986)

Albertini, C., Montagnani, M.: Dynamic material properties of several steels for fast breeder reactor safety analysis. Report EUR 5787 EN, Applied Mechanics Division, Joint Research Centre, Ispra, Italy (1977)

Apostol M., Vuoristo T., Kuokkala V.T.: High temperature high strain rate testing with a compressive SHPB. J de Physique IV **110**, 459-464 (2003)

ASTM Standard C1421-01b: Standard test methods for determination of fracture toughness of advanced ceramics at ambient temperature. Annual Book of ASTM Standards, ASTM, West Conshohocken, PA (2001)

ASTM Standard C1499–05: Standard test method for monotonic equibiaxial flexural strength of advanced ceramics at ambient temperature. Annual Book of ASTM Standards, ASTM, West Conshohocken, PA (2003)

ASTM Standard D4543: Preparing rock core specimens and determining dimensional and shape tolerances. Annual Book of ASTM Standards, 687-690, ASTM, Philadelphia, PA (1991)

ASTM Standard F394-78: Standard test method for biaxial flexural strength (modulus of rupture) of ceramic substrates. Annual Book of ASTM Standards, 469-473, ASTM, West Conshohocken, PA (1995)

Baker, W.E., Yew, C.H.: Strain-rate effects in the propagation of torsional plastic waves. J. Appl. Mech. **33**, 917-923 (1966)

Basak, D., Yoon, H.W., Rhorer, R., Burns, T.J., Matsumoto, T.: Temperature Control of Pulse Heated Specimens in a Kolsky Bar Apparatus Using Microsecond Time-Resolved Pyrometry. Int. J. Thermophys. **25**, 561-574 (2004)

Bhushan, B., Jahsman, W.E.: Measurements of dynamic material behavior under nearly uniaxial strain conditions. Int. J. Solids Struct. **14**, 739-753 (1976)

Bishop, A.W., Henkel, D.J.: The Measurement of Soil Properties in the Triaxial Test. Edward Arnold Ltd., London (1962)

Böhme, W., Kalthoff, J.F.: The behavior of notched bend specimens in impact testing. Int. J. Fracture **20**, R139-143 (1982)

Boyce, J.R., Brown, S.F.: Measurement of elastic strain in granular material. Geotechnique **26**, 637-640 (1976)

Brace, W.F., Bombolakis, E.G.: A note on brittle crack growth in compression. J. Geophys. Res. **68**, 3709–3713 (1963)

Bragov, A.M., Lomunov, A.K.: Methodological aspects of studying dynamic material properties using the Kolsky method. Int. J. Impact Eng. **16**, 321-330 (1995)

Briscoe, B.J., Nosker, R.W.: The influence of interfacial friction on the deformation of high density polyethylene in a split Hopkinson pressure bar. Wear **95**, 241-262 (1984)

Cadoni, E., Solomos, G., Albertini, C.: Mechanical characterization of concrete in tension and compression at high strain rate using a modified Hopkinson bar, Mag. Concrete Res. **61**, 221-228 (2009)

Casem, D.: A small diameter Kolsky bar for high-rate compression. In: Proceedings of the SEM Annual Conference and Exposition on Experimental and Applied Mechanics, Albuquerque, NM, June 1-4 (2009)

Casem, D., Weerasooriya, T., Moy, P.: Inertial effects of quartz force transducers embedded in a split Hopkinson pressure bar. Exp Mech **45**, 368–376 (2005)

Casem, D., Grunschel, S., Schuster, B.E.: Interferometric measurement techniques for small diameter Kolsky bars. Presentation at 2010 SEM Annual Conference & Exposition on Experimental and Applied Mechanics, Indianapolis, IN, June 7 - 10 (2010)

Casem, D.T.: Hopkinson bar pulse-shaping with variable impedance projectiles—an inverse approach to projectile design. ARL-TR-5246, US Army Research Laboratory, Aberdeen Proving Ground, MD (2010).

Chan, D., Nie, X., Bhate, D., Subbarayan, G., Chen, W., Dutta, I.: High strain rate behavior of Sn3.8Ag0.7Cu solder alloys and its influence on the fracture location within solder joints (IPACK2009-89404). In: Proceedings of IPACK2009, San Francisco, CA, July 19-23 (2009)

Chen, D., Hu, S., Zhang, S., Wu, X, Yu, Z.: Large dimension Hopkinson pressure bar and its application. J. Exp. Mech. **20**, 398-402 (2005) (in Chinese)

Chen, R., Huang, S., Xia, K.: A modified Kolsky bar system for testing ultrasoft materials under intermediate strain rates. Rev. Sci. Instru. **80**, 076108 (2009)

Chen, W., Luo, H.: Dynamic compressive testing of intact and damaged ceramics. Ceram. Eng. Sci. Proc. **24**, 411–416 (2003)

Chen, W., Luo, H.: Dynamic compressive responses of intact and damaged ceramics from a single split Hopkinson pressure bar experiment. Exp. Mech., **44**, 295–299 (2004)

Chen, W., Ravichandran, G.: Dynamic compressive behavior of a glass ceramic under lateral confinement. J. Mech. Phys. Solids **45**, 1303-1328 (1997)

Chen, W., Song, B.: Dynamic compression testing on polymeric foams. In: Experiments in Automotive Engineering – Optical Techniques, SAE Transactions, 2005 SAE World Congress, Detroit, MI, April 11-14 (2005)

Chen, W., Song, B.: Temperature dependence of a NiTi shape memory alloy's superelastic behavior at a high strain rate. J. Mech. Mater. Struct. **1**, 339-356 (2006)

Chen, W., Zhou, B.: Constitutive behavior of epon 828/T-403 at various strain rates. Mech. Time-Depend. Mater. **2**, 103-111 (1998)

Chen, W., Subhash, G., Ravichandran, G.: Evaluation of ceramic specimen geometries used in split Hopkinson pressure bar. DYMAT J. **1**, 193-210 (1994)

Chen, W., Zhang, B., Forrestal, M.J.: A split Hopkinson bar technique for low-impedance materials. Exp. Mech. **39**, 81-85 (1999)

Chen, W., Lu, F., Zhou, B.: A quartz-crystal-embedded split Hopkinson pressure bar for soft materials. Exp. Mech. **40**, 1-6 (2000)

Chen, W., Lu, F., Cheng, M.: Tension and compression tests of two polymers under quasi-static and dynamic loading. Polymer Testing **21**, 113-121(2002a)

Chen, W., Lu, F., Frew, D.J., Forrestal, M.J.: Dynamic compression testing of soft materials. asme trans. J. Appl. Mech. **69**, 214-223 (2002b)

Chen, W., Song, B., Frew, D.J., Forrestal, M.J.: Dynamic small strain measurements of metal specimen with a split Hopkinson bar. Exp. Mech. **43**, 20-23 (2003)

Chen, W.W., Rajendran, A.M., Song, B., Nie, X.: Dynamic fracture of ceramics in armor applications. J. Amer. Ceram. Soc. **90**, 1005-1018 (2007)

Chen, W.W., Song, B.: Chapter 1: Dynamic characterization of soft materials. In: A. Shukla, G. Ravichandran, Y.D.S. Rajapaske (eds.) Dynamic Failure of Materials and Structures, Springer, pp.1-28 (2009)

Cheng, M., Chen W.: Experimental investigation of the stress-stretch behavior of EPDM rubber with loading rate effects. Int. J. Solids Struct. **40**, 4749-4768 (2003)

Cheng, M., Chen, W., Sridhar, K.R.: Experimental method for a dynamic biaxial flexural strength test of thin ceramic substrates. J. Amer. Ceram. Soc. **85**, 1203-1209 (2002)

Cheng, M., Chen, W., Weerasooriya, T.: Mechanical properties of Kevlar® KM2 single fiber. Trans. ASME, J.Eng. Mater. Tech. **127**, 197-203 (2005)

Cheng, M., Chen, W., Weerasooriya, T.: Mechanical behavior of bovine tendon with stress-softening and loading rate effects. Adv. Theor. Appl. Mech. **2**, 59-74 (2009)

Chiddister, J.L., Malvern, L.E.: Compression-impact testing of aluminum at elevated temperatures. Exp. Mech. April, 81-90 (1963)

Chree, C.: The equations of an isotropic elastic solid in polar and cylindrical coordinates, their solutions and applications. Trans. Cambridge Phil. Soc. **14**, 250-369 (1889)

Christensen, R.J., Swanson, S.R., Brown, W.S.: Split-Hopkinson-bar tests on rocks under confining pressure. Exp. Mech. November, 508-513 (1972)

Davis, E.D.H., Hunter, S.C.: The dynamic compression test of solids by the method of the split Hopkinson pressure bar. J. Mech. Phys. Solids **11**, 155-179 (1963)

Davis, R.M.: A critical study of the Hopkinson pressure bar. Proc. R. Soc. London **A240**, 375-457 (1948)

Deobald, L.R, Kobayashi, A.S.: A bar impact tester for dynamic fracture testing of ceramics and ceramic composites. Exp. Mech. **32**, 109-116 (1992)

Duffy, J., Campbell, J.D., Hawley, R.H.: On the use of a torsional split Hopkinson bar to study rate effects in 1100-0 aluminum. Trans. ASME, J. Appl. Mech. **37**, 83-91 (1971)

Ellwood, S., Griffiths, L.J., Parry, D.J.: Materials testing at high constant strain rates. J. Phys. E: Sci. Instru. **15**, 280-282 (1982)

Espinosa, H.D., Patanella, A., Fisher, M.: A novel dynamic friction experiment using modified Kolsky bar apparatus. Exp. Mech. **40**, 138-153 (2000)

Feng, R., Raiser, G.F., Gupta, Y.M.: Material strength and inelastic deformation of silicon carbide under shock wave compression. J. Appl. Phys. **83**, 79-86 (1998)

Field, J.E., Walley, S.M., Proud, W.G., Goldrein, H.T., Siviour, C.R.: Review of experimental techniques for high rate deformation and shock studies. Int. J. Impact Eng. **30**, 725-775 (2004)

Follansbee, P.S.: The Hopkinson bar. In: Mechanical Testing, ASM Handbook (9^{th} edition), Metals Park, Ohio, **8**, 198-217 (1995)

Follansbee, P.S., Frantz, C.: Wave propagation in the split Hopkinson pressure bar. Trans. ASME, J. Eng. Mater. Technol., **105**, 61-66 (1983)

Follansbee, PS., Regazzoni, G., Kocks, U.E.: The transition to drag controlled deformation in copper at high strain rates. Inst. Phys. Conf. Ser. **70**, 71-80 (1984)

Forrestal, M.J., Frew, D.J., Hickerson, J.P., Rohwer, T.A.: Penetration of concrete targets with deceleration-time measurements. Int. J. Impact Eng., **28**, 479-497 (2003)

Forrestal, M.J., Wright, T.W., Chen, W.: The effect of radial inertia on brittle samples during the split Hopkinson pressure bar test. Int. J. Impact Eng. **34**, 405-411 (2006)

Frantz, C.E., Follansbee, P.S., Wright, W.T.: Experimental techniques with the split Hopkinson pressure bar. In: Proceedings of the 8th International Conference on High Energy Rate Fabrication, Texas, 229-236 (1984)

Frew, D.J.: Dynamic Triaxial Experiments on a Limestone. private communication (2010)

Frew, D.J., Forrestal, M.J., Chen, W.: A split Hopkinson pressure bar technique to determine compressive stress-strain data for rock materials. Exp. Mech. **41**, 40-46 (2001)

Frew, D.J., Forrestal, M.J., Chen, W.: Pulse shaping techniques for testing brittle materials with a split Hopkinson pressure bar. Exp. Mech. **42**, 93-106 (2002)

Frew, D.J., Forrestal, M.J., Chen, W.: Pulse shaping techniques for testing elastic-plastic materials with a split Hopkinson pressure bar. Exp. Mech. **45**, 186-195 (2005)

Frew, D.J., Doung, H., Sill, R.D.: A modified Hopkinson pressure bar experiment to evaluate a damped piezoresistive MEMS accelerometer. In: Proceedings of the 2009 SEM Annual Conference and Exposition on Experimental and Applied Mechanics, Albuquerque, NM, June 1-4 (2009)

Frew, D.J., Akers, S.A., Chen, W., and Green, M.A.: Development of a dynamic tri-axial Kolsky bar. Measurement Science and Technology, in printing (2010)

Gama, B.A., Lopatnikov, S.L., Gillespie, J.W. Jr.: Hopkinson bar experimental technique: a critical review. Trans. ASME, Appl. Mech. Rev. **57**, 223-249 (2004)

Gilat, A., Schmidt, T.E., Walker, A.L.: Full field strain measurement in compression and tensile split Hopkinson bar experiments. Exp. Mech. **49**, 291-302 (2009)

Gong, J.C., Malvern, L.E., Jenkins, D.A.: Dispersion investigation in the split Hopkinson pressure bar. Trans. ASME, J. Eng. Mater. Technol. **112**, 309-314 (1990)

Gorham, D.A.: A numerical method for the correction of dispersion in pressure bar signals. J. Phys. E: Sci. Instru. **16**, 477-479 (1983)

Gorham, D.A.: Specimen inertia in high strain-rate compression. J. Phys. D: Appl. Phys. **22**, 1888-1893 (1989)

Gray, G.T.: Classic split-Hopkinson pressure bar testing. ASM Handbook, Mechanical Testing and Evaluation, Materials Park, OH, **8**, 462-476 (2000)

Gray, G.T., Blumenthal, W.R.: Split Hopkinson pressure bar testing of soft materials, ASM Handbook, Mechanical Testing and Evaluation, Materials Park, OH, **8**, 488-496 (2000)

Gray, G.T., Blumenthal, W.R., Trujillo, C.P., Carpenter, R.W.: Influence of temperature and strain rate on the mechanical behavior of adiprene l-100. J. Phys. IV France Colloque C3 (DYMAT 97), **7**, 523-528 (1997)

Greene, C.H.,: Flow Distributions and variation of glass strength with dimensions of sample. J. Am. Ceram. Soc. 39, 66-72 (1956)

Guzman, O., Frew, D.J., Chen, W.: A Kolsky bar with a hollow incident tube. Paper # 91, 2010, Proceedings of the SEM Annual Conference & Exposition on Experimental and Applied Mechanics, Indianapolis, IN, June 7 - 10 (2010)

Hall, I.W., Guden, M.: Split Hopkinson pressure bar compression testing of an aluminum alloy: effect of lubricant type. J. Mater. Sci. Letter **22**, 1533-1535 (2003)

Harding, J., Welsh, L.M.: A tensile testing technique for fiber-reinforced composites at impact rates of strain. J. Mater. Sci. **18**, 1810-1826 (1983)

Harding, J., Wood, E.O., Campbell, J.D.: Tensile testing of materials at impact rates of strain. J. Mech. Eng. Sci. **2**, 88-96 (1960)

Hartley, K.A., Duffy, J., Hawley, R.H.: Measurement of the temperature profile during shear band formation in steels deforming at high strain rates. J. Mech. Phys. Solids **35**, 283-301 (1987)

Hauser, F.E.: Techniques for measuring stress-strain relations at high strain rates. Exp. Mech. **6**, 395-402 (1966)

Hauser, F.E., Simmons, J.A., Dorn, J.E.: Strain rate effects in plastic wave propagation. In: P.G. Shewmon, V.F. Zackay, (eds.), Response of Metals to High Velocity Deformation,., Interscience, New York, 93-114 (1961)

Hodowany, J., Ravichandran, G., Rosakis, A.J., Rosakis, P.: Partition of plastic work into heat and stored energy in metals. Exp. Mech. **40**, 113–123 (2000)

Hopkinson, B.: A method of measuring the pressure produced in the detonation of high explosives or by the impact of bullets. Phil. Trans. Royal Soc. London, **A213**, 437-456 (1914)

Hopkinson, J.: Further experiments on the rupture of iron wire (1872), Article 39, B. Hopkinson (ed.), Original Papers-by the late John Hopkinson, Vol. II, Scientific Papers, Cambridge (1901)

Horii, H., Nemat-Nasser, S.: Compression-induced macrocrack growth in brittle solids: axial splitting and shear failure. J. Geophys. Res., **90**, 3105–25 (1985)

Huang, H., Feng, R.: A study of the dynamic tribological response of closed fracture surface pairs by Kolsky-bar compression-shear experiment. Int. J. Solids and Struct. **41**, 2821-2835 (2004)

Jia, D., Ramesh, K.T.: A rigorous assessment of the benefits of miniaturization in the Kolsky bar system. Exp. Mech. **44**, 445-454 (2004)

Jiang, F, Vecchio, K.S.: Experimental investigation of dynamic effects in a two-bar/three-point bend fracture test. Rev. Sci. Instru. 78, 063903-1-12 (2007)

Jiang, F, Vecchio, K.S.: Hopkinson bar loaded fracture experimental technique: a critical review of dynamic fracture toughness tests. Trans. ASME, Appl. Mech. Rev. **62**, 060802-1-39 (2009)

Kabir, M.E., Chen, W.: Measurement of specimen dimensions and dynamic pressure in dynamic triaxial experiments. Review Sci. Instrum. **80** (2010), in press.

Kabir, M.E., Song, B., Martin B., Chen, W.: Compressive behavior of fine sand. Sandia Report SAND 2010-2289 (2010)

Kawata, K., Hashimoto, S., Kurokawa, K., Kanayama, N.: A new testing method for the characterization of materials in high-velocity tension. In: J. Harding (ed.), Mechanical Properties at High Rates of Strain, Inst. Phys. Conf. Ser. **47**, 71-80 (1979)

Kimberley, J., Lambros, J., Chasiotis, I., Pulskamp, J., Polcawich, R., Dubey, M.: A hybrid experimental/numerical investigation of the response of multilayered MEMS devices to dynamic loading. Exp. Mech. **50**, 527-544 (2010)

Klepaczko, J.R.: Discussion of a new experimental-method in measuring fracture-toughness initiation at high loading rates by stress waves. Trans. ASME, J. Eng. Mater. Technol. **104**, 29-35 (1982)

Kolsky, H.: An investigation of the mechanical properties of materials at very high rates of loading. Proc. Phys. Soc. London **B62**, 676-700 (1949)

Kolsky, H.: Stress Waves in Solids. Dover, New York (1963)

Krafft, J.M., Sullivan, A.M., Tipper, C.F.: The effect of static and dynamic loading and temperature on the yield stress of iron and mild steel in compression. Proc. Roy. Soc, London **A221**, 114-127 (1954)

Landon, J.W., Quinney, H.: Experiments with the Hopkinson Pressure bar. Proc. Royal Soc. London **A103**, 622-643 (1923)

Lennon, A.M., Ramesh, K.T.: A technique for measuring the dynamic behavior of materials at high temperatures. Int J Plasticity **14**, 1279-1292 (1998)

Li, Y., Ramesh, K.T.: An optical technique for measurement of material properties in the tension Kolsky bar. Int. J. Impact Eng. **34**, 784-798 (2007)

Li, M., Wang, R., Han, M.B.: A Kolsky bar: tension, tension-tension. Exp. Mech. **33**, 7-14 (1993)

Lim, J., Zheng, J.Q., Masters, K., Chen, W.W.: Mechanical behavior of A265 single fibers. J. Mater. Sci. **45**, 652-661 (2010)

Lindholm, U.S.: Some experiments with the split Hopkinson pressure bar. J. Mech. Phys. Solids **12**, 317-335 (1964)

Lindholm, U.S., Yeakley, L.M.: High strain rate testing: tension and compression. Exp. Mech. **8**, 1-9 (1968)

Lindholm, U.S., Yeakley, L.M., Nagy, A.: The dynamic strength and fracture properties of dresser basalt. Int. J. Rock Mech. Min. Sci. & Geomech. Abstr. **11**, 181-191 (1974)

Liu X., Hu, S., Wave propagation characteristics in cone bars used for variable cross-section SHPB, Explos. Shock Waves **20**, 110-114 (2000) (in Chinese)

Lok, T.S., Li, X.B., Liu, D., Zhao, P.J.: Testing and response of large diameter brittle materials subjected to high strain rate. J. Mater. Civil Eng. **14**, 262-269 (2002)

López, J.R., Allen, P.D., Alamo, L., Jones, D., Sreter, F.A.: Myoplasmic free [Ca2+] during a malignant hyperthermia episode in swine. Muscle Nerve **11**, 82–88 (1988)

Lu, W.-Y., Jin, H., Korellis, J., Gwinn, K., Chen, W., Song, B.: Dynamic loading of LIGA structures, In: Proceedings of the 2006 SEM Annual Conference and Exposition on Experimental and Applied Mechanics, Saint Louis, MO, June 4-7 (2006)

Luo, H., Chen, W.: Dynamic compressive response of intact and damaged AD995 alumina. Int. J. Appl. Ceram. Tech. **1**, 254–60 (2004)

Luo, H., Chen, W., Rajendran, A.M.: Dynamic compressive response of damaged and interlocked SiC–N ceramics. J. Am. Ceram. Soc. **89**, 266–73 (2006)

Maekawa, I., Shibata, H.: Characteristic property of impact fracture-toughness. JSME Int. J. Ser. A- Mech. Mater. Eng. **38**, 80-83 (1995)

Martin, B.E., Chen, W., Song, B., Akers, S.A.: Moisture effects on the high strain-rate behavior of sand. Mech. Mater. **41**, 786-798 (2009)

Mates, S.P., Rhorer, R., Whitenton, E., Burns, T., Basak, D.: A pulse-heated Kolsky bar technique for measuring the flow stress of metals at high loading and heating rates. Exp. Mech. 48, 799-807 (2008)

Meyers, M.A., Chawla, K.K.: Mechanical Behavior of Materials, Prentice Hall, Upper Saddle River, NJ (1999)

Meng, Y.-P., Hu, S.-S.: Some improvements on stress homogeneity for concrete test under impact compressive loading. J. Exp. Mech. **18,** 106-112 (2003) (in Chinese)

Miller, K.: How to test very soft biological tissues in extension. J. Biomech. **34**, 651-657 (2001)

Miller, K., Chinzei, K.: Constitutive modeling of brain tissue experiment and theory. J. Biomech. **30**, 1115-1121 (1997)

Mohr, D., Gary, G.: M-shaped specimen for the high strain rate tensile testing using a split Hopkinson pressure bar apparatus. Exp. Mech. **47**, 681-692 (2007)

Mott, P.H., Twigg, J.N., Roland, D.F., Schrader, H.S., Pathak, J.A., Roland, C.M.: High-speed tensile test instrument. Rev. Sci. Instru. **78**, 045105 1-6 (2007)

Moy, P., Weerasooriya, T., Juliano, T.F., VanLandingham, M.R.: Dynamic response of an alternative tissue simulant, physically associating gels (PAG), In: Proceedings of the SEM Annual Conference and Exposition on Experimental and Applied Mechanics, St. Louis, MO, June 4–7 (2006)

Nemat-Nasser, S.: Introduction to high strain rate testing. ASM Handbook, Mechanical Testing and Evaluation, Materials Park, OH, **8**, 427-446 (2000)

Nemat-Nasser S., Horii, H.: Compression-induced nonplanar crack extension with application to splitting, exfolation, and rockburst. J. Geophys. Res. **87**, 6805–6821 (1982)

Nemat-Nasser, S., Isaacs, J.B., Starrett, J.E.: Hopkinson techniques for dynamic recovery experiments. Pro. Royal Soc. London **435**, 371-391 (1991)

Nemat-Nasser, S., Choi, J.Y., Guo, W.G., Isaacs, J.B.: Very high strain-rate response of a NiTi shape-memory alloy. Mech. Mater. **37**, 287-298 (2005)

Nicholas, T.: Tensile testing of materials at high rates of strain. Exp. Mech. **21**, 177-188 (1981)

Nie, X., Chen, W., Sun, X., Templeton, D.W.: Dynamic failure of borosilicate glass under compression/shear loading: experiments. J. Amer. Ceram. Soc. **90**, 2556-2562 (2007)

Nie, X., Song, B., Ge, Y., Chen W.W., Weerasooriya, T.: Dynamic tensile testing of soft materials. Exp. Mech. **49**, 451-458 (2009)

Nie, X., Chen, W., Templeton, D.W.: Effects of loading rates and surface conditions on equi-biaxial flexural strength of borosilicate glass. J. Amer. Ceram. Soc. Accepted (2010)

Ogawa, K.: Impact-tension compression test by using a split-Hopkinson bar. Exp. Mech. **24**, 81-86 (1984)

Owen, D.M., Zhuang, S., Rosakis, A.J., Ravichandran, G.: Experimental determination of dynamic crack initiation and propagation fracture toughness in thin aluminum sheets. Int. J. Fracture, **90**, 153-174 (1998)

Owens, A.T., Tippur, H.V.: Tensile stress-strain response of glass-filled epoxy under elevated rates of loading using a split Hopkinson bar apparatus. Exp. Mech. **49**, 799-811 (2009)

Paliwal, B., Ramesh, K.T., McCauley, J.W., Chen, M.W.: Dynamic compressive failure of AlON under controlled planar confinement. J. Amer. Ceram. Soc. **91**, 3619-3629 (2008)

Pan, Y., Chen, W., Song, B.: The upper limit of constant strain rate in a split Hopkinson pressure bar experiment. Exp. Mech. **45**, 440-446 (2005)

Parry, D.J., Walker, A.G., Dixon, P.R.: Hopkinson bar pulse smoothing. Measur. Sci. Technol. **6**, 443-446 (1995)

Pervin, F., Chen, W.: Dynamic mechanical response of bovine gray matter and white matter brain tissues under compression. J. Biomech. **42**, 731-735 (2009)

Pochhammer, L.: On the propagation velocities of small oscillations in an unlimited isotropic circular cylinder. J. fur die Reine und Angewandte Mathematik **81**, 324-326 (1876)

Ramesh, K.T., Narasimhan, S.: Finite deformations and the dynamic measurement of radial strains in compression Kolsky bar experiments. Int. J. Solids Struct. **33**, 3723-3738 (1996)

Rajagopalan, S., Prakash, V.: A modified torsional Kolsky bar for investigating dynamic friction. Exp. Mech. **39**, 295-303 (1999)

Rojas, R.R., Chen, W.: Instrumented low-speed penetration into granular alumina. Instru. Measur. Metrol. **3**, 213-236 (2003)

Ravichandran, G., Subhash, G.: Critical appraisal of limiting strain rates for compression testing of ceramics in a split Hopkinson pressure bar. J. Amer. Ceram. Soc. **77**, 263-267 (1994)

Rosenberg, Z., Dawicke, D., Strader, E., Bless, S.J.: A new technique for heating specimens in split-Hopkinson-bar experiments using induction-coil heaters. Exp. Mech. September, 275-278 (1986)

Safa, K., Gary, G.: Accounting for the effect of local punching at the bar/specimen interface in SHPB experiments. In: Proceedings of 9th International Conference on the Mechanical and Physical Behaviour of Materials under Dynamic Loading (DAMAT2009), Brussels, Belgium, 81-87, September 7-11 (2009)

Samanta, S.K.: Dynamic deformation of aluminum and copper at elevated temperatures. J. Mech. Phys. Solids **19**, 117-135 (1971)

Seo, S., Min, O., Yang, H.: Constitutive equation for Ti-6Al-4V at high temperatures measured using the SHPB technique. Int. J. Impact Eng. **31**, 735-754 (2005)

Sharpe, W.N.: An interfrometric strain/displacement measurement system. NASA TM-101638 (1989)

Shazly, M., Prakash, V., Draper, S.: Mechanical behavior of Gamma-Met PX under uniaxial loading at elevated temperatures and high strain rates. Int. J. Solids Struct. **41**, 6485-6503 (2004)

Sheehy, M., Punch, J., Goyal, S., Reid, M., Lishchynska, M., Kelly, G.: The failure mechanisms of micro-scale cantilevers under shock and vibration stimuli. Strain **45**, 283–294 (2009)

Shergold, O.A., Fleck, N.A., Radford, D.: The uniaxial stress versus strain response of pig skin and silicone rubber at low and high strain rates. Int. J. Impact Eng. **32**, 1384-1402 (2006)

Song, B., Chen, W.: Dynamic compressive constitutive behavior of EPDM rubber. Trans. ASME, J. Eng. Mater. Technol. **125**, 294-301 (2003)

Song, B., Chen, W.: Dynamic compressive behavior of EPDM rubber under nearly uniaxial strain conditions. Trans. ASME, J. Eng. Mater. Technol. **126**, 213-217 (2004a)

Song, B., Chen, W.: Dynamic stress equilibrium on a rubber specimen during a split Hopkinson pressure bar experiment. Exp. Mech. **44**, 300-312 (2004b)

Song, B., Chen, W.: Loading and unloading split Hopkinson pressure bar pulse-shaping techniques for dynamic hysteretic loops. Exp. Mech. **44**, 622-627 (2004c)

Song, B., Chen, W.: Split Hopkinson pressure bar techniques for characterizing soft materials. Latin Amer. J. Solids Struct. **2**, 113-152 (2005)

Song, B., Chen, W.: Energy for specimen deformation in a split Hopkinson pressure bar experiment. Exp. Mech. **46**, 407-410 (2006)

Song, B., Chen, W., Frew, D.J.: Split Hopkinson bar testing of an aluminum with pulse shaping. In: Proceedings of the JSME/ASME International Conference on Materials and Processing, Honolulu, HI, October 15-18 (2002)

Song, B., Chen W., Weerasooriya, T.: Quasi-static and dynamic compressive behaviors of a S-2 glass/SC15 composite. J. Composite Mater. **37**, 1723-1743 (2003)

Song, B., Chen, W., Cheng, M.: A novel model for uniaxial strain-rate-dependent stress-strain behavior of EPDM rubber in compression or tension. J. Appl. Polymer Sci. **92**, 1553-1558 (2004a)

Song, B., Chen, W., Frew, D.J.: Quasi-static and dynamic compressive and failure behaviors of an epoxy syntactic foam. J. Composite Mater. **38**, 915-936 (2004b)

Song, B., Chen, W., Dou, S., Winfree, N.A., Kang, J.H.: Strain-rate effects on elastic and early cell-collapse responses of a polystyrene foam. Int. J. Impact Eng. **31**, 509-521 (2005a)

Song, B., Chen, W., Jiang X.: Split Hopkinson pressure bar experiments on polymeric foams. Int. J. Vehicle Des. **37**, 185-198 (2005b)

Song, B., Chen, W., Yanagita, T., Frew, D.J.: Confinement effects on the dynamic compressive proeprties of an epoxy syntactic foam. Composite Struct. **67**, 279-287 (2005c)

Song, B., Chen, W., Yanagita, T., Frew, D.J.: Temperature effects on dynamic compressive behavior of an epoxy syntactic foam. Composite Struct. **67**, 289-298 (2005d)

Song, B., Chen, W., Liu, Z., Erhan, S.: Compressive properties of epoxidized soybean oil/clay nanocomposites. Int. J. Plasticity **22**, 1549-1568 (2006a)

Song, B., Chen, W., Liu, Z., Erhan, S.Z.: Compressive mechanical behavior of soybean oil-based polymers at low and high strain rates. J. Appl. Polymer Sci. **99**, 2759-2770 (2006b)

Song, B., Forrestal, M.J., Chen, W.: Dynamic and quasi-static propagation of compaction waves in a low-density epoxy foam. Exp. Mech. **46**, 127-136 (2006c)

Song, B., Chen, W., Antoun, B.R., Frew, D.J.: Flow stress obtained on ductile specimens deforming at high strain rates. Exp. Mech. **47**, 671-679 (2007a)

Song, B., Chen, W., Ge, Y., Weerasooriya, T.: Dynamic and quasi-static compressive response of porcine muscle. J. Biomech. **40**, 2999-3005 (2007b)

Song, B., Chen, W., Lu, W.-Y.: Compressive mechanical response of a low-density epoxy foam at various strain rates. J. Mater. Sci. **42**, 7502-7507 (2007c)

Song, B., Chen, W., Lu, W.-Y.: Mechanical characterization at intermediate strain rates for rate effects on an epoxy syntactic foam. Int. J. Mech. Sci. **49**, 1336-1343 (2007d)

Song, B., Chen, W.W., Ge, Y., Weerassoriya, T.: Radial inertia effects in Kolsky bar testing of extra-soft materials. Exp. Mech. **47**, 659-670 (2007e)

Song, B., Syn, C.J., Grupido, C.L., Chen, W., Lu, W.-Y.: A long split Hopkinson pressure bar (LSHPB) for intermediate-rate characterization of soft materials. Exp. Mech. **48**, 809-815 (2008)

Song, B., Chen, W., Luk, V.: Impact compressive response of dry sand. Mech. Mater. **41**, 777-785 (2009a)

Song, B., Connelly, K., Korellis, J., Lu, W.-Y., Antoun, B.R.: Improvements in Kolsky-bar design for mechanical characterization of materials at high strain rates. Measur. Sci. Technol. **20**, 115701-1-8 (2009b)

Song, B., Forrestal, M.J., Chen, W., Montgomery, S.T.: Mechanical properties of an alumina-filled epoxy at various strain rates. J. Composite Mater. **43**, 1519-1536 (2009c)

Song, B., Lu, W.-Y., Syn, C.J., Chen, W.: The effects of strain rate, density, and temperature on the mechanical properties of polymethylene

diisocyanate (PMDI)-based rigid polyurethane foams during compression. J. Mater. Sci. **44**, 351-357 (2009d)

Song, B., Antoun, B.R., Nie, X., Chen, W.: High-rate characterization of 304L stainless steel at elevated temperatures for recrystallization investigation. Exp. Mech. **50**, 553-560 (2010)

Song, B., Antoun, B.R., Connelly, K., Korellis, J., Lu, W.-Y.: A newly developed Kolsky tension bar. Paper # 83, 2010, Proceedings of the SEM Annual Conference & Exposition on Experimental and Applied Mechanics, Indianapolis, IN, June 7 - 10 (2010)

Staab, G.H., Gilat, A.: A direct-tension split Hopkinson bar for high-strain-rate testing. Exp. Mech. **31**, 232-235 (1991).

Subhash, G. Ravichandran, G.: Split Hopkinson Bar Testing of Ceramics, ASM Handbook on Mechanical Testing and Evaluation, Vol. 8, H. Kuhn and D. Medlin (Eds.), pp. 497-504, ASM International (2000).

Sun, C.T., Han, C.: A method for testing interlaminar dynamic fracture toughness of polymeric composites. Composites Part B: Eng. **35**, 647-655 (2004)

Suresh, S., Nakamura, T., Yeshurun, Y., Yang, K.H., Duffy, J.: Tensile fracture-toughness of ceramic materials – effects of dynamic loading and elevated-temperatures. J. Amer. Ceram. Soc. **73**, 2457-2466 (1990)

Trautmann, A., Siviour, C.R., Walley, S.M., Field, J.E.: Lubrication of polycarbonate at cryogenic temperatures in the split Hopkinson pressure bar. Int. J. Impact Eng. **31**, 523-544 (2005)

Ueberschlag, P.: PVDF piezoelectric polymer. Sensor Rev. **21**, 118-125 (2001)

Wang, L.-L.: Foundations of stress waves. Elsevier (2007)

Warren, T., Forrestal, M.J.: Effects of strain hardening and strain-rate sensitivity on the penetration of aluminum targets with spherical-nosed rods. Int. J. Impact Eng. **35**, 3737-3753 (1997)

Warren, T.L., Forrestal, M.J.: Comments on the effect of radial inertia in the Kolsky bar test for an incompressible material. Exp. Mech. (in press), DOI 10.1007/s11340-009-9322-x (2010)

Weerasooriya, T., Moy, P., Casem, D., Cheng, M., Chen, W.: A four point bending load technique for determination of dynamic fracture toughness for ceramics. J. Amer. Ceram. Soc. 89, 990-995 (2006)

Wischmann, K.B., Assink, R.A.: A removable encapsulant-polystyrene foam. SAMPE J. March/April, 15–19 (1977)

Wu, X.: Study of dynamic properties of steel fiber reinforced high strength concrete. Ph.D. Thesis, Univ. Sci. Technol. China (2006) (in Chinese)

Zencker, U., Clos, R.: Limiting conditions for compression testing of flat specimens in the split Hopkinson pressure bar. Exp. Mech. **39**, 343-348 (1998)

Zhao, H., Gary, G.: On the use of SHPB techniques to determine the dynamic behavior of materials in the range of small strains. Int. J. Solids Struct. **33**, 3363-3375 (1996)

Zhao, H., Gary, G.: A new method for the separation of waves. application to the SHPB technique for an unlimited duration of measurement. J. Mech. Phys. Solids **45**, 1185–1202 (1997)